Electric control of skyrmions for spintronic applications

Charles-Elie Fillion

▶ **To cite this version:**

Charles-Elie Fillion. Electric control of skyrmions for spintronic applications. Material chemistry. Université Grenoble Alpes [2020-..], 2023. English. NNT : 2023GRALY005 . tel-04122631

HAL Id: tel-04122631
https://theses.hal.science/tel-04122631

Submitted on 8 Jun 2023

HAL is a multi-disciplinary open access archive for the deposit and dissemination of scientific research documents, whether they are published or not. The documents may come from teaching and research institutions in France or abroad, or from public or private research centers.

L'archive ouverte pluridisciplinaire **HAL**, est destinée au dépôt et à la diffusion de documents scientifiques de niveau recherche, publiés ou non, émanant des établissements d'enseignement et de recherche français ou étrangers, des laboratoires publics ou privés.

THÈSE

Pour obtenir le grade de

DOCTEUR DE L'UNIVERSITÉ GRENOBLE ALPES

École doctorale : PHYS - Physique
Spécialité : Physique des matériaux
Unité de recherche : Spintronique et Technologie des Composants

Contrôle électrique des skyrmions en vue d'applications spintroniques

Electric control of skyrmions for spintronic applications

Présentée par :

Charles-Elie FILLION

Direction de thèse :

Claire BARADUC Ingénieur HDR, CEA Centre de Grenoble	Directrice de thèse
Hélène BEA MAITRE DE CONFERENCES, Université Grenoble Alpes	Co-encadrante de thèse

Rapporteurs :

ANDRE THIAVILLE
Directeur de recherche, CNRS DELEGATION ILE-DE-FRANCE SUD
MICHEL HEHN
Professeur des Universités, UNIVERSITE DE LORRAINE

Thèse soutenue publiquement le **12 janvier 2023**, devant le jury composé de :

FELIX CASANOVA Directeur de recherche, CIC nanoGUNE	Examinateur
NORA DEMPSEY Directeur de recherche, CNRS DELEGATION ALPES	Examinatrice
LIZA HERRERA-DIEZ Chargé de recherche HDR, CNRS DELEGATION ILE-DE-FRANCE SUD	Examinatrice
LILIANA BUDA PREJBEANU Professeur des Universités, GRENOBLE INP	Présidente
ANDRE THIAVILLE Directeur de recherche, CNRS DELEGATION ILE-DE-FRANCE SUD	Rapporteur
MICHEL HEHN Professeur des Universités, UNIVERSITE DE LORRAINE	Rapporteur

Electrical control of magnetic skyrmions for spintronic applications

---

Author:
Charles-Élie Fillion

Supervisors:
Prof. Hélène Béa
Dr Claire Baraduc

A thesis submitted in fulfillment
of the requirements for the degree of
Doctor of Philosophy

SPINtronique et TEchnologie des Composants
École Doctorale de Physique de Grenoble

Université Grenoble Alpes
Grenoble, France

January 2023

Electrical control of magnetic skyrmions for spintronic applications, © January 2023

Author:
Charles-Élie Fillion

Supervisors:
Prof. Hélène Béa
Dr Claire Baraduc

Institute:
Université Grenoble Alpes, Grenoble, France

ACKNOWLEDGMENTS

Cette période de thèse à SPINTEC a été une expérience extraordinaire, que je considère comme mon apogée en termes de bonheur, d'épanouissement personnel et professionnel. J'en ressors même convaincu d'avoir trouvé mon idéal de vie dans la région de Grenoble, et je compte bien y revenir pour cette raison. J'y ai trouvé tout ce qui pour moi mène à un équilibre : des personnes incroyables, dont la plupart sont aujourd'hui mes ami(e)s, un environnement de travail exceptionnel et une recherche de qualité. Pour cette raison, vous remercier tous au travers de quelques paragraphes est impossible, et selon moi, la meilleure façon de vous remercier comme il se doit est de vous revoir pour passer du bon temps ensemble.

Je voudrais commencer par remercier Sébastien Petit-Watelot pour m'avoir mis en contact avec Claire Baraduc et Hélène Béa, qui sont devenues quelques mois plus tard mes directrices de thèse.

Je souhaite donc par dessus tout vous remercier, Claire et Hélène, pour avoir fourni un cadre de travail très agréable et motivant tout au long de ce travail de thèse. Comme j'avais l'habitude de le dire : vous faites une super équipe ! Votre complicité, votre bonne humeur et votre savoir favorisent un environnement de travail très efficace et agréable. Et quand malgré tout, les choses deviennent difficiles, vous trouvez les bons mots, ou la bonne plaque de chocolat Bonnat, pour se remettre d'aplomb !

Je voudrais aussi particulièrement remercier les occupants du bureau 424, avec qui j'ai partagé mon quotidien ! Merci à toi Éric, pour tes blagues d'une grande finesse, nos discussions et nos pauses café très réparatrices, nos soirées jeux, et tous les moments vécus ensemble qui m'ont été du plus grand soutien (et c'est loin d´être fini !). Merci aussi à toi Jérôme pour ta bonne humeur, pour les discussions intéressantes et les conseils que tu as pu me donner. Merci aussi à Sylvain Moulis pour (entre autres) m'avoir tant aidé sur mes programmes Python ahah. Merci également à toi Johanna pour ton smile et ta tchatch légendaire au quotidien, ainsi que pour avoir refait la déco de mon bureau avec très bon goût !

Cette thèse n'aurait pas été aussi agréable à vivre sans tous les moments passés en dehors du laboratoire avec des personnes incroyables, que je tiens à remercier ici. Au cours de cette thèse, j'ai même découvert la recette du bonheur : une bonne soirée jeux avec Stef et Wissal, et un bon taco ! Merci à vous pour tous ces bons moments vécus ensemble, et auxquels je suis si attaché aujourd'hui. Merci à Fred et Sophie, avec qui les moments passés ensemble, bien que trop rares à notre goût, sont plus que ressourçants. Un grand

merci à Samuel pour tous les bons moments passés ensemble, pour ta bonne humeur naturelle et inébranlable et pour ta bienveillance quotidienne. Un grand merci pour les soirées, les balades à vélo, les bivouacs, les randos et l'alpi ensemble, pour tous ces moments de pure vie ! Merci aussi à Aurélie pour ton sourire et ta bonne humeur ! Mais aussi pour les balades à vélo, les randos et les soirées ! Je remercie également Capucine et Hanna, pour votre gentillesse, vos gestes quotidiens et vos fous-rires légendaires. Merci également à Mattéo pour ta bonne humeur, pour les randos et tous les bons moments passés ensemble. Merci au poto Andréa pour l'initiation au ski freestyle, et pour les supers soirées et moments passés ensemble. Merci à toi Javier pour les supers fêtes, les randos, le ski et même l'alpinisme dans lesquels tu as immortalisé ce moment où je fais ma déclaration à Solène. Merci à Yohanna Bouvetier, la meilleure des voisines !! Merci pour ton accueil, sans lequel on aurait dormi par terre, et toutes les supers soirées ! Je voudrais aussi remercier la fine équipe des Zous, pour ces week-ends de folie (Margot, JC, Marie, Seb, Eline, Thib, Guigui, Margot, Nico) ! Je voudrais aussi remercier tant de personnes, toutes aussi incroyables les unes que les autres : Khasan (merci pour le tubeteika, maintenant dans mon bureau en Espagne), Joseba (the rocket !), Libor (the rocket 2 !), Laura (merci pour ta bonne humeur légendaire), Pau, Nuno, Louis, Quentin, Miina, David, Ryuhei (merci pour cette nuit mémorable à la Nouvelle-Orléans), Kaushik (merci pour les conseils de Talent House, c'est très sympa !) Thomas, Ralph, Colin (merci à toi et Johanna pour les bons souvenirs de Pralognan), Lucile (merci pour ta bonne humeur ! !), Ahmed, Salvatore, Georgy, Jérémie, Zakaria.

Je tiens également à remercier de nombreuses personnes qui m'ont beaucoup aidées au laboratoire et dans la vie de tous les jours : merci à Laurent Ranno pour les belles discussions et les conseils que tu as partagés avec moi. Merci également à Liliana pour ta bienveillance, et tous les conseils que tu m'as donnés. Pour les mêmes raisons, un grand merci à Gilles Gaudin (et merci aussi de m'avoir motivé à finir mon premier St Eynard à vélo !). Merci à Mair pour ta gentillesse et pour les discussions très intéressantes, ainsi que pour les moments captivants "histoire et généalogie de la spintronique". Merci à Jérôme Faure-Vincent pour les discussions revigorantes autour d'un café. Merci à Olivier Boulle, Olivier Fruchart, Bernard Dieny, Vincent Baltz et Kevin Garello pour les discussions pleines de physique intéressante. Merci à Raj Kumar pour m'avoir transmis ses connaissances au début de la thèse, et pour ta bienveillance et ta gentillesse. Merci à Aymen Fassatoui pour ton aide précieuse à utiliser l'ALD. Merci aussi à l'équipe du Laboratoire des Sciences des Procédés et des Matériaux (LSPM) à Villetaneuse pour votre acceuil et votre aide à réaliser les mesures BLS, pilier de ce travail. Ainsi, un grand merci à Djoudi Ourdani, Mohamed Belmeguenai, Yves Roussigné et Salim-Mourad Chérif. Merci à Aurélien Masseboeuf, Mihai Miron pour les conseils et les discussions. Merci également à Stéphane Auffret pour ta bonne humeur, ta tchatch légendaire, et pour tous les supers dépôts d'une reproductibilité sans faille qui ont conduit aux résultats de cette thèse. Merci à Eric Billiet, Philippe Sabon, Isabelle Joumard et Christophe Lemonias pour votre aide précieuse dans le quotidien d'un expérimentateur. Merci également à Catherine Broisin,

Céline Bellavia et Adriana Stoenesciu pour votre sourire et votre aide dans les tâches administratives.

Et finalement, il est plus qu'important de noter que tout cela n'aurait été possible sans le soutien sans faille de mes proches, qui sont l'un des piliers les plus importants de mon équilibre et de mon bien-être. Ainsi, je souhaite remercier ma compagne, Solène, pour les concessions que tu as faites, et que tu continues de faire pour nous. Sans toi, rien de tout cela ne serait possible. Je souhaite aussi remercier ma belle famille, pour être si apaisante et bienveillante: merci à Catherine, Jean-Marie, Hélène, Clément et Pierre (merci aussi pour les supers week-end ski ou rando !). Merci aussi à mes parents, Valérie et Jean-Marc, pour leur solide soutien et le réconfort qu'ils peuvent me procurer dans toutes les épreuves de la vie. Merci à mes frères, Alexandre et Pierre, pour ces moments passés ensemble et cette complicité à toute épreuve. A nous trois, on est inébranlables et forts. Merci à ma tati Marie-Claire pour les moments passés ensemble, de bienveillance et de légèreté qui font tant de bien et nous ramènent à l'essentiel. Merci à mes grands-parents Michèle et Jean-Claude pour les mêmes raisons. Pour finir, et bien qu'ils ne soient plus là, je remercie mes grands-parents, Madelon et Guy, pour tous ces bons souvenirs auxquels je suis accroché, et qui me font beaucoup de bien dans les moments difficiles.

CONTENTS

LIST OF FIGURES

LIST OF TABLES

..

ACRONYMS

iDMI - interfacial Dzyaloshinskii-Moriya Interaction
SOT - Spin-Orbit Coupling
CW - Clockwise
CCW - Counterclockwise
CIM - Current-Induced Motion
FIDWN - Field-Induced Domain Wall Motion
PMA - Perpendicular Magnetic Anistropy
OOP - Out Of Plane
IP - In-plane
VCMA - Voltage Control of Magnetic Anistropy
VCDMI - Voltage Control of Dzyaloshinskii-Moriya Interaction
DL - Damping Like
FL - Field Like
PM - Paramagnetic
FM - Ferromagnetic
HM - Heavy-Metal
SkHE - Skyrmion Hall Effect
SkHA - Skyrmion Hall Angle

ABSTRACT

Facing with the ever-increasing demand for data storage and fast computing in a future energy sober society is a challenge that is difficult for microelectronics to meet. In this regard, spintronic stands as the most promising alternative to complement standard microelectronics. As its name suggests, spintronic uses the spin magnetic moment of the electrons (in addition to its electric charge) to store and process information at the nanoscale.
Notably, information processing is one of the growing fields of spintronics, and one of the most promising information carrier is the magnetic skyrmion: a nanometer size, circular magnetic object with particle-like properties. Within a skyrmion, the magnetization rotates with a fixed direction, defining its chirality (clockwise or counter-clockwise), fixed by the sign of the interfacial Dzyaloshinskii-Moriya Interaction (iDMI). The iDMI is present in particular in magnetic ultrathin trilayers composed of heavy-metal/ferromagnet/metal-oxide (HM/FM/MO_x). In such trilayers, a precise local and dynamic control of the iDMI is still missing for an efficient control of the skyrmion properties. In this thesis work I report on the experimental observation of two distinct ways of controlling the iDMI amplitude and more importantly, its sign.
On the one hand, I show that the iDMI sign can be tuned by the material parameters. In Ta/FeCoB/TaO_x trilayer, we found that modulation of the FeCoB thickness or the oxidation state at the FeCoB/TaO_x interface both lead to an inversion of the iDMI sign. In addition I show that the iDMI sign crossover is accompanied by an inversion of skyrmion chirality, as confirmed by the opposite direction of motion of magnetic skyrmions under current injection.
On the other hand, I show for the first time that the iDMI sign can be reversed with a gate voltage leading to a local and dynamical control of the skyrmion chirality. It is attributed to magneto ionic effects, since a positive (resp. negative) gate voltage leads to the reduction (resp. oxidation) of the FeCoB/TaO_x interface, allowing to change iDMI sign by applying the appropriate voltage polarity.
Finally we performed micromagnetic simulations and developed analytical models for a deeper understanding of the effect of an iDMI amplitude and sign modulation on the skyrmion. We show that a fine control of the iDMI allows for a fine tuning of (i) the skyrmion equilibrium structure and (ii) the skyrmion dynamic properties, such as its trajectory angle under injected current. It allows notably to suppress the skyrmion Hall effect, detrimental for applications. Realizing experimentally such fine control of skyrmion properties would pave the way towards all-electrical, power efficient spintronic devices and multidirectional logic functionalities.

RÉSUMÉ

Faire face à la demande toujours croissante de stockage de données et de calcul rapide dans une société qui doit tendre vers la sobriété énergétique est un défi difficile à relever pour la microélectronique. À cet égard, la spintronique se présente comme l'alternative la plus prometteuse pour complémenter l'électronique standard. Comme son nom l'indique, la spintronique utilise le spin des électrons en plus de leur charge électrique pour stocker et traiter les informations à l'échelle nanométrique.

L'application de la spintronique au traitement de l'information est un sujet en pleine expansion, pour lequel le skyrmion magnétique est un candidat prometteur. Il s'agit d'un objet magnétique circulaire de taille nanométrique envisagé comme le futur porteur d'information dans les dispositifs spintroniques. Dans un skyrmion, l'aimantation tourne dans une direction fixe, définissant sa chiralité (horaire ou anti-horaire), fixée par le signe de l'interaction interfaciale dite de Dzyaloshinskii-Moriya (iDMI). L'iDMI est présente en particulier dans les tricouches magnétiques ultraminces composées de métal-lourd/ferromagnétique/oxyde métallique (HM/FM/MO_x). Dans ces matériaux, un contrôle précis, local et dynamique de l'iDMI est encore à démontrer pour un contrôle efficace des propriétés du skyrmion. Dans ce travail de thèse, je rapporte l'observation expérimentale de deux méthodes distinctes pour contrôler l'amplitude de l'iDMI et, plus important encore, son signe.

D'une part, je montre que le signe de l'iDMI dépend des paramètres matériau. Dans une tricouche Ta/FeCoB/TaO_x, nous avons montré que le signe de l'IDMI peut être inversé avec une modulation de l'épaisseur de FeCoB ou de l'état d'oxydation à l'interface FeCoB/TaO_x. De plus, l'inversion du signe de l'iDMI s'accompagne d'une inversion de la chiralité des skyrmions, comme le confirme de changement de direction des skyrmions mis en mouvement par un courant électrique.

D'autre part, nous montrons pour la première fois que le signe de l'iDMI peut être inversé avec une tension de grille, conduisant à un contrôle local et dynamique de la chiralité du skyrmion. Nous attribuons cela à des effets migration ioniques qui modifient l'état d'oxydation d'interface, dont le signe de l'iDMI dépend.

Enfin, grâce à des simulations micromagnétiques et des modèles analytiques, nous avons réalisé une étude plus approfondie qui montre qu'un contrôle fin de l'amplitude et du signe de l'iDMI permet d'ajuster (i) la structure d'équilibre du skyrmion et (ii) ses propriétés dynamiques, comme l'angle de sa trajectoire sous courant injecté, permettant notamment de supprimer l'effet Hall skyrmionique, indésirable pour les applications. La réalisation expérimentale d'un tel contrôle fin des propriétés du skyrmion ouvrirait la voie à des dispositifs spintroniques tout électriques, économes en énergie et à des portes logiques multidirectionnelles.

INTRODUCTION / OUTLINE

In the current societal and environmental context, our society is facing a situation in which current microelectronics is challenged: On the one hand, an ever-growing demand for data storage and fast information processing and, on the other hand, a concern for low energy consumption. Although these two aspects are fundamentally incompatible, spintronics is a very promising research field which can complement microelectronics and fulfill criteria of new generation devices.

As its name suggests, spintronics involves the active control and manipulation of spin degree of freedom of the electrons in solid-state systems. The rise of spintronics in the microelectronic market started in 1988 [1] with the discovery of the Giant Magneto Resistance (GMR) [2], which earned Albert Fert and Peter Grünberg the Nobel Prize in 2007. Since this date, spintronics is considered as the best candidate for next generation low power devices [3] and is a rapidly rising research field (see Fig. 0.1a). Nowadays, spintronics is omnipresent in several devices of the everyday life, such as the read head of the Hard Disk Drives, and many other spintronics sensors in smartphones, cars, robotics etc. The advantages of spintronic sensors is their high sensitivity to small magnetic signal [4], their small dimensions and reduced cost [5]. Another major breakthrough of spintronics is the Magnetic Random Access Memory (MRAM) [6]. When the standard RAMs (the Dynamical or Static Random Access Memory (resp. SRAM and DRAM)) continuously consume energy to conserve information, the spintronic devices such as the MRAM have the advantage on non-volatility and thus low power consumption. Spintronics is also a very good candidate for unconventional computing, replacing the Von-Neumann architecture (where memory and computing are done in two separated units) to an architecture in which computing and memory are in the same unit, limiting the energy losses. Such in-memory computing is naturally done in the human brain, and spintronics should be able to mimic this behaviour in the rising field of neuromorphic spintronics [7]. Other important aspects of spintronic is the ability to generate high frequency signal on a broad frequency range (300 kHz- 8 GHz [8]), and to realize spin to charge interconversion.

In this growing field of spintronics, this thesis focuses on a promising magnetic object: the magnetic skyrmion [9], which rapidly became a *hot* topic in spintronic research (see Fig. 0.1b). It is one of the smallest existing magnetic object, a magnetic quasiparticle (see inset of Fig. 0.1b) with sizes down to a few nanometer. Skyrmions are envisioned as the future information carrier in spintronics memory and computing devices [10], such as skyrmion based racetrack memories [11]. On the one hand, the presence or absence of a skyrmion can be detected electrically [12], which respectively defines the logical "1" and

"0". On the other hand, skyrmions can be efficiently manipulated by electrical currents [13], at velocities up to km/s [14]. These two aspects associated to the very small size of the skyrmion would allow high storage densities and fast information processing. The efficient motion of magnetic skyrmions in designed tracks is also envisioned to realize next generation logic devices [15–19] and neuromorphic computing [20, 21].

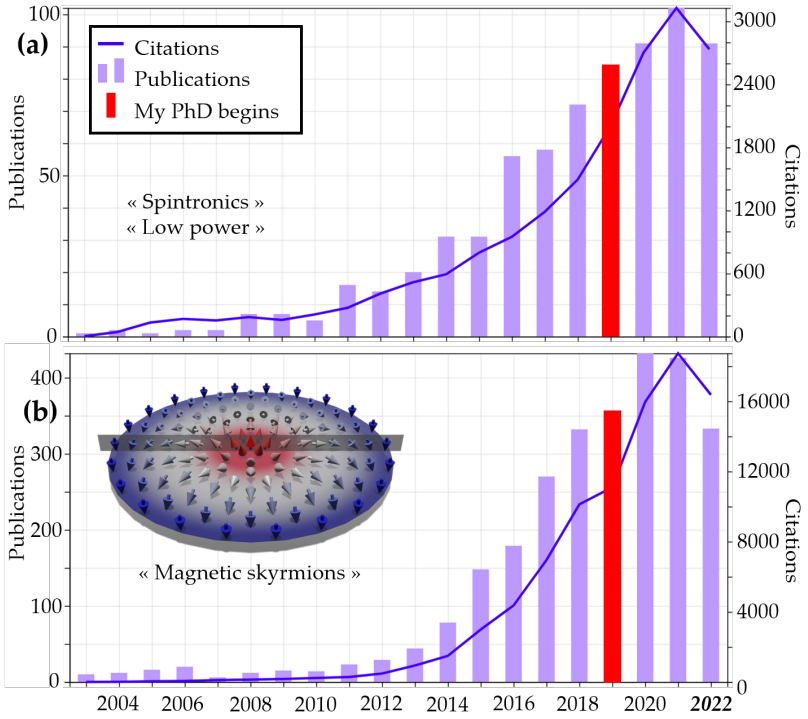

Figure 0.1: **Skyrmions in low power spintronics: a growing topic:** (a) Number of publications (left) and citations (right) including the key-words "spintronics" and "low power" (extracted from [22]). (b) Number of publications (left) and citations (right) including the key-words "magnetic skyrmions" (extracted from [23]).

However, at the beginning of this thesis, the logic gate functionalities and geometries based on skyrmions were limited due to a lack of efficient local and dynamical tuning of skyrmions static and dynamic properties. The control of skyrmion properties requires a fine tuning of the interaction that stabilizes it: the Dzyaloshinskii-Moriya Interaction (DMI) [24–26]. My PhD work was motivated by such need and aimed at providing answers to improve the control of skyrmion properties in HM/FM/MO_x trilayers, where the DMI has interfacial origins and is thus called interfacial DMI (iDMI). In this way, the gate voltage emerged as a promising, low power and versatile technique to achieve both a local and dynamical control of interfacial magnetism and notably of iDMI. We experimentally demonstrated in this thesis two different ways for a fine tuning of the iDMI amplitude and more importantly sign, in HM/FM/MO_x: (i) a material dependent tuning, and (ii) the application of a gate voltage. Using this additional degree of freedom, I performed a theoretical study of the effect of a fine iDMI modulations on the static and dynamic properties of skyrmion in low iDMI systems, through analytical model and micromagnetic simulations.

Outline

This thesis manuscript is divided into three main parts : Background, Methods and characterization techniques and a Results part. Each part is divided into several chapter so that, overall, this work is organized as follows:

Part I : Background

Chapter 1 establishes the essential knowledge for the understanding of this PhD work. Notably I present the different magnetic energies/interactions whose competition determines the equilibrium magnetic configuration in a ferromagnet. I give a special focus to magnetic trilayer heterostructure composed of heavy-metal/ferromagnet/metal-oxide, which is the structure of interest in this thesis work.

Chapter 2 introduces the different magnetization configuration resulting from the competition between the magnetic energies. It presents the magnetic domains and domain walls and more importantly the magnetic skyrmions, which is the magnetic object of interest of this thesis work. It describes both the static and dynamic properties of these objects.

Part II : Methods and characterization techniques

Chapter 3 is dedicated the the different experimental techniques I used in this thesis work that helped obtaining the results presented in the next chapters. I give a global overview of the sample manufacturing (from the thin film deposition to the patterning of the voltage electrode) and characterization (presentation of the main characterization techniques used to obtain the results).

Part III : Results

Chapter 4 presents the magnetic properties of the sample, composed of Ta/FeCoB/TaO_x. I introduce the richness of the physics in such trilayer by presenting the variety of magnetic states present on a unique sample. More importantly, I show that our sample allows to ensure the stabilization of magnetic skyrmions and to study their properties as a function of material parameters. In particular I present the material dependence of the iDMI, whose sign can be inverted by tuning the FeCoB thickness or the oxidation state at the FeCoB/TaO_x interface. I also show that the iDMI sign inversion is accompanied by an inversion of the skyrmion chirality, through the inversion of their current induced motion direction.

Chapter 5 presents the main experimental result obtained in this thesis work: I show that the application of a gate voltage to the magnetic sample can locally and dynamically

invert the chirality of skyrmions and magnetic domain walls. Such an observation is attributed to the inversion of the sign of the interaction at the origin of magnetic skyrmions (the iDMI).

Chapter 6 is a theoretical study, motivated by the experimental observation from the previous chapter. It shows that a fine control of the iDMI leads to a precise control of both the skyrmion equilibrium structure (helicity, chirality, radius etc.) and its dynamics driven by spin orbit torques (trajectory angle, skyrmion Hall effect, velocity etc.). In each case, I compare micromagnetic simulations to an analytical model that we have developed. Based on the previous chapter, it allows to envision a very fine tuning of skyrmion motion with a gate voltage. This all electrical, low power control of skyrmion trajectory is of high interest for future skyrmion-based logic devices.

Chapter 7 contains the general conclusion and the perspectives of this work.

Annexes

Annex 8.1 shows the details about the calculation of the magnetic energies in the micromagnetic framework.

Annex 8.2 contains details about the origin of orbital and spin momenta of the electron and presents the physics of the spin-orbit interaction.

Annex 8.3 presents a derivation of the classical profile of a Bloch domain wall from the energy functional.

Annex 8.4 contains details about the skyrmion winding number, as well as a derivation of its expression.

Annex 8.5 presents a derivation of Thiele equation from the LLG equation, and applied the Thiele equation to our sample geometry.

Annex 8.6 contains details about the Brillouin Light Scattering technique, and a derivation of the expression that allows to extract iDMI from this technique.

Annex 8.7 presents a simple model that allows to obtain the current distribution in a full-sheet sample, and thus to estimate the current density.

DEDICATION

À ma grand-mère, Madelon.

1 INTERFACIAL MAGNETISM

This chapter introduces the physics of the magnetic system studied in this thesis, which consists in an ultrathin magnetic film, stacked between two different materials. After introducing basic and general concepts in magnetism, I progressively focus on interfacial magnetism in our trilayer samples composed of heavy-metal/ferromagnet/metal-oxide.
I present the different magnetic energies that compete to result in the magnetic object that is studied in this work: the magnetic skyrmion. Then, I give a brief state of the art of the tunability of magnetic properties in this kind of sample. I show that the interfacial magnetism in our sample depends on the deposition and material parameters, and can be tuned after the deposition by applying a gate voltage across the trilayer.

In nature, magnetic materials are exceptions. Most isolated atoms are magnetic due to the motion of unpairred electrons in the outermost orbitals. However, when atoms come together to form condensed matter, the orbitals fill up to form the bonds, and the magnetism is generally lost. But there are some exceptions, for which some orbitals are not full. In this case, every single atom in the material carry a magnetic moment, whose origin is twofold:

- **Orbital magnetic moment** $\vec{m}_L = -\mu_B \frac{\vec{L}}{\hbar}$ with μ_B the Bohr magneton, $\hbar$ the reduced Planck constant and $\vec{L}$ is the electron orbital angular momentum. It is called "orbital" magnetic moment because, in a simple picture, the electrons orbiting around the nuclei generate current loops at the origin of this magnetic moment. However, orbital moment is not sufficient to account for the whole magnetization of a magnetic material.
- **Spin magnetic moment** $\vec{m}_S = -2\mu_B \frac{\vec{S}}{\hbar}$ with $\vec{S}$ is the electron spin angular momentum. In addition to their orbital motion, each electron can be seen (in a classical way) as spinning entities, which generate an additional intrinsic magnetic moment, so called the spin.

Thus, a magnetic material can be seen as an assembly of atomic magnetic moments interacting together in different ways, leading to the different magnetic behaviours described below. Among the different magnetic behaviours, this work focuses on ferromagnetic materials (see below), which owe their magnetism mostly to the spin momentum. Thus, in the following, the magnetic moment of each atomic site i is called the spin[1], $\vec{S}_i$ (in A·m²). The magnetization $\vec{M}$ (in A/m) is defined as the volume density of magnetic moment and the saturation magnetization M_S is the maximum magnetization the solid can have when all the magnetic moments are aligned.

1.1 MAGNETIC BEHAVIOURS

The existence or the absence of atomic magnetic moments, as well as their relative orientation, give rise to several magnetic behaviours, described below. It is possible to classify magnetic material by their response to an external magnetic field H, through the magnetic susceptibility, defined as $\chi = \frac{M}{H}$ (or $\chi = \left.\frac{dM}{dH}\right|_{H=0}$ in case of non-linear behaviours)

Diamagnetism: Most of the materials are diamagnetic[2]. It corresponds to the situation where all the electrons are paired and there is no net magnetic moment per atom, leading to zero magnetization. This type of material is often thought as non-magnetic but in the presence of an external magnetic field, a small induced magnetic moment is created in the opposite direction by the electron cloud (Lenz like effect, see Fig. 1.1a). The effect is very small, corresponding to negative magnetic susceptibilities $\chi \simeq -10^{-6}$ to -10^{-5}.

1 If we refer to the spin of the electron, it will be clearly precised
2 All materials present diamagnetism, but it is not always the predominant behaviour

Paramagnetism: In this kind of material, unpaired electrons from inner orbitals contribute the the establishment of a net magnetic moment per atom. However, the interaction between atomic magnetic moments is weak and thermal agitation leads to a randomization of their direction, leading to a zero net magnetization in the absence of external magnetic field (top part of Fig. 1.1b). Nevertheless, an applied magnetic field results in an partial alignment of the atomic moments in the direction of the magnetic field resulting in a net magnetization (bottom part of Fig. 1.1b). The response of the material to the magnetic field is thus characterized by a positive susceptibility, about $\chi \simeq 10^{-5}$ at room temperature.

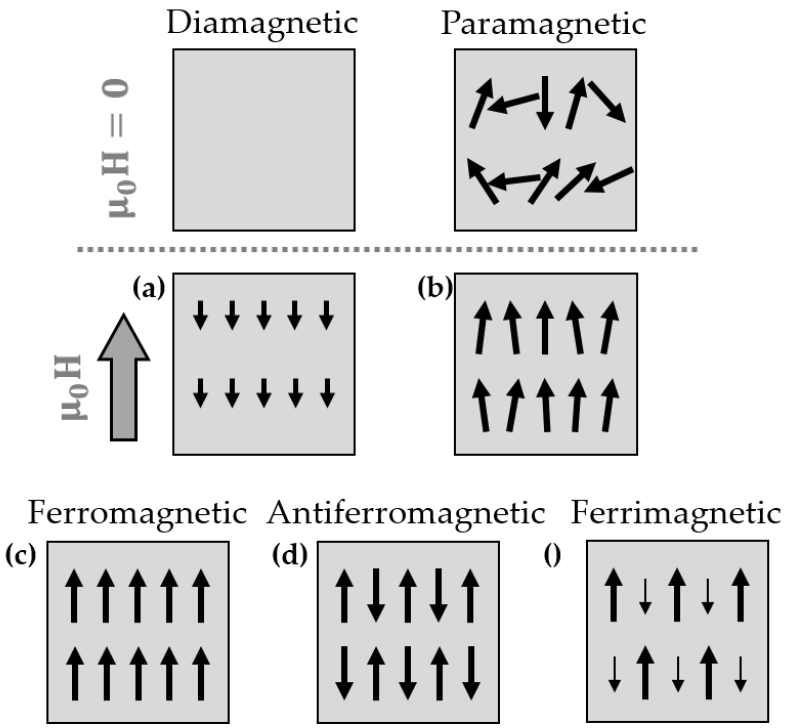

Figure 1.1: **Different types of magnetic ordering:** (a) Diamagnetic ordering (b) paramagnetic ordering (for (a) and (b) the top (resp. bottom) part corresponds to non-zero (resp. zero) applied magnetic field, whose direction is depicted by the gray arrow) (c) Ferromagnetic ordering (d) antiferromagnetic ordering and (e) Ferrimagnetic ordering

Ferromagnetism: Similarly to paramagnetic materials, in ferromagnetic material every atomic site carries a net magnetic moment. However in this case, the Heisenberg exchange interaction between neighbouring moments (see next section) is stronger than thermal agitation, resulting in their alignment in the same direction (see Fig. 1.1c). This ordering exists below a critical temperature, called the Curie Temperature T_C. Above T_C, a ferromagnetic material becomes paramagnetic, the thermal agitation overcoming the Heisenberg exchange. More precisely, below T_C, magnetic moments are aligned in small regions called magnetic domains (see Sec. 2.1), and the ferromagnetic material consists of neighbouring domains which are individually ordered but collectively point in different directions. Consequently, for $T < T_C$, a ferromagnetic material is characterized by a local net magnetization in the absence of magnetic field. Contrary to diamagnetism or paramagnetism the relation between M and H is not linear. Thus, the magnetic

susceptibility of a ferromagnetic material is defined as $\chi = \frac{dM}{dH}\Big|_{H=0}$, typically about 10^4 to 10^6, much larger than for diamagnetic or paramagnetic materials.

Antiferromagnetism: Antiferromagnets are another kind of magnetically ordered material, but contrary to ferromagnets, there is a tendency for neighbouring spins to be oriented in opposite directions (see Fig. 1.1d), because of the negative exchange interaction between them (see next section). It can be the case of a compound material having to sub-lattices of opposite and equal magnetization. Consequently, there is zero net magnetization although the material is magnetically ordered. In this case the ordering temperature is called the Néel temperature, T_N, from the name of the physicist who discovered this class of magnetic materials in the early 1940's. Similarly to ferromagnetism, the material becomes paramagnetic above T_N. The typical susceptibility of antiferromagnetic material is much weaker than for ferromagnetic material, because the magnetic field has a weak effect on magnetic moments compared to the strong negative exchange interaction between neighbouring spins.

Ferrimagnetism: Ferrimagnets correspond to a peculiar case of antiferromagnets in which the magnetization of the two sub-lattices are pointing in the opposite direction but do not compensate (see Fig. 1.1e). Ferrimagnets thus exhibits a non-zero net magnetization and behave like ferromagnet, even if the ordering of their atomic moments is different. Moreover, the variation of the magnetization versus temperature can be different for the two sub-lattices, resulting in complex $M_S(T)$ curves.

Note also that magnetic order can also be artificially synthesized. For example, the Synthetic Anti-Ferromagnets (SAFs) consist in a stacking of ferromagnetic layers which are antiferromagnetically coupled through a non-magnetic spacer such as Ruthenium [27]. This kind of material is very promising in spintronics, notably because the net zero magnetization leads to zero stray field, allowing miniaturization of the devices. Moreover, such a material triggered a huge interests for skyrmion dynamics since skyrmions can be moved efficiently by electrical current in SAFs, without the undesired skyrmion Hall effect [28–31] (see Sec. 2.6).

In the context of this work we will focus on ferromagnetic materials in the form of ultrathin films, whose thickness is typically of one nanometer. More precisely, throughout this thesis the discussions are oriented toward magnetic trilayer heterostructures defined by heavy-metal/ferromagnet/metal-oxide (HM/FM/MO_x)[3]. In this kind of layered structure there are many properties stemming from the ferromagnet interfaces, that we propose to present in the following sections.

3 The notation A/B/C means that A is the bottom layer (first deposited) and C is the top layer (last deposited).

1.2 MAGNETIC ENERGIES

In any ferromagnetic material, the balance of magnetic energies governs the equilibrium magnetization configuration and the dynamical behaviour[4] of any spin texture [32]. It is usually considered that the equilibrium state of a ferromagnetic material is the result of the competition between four energy terms : the Zeeman, exchange, dipolar and anisotropy energies. In the following we introduce these four terms, in addition to another one, called the Dzyaloshinskii-Moriya interaction, which also plays a central role in this work.

1.2.1 *Zeeman energy*

The Zeeman energy corresponds to the energy of a magnetic system in an external magnetic field. It favours the alignment of the magnetization along the external magnetic field, and the Zeeman energy density reads as

$$\varepsilon_{Zee} = -\mu_0 \vec{M} \cdot \vec{H}_{ext} \tag{1.1}$$

where $\vec{M}$ is the magnetization (in A/m), $\mu_0 \vec{H}_{ext}$ is the external magnetic field (in T), with $\mu_0 = 4\pi \times 10^{-7}$ kg·m·A^{-2} ·s^{-2} the vacuum permeability. Zeeman interaction is responsible, among other things, for the familiar alignment of the compass with the Earth magnetic field.

1.2.2 *Exchange energy*

This interaction between spins originates from the quantum Pauli's principle associated to the electrostatic repulsion between electrons. As a consequence, in some materials, electrons naturally align their spins in order to minimize the energy. At the atomic scale the expression of this interaction reads as

$$\mathcal{H}_{ex} = -J_{ij} \vec{S}_i \cdot \vec{S}_j \tag{1.2}$$

where J_{ij} (in J) is the exchange constant whose sign favors the ferromagnetic ($J_{ij} > 0$) or the antiferromagnetic ($J_{ij} < 0$) magnetic ordering (see Sec. 1.1), and $\vec{S}_i$, $\vec{S}_j$ are two neighboring spins at atomic sites i and j. By considering an isotropic material, one has $J_{ij} = J \quad \forall (i,j)$, where i and j are neighbouring sites. In the continuous approximation of micromagnetism, the discrete nature of the lattice is ignored and the assembly of atomic spins are replaced by a continuous magnetization field $\vec{M}(\vec{r})$ where $\vec{r}$ is the spatial coordinate and $\vec{M}$ a vector of constant amplitude M_S. It is convenient to define the reduced magnetization $\vec{m} = \frac{\vec{M}}{M_S}$, a unit vector describing locally the orientation of the magnetization. Thus, the micromagnetic energy density associated to the exchange interaction is written as (demonstration in Annex 8.1)

4 Via an effective magnetic field defined in section 2.3 from chapter 2

$$\varepsilon_{ex} = A_{ex}\left[\left(\vec{\nabla}m_x\right)^2 + \left(\vec{\nabla}m_y\right)^2 + \left(\vec{\nabla}m_z\right)^2\right] \tag{1.3}$$

where A_{ex} is called the exchange stiffness constant (in J/m) given by $A_{ex} = JS^2n/a$, with a the lattice parameter, n the number of atoms per unit cell and S the electron spin. The order of magnitude of A_{ex} for ferromagnetic transition metal (Fe, Co, Ni) is in the range 10-30 pJ/m. As well as the sign of J determines the magnetic ordering, its amplitude is related to the Curie or Néel temperature, at which the ordering disappears, leading to a paramagnetic state.

1.2.3 *Demagnetizing energy*

In a ferromagnetic material, the exchange energy locally acts to align magnetic moments in the same direction, generating a dipolar magnetic field which can interact with magnetic objects. On the one hand, if this field interacts with a distinct magnetic object, it is called stray field and the two objects are coupled by a Zeeman interaction.
On the other hand, if this magnetic field interacts with the ferromagnet that generates it, it is called the demagnetizing field $\vec{H}_{dem}$ (because it is opposite to the magnetization as we show below), whose origin can be understood by introducing the concept of magnetic charges: The static maxwell equation $\vec{\nabla}\cdot\vec{B} = \mu_0\vec{\nabla}\cdot(\vec{H}_{dem}+\vec{M}) = 0$ in the absence of external magnetic induction leads to $\vec{\nabla}\cdot\vec{H}_{dem} = -\vec{\nabla}\cdot\vec{M}$. Thus, by analogy to electrostatic charges, one can define the magnetostatic volume charges $\rho_m = -\vec{\nabla}\cdot\vec{M}$. Moreover at the surface, the singularity due to the abrupt transition from $M = M_S$ to $M = 0$ can be lifted by introducing surface magnetic charges $\sigma_m = \vec{M}\cdot\vec{n}$ where $\vec{n}$ is the unit vector normal to the ferromagnet surface. To minimize the energy cost associated to magnetostatic interaction, the magnetization orientates preferentially in direction(s) that minimize(s) the magnetic charges, which is called the *shape anisotropy*. In other words the magnetization orientation depends on the shape of the magnetic object that is considered and, in the case of an homogeneous magnetization (and an object with a second degree surface, like an ellipsoid), the demagnetizing field can be expressed as

$$\vec{H}_{dem} = -\bar{\bar{\mathcal{N}}}\cdot\vec{M} \tag{1.4}$$

where $\bar{\bar{\mathcal{N}}}$ is called the demagnetizing tensor, whose elements are shape-dependent. For an ellipsoid-like shape this tensor is diagonal and of unitary trace ($\mathcal{N}_{xx}+\mathcal{N}_{yy}+\mathcal{N}_{zz} = 1$).
The corresponding energy is expressed as a Zeeman interaction between the magnetization, and the demagnetizing field that it produces

$$\varepsilon_d = -\frac{\mu_0 M_S}{2}\vec{m}\cdot\vec{H}_{dem} \tag{1.5}$$

For example, let's consider a magnetic thin film whose lateral dimension is considered infinitely larger than its thickness t_{FM}. In this case, one has $\mathcal{N}_{xx} \simeq \mathcal{N}_{yy} \simeq 0$ and $\mathcal{N}_{zz} \simeq 1$. Thus, the demagnetizing field being maximum along the normal to the plane, the magnetization is preferentially oriented in the plane, which is called *easy plane anisotropy*. If

we define by θ the angle between the magnetization and the normal to the film plane, from equation 1.4 one has $\vec{H}_{dem} = -M_z\vec{z} = -M_S \cos\theta$. Injecting it in equation 1.5 leads to $\varepsilon_d = \frac{\mu_0 M_S^2}{2} \cos^2\theta$ and thus (up to a constant multiplier)

$$\varepsilon_d = -\frac{\mu_0 M_S^2}{2} \sin^2\theta \tag{1.6}$$

where we usually define $K_d = \frac{1}{2}\mu_0 M_S^2$ as the shape anisotropy constant (in J/m^3), relative to the strength of the dipolar interactions. Such an expression is typical from magnetic anisotropy energy, which is presented with more details in Sec. 1.2.4.

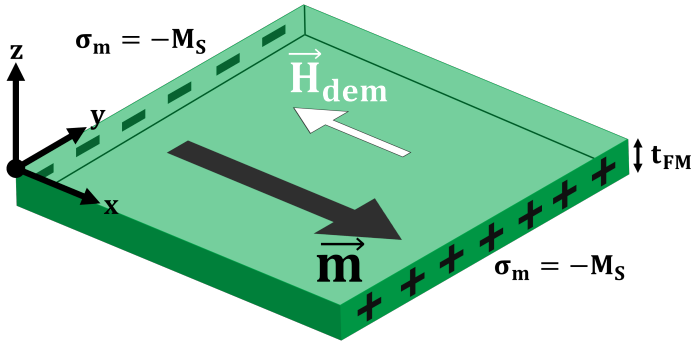

Figure 1.2: **Shape Anisotropy:** In a thin film geometry, the magnetization prefers to lie in the plane (x, y) since it minimizes the total magnetic surface charge σ_m, at the origin of the demagnetizing field $\vec{H}_{dem}$.

In fact, the demagnetizing field has two majors consequences: (i) the *shape anisotropy described above* and (ii) when the exchange wants to align the magnetization on a short range, the demagnetizing field favors an antiparallel configuration on the long-range, resulting in magnetic domains described in Sec. 2.1.

1.2.4 *Magnetic anisotropy energy*

The magnetic anisotropy favors the alignment of the magnetization along preferential axis (resp. plane), called the *easy axis* (resp. *easy plane*). We discussed above the case of the shape anisotropy, arising from the dipolar energy (see Sec. 1.2.3), which favours the magnetization to align along the long dimensions of the sample to minimize the magnetic charges. Here we present two other sources of anisotropy, the magnetocrystalline and surface anisotropies, respectively arising from the bulk of the magnetic material and from its interfaces with other materials.

Magnetocrystalline anisotropy

To understand the magnetocrystalline anisotropy (MCA), it can be useful to remind the Curie principle, saying that "*the symmetries of the causes are to be found in the effects*" [33].

In a solid, if the crystal field[5] is anisotropic, the motion of electrons will be and, by spin orbit coupling (see Sec. 1.2.5), it results in preferential orientation for the magnetization. The easy axis of magnetization are thus linked to the crystal symmetries, and this phenomenon is called MCA. The corresponding energy cost is minimal when the magnetization is aligned with the easy axis/plane and maximum along the hard axis/plane. In the following we focus on one particular kind of magnetic anisotropy which is the uniaxial anistropy, whose energy density is given by

$$\varepsilon_{an}^{MC} = K_{MC} \sin^2 \theta \tag{1.7}$$

where K_{MC} is the MCA constant (in J/m^3). The angle θ correspond to the angle between the magnetization and the easy axis. It is called uniaxial because if $K_{MC} > 0$ the energy cost is minimum when the magnetization is aligned with the easy axis. Otherwise if $K_{MC} < 0$ the the energy cost is minimum when the magnetization is aligned with the hard axis (or hard plane, $\perp$ to the easy axis).

Interfacial anisotropy

As first pointed out by Néel, the broken inversion symmetry at a ferromagnetic interface may induce additional anisotropy energy [34], called surface, or interface anisotropy. In ultra-thin HM/FM/MO$_x$ trilayers, this term can become predominant over the volume contribution (MCA and shape anisotropies) for very small FM thickness (nanometer range). An important consequence of the surface anisotropy is the Perpendicular Magnetic Anisotropy (PMA) in ultra-thin films systems, on which rely most of the recent spintronic devices, like STT-MRAM devices based on magnetic tunnel junctions with PMA [35]. PMA consists in an easy axis for the magnetization which is normal to the sample plane, although not favoured by the shape anisotropy. In the following it is often called out of plane (OOP) magnetization. Since its first experimental observation in a Pd/Co bilayer heterostructure [36], the PMA has been extensively studied in order to understand its origins. It is now established in the literature that the PMA is linked to the FM/MO$_x$ interface oxidation state (through complex hybridization, as shown in Fig. 1.3a), as demonstrated many times using X-ray photoelectron spectroscopy (XPS) [37–39]. Nonetheless, elastic stress due to lattice distortion at the interface (Fig. 1.3b), as well as crystal symmetry breaking at the interface (Fig. 1.3c) have been shown to contribute also to this effect [40]. The energy density associated to the surface anisotropy is written as

$$\varepsilon_{an}^{S} = \frac{K_s}{t_{FM}} \sin^2 \theta \tag{1.8}$$

where K_s is the surface anisotropy constant (in J/m^2) and t_{FM} is the ferromagnetic film thickness.

5 the electric field produced by the surrounding charge distribution of the crystal atoms

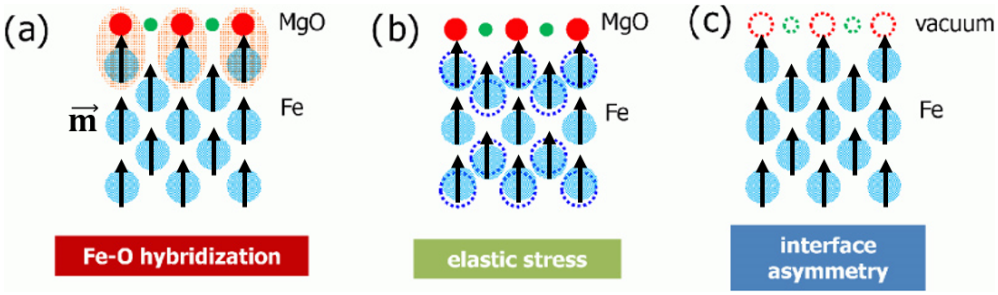

Figure 1.3: **Perpendicular Magnetic Anisotropy in thin magnetic films:** (Adapted from reference [40]) The three origins of PMA at the ferromagnet interface (a) Orbital hybridization: the presence of oxygen atoms at the interface distort the orbitals and leads to complex hybridization that have been linked to the PMA. The blue, green and red circles correspond respectively to Fe, Mg and O atoms. The red ellipses correspond to the Fe-O orbitals hybridization. (b) Elastic stress at the interface, due to the presence of the oxide, the Fe atoms are shifted from ther initial position, depicted by the dotted circles (c) Symmetry breaking at the interface: the dotted circle represent the removed MgO, leading to the inversion symmetry breaking at the new Fe/vacuum interface.

Total effective anisotropy in thin film systems

One can notice that when summing up the energies to get the total energy, it is possible to factorize equation 1.6, equation 1.7 and equation 1.8 which gives a total effective anisotropy energy that reads as:

$$\varepsilon_{an} = K_{eff} \sin^2 \theta \tag{1.9}$$

with an effective anisotropy expressed as the sum of surface and volume contributions [41–45] :

$$K_{eff} = \frac{K_s}{t_{FM}} + K_{MC} - K_d \tag{1.10}$$

where t_{FM} is the ferromagnetic thickness, K_s is the surface anisotropy constant, K_{MC} the MCA constant and $K_d = \frac{1}{2}\mu_0 M_S^2$ the shape anisotropy constant (see Sec. 1.2.3).

In magnetic thin film composed of Fe or Co, the MCA is negligible compared to the shape anisotropy so that one has $K_{eff} = \frac{K_s}{t_{FM}} - K_d$. Moreover, from equation 1.9 one can see that the preferential magnetization orientation depends on the sign of K_{eff} : if $K_{eff} > 0$ it corresponds to an easy axis out of the thin film plane, and then to PMA. On the contrary, if $K_{eff} < 0$ it corresponds to an easy plane which is the ferromagnet layer plane. The transition between the two magnetic orientations is driven by the ferromagnetic thickness and there is a sign crossover of K_{eff} at a critical thickness $t_c = \frac{K_s}{K_d}$ (see Fig. 1.4). Thus, for $t_{FM} < t_c$ the surface contribution overcomes the volume one and the magnetization points out of the sample plane (so called OOP magnetization state in the following). Then, increasing t_{FM} leads to the decrease of the surface anisotropy and for $t_{FM} > t_c$ the magnetization re-orientates in the sample plane due to the shape anisotropy. Typical behaviour of the product $t_{FM} \times K_{eff}$ is shown in Fig. 1.4. For thick ferromagnetic the curve has a linear

behaviour with a negative slope, equal to K_d, which shows the competition between the surface and shape anisotropy when increasing the ferromagnetic thickness.
The intercept is expected to give the surface anisotropy contribution K_s. However when the thickness is below a certain value t_{DL}, which is called the *magnetically dead layer thickness* (see note page 86), the magnetic parameters collapse and lead to a paramagnetic state (at room temperature). Such a behaviour can be understood by the thickness dependence of the Curie temperature, well established in the literature [46, 47]. Thus, the magnetization also depends on the thickness and quickly drops close to t_{DL} [48, 49]. As described by the Callen & Callen law [50], the decrease of the magnetization induces the decrease of the anisotropy via a power law [51–54]. Thus, when reducing the dimensionality (going from 3D to 2D by reducing the feromagnetic thickness), all the magnetic parameters drop down to zero.
Finally, when reducing the ferromagnetic thickness, an in plane magnetic state can be observed before the paramagnetic state (not represented in Fig. 1.4). Indeed, if $\frac{K_s}{t_{FM}}$ decreases faster to zero than K_d, a negative K_{eff} can be obtained just before the transition towards paramagnetic [55].

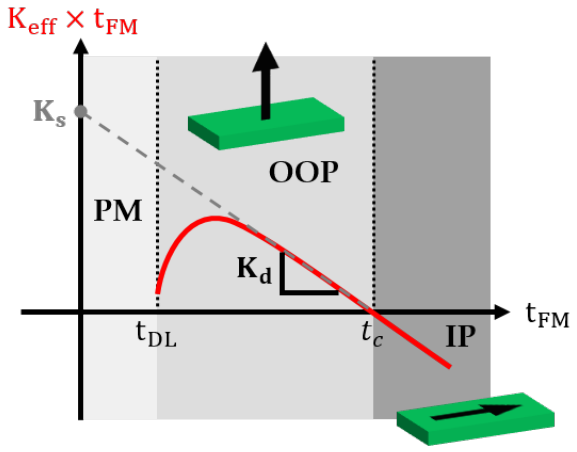

Figure 1.4: **Effective anisotropy versus ferromagnetic thickness:** Sketch of the variation of $t_{FM} \times K_{eff}$ versus t_{FM} (red curve). "PM" stands for paramagnetic state, appearing when the thickness is below the dead layer thickness t_{DL}. "OOP" means that the magnetization points preferentially out of the sample plane, when $K_{eff} > 0$. Finally, above a critcial thickness t_c magnetization reorients in the sample plane, when $K_{eff} < 0$. The slope of the linear part (for thicker ferromagnet) is given by $-K_d$ and the intercept of this linear behaviour gives K_s (dashed gray line).

1.2.5 *Spin-orbit coupling*

As its name suggests, the spin-orbit coupling (SOC)[6] refers to the coupling between the spin and orbital momentum of the electron moving in an electric field. In a solid, the electric field, also called the *crystal field* originates from the atoms nuclei, positively charged by an amount Ze, Z being the atomic number (number of protons) and e the elementary elec-

6 This effect is not directly an energy term, but it plays a key role in inducing magnetic energies from several physical phenomena at the interfaces in HM/FM/MO_x trilayers.

tric charge[7]. In the rest frame of the electron, this electric field is equivalent to a magnetic field $\mu_0\vec{H}_{SO} = -\gamma\frac{\vec{v}\times\vec{E}}{c^2}$ [8], as schematically represented in Fig. 1.5a. The solid blue circle is the orbit of the electron around the nucleus and the dashed red circle is the trajectory of the nucleus in the rest frame of the electron, creating $\mu_0\vec{H}_{SO}$ (yellow arrow). Considering the non-relativistic case, one has with $\gamma \overset{v\ll c}{\simeq} 1$ and thus

$$\mu_0\vec{H}_{SO} = -\frac{\vec{v}\times\vec{E}}{c^2} \tag{1.11}$$

where c is the speed of light. The interaction of this magnetic field with the electron's spin ($\vec{m_S} = 2\mu_B\frac{\vec{S}}{\hbar}$) can be seen as a Zeeman coupling with energy contribution :

$$E_{SO} = -\mu_0\vec{m_S}\cdot\vec{H}_{SO} = -\frac{\mu_B}{\hbar c^2}\vec{S}\cdot(\vec{v}\times\vec{E}) \tag{1.12}$$

where a correction by a factor $\frac{1}{2}$ has been done (justified in Annex 8.2, due to the fact that we use eq. 1.11 while the electron is not in an inertial frame). If we assume a central field of the Coulomb form, *ie* $\vec{E} = -\frac{\partial V(r)}{\partial r}\frac{\vec{r}}{r}$ we have (see demonstration in Annex 8.2) :

$$E_{SO} = -\frac{\mu_B}{\hbar m_e c^2}\frac{1}{r}\frac{\partial V(r)}{\partial r}\vec{L}\cdot\vec{S} = \lambda_{SO}\vec{L}\cdot\vec{S} \tag{1.13}$$

where $\vec{L}$ and $\vec{S}$ are respectively the orbital and spin momentum, coupled by the electric field in which the electron is moving, and λ_{SO} is a coefficient related to the strength of the spin orbit coupling. The electric field responsible for the spin orbit coupling can have different origins.

On the one hand, as described above, it can originate from the atoms nuclei in the solid bulk. In this case, the strength of the SOC scales as $\lambda_{SO} \propto Z^4$ as shown in Fig. 1.5b [56–58], indicating that the SOC is much larger in metals composed of heavy atoms. In the bulk, a striking example of the SOC consequence is the magnetocrystalline anisotropy (see Sec. 1.2.4) and the spin Hall effect (see Sec. 2.5.2.2).

On the other hand, in system with Structural Inversion Asymmetry (SIA), such as the HM/FM/MO_x trilayers studied in this work, the electric field at the origin of the SOC can originate from the interfaces. Indeed, the inversion symmetry is broken at the interface between two different materials, leading to the establishment of an interfacial electric field, called the Rashba field and oriented along the axis of symmetry breaking. At interfaces, it induces a great richness of phenomena which have a huge impact on the magnetization of the ferromagnet: (i) On the one hand, we shown in Sec. 1.2.6.2 that it is one of the origin of the interfacial Dzyaloshinskii-Moriya interaction, which stabilizes non collinear spin textures. (ii) On the other hand, we show in Sec. 2.5.2.3 that it can exert torques on the magnetization at the interface with the ferromagnet, thus contributing to magnetization dynamics. Another striking example of SOC at the interfaces is the perpendicular magnetic anisotropy (see Sec. 1.2.4), which orients the magnetization out of the sample plane while it is against the shape anisotropy described above. All these phenomena are at the heart of

7 $e = 1.6\times10^{-19}$ Coulombs

8 In this section only, γ is the Lorentz factor that defines the Lorentz transformations shown in Annex 8.2

this work, and work together to stabilise magnetic skyrmions, the entity of interest in this thesis.

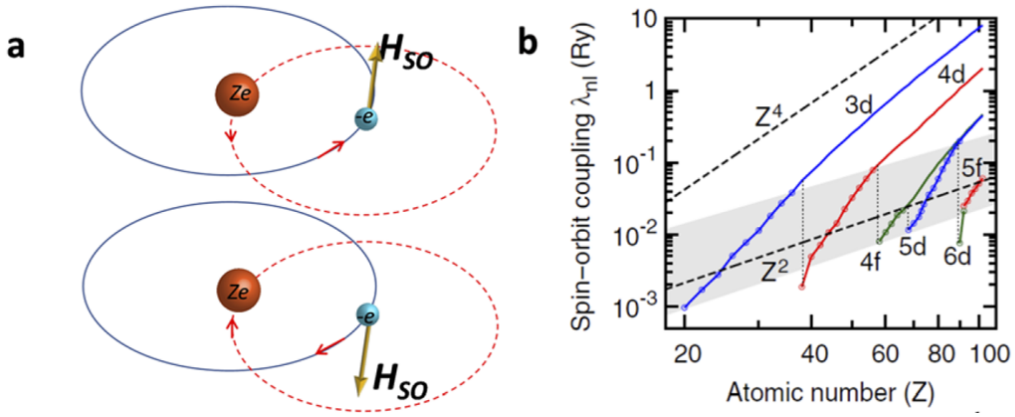

Figure 1.5: **Spin orbit Coupling:** (Extracted from reference [56]) (a) Schematic representation of the spin-orbit coupling. The electron (blue dot) orbits around the nucleus (orange sphere), as depicted by the blue circle. In the rest frame of the electron, the nucleus is seen as a moving charge (dashed red circle) which generates a magnetic field $\mu_0 \vec{H}_{SO}$ with whom the electron spin will couple (b) The Z^4 dependence of the spin orbit orbit coupling coefficient (λ_{nl} corresponds to λ_{SO} in the text). One can see that the orbital filling has also an importance.

1.2.6 *The Dzyaloshinskii-Moriya energy*

In HM/FM/MO_x trilayer heterostructure, the SOC together with the SIA induce many interesting phenomena, such as the PMA, described in Sec. 1.2.4. Another striking consequence is the emergence of an additional exchange interaction : the interfacial Dzyaloshinskii Moriya Interaction (iDMI), which is central to this thesis work. In fact, in 1958, I. E. Dzyaloshinskii realized that the symmetric Heisenberg exchange interaction could not explain the weak magnetic moment observed in several antiferromagnetic materials [26]. Based on symmetry argument, he proposed an antisymmetric exchange interaction, that was further calculated by T. Moriya in 1960 considering SOC in a material lacking inversion symmetry [24, 25]. Thus, this additionnal, antisymmetric exchange interaction was named the Dzyaloshinskii-Moriya interaction. If we consider that the inversion symmetry is broken along the $\vec{z}$ axis, the atomistic DMI energy density reads as

$$\epsilon_{iDMI} = \vec{d}_{ij} \cdot \left(\vec{S}_i \times \vec{S}_j \right) \tag{1.14}$$

The corresponding energy cost is thus minimum when $\vec{S}_i \times \vec{S}_j$ is antiparallel to $\vec{d}_{ij}$. In other words, this interaction favors canted[9] neighbouring spins, and the direction of $\vec{d}_{ij}$ imposes a unique direction of rotation between neighbouring spins, which is called the *chirality*. This interaction plays a key role in the stabilization of non-collinear and non trivial spin textures such as the magnetic skyrmions studied in this work (see Sec. 2.2.1). The DMI can have different origin, as a function of the source of symmetry breaking.

9 If considering only DMI, orthogonal neighbouring spins are favoured, but the competition with the Heisenberg exchange results in canted neighbouring spins

On the one hand, he DMI can originate from the bulk (so called bulk-DMI) in non-centrosymmetric crystals such as the B20 structure (like MnSi) where skyrmions where first observed (see Sec. 2.2.1). In the bulk, the DMI vector $\vec{d}_{ij}$ is collinear to the unit vector $\vec{r}_{ij}$ that links to neighbouring spins $\vec{S}_i$ and $\vec{S}_j$, which favors homochiral Bloch domain walls, and more especially Bloch skyrmions (see section 2.2.1).
On the other hand, in SIA systems like HM/FM/MO_x trilayers, the inversion asymmetry arises due to the asymmetric stacking and the DMI originate from the interfaces. In this case, it is called interfacial DMI (iDMI), and the iDMI vector reads as $\vec{d}_{ij} = d\left(\vec{z} \times \vec{r}_{ij}\right)$, with d is the atomistic iDMI coefficient (in J$\cdot$ m^{-3}) and $\vec{z}$ is the axis along which the inversion symetry is broken by the asymmetric stacking. The iDMI thus favors homochiral Néel magnetic domain walls, with a chirality that depends on the sign of the iDMI coefficient [9, 10].
In the case of a magnetic thin film in the (x, y) plane, the micromagnetic iDMI energy density can be expressed as (see demonstration in Annex 8.1):

$$\varepsilon_{iDMI} = D\left[\vec{y} \cdot \left(\vec{m} \times \frac{d\vec{m}}{dx}\right) - \vec{x} \cdot \left(\vec{m} \times \frac{d\vec{m}}{dy}\right)\right] \tag{1.15}$$

where the iDMI coefficient (in J/m²) is defined as $D = \frac{dS^2}{at_{FM}} n = \frac{D_S}{t_{FM}}$ with D_S the interfacial iDMI coefficient (in J/m). The inverse proportionality of the iDMI coefficient versus the ferromagnetic thickness is a signature of the interfacial nature of the interaction, similar to the surface anisotropy $\frac{K_S}{t_{FM}}$ introduced previously.
Within the framework of this PhD we are interested in the iDMI arising in our trilayer structures HM/FM/MO_x. Because the FM has two different interfaces in this trilayer, there are two origins for the iDMI, depending of the interface considered (top or bottom), as presented below.

Note : Conventions about iDMI sign and chirality

The preferred direction of rotation depends on the direction of $\vec{d}_{ij}$. Thus, the sign of d is necessary but insufficient to state on the favoured chirality, since $\vec{d}_{ij}$ also depends on the cross product between $\vec{z}$ and $\vec{r}_{ij}$. The link between the sign of D and the preferred chirality thus depends on the definition of $\vec{d}_{ij}$, as shown in the next table.

	$\vec{d}_{ij} = d(\vec{z} \times \vec{r}_{ij})$	$\vec{d}_{ij} = d(\vec{r}_{ij} \times \vec{z})$
$d < 0$	Clockwise	Counter Clockwise
$d > 0$	Counter Clockwise	Clockwise

Figure 1.6: **Conventions for the correspondence between iDMI sign and domain wall chirality:** Depending on the definition of $\vec{d}_{ij}$, the relation between the sign of D (or equivalently the sign of d) and the favoured chirality is opposite.

In this work, we have chosen to use the conventions highlighted in green, so that a CW chirality is due to a negative iDMI and a CCW chirality is due to a positive iDMI.

In each of the two iDMI mechanisms presented in the following, two ingredients are necessary. On the one hand, broken inversion symmetry is needed, otherwise the contributions from the bottom and top interface of the FM layer cancel each other by symmetry. This ingredient is provided by the HM/FM/MO_x trilayer with SIA, and thus has the same origin for the two iDMI contributions. One the other hand, the iDMI needs a source of electric field to induce the spin-orbit coupling in which the two iDMI mechanisms find their origin. This second ingredient distinguishes the two iDMI types, and we present in the following the two different origins of the electric field that lead to the two iDMI contributions.

1.2.6.1 *HM/FM interface: Fert-Levy DMI*

At the HM/FM interface, the presence of heavy atoms from the HM layer induces a source of SOC. The electrons experience the electric field of the nuclei, inducing spin orbit coupling via the Fert-Levy model. In this model, the iDMI interaction between two spins in the FM layer is mediated by a third atom from the heavy metal layer, which has a large SOC [59]. The iDMI vector is normal to the triangle formed by the three atoms and lies in the plane of the interface (see Fig. 1.7). As a quick reminder the effect of iDMI it to tilt neighbouring spins by a rotation around the iDMI vector. Hence, considering a magnetic thin film with PMA, it explains the formation of Néel domain walls with a chirality that depends on the orientation of the iDMI vector and thus on the sign of the interaction (*i.e.* the sign of the iDMI coefficient).

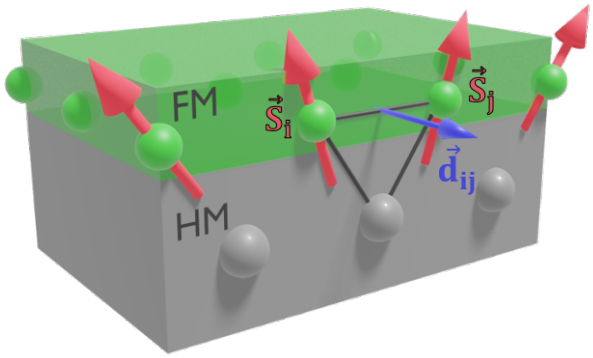

Figure 1.7: **Fert-Levy mechanism for iDMI:** The iDMI interaction between two spins $\vec{S}_i$ and $\vec{S}_j$ (depicted by red arrows) in the ferromagnetic (FM) layer is mediated by a third atom from the heavy metal (HM) layer, which has a large spin orbit coupling. The effect of the iDMI is to rotate the magnetization around the iDMI vector which lies in the plane of the interface.

1.2.6.2 *FM/MO_x interface: Rashba DMI*

The Rashba effect is due to an interfacial electric field appearing at the at FM/MO_x interface due to the broken symmetry and the presence of the oxygen atoms which

leads to a charge transfer at the interface[10]. Such electric field is normal to the interface and oriented from the FM layer to the oxide layer, *ie* $\vec{E}_R = E_R\vec{z}$ (pink arrows in Fig. 1.8). In the rest frame of the electron, it is equivalent to a magnetic field, called the Rashba magnetic field $\mu_0\vec{H}_R = -\frac{\vec{v}\times\vec{E}_R}{c^2}$. Thus, two electrons moving in opposite direction experience a Rashba magnetic field in the opposite direction, as depicted by the blue arrow in Fig. 1.8(a,b). The precession of their spins around $\mu_0\vec{H}_R$ is transmitted to the localized magnetic moments, leading to non collinear magnetization with a given direction of rotation, which is the effect of the iDMI interaction presented previously.

Two sections of this thesis are dedicated to the Rashba effect. On the one hand, it has consequences of the equilibrium magnetization configuration by contributing to the presence of iDMI at at FM/MO_x interfaces, as shown here. On the other hand, it has consequence on the magnetization dynamics, as explained in Sec. 2.5.2.3.

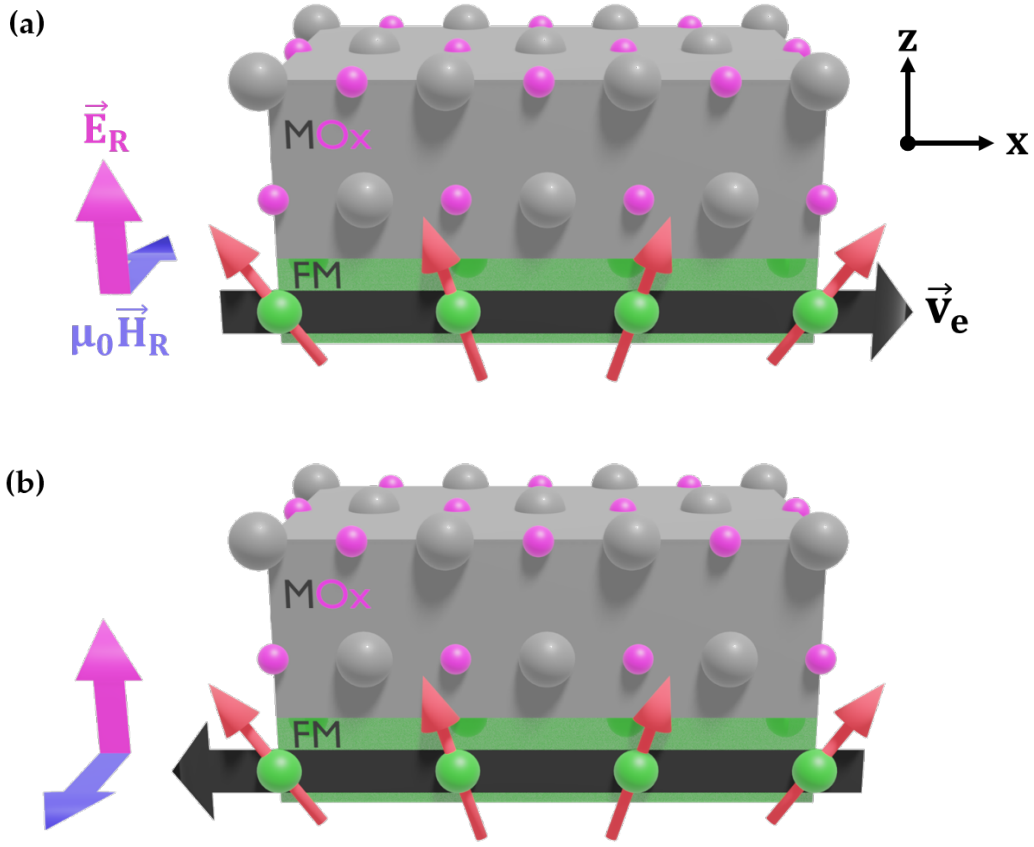

Figure 1.8: **Rashba mechanism for iDMI:** (a) The spins of the itinerant electrons moving in the $\vec{x}$ direction experience a precession around the Rashba magnetic field $\mu_0\vec{H}_R$ (blue arrow), induced by the interfacial electric field (pink arrow). (b) same situation for electrons moving in the $-\vec{x}$ direction: the direction of $\mu_0\vec{H}_R$ is reversed, resulting in the same canting between neighbouring spins, transmitted to localized magnetic moments (red arrows) by $s-d$ exchange.

10 In can also be due to the absence of adjacent layer to the FM.

1.3 CONTROL OF INTERFACIAL MAGNETISM

In the previous section we introduced the different energies and magnetic parameters that compete to result in the equilibrium magnetic configuration. We gave a particular focus on magnetic thin films such as HM/FM/MO_x, where most of the physical properties stem from the interfaces, such as the magnetic anisotropy and the interfacial DMI. Thus, the control of the magnetic configuration requires a precise adjustment of the interfacial properties. In this section, we present different techniques to control the interfacial magnetism in HM/FM/MO_x trilayer heterostructures. In a first part, we show how the magnetic properties depend on the material and deposition parameters. In a second part, we show that some of the magnetic properties can also be controlled by a gate voltage.

1.3.1 *Material dependent magnetic properties*

There exist several ways to control the interfacial magnetism in HM/FM/MO_x trilayer heterostructures. First, a direct tuning of the ferromagnetic thickness leads to modification of the magnetic properties, as shown in the first part of this section. But also, modifying the interfaces of the ferromagnet leads to changes in the magnetic properties, since most of them stem from the interfaces (like PMA, interfacial DMI...). Changing the ferromagnet interfaces can be done either by changing the oxidation state of the FM/MO_x interface, as shown in the second part of this section, or by directly changing the bottom heavy-metal type, as shown in the third part.

Changing the ferromagnetic thickness

Magnetic surface anisotropy and iDMI, stemming from the ferromagnet interfaces, are inversely proportional to its thickness, as shown in equation 1.10 for the surface anisotropy contribution and in equation 1.15 for the interfacial DMI coefficient. Thus, modifying the ferromagnetic thickness changes the surface to volume ratio and directly affects these interfacial magnetic parameters. We have explained in Sec. 1.2.4 that the effective anisotropy K_{eff} and the magnetization M_S depend on the ferromagnetic thickness. The dependence of K_{eff} on t_{FM} has been measured many times in the literature [41–45], as shown in Fig. 1.9a, where the variation of K_{eff} versus Co thickness in a Pt/Co multilayer reproduces nicely the curve shown in Fig. 1.4. For the thinner Co, one can clearly see the decreased effective anisotropy induced by the decreased Curie temperature in reduced dimensions. The maximum of anisotropy is reached around $t_{Co} \simeq 0.5$ nm, and for thicker Co the anisotropy decreases again due to the decrease of the surface contribution compared to the volume contribution (shape anisotropy).

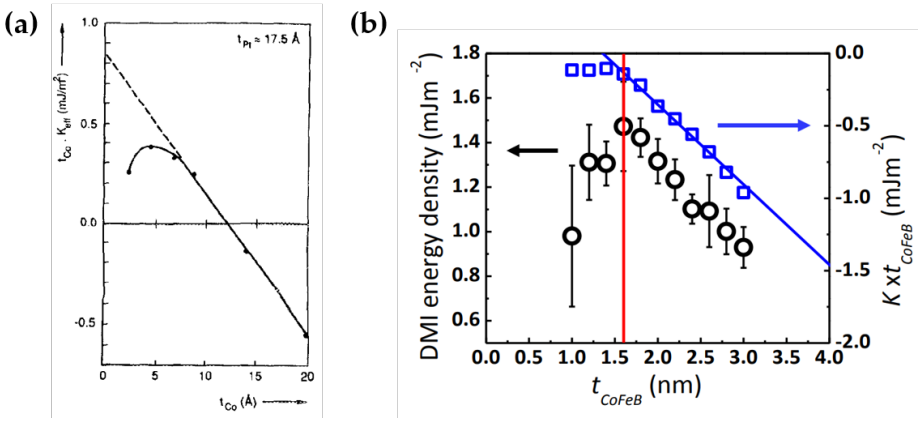

Figure 1.9: **Dependence of magnetic properties on the ferromagnetic thickness:** (a) Measurement of the effective anisotropy in a Pt/Co multilayer versus the Co thickness (extracted from [43]). (b) Measurement of the iDMI (left y-axis) and of the effective anisotropy (right y-axis) in a Pt/CoFeB/AlO_x versus the CoFeB thickness ((extracted from [60]). The effective anisotropy starts to decrease at the same thickness as does the iDMI, showing their common interfacial origin.

In more recent works, it was shown experimentally that the iDMI amplitude depends of the ferromagnetic thickness in Pt/Co/AlO_x and Pt/CoFeB/AlO_x (see Fig. 1.9b) trilayer heterostructures [60]. It shows that in such HM/FM/MO_x trilayers, the DMI is purely originating from the interfaces. Moreover, as shown in Fig. 1.9b the decrease of iDMI for the thinner CoFeB is correlated with the decrease of effective anisotropy due to the lower Curie temperature in reduced dimensions. It enables to show the common interfacial origin of iDMI and PMA in HM/FM/MO_x trilayer systems. Moreover, this interfacial origin was confirmed in another study where the iDMI amplitude showed a monotonous behaviour versus the Co thickness in a Pt/Co(t_{Co})/AlO_x trilayer [61].

Changing the oxidation state at the FM/MO_x interface

As shown in Fig. 1.3a, the presence of oxygen at the ferromagnet interface can be a source of PMA. More precisely, it is now established that the surface anisotropy depends on the oxygen content of the FM/MO_x interface (*ie* its oxidation state). As explained in Sec. 1.2.4, XPS measurements have been able to link the oxidation state of the FM/MO_x interface with the effective anisotropy [37–39]. In reference [37], the authors observed that varying the oxidation time of a Pt/Co/AlO_x trilayer modifies the magnetic properties of the Co layer, notably changing the amplitude and sign of the effective anisotropy. As shown in Fig. 1.10(a-d), from XPS measurements the authors were able to give a schematic representation of the trilayer as a function of the oxidation time. The longer the trilayer is oxidized, the deeper the oxygen atoms penetrates and the more oxidized is the FM/MO_x interface is oxidized. Simultaneously, the authors measured the effective anisotropy (named H_{an} in their work) as a function of the oxidation time, as shown in Fig. 1.10e. For an *optimally oxidized* Co/AlO_x interface (see Fig. 1.10c), the oxygen front stops at the interface of the ferromagnet and the effective anisotropy is maximum, as shown in Fig. 1.10e for oxidation times around 40 s. For smaller oxidation time, the oxygens do not reach the ferromagnetic

interface, leading to an *underoxidized* Co/Al/AlO_x interface (see Fig. 1.10(a-b)), which has a smaller effective anisotropy. Similarly, for an *overoxidized* Co/CoO/AlO_x, in which oxygen front starts to penetrate the FM layer, the effective anisotropy decreases. In our work we used these results to find the optimal oxidation on our sample, by finding the maximum of effective anisotropy.

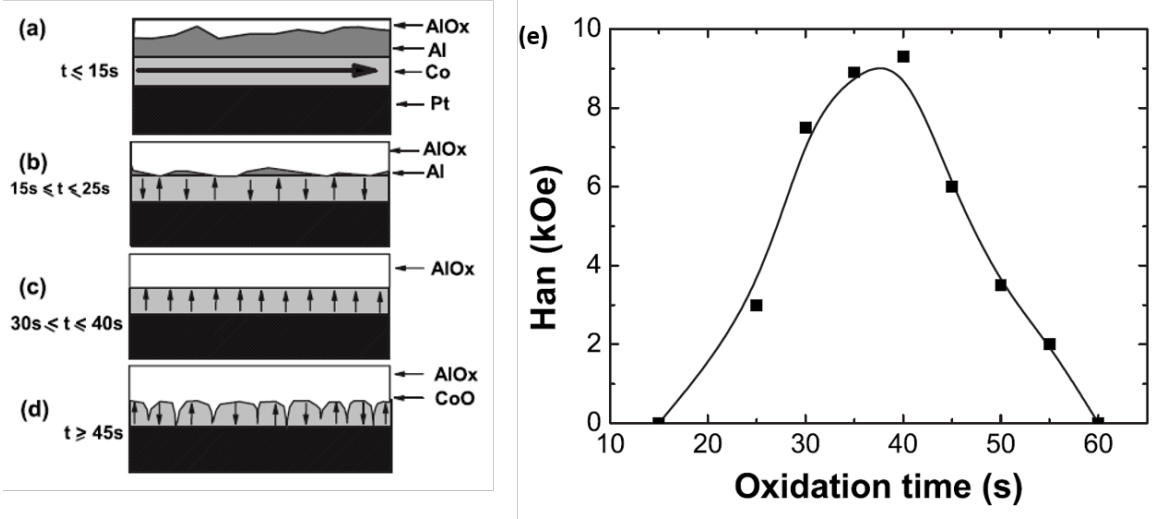

Figure 1.10: **Effective anisotropy versus FM/MO_x interface oxidation state:** (Extracted from [37]) (a-d) Schematic representation of the trilayers as a function of the oxidation time. (e) Measurement of the effective anisotropy as a function the oxidation time.

In addition to K_{eff}, it has been shown in Pt/Co/MO_x (for M = Al or Gd) that the amplitude of the iDMI depends on the FM/MO_x interface oxidation state [62]. In order to tune the oxidation state at the top Co interface, a wedge of the top metallic layer was deposited and followed by an oxidation in a plasma chamber. Thus, the thinner the top metallic layer, the more oxidized the top Co interface (see Fig. 1.11a). The magnetic properties could then be measured as a function of the Co/MO_x interface oxidation state, by measuring in different positions on the sample. First, the authors observed a decrease of the magnetization for overoxidized Co/MO_x interface (see Fig. 1.11b), since the ferromagnetic layer starts to get oxidized. Second, the authors have measured the variation of iDMI versus the oxidation degree of the top Co interface (see Fig. 1.11c), which is shown to be correlated to the variation of the surface anisotropy (see Fig. 1.11d). The iDMI is maximum where the K_s is maximum, giving another clue that the surface anisotropy and the iDMI have common interfacial origins. In a theoretical work, it has been observed that the sign of the iDMI could also be reversed by varying the oxygen coverage in a Ir/Fe/O trilayer [63] (gray dots in Fig. 1.11e). The iDMI amplitude and sign has even been linked to the interfacial dipole (red dots in Fig. 1.11e), which is related to the interfacial electric field at the origin of Rashba iDMI discussed in Sec. 1.2.6.2.

During my PhD, several studies have been published showing the dependence of the iDMI on the oxidation state at the FM/MO_x interface. Recently, it has been experimentally shown that the DMI sign in Cu/CoFe/$CoFeO_x$/Ta and Cu/CoFe/Ta(t_{Ta})/TaO_x/Ta is

changed when the oxide type (either CoFeOx or TaO_x) or Ta thickness is modified [64]. Besides, very recent experimental results showed that the oxygen adsorbed content at Pd/-Co/Ni/O surface can invert DMI sign and domain wall chirality [65]. Finally, just as the addition of oxygen to an interface changes its oxidation state, so does the addition of hydrogen ions (proton). In this way, hydrogen adsorbed content has also been shown to induce an iDMI sign crossover and thus an inversion of the DW chirality [66].

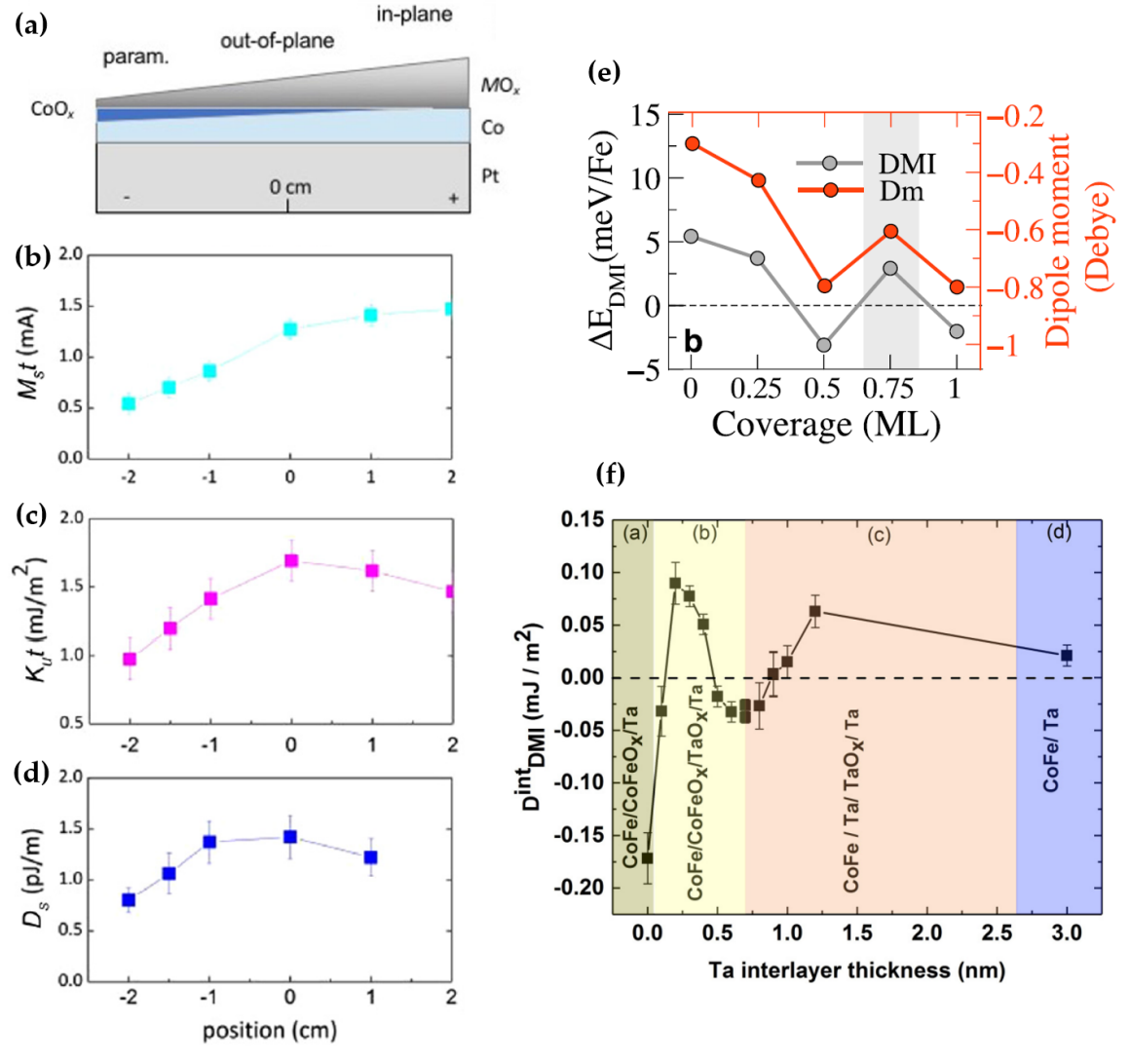

Figure 1.11: **Interfacial iDMI versus FM/MO_x interface oxidation state:** (a-d) (Adapted from [62]) (a) Sample geometry, in which a wedge of MO_x is used to vary the oxidation level of the Co/MO_x interface, as a function of the position along this wedge. In (b), (c), (d) are respectively shown the surface magnetic moment $M_S t$, the surface anisotropy and the surface iDMI coefficient as a function of the position along the wedge of MO_x. (e) iDMI energy (gray) and dipole moment (red) as a function of the oxygen coverage in a Ir/Fe/O trilayer (Extracted from [63]) (f) Variation of the IDMI coefficient as a function of the Ta thickness (which changes the oxidation state of the top CoFe interface) in Cu/CoFe/Ta(t_{Ta})/TaO_x/Ta (Extracted from [64])

Changing the underlayer heavy-metal type

In HM/FM/MO_x trilayer, the bottom heavy metal layer is a source of SOC, in which iDMI finds its origin. Thus, changing the type of heavy-metal leads to the modification of the iDMI from the bottom interface. For example, it has been observed experimentally that the iDMI amplitude and sign can be adjusted by changing the heavy metal underlayer in a HM/Co/MgO (HM = Hf, Ta, TaN, W) [67]. The authors observed a correlation between the iDMI and the filling of the 5*d* orbital of the HM adjacent to the ferromagnetic layer. This result was strengthened by the experimental observation that the iDMI amplitude and sign can be adjusted by changing the heavy metal underlayer in a HM/FM/MgO (FM = Co and CoFeB) [68]. It is shown in Fig. 1.12a for a CoFeB FM layer and in Fig. 1.12b for a Co FM layer. These experimental works have also been completed by first principle calculations in HM/FM bilayers showing the variation of iDMI amplitude and sign when changing the bottom HM type [69].
It is worth noting that the sign of the spin orbit coupling coefficient of the HM adjacent layer is not correlated to the sign of the iDMI. For example, it can be seen that an Ir sublayer can induce a positive iDMI when adjacent to a CoFeB layer (see Fig. 1.12a), whereas a negative iDMI is favoured when adjacent to a Co layer (see Fig. 1.12b).

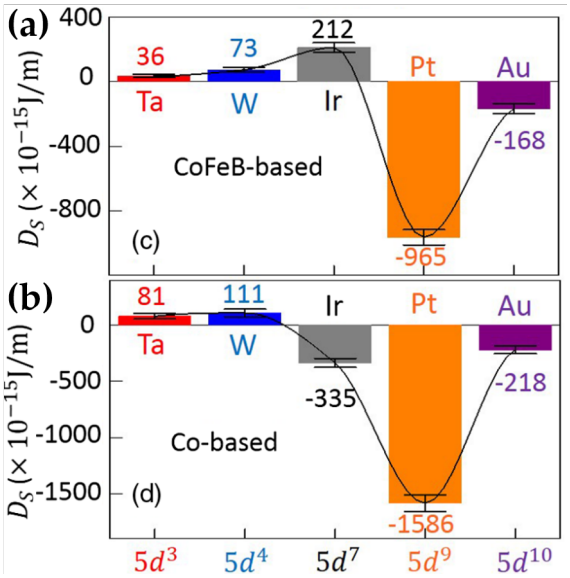

Figure 1.12: **Interfacial iDMI versus versus heavy-metal underlayer type:** (a) Interfacial DMI coefficient for several heavy-metal underlayers in a HM/CoFeB/MgO trilayer and (b) in a HM/Co/MgO trilayer (Extracted from [68])

Besides, the thickness of the heavy-metal layer also influences the iDMI. On the one hand, it has been experimentally observed that the iDMI amplitude depends on the Pt thickness in a Pt(t_{Pt})/CoFeB bilayer [70]. The iDMI first increases quickly and then saturates to $D = 0.45$ mJ/m² at $t_{Pt} \simeq 2$ nm. On the other hand, the insertion of a Pt wedge layer in Ta/FeCoB/Pt(wedge)/MgO thin films [71] also results in a modification of the iDMI amplitude versus the inserted Pt thickness. In this case, the iDMI continuously decreases as the Pt interlayer thickness increases, since the iDMI from the FeCoB/Pt interface progressively

compensates the one of the Ta/FeCoB interface. Finally, recent observation of a non-zero DMI in nominally symmetric structures of Au/Fe/Au was attributed to different strains at the top and bottom interface [72].

1.3.2 *Voltage control of interfacial magnetism*

In the previous section, we have shown that the interfacial magnetism in HM/FM/MO_x trilayer can be adjusted in many ways, leading to a fine control of the iDMI amplitude and sign, of the magnetic anisotropy and also of the magnetization. However, each of the techniques described above are based on the tuning of deposition parameters and thus do not allow for a dynamical modification of the interfacial magnetism after the sample deposition. In this way, the gate voltage emerged as a promising, low power and versatile technique to achieve both a local and dynamical control of interfacial magnetism and notably of iDMI. [73–77].

1.3.2.1 *Voltage Control of Magnetic Anisotropy*

It is well-established that a gate voltage (V_g) can modify the charge distribution [78–81] and tune the oxidation state at the FM/MO_x interface [82–84], both mechanisms leading to changes in interfacial magnetic anisotropy, which is called Voltage Control of Magnetic Anisotropy (VCMA) [85]. In Sec. 1.2.4 and 1.3.1, we have seen that the interfacial anisotropy is strongly dependent on the oxidation state at the FM/MO_x interface. Consequently, the strongest VCMA effect has been explained as driven by O^{2-} ionic migration towards the interface or away from it, depending on the voltage polarity [86–89]. The efficiency of the effect is described by the ratio $\beta = t_{FM}\frac{\Delta K_{eff}}{\Delta E}$ (in J/(Vm)), which correspond to the change of effective anisotropy for a given change in the applied electric field. In Fig. 1.13, we show a summary of the VCMA efficiencies at FM/oxide interfaces and in magnetic tunnel junctions, extracted from a review done in SPINTEC by B. Dieny and M. Chsiev [85]. It is clear that the efficiency associated to ionic migration effect ($\beta \simeq 10^2$ to 10^4 fJ/(Vm)) is orders of magnitude larger than the efficiency associated to charge effects ($\beta \simeq 10$ to 10^2 fJ/(Vm)).

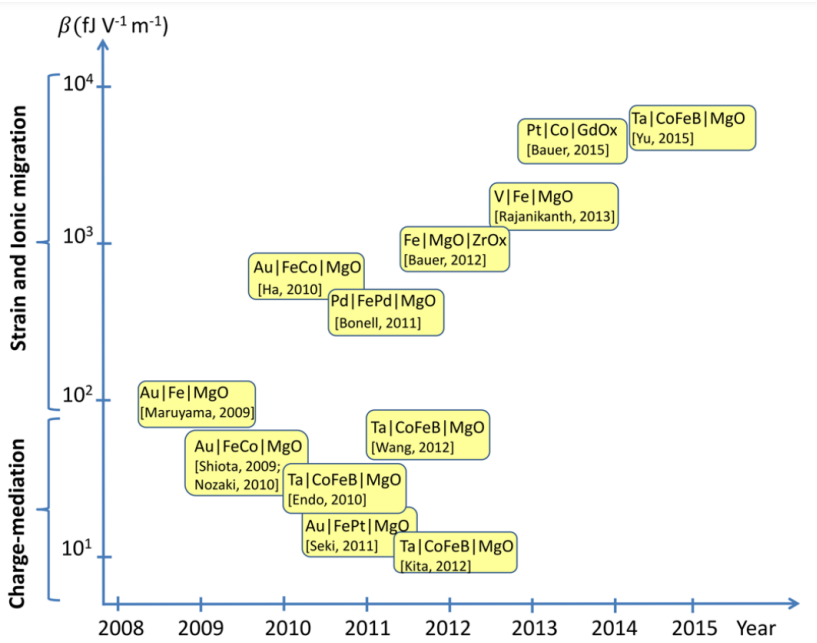

Figure 1.13: **Efficiency parameter β for the voltage control of magnetic anisotropy:** Summary of efficiency parameters value for the electric-field control of magnetic anisotropy at FM/oxide interfaces and in magnetic tunnel junctions. The effect associated to ionic migration (and strain) is larger than the one related to charge effects. (Extracted from [85])

The oxygen migration induced by an applied gate voltage has been observed experimentally in a Pt/Co/AlO_x trilayer [88], as shown in Fig. 1.14. The authors used STEM-EELS[11] technique to directly locate the oxygen front inside the trilayer. At $V_g = 0$, the oxygen front is located at the Co/AlO_x interface, as shown in Fig. 1.14a, with the raw data on top and a schematic representation in the bottom part (the oxygen front is depicted by the bottom boundary of the pink region). The authors further observed that $V_g > 0$ leads to the withdrawal of the oxygen front away from the interface (schematically represented in the bottom part of Fig. 1.14b), and that $V_g < 0$ brings the oxygen front closer to the interface (see Fig. 1.14c).

11 Scanning Transmission Electron Microscope - Electron Energy-Loss Spectroscopy

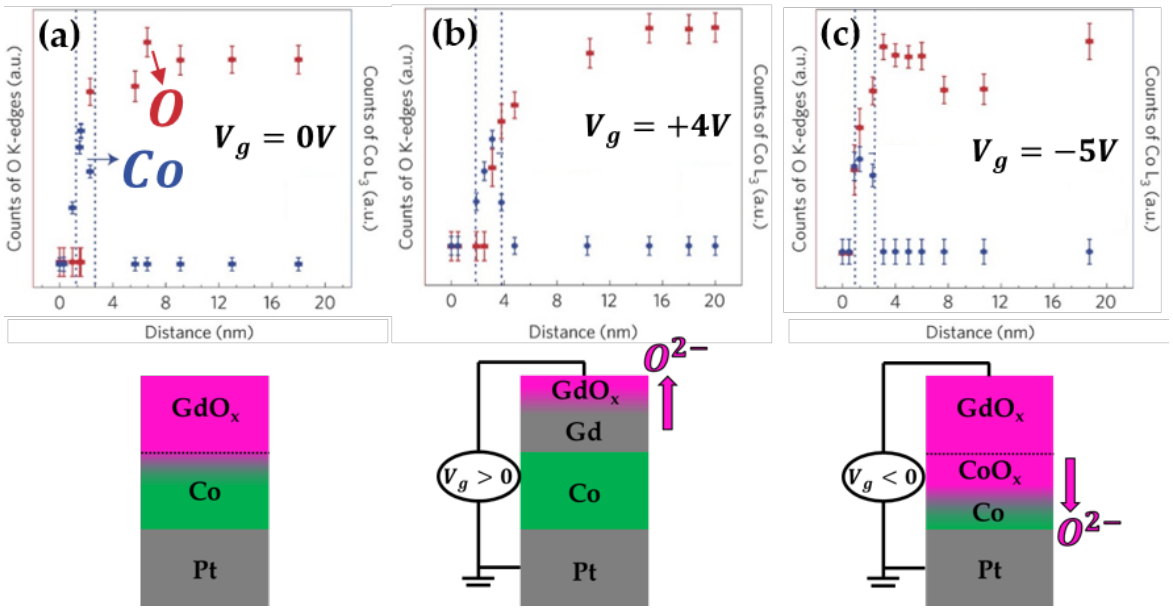

Figure 1.14: **Gate voltage induced oxygen migration:** STEM-EELS measurement at the O-K and Co-L edges, allowing to locate the oxygen front with respect to the Co layer. (a) (top) Experimental STEM-EELS data showing the position of the oxygen front at $V_g = 0$, located at the Co/AlO_x interface. (bottom) Schematic representation of the trilayer at $V_g = 0$, showing the position of the oxygen front (bottom limit of the pink region) (b) Same as (a) at $V_g > 0$ and (c) at $V_g < 0$ (Adapted from [88])

As a reminder, K_{eff} evolves with the FM/MO_x interface oxidation state following a bell-like curve, with a maximum at the optimal interface oxidation (see Fig. 1.10). Thus, it has been shown that applying a gate voltage is equivalent to move on this curve, in a direction that depends on the voltage polarity [86] (as schematically shown in see Fig. 1.15b). Notably, starting from an overoxidized Co/TbO_x interface, the application of a positive gate voltage progressively reduces the interface, leading to a progressive change in the coercive field ($\propto K_{eff}$) following the bell-like curve, with a distortion due to the kinetics of the reaction. Moreover, the larger was the voltage, the faster was the anisotropy change (see 1.15a), indicating that the gate voltage is the driving force of the oxygen ions.

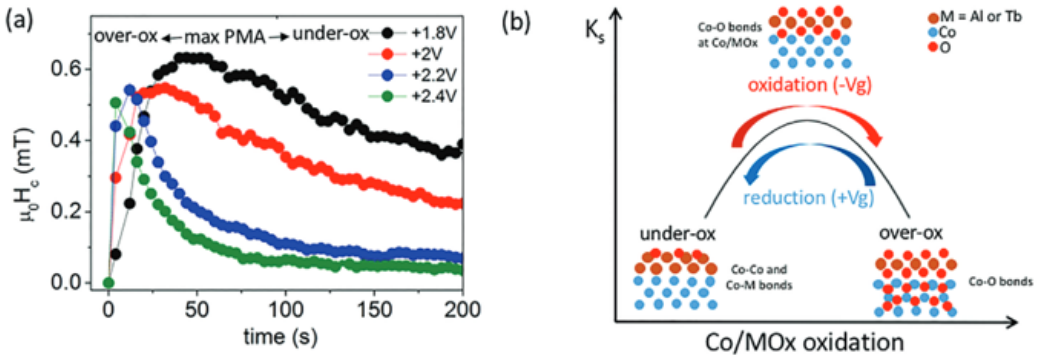

Figure 1.15: **Gate control of magnetic anisotropy with oxygen migration:** (a) Variation of the coercive field ($\propto K_{eff}$) versus time for different values of positive gate voltage. Initially the anisotropy is zero, and progressively increases until a maximum, to finally decrease. It corresponds to the progressive reduction of the Co/TbO_x interface, associated to the (b) bell-like variation of the effective anisotropy ($K_s \propto K_{eff}$) versus the Co/TbO_x interface oxidation, with schematic representation of the interface oxidation in the limiting cases of overoxidized, optimally oxidized and underoxidized. (Extracted from [86])

As explained above, the VCMA in HM/FM/MO_x trilayers can also originate from accumulation/depletion of electrons at the FM/MO_x interface due to the applied gate voltage. Due to the short screening length in metals, this effect is mostly located at the FM/MO_x interface. Although the efficiency associated to this effect is smaller than for the ionic migration, it is much faster and thus more suitable for fast computational operations. However, this effect is volatile, *ie* when switching-off the gate voltage, the configuration, and thus the magnetic parameters, are restored to their initial value. This tuning of interfacial magnetic anisotropy has allowed to control with a gate voltage the creation and annihilation of skyrmions. It was first demonstrated via micromagnetic simulations in magnetic nanodisks with CoFeB/MgO-based parameters [90]. The authors were able to switch between a saturated magnetic configuration to a confined skyrmion in the nanodisk with alternate directions of magnetization in the center, as shown in Fig. 1.16(a-e). One year later, electric field switching of magnetic skyrmions at room temperature was demonstrated experimentally for the first time in a collaboration between SPINTEC and Institut Néel in a Pt/Co/AlO_x trilayer [91]. As shown in Fig 1.16f, the use of transparent Indium Tin Oxide electrodes under a Magneto-Optical Kerr effect microscope (see Sec. 3.2.1) allows to probe the magnetization under the electrode, during the gate voltage application. Thus, the authors were able to demonstrate that it is possible to switch between a skyrmion state and a saturated state by applying opposite voltage polarity (see Fig. 1.16f), which was mostly explained in terms of VCMA due to charge effect. Later on, another work reported on the observation of voltage induced skyrmion creation and annihilation in GdO_x/Gd/Co/Pt [92] and in Pt(0.5 nm)/CoNi(0.5 nm)/Pt(0.5 nm)/CoNi(0.5 nm)/Pt(1.0 nm) [93].

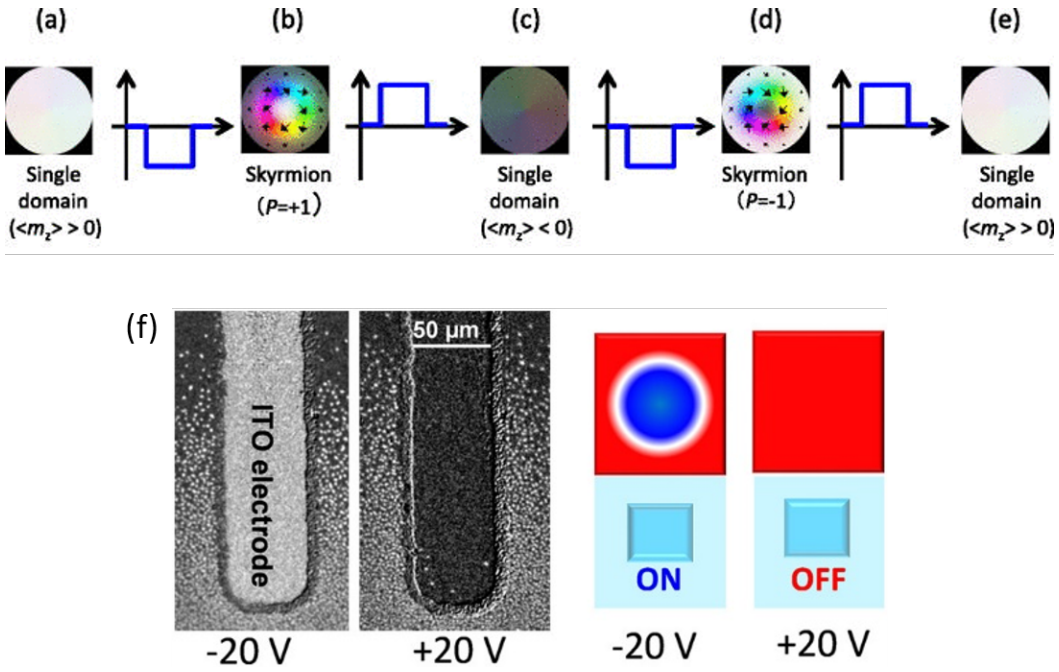

Figure 1.16: **Skyrmion nucleation / annihilation with a gate voltage:** (a-e) Micromagnetic simulations of a switching between the saturated magnetic state and the skyrmion state in magnetic nanodisks (Extracted from [90]) (f) (left) First experimental observation of the switching between a state with many skyrmions at -20V and a nearly saturated magnetic state at +20V (right) schematic representation of a skyrmion (on-state at -20V) and of the saturated magnetic state (off-state at +20V) (Extracted from [91])

1.3.2.2 *Voltage control of the interfacial Dzyaloshinskii-Moriya interaction*

Due to the short screening length in metals, the application of a gate voltage mainly modifies the interfaces in HM/FM/MO_x trilayers. Thus, not only the anisotropy but all the magnetic properties stemming from the interfaces are susceptible to be modified under gate voltage.

Electric field modulation of the iDMI has first been demonstrated experimentally in a Au/Fe/MgO trilayer with thick 20 nm Fe layer. However, it corresponded to very small variations, with an efficiency about $\beta_{DMI} = \frac{\Delta D}{\Delta E} = 3$ fJ/Vm [94]. Later, a much larger 130% voltage tuning of the iDMI has been observed in a Ta/FeCoB/TaO_x trilayer [76] during the PhD of Titiksha Srivastava in SPINTEC (see Fig. 1.17a). The authors performed both short (a few minutes) and long ($\simeq 4-15$h) time scale voltage application. For small applied voltage, both short and long time scales effect were reversible, *ie* the initial magnetic parameters are recovered at 0V after the voltage application. The efficiency is about $\beta_{DMI} = 150$ fJ/Vm for the short time scales effect, and $\beta_{DMI} = 600$ fJ/Vm for the long time, much larger than in previous theoretical works ($\beta_{DMI} = 26$ fJ/Vm) [95] and in the experimental work presented above [94]. The high efficiency at long time scale was ascribed to oxygen ions migration, directly modifying the interface and thus the iDMI origin: Fert-Levy iDMI for underoxidized FeCoB/Ta interface and Rashba iDMI for oxidized FeCoB/TaO_x interface. For the short time scale measurement (see Fig. 1.17a), the linear behaviour was explained in terms of the linear superposition of the Rashba electric field E_R (see Sec. 1.2.6.2) and the applied electric field. A negative electric field would add up to the Rashba

field (see top right of Fig. 1.17a) leading to an increase of the iDMI while a positive electric field partially compensates the Rashba electric field (see bottom right of Fig. 1.17a) and decreases the iDMI. Just before the beginning of my PhD, the modification of iDMI by ionic-liquid gating was observed in a $Pt/Co/HfO_2$ ultrathin film [96]. The authors measured the iDMI coefficient as a function of the biasing time, using BLS. The absolute value of iDMI first decreases and tends to stabilize after $\simeq 2$ min of voltage application time. The time scale of the effect and the irreversibility are factors which led the authors to explain their observation in terms of migration of the oxygen ions from the HfO_2 layer into the Co and Pt layers and subsequent anchoring.
Finally, during my PhD, even larger values of $\beta_{DMI} = 1100 - 2000$ fJ/Vm have been reported in a ultrathin $Pt/Co/AlO_x$ trilayer [77], and were ascribed to charge effect (see fig. 1.17b).

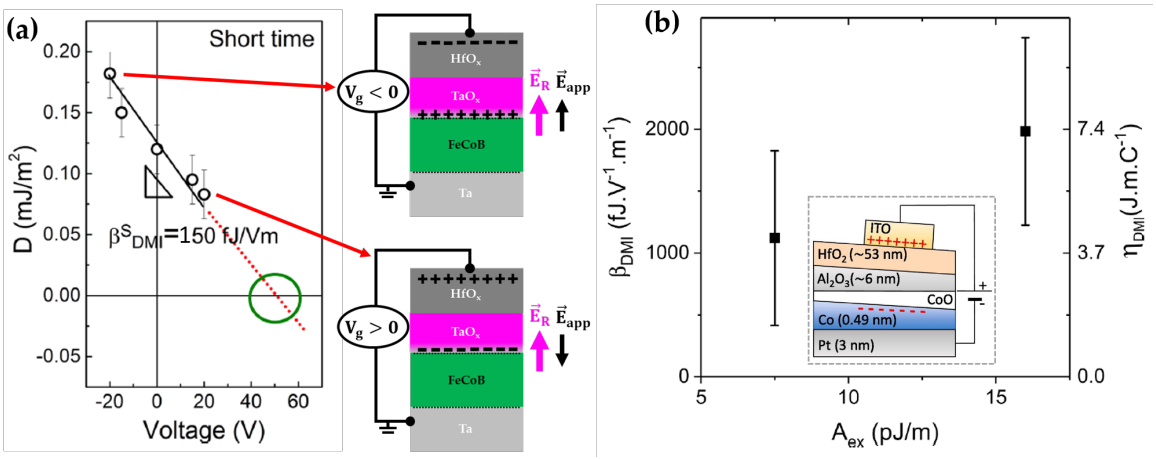

Figure 1.17: **Voltage tuning of the interfacial Dzyaloshinskii-Moriya interaction:** (a) First experimental osbservation of a large voltage tuning of the iDMI in a $Ta/FeCoB/TaO_x$ trilayer (Extracted from [76]) (left) short time scale iDMI measurements (top right) Negative voltage leads to the increase of the interfacial electric field due to the addition of the Rashba and applied electric fields (bottom right) Positive voltage decreases the interfacial electric field (b) Voltage efficiencies for iDMI in a $Pt/Co/AlO_x$ trilayers as a function of the exchange stiffness chosen on the calculation. The voltage is applied in a capacitor geometry, as schematically represented in the inset. (Extracted from [77])

It is important to notice that the effect is not always reversible. In reference [76], applying high voltages for long time scales led to irreversibility. In addition, [ref fatima] Until the beginning of this thesis work, few results were obtained on the control of the gate voltage of the iDMI amplitude, and none for the control of its sign. It would offer a local and dynamical way to precisely control the internal structure of the magnetic domain walls, and especially of the properties of magnetic skyrmion, presented in the next section. In Fig. 1.17a, one can see that the extrapolation of the data towards higher voltages predicts an inversion of the iDMI sign. However at that time such voltage were too high and led to dielectric breakdown. This observation triggered a huge interest since the local control of skyrmion chirality would represent a new degree of freedom for skyrmion dynamics, especially in skyrmion-based logic devices. Within this framework, my PhD project ad-

dresses the electrical control the interfacial Dzyaloshinskii-Moriya interaction in order to control the skyrmion static and dynamic properties.

1.4 CONCLUSION

Starting from the basics, I introduced the notion of magnetic moment and I presented how they arrange themselves to form the different magnetic orders. I progressively focused on ferromagnetic thin films in magnetic trilayers composed of heavy-metal/ferromagnet/metal-oxide, which are the arenas of many interfacial phenomena, and the playground of this thesis work. In such trilayer, I have shown that the magnetic configuration results from the competition between different energies, and that the broken inversion symmetry acts in concert with the spin orbit coupling to bring additional and interesting physics. Particularly, most of the properties stem from the interfaces, like the Perpendicular Magnetic Anisotropy, and the interfacial Dzyaloshinskii-Moriya interaction, which together can stabilize the magnetic skyrmion, presented in the following chapter. Finally, I briefly showed that the different magnetic parameters can be tuned in several ways, the most promising being the local application of a gate voltage. Some of the results obtained in this work are based on the underlying mechanism of gate voltage application introduced in this chapter.

2

MAGNETIC DOMAIN WALLS AND THEIR DYNAMICS

Here, I present the different spin textures that result from the competition between the magnetic energies introduced in the previous chapter. In particular I focus on the magnetic skyrmion in magnetic thin films, which is a chiral spin texture stabilized by the interfacial Dzyaloshinskii-Moriya interaction. Before presenting the skyrmion, I briefly introduce the notion of magnetic domain and domain wall, with a special attention to chiral domain walls. Then, I introduce the magnetization dynamics described by Landau-Lifschitz-Gilbert equation, and more especially the skyrmion dynamics driven by spin-orbit torques via the Thiele equation.

2.1 MAGNETIC DOMAINS AND DOMAIN WALLS

The balance between the magnetic energies introduced in the previous chapter is at the origin of the equilibrium magnetic configuration in the magnetic layer. It often consists in *magnetic domains* separated by *magnetic domain walls*, both described in the following.
Here, we focus on magnetic thin films magnetized perpendicular to the sample plane, *ie* in the $\pm z$ direction, as shown in Fig. 2.1a. The magnetic moments inside such a ferromagnetic layer are not all aligned in the same direction over the entire sample. Actually, it is composed of small regions in which the magnetization is uniform, but opposite to the one of the neighbouring regions. Each of these regions in which the magnetization is uniform is called a *magnetic domain*, as shown in Fig. 2.1a. Their existence results from the competition between energies. On the one hand, the Heisenberg exchange favors all the magnetic moments to be aligned in the same direction (see Fig. 2.1b). One the other hand, the stray field from each magnetic moments, related to the dipolar energy, favours neighbouring magnetic moments in the opposite direction (see Fig. 2.1c).

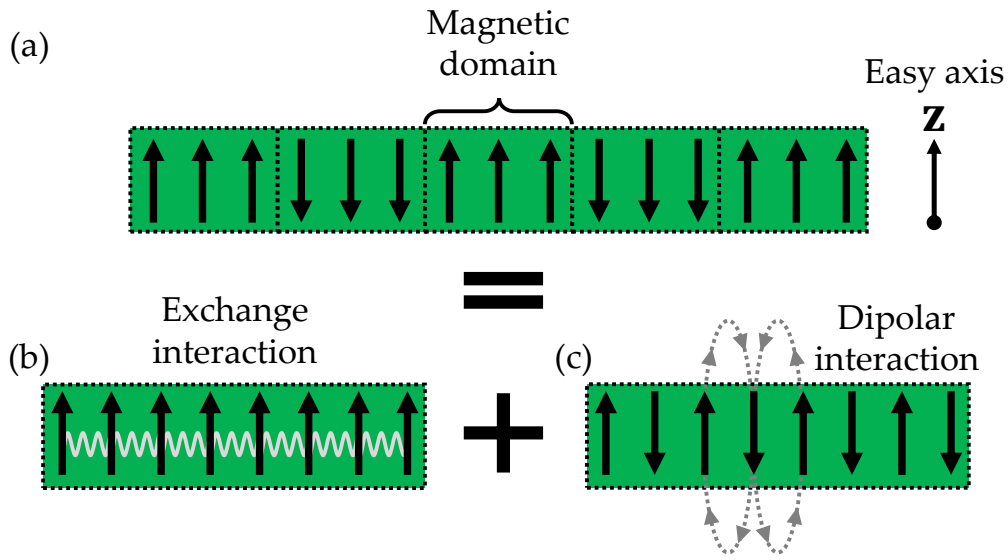

Figure 2.1: **Magnetic domain:** In a ferromagnetic material, a magnetic domain is a region with uniform magnetization (see top part). The creation of magnetic domains is the result of the competition between the different energy terms, but can be understood only considering the competition between the exchange (bottom left) and dipolar (bottom right) interaction.

Moreover, two magnetic domains are separated by a *magnetic domain wall* (DW), in which the magnetization rotates progressively from one direction to the opposite one. The characteristic length of this transition is called the *domain wall width*. In magnetic thin films with Perpendicular Magnetic Anisotropy (PMA), it results mainly from the competition between two energies. On the one hand, the exchange energy requires to minimize the angle between neighbouring spins, maximizing the DW width. On the other hand, the PMA requires to minimize the amount of magnetization misaligned with the easy axis, *ie*

the z-axis. As a result, the DW width is expressed as $\delta_{DW} = \pi\sqrt{\frac{A_{ex}}{K_{eff}}} = \pi\Delta$[1] where Δ is called the Bloch parameter, A_{ex} is the exchange stiffness and K_{eff} is the effective anisotropy constant, both defined in section 1.2.

Inside the DW, the magnetization can rotate around different axis, defining the *DW type*. In the following, we first present the different types of DW and then discuss what favours one type of DW over another. In Fig. 2.2 we propose a 1D representation of a DW in which the magnetization changes along the x direction. The DW type depends on the *helicity* of the DW, ξ, defined as the angle between the normal to the DW (here the x-axis) and the magnetization in the middle of the DW. A *Bloch DW* is defined by $\xi = \pm\frac{\pi}{2}$, thus the axis of rotation is the normal to the DW (*ie* the x axis, see Fig. 2.2a). On the contrary, a *Néel DW* is defined by $\xi = 0 + k\pi$ ($k \in \mathbb{Z}$), thus the axis of rotation is tangent to the DW (*ie* the y axis in see Fig. 2.2c). Finally, an *intermediate* DW corresponds to a DW defined by a combination of a Bloch and a Néel component [97]. They are defined by intermediate helicities, as shown in Fig. 2.2b.

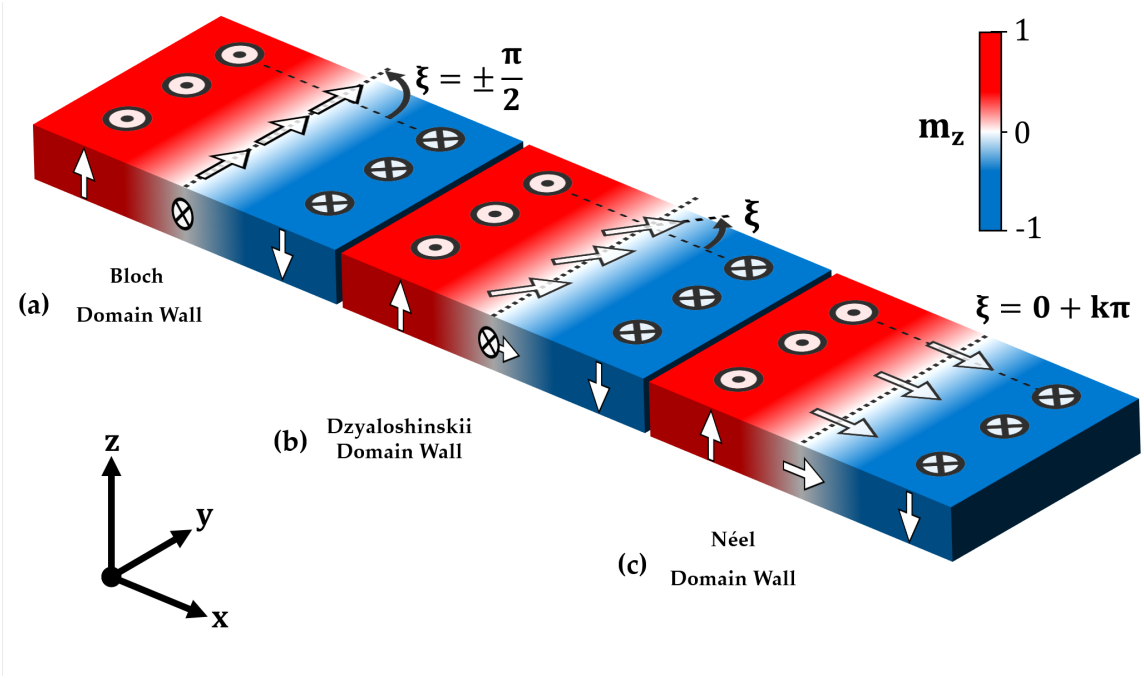

Figure 2.2: **Domain wall types:** The three domain wall (DW) type, defined as a function of the helicity. (a) A Bloch domain wall, defined by $\xi = +\frac{\pi}{2}$ (b) A Dzyaloshinskii domain wall, defined by an intermediate helicity and (c) a Néel domain wall, defined by $\xi = 0 \pm k\pi$ ($k \in \mathbb{Z}$).

Depending on the material and deposition parameters, a given DW type is favoured. Notably the iDMI, presented in the previous chapter, is a key parameter that drives the DW type in magnetic thin films. For example, in the absence of iDMI in magnetic thin films with PMA, the minimization of volume magnetic charges leads to the stabilization of Bloch-type DWs. On the other hand, it is generally considered that the addition of iDMI in these systems stabilizes Néel DWs [9, 10]. However if the iDMI is not large enough, the com-

1 if considering the polar angle profile, in this case δ_{DW} is called the Lilley width. If considering the m_z profile, the DW width is given by $\delta_{DW} = 2\Delta$, called the Hubert width, which we use in this work.

petition with the volume magnetic charges lead to the stabilization of intermediate Dzyaloshinskii DW [97]. In section 6.1, we propose a precise study of the DW type in thin films with PMA as a function of the iDMI coefficient amplitude and sign. We performed micromagnetic simulations to study the DW internal structure versus iDMI coefficient. We systematically compare the simulations to an analytical model which enables to unveil the role of iDMI versus volume magnetic charges in the stabilization of the DW type. During my PhD, it was shown in the literature that the DW type can also be driven by anisotropy modulations in magnetic thin films, by tuning the ratio between in-plane (IP) and out-of-plane (OOP) anisotropy [98]. The authors of this work have computed the energy difference between a Bloch and a Néel DW configuration, and shown that it depends on both the IP and OOP anisotropy. They compared their model to micromagnetic simulations, showing an excellent agreement.

Finally, the *DW profile* defines the spatial variation of the magnetization while crossing the DW along its normal. As it is demonstrated in Annex 8.3, the DW profile can be calculated using a 1D model with the same geometry as in Fig. 2.2, where the magnetization changes along the x direction. We thus consider a magnetic layer with PMA and we describe the orientation of the magnetization by the polar angle $\theta(x)$ between the easy axis and the magnetization (see Fig. 2.3). We consider in the following the case of a Bloch DW, or equivalently the case of a Néel DW when the volume magnetic charges can be neglected (for example for large iDMI amplitude, as presented in the following). In these conditions, the total micromagnetic energy density reads as:

$$\epsilon\left[\theta, \partial_x\theta\right] = A_{ex}\left(\partial_x\theta\right)^2 - D\partial_x\theta + K_{eff}\sin^2(\theta) \tag{2.1}$$

where the first term corresponds to the micromagnetic exchange energy density, the second corresponds to the iDMI energy density and the last one contains the contributions of the uniaxial anisotropy and the dipolar energy. It is noteworthy that the sign of $\partial_x\theta$ only matters for the iDMI. This if a first consequence of the fact that this interaction is a chiral interaction in which the direction of rotation of spins inside the DW is important. The applications of the Euler's minimization principle gives the profile that minimizes this total micromagnetic energy:

$$\theta(x) = 2\arctan\left(e^{\pm\frac{x-x_0}{\delta_{DW}/2}}\right) + k\pi \qquad k \in \mathbb{Z} \tag{2.2}$$

where x_0 is the position of the center of the domain wall (where $\theta = \pm\frac{\pi}{2}$), whose width is described considering the z-component of magnetization (and thus $\Delta = \delta_{DW}/2$, the Hubert width). The $\pm$ sign depicts the chirality of the domain wall. The integer k just takes into account the two possible orientation of the magnetic domains on the boundaries of the domain wall. This profile minimizes the energy in equation 2.1 and it is plotted in Fig. 2.3. By injecting this profile in equation 2.1 and integrating, one can obtain the *domain wall energy*:

$$\sigma_{DW} = 4\sqrt{AK_{eff}} \mp \pi D \tag{2.3}$$

The $\mp$ shows that the domain wall energy is lowered when the sign of D is the sign of $\partial_x\theta$ and is increased in the other case. This is another demonstration that the effect of the iDMI favors one direction of rotation of the magnetization inside the DW. Thus, if the iDMI amplitude is large enough, it stabilizes Néel DW with a given chirality, depending on its sign. More precisely, to stabilize Néel DW, the iDMI amplitude as to be large enough to overcome the magnetic volume charges arising from the Néel domain wall configuration [97]. In the next section, we propose to discuss more about the notion of chirality due to the iDMI.

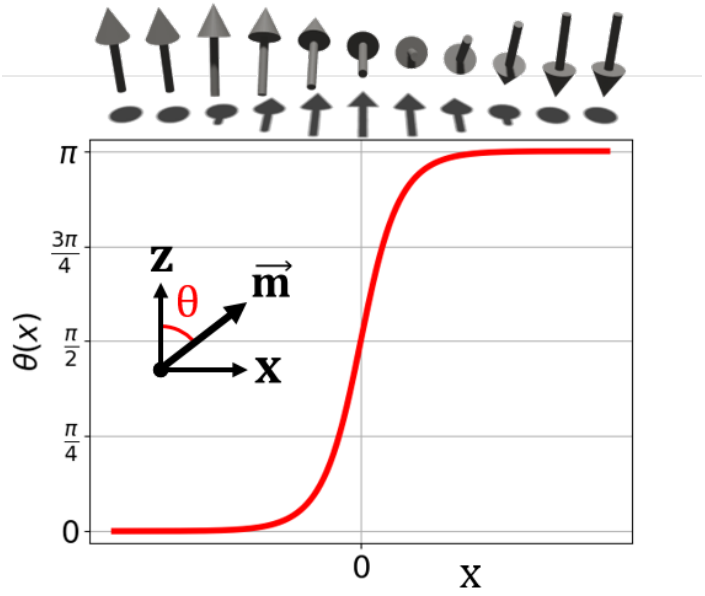

Figure 2.3: **Domain wall profile:** Variation of the polar angle on the magnetization $\theta(x)$ while crossing the domain wall.

2.2 MAGNETIC CHIRAL SPIN TEXTURE

As mentioned in the previous section, iDMI plays a key role in establishing the internal structure of the DW. On the one hand, its amplitude sets the DW type: from Bloch type at zero iDMI to Néel type when the iDMI is large enough, *ie* when it is larger than a critical value called D_C^N (see section 6.1). On the other hand, its sign sets the preferred chirality of the Néel DW. The chirality is a general notion that concerns objects that cannot be superimposed to their mirror image. It originates from the greek $\chi\epsilon\iota\rho$ (kheir) which means "hand" which is a familiar chiral object. Similarly, two DWs in PMA systems inside which the magnetization rotates in opposite direction are mirror image which cannot be superimposed (see Fig. 2.4). Thus the magnetic domain wall in PMA systems is a chiral object, and it is (inaccurately)[2] customary to define its *chirality* by the direction of rotation of the magnetization inside it. In Fig. 2.4a we represent schematically a Néel domain wall with a clockwise (CW) chirality, also called right-handed chirality, and in Fig. 2.4b we represent schematically a Néel domain wall with a counterclockwise (CCW) chirality, also

2 As described above, the chirality is a property of an object, and defining several chiralities makes no sense from the fundamental point of view.

called left-handed chirality. These two DWs are mirror images and the normal to the mirror is set by the axis along which the inversion symmetry is broken, *ie* the z direction (normal to the film plane) in our magnetic thin films with PMA. In another picture this mirror is equivalent to invert the substrate position and thus the iDMI sign, inverting the DW chirality.

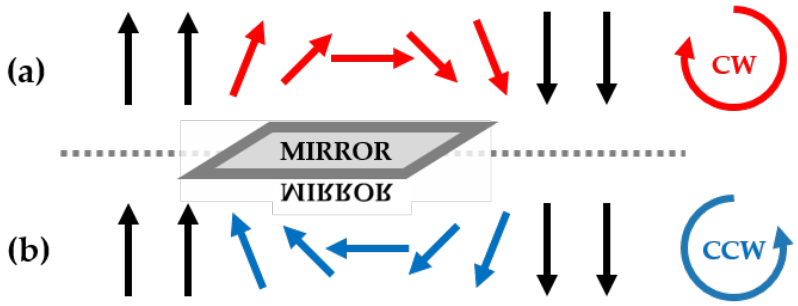

Figure 2.4: **The "chirality" of magnetic domain walls:** (a) Schematic representation of a clockwise, or right-handed Néel domain wall and (b) its mirror image, a counterclockwise or left-handed Néel domain wall. Note that magnetization is a pseudo-vector with specific miror symmetry (see Sec. 2.5.2.1)

As introduced in section 1.2.6 and demonstrated in the previous section 2.1, the iDMI is a chiral interaction that favours a given chirality for the Néel DW depending on the sign of the iDMI coefficient D. With our conventions, a negative iDMI ($D < 0$) favors a clockwise (CW) chirality for the Néel DW (see Fig. 2.4a), and a positive iDMI ($D > 0$) favors a counterclockwise (CCW) chirality for the Néel DW (see Fig. 2.4b).
More precisely, the effect of the iDMI becomes meaningful when considering several DWs in a magnetic material. In the absence of iDMI ($D = 0$), nothing favors energetically one chirality over the other, leading to the simultaneous presence of Bloch DWs with CW and CCW chirality, so called non-homochiral Bloch DWs, as shown in Fig. 2.5a. On the contrary, the presence of iDMI leads to Néel DWs with a unique chirality, depending on the sign of D. Thus, a negative iDMI favours *homochiral* CW Néel DWs, meaning that each DW in the magnetic material has a CW chirality, as shown in Fig. 2.5b. In the same way, a positive iDMI favours *homochiral* CCW Néel DWs, as shown in Fig. 2.5c.

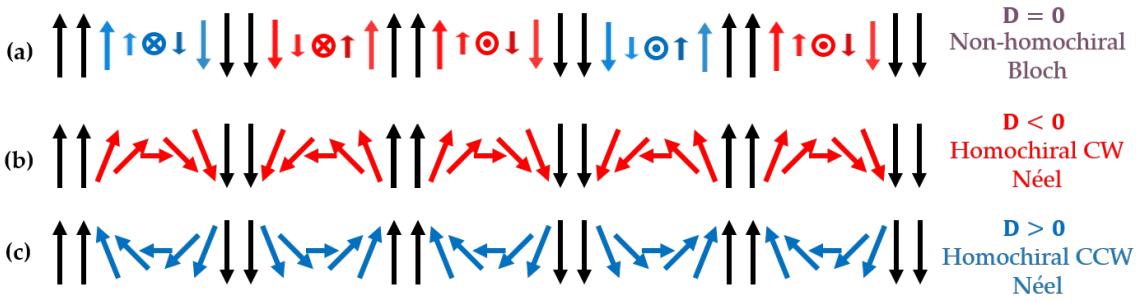

Figure 2.5: **Homochirality of domain walls due to interfacial Dzyaloshinskii-Moriya interaction:** (a) Schematic representation of non-homochiral Néel domain walls in absence in iDMI (b) (resp. (c)) clockwise (resp. counterclockwise) homochiral Néel domain wall favoured by negative iDMI (resp. positive iDMI).

2.2.1 *The magnetic skyrmion*

Magnetic skyrmions are spin-swirling, topologically nontrivial spin textures that hold promise for next-generation spintronic devices [9, 99–102]. Their nanometric size and efficient manipulation by electric current [13] would enable high storage density and fast computational operations. In magnetic thin films with PMA, a magnetic skyrmion is characterized by localized, axisymmetric magnetization configuration in which the direction of the central spin is opposite to the one on its edges [9] (see Fig. 2.6). As a result, by radially crossing a skyrmion, the magnetization rotates by 2π with a fixed sense of rotation (chirality). A good picture to visualize a magnetic skyrmion is to apply a rotational symmetry to a 1D DW, with the revolution axis along one of its boundary spins. Thus, in the same way as there exist different DW types as a function of the iDMI amplitude and sign (see previous section), there exist different types of skyrmion, and their helicity is set by the iDMI sign/amplitude. Notably, the two limiting cases are the Néel and Bloch skyrmions, shown respectively in Fig. 2.6a (CW Néel skyrmion) and 2.6b (CCW Bloch skyrmion)[3]. The 2π rotation of the magnetization, due the the homochirality imposed by the iDMI, is evidenced by the radial cut view in 2.6c (resp. 2.6d) for the Néel skyrmion (resp. the Bloch skyrmion). Moreover, all intermediate iDMI value give rise to Dzyaloshinskii skyrmions, not shown in this section but precisely studied in section 6.1 (equilibrium properties) and 6.2 (SOT driven motion).

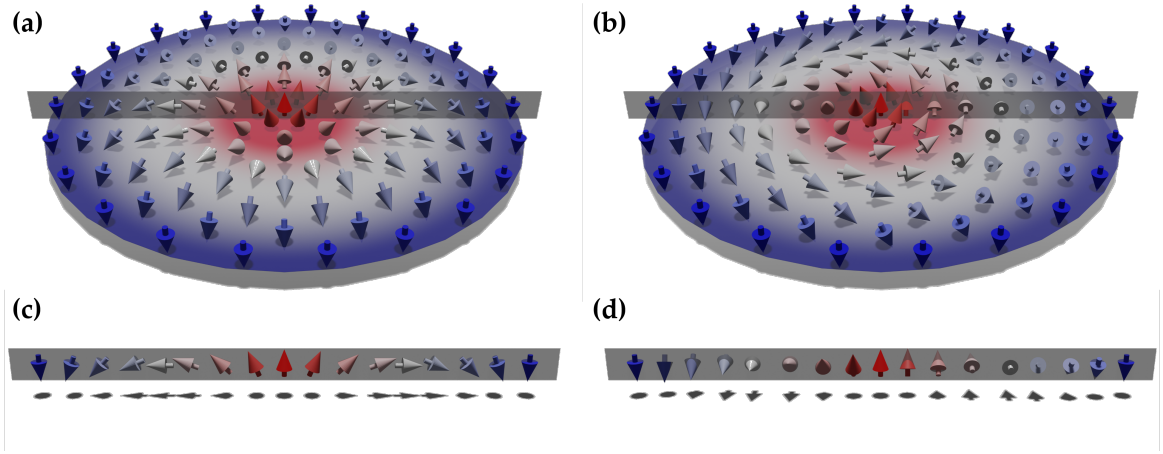

Figure 2.6: **The skyrmion spin texture:** (a) Schematic representation of a clockwise Néel skyrmion and (b) of a counterclockwise Bloch skyrmion. (c) and (d) represent respectively a cut section view of (a) and (b) across the skyrmion diameter. It shows the homochirality of the domain walls imposed by the iDMI.

The name "skyrmion" originates from a much more general object introduced by Tony Skyrme in 1962 [103]. It is the name given to a field configuration used to describe interaction between baryons and pions. Hence, we talk about "magnetic skyrmions" only because their magnetization field $\vec{m}$ has properties similar to those of the Skyrme's field solution [99]. This similitude lies within the notion of topology, the study of continuous de-

3 In the case of Bloch skyrmions we choose to define the chirality as the sense of rotation of the spins observed from a top view of the skyrmion.

formations between two different shapes. Mathematically it turns out that there exists no continuous transformation between the skyrmion configuration and the uniformly magnetized state. In a simple picture, the 2π-rotation over the skyrmion diameter results in a "knot" in the magnetization's field $\vec{m}$ that cannot be unwound without passing through a singularity. More rigorously, it can be understood by introducing the skyrmion *winding number*[4] of a field configuration (which is the magnetization in our case), which reads as:

$$n = \frac{1}{4\pi}\int_{r=0}^{+\infty}\int_{\varphi=0}^{2\pi}\sin\theta(r)\frac{d\theta(r)}{dr}\frac{d\phi(\varphi)}{d\varphi}drd\varphi = \frac{[\cos\theta(r)]_{r=+\infty}^{0}}{2}.\frac{[\phi(\varphi)]_{\varphi=0}^{2\pi}}{2\pi} = p.W \qquad (2.4)$$

This expression is written the the cylindrical coordinate system (r,φ,z) with origin at the skyrmion center (see Fig. 2.7a). Each spin position is described in this cylindrical coordinate system while locally, its orientation is described in the spherical coordinates (1,θ,ϕ) (see Fig. 2.7b). More precisely, $\theta(r)$ is the radial profile of the skyrmion (polar angle) DW and $\phi(\varphi)$ is the local azimuthal angle of the magnetization. The number p is the skyrmion *polarity*, which is linked to the direction of the magnetization at the skyrmion center ($p = +1$ for $\vec{m} \uparrow\uparrow \vec{z}$ and $p = -1$ for $\vec{m} \downarrow\uparrow \vec{z}$). This number has important consequence on the current-driven motion of skyrmions (see section 2.6). The second number, W depends on the behavior of the magnetization along the perimeter of the skyrmion. One can define $\phi(\varphi) = \kappa\varphi + \xi$ where κ is called the *vorticity* and ξ is an additional phase that defines the *helicity* of the spin texture, as shown in Fig. 2.7c. Hence, a spin texture is well defined by its *polarity*, *vorticity* and *helicity*, *ie* the three number (p, κ, ξ). Examples of topological spin textures are shown on Fig. 2.8, for different values of (p, κ, ξ)[5]. In all cases, the skyrmion spin texture is defined by $p = \pm 1$ and its rotational symmetry implies that $\kappa = 1$, and thus $n = \pm 1$. It is important to notice that the winding number is not sufficient to describe a spin texture, and leads to degeneracy. Indeed, all the spin textures from the top (resp. bottom) of Fig. 2.8 correspond to $n = 1$ (resp. $n = -1$). Another visual way to understand the winding number is the number of times the magnetization of a spin texture wraps the unit sphere. For example, by combining all the spin directions in a skyrmion-like spin texture, one can see that it covers exactly one time the unit sphere, leading to $|n| = 1$.

4 Also named "topological charge", "topological number" or "skyrmion number"

5 The correspondance between the helicity and chirality (for example CW Néel for $\xi = 0$) is valid for a positive polarity $p = 1$. If $p = -1$, one has to add π to the helicity to keep the same conventions.

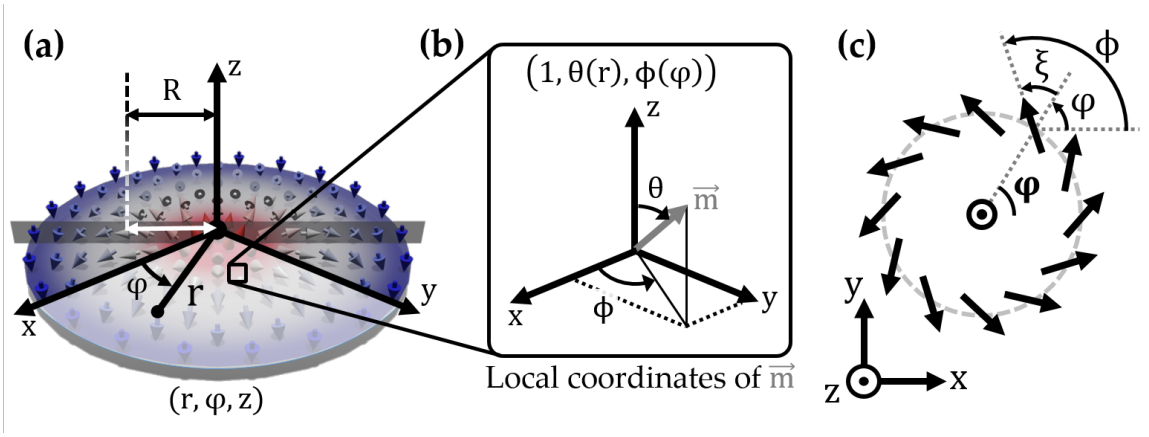

Figure 2.7: **Coordinate system to define the skyrmion spin texture:** Coordinate system used to describe the skyrmion spin texture. (a) Sketch of a Néel-type skyrmion, on which a given spin is located in polar coordinates (r, φ). (b) Locally the orientation of each spin is described using spherical angles $(1,\theta(r),\phi(\varphi))$. The angle ϕ is the sum of the cylindrical angle φ and the helicity ξ, as it shown in (c), a top view of an Dzyaloshinskii skyrmion.

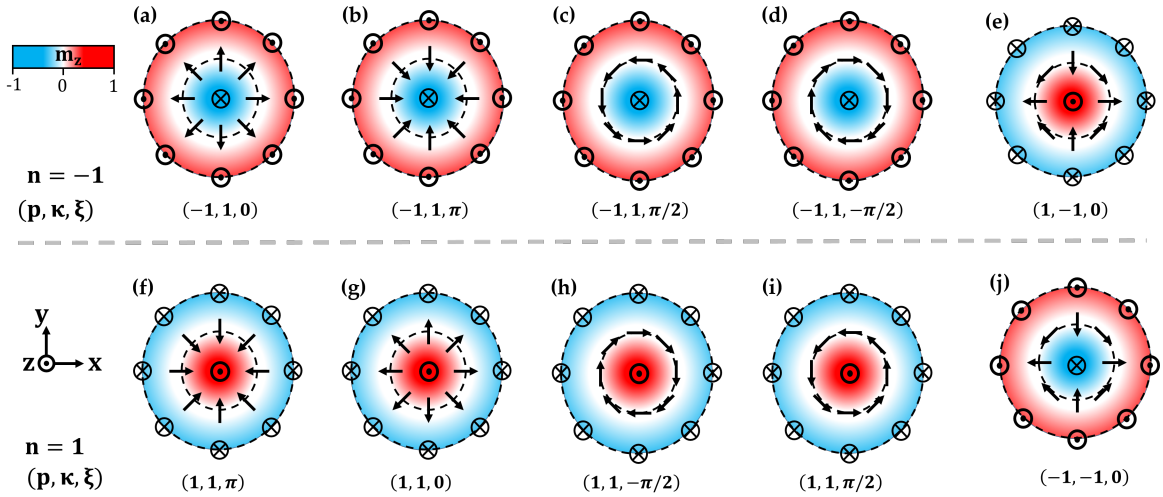

Figure 2.8: **Spin textures as a function of the structural parameters (p, κ, ξ):** Schematic representation of spin textures with (a-e) $n = 1$ and (f-j) $n = -1$. (a) (resp. (f)) CCW Néel skyrmion with $p = 1$ (resp. $p = -1$) (b) (resp. (g)) CW Néel skyrmion with $p = 1$ (resp. $p = -1$) (c) (resp. (h)) CW Bloch skyrmion with $p = 1$ (resp. $p = -1$) (d) (resp. (i)) CCW Bloch skyrmion with $p = 1$ (resp. $p = -1$) (e) (resp. (j)) Antiskyrmion with $p = 1$ (resp. $p = -1$).

Finally, one can find that the usual ferromagnetic state is topologically trivial ($n = 0$) contrary to the skyrmion configuration that possesses a non-zero topological charge $n = \pm 1$. Mathematically, a transformation that changes the winding number such as the transformation from a skyrmion to the saturated state leads (mathematically) to a singularity. It is partially at the origin of the skyrmion stability, and is called "topological protection". However, one has to be careful and not confuse between topological stability and energetic stability. Moreover, a singularity in mathematics becomes an energy barrier in physics, which contributes to stability but which can be overcome. In Annex 8.4, we give a demonstration of eq. 8.65 as well as more details for about the winding number.

Experimental observation of magnetic skyrmions

As presented above, the concept of skyrmion is a general notion [104] introduced in the 60's by Tony Skyrme. Skyrmions in ferromagnets have been first predicted in 1989 by Bogdanov et al. [99]. In 2001, Bogdanov and Rößler developed a theoretical model to describe the chiral symmetry breaking in thin films and multilayers, which predicts the existence of magnetic skyrmions in these kinds of systems [105]. Few after this work, in 2006, Rößler et al. predicted that the skyrmion state could be the ground state of magnetic materials [106], which induced great enthusiasm in research on magnetic skyrmions.
Following these pioneer theoretical works, skyrmions have been observed in many different media. Magnetic skyrmions were first observed in 2009 in the reciprocal space using neutron scattering in bulk-MnSi [107]. At a temperature of 29K, they observed an hexagonal lattice of Bloch skyrmions, as shown in Fig. 2.9a. The skyrmion phase was only stable in a narrow range of temperature and magnetic field. One year after, skyrmions were observed for the first time in the real space in $Fe_{0.5}Co_{0.5}Si$ using Lorentz microscopy, at a temperature of 25K [108]. They also observed an hexagonal Bloch skyrmion lattice (see Fig. 2.9a), stabilized in a narrow window of temperature and magnetic field as depicted by the "SkX" phase in figure 2.9b. It is important to notice that in Fig. 2.9a the bulk Bloch skyrmions are not disks-like 2D spin textures as shown in Fig. 2.6b. In fact each bulk type Bloch skyrmion in Fig. 2.9a is a tube-like shape, elongated in the vertical direction, whose section looks like the 2D Bloch skyrmion presented in Fig. 2.6b. These tubes arrange themselves in an hexagonal lattice to form a 3D bulk Bloch skyrmion lattice. In 2011, the hexagonal Bloch skyrmion lattice was observed near the room temperature (260 K) in bulk-FeGe [109]. All of these result have been obtained in non-centroymmetric B20 structure, leading to a **B**ulk **I**nversion **A**symmetry (**BIA**). The orientation of the DMI vector in such material leads to the stabilization of Bloch type skyrmions, as shown in Fig. 2.9a.

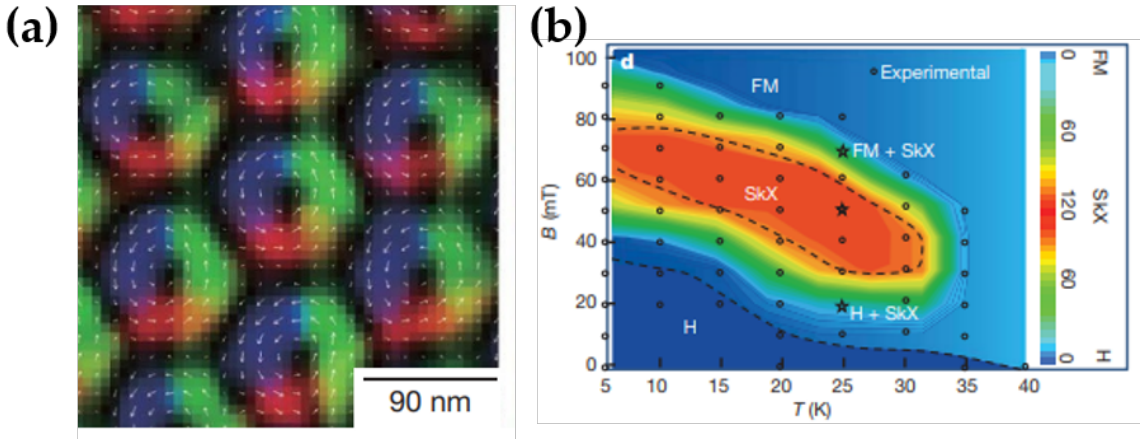

Figure 2.9: **Magnetic skyrmions in bulk systems:** (a) First real space space observation of an hexagonal skyrmion lattice in B20 bulk-MnSi using Lorentz microscopy and (b) the associated (B,T) phase diagram (adapted from [108])

In the context of my PhD we are interested in magnetic thin films where the inversion symmetry is broken by the asymmetric stacking of multilayered structures, so-called **S**tructural

Inversion **A**symmetry (**SIA**). In such system, the DMI has an interfacial origin (see section 4.3) and stabilizes preferentially Néel skyrmions [9], with a disk-like shape as shown in Fig. 2.6a (since the FM layer in very thin). Skyrmions in magnetic thin films were first observed in 2011, when a square Néel skyrmion lattice was observed in a thin layer of Fe deposited on Ir(111) [110]. A low temperature (11 K) and a large magnetic field ($2T$) were necessary to image the skyrmions with a spin-polarized scanning tunneling microscope. A major breakthrough was obtained in 2016 with the first room temperature observation of an isolated skyrmion in a Pt/Co/MgO trilayer heterostructure [101]. Using X-ray magnetic circular dichroism microscopy, they imaged the isolated Néel skyrmion of about 65 nm of radius in a magnetic square dot, as shown in Fig. 2.10a. This result triggered a huge interest to skyrmions in SIA systems such as heavy-metal/ferromagnet/metal-oxide trilayer heterostructure.

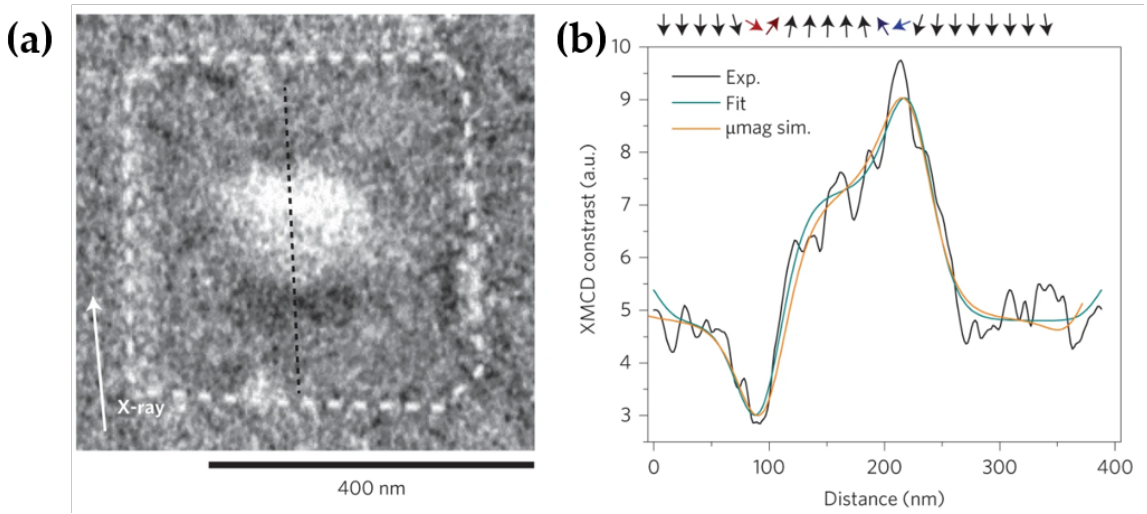

Figure 2.10: **Magnetic skyrmions in magnetic thin films:** (a) first real space observation of an isolated Néel skyrmion in a square magnetic dot, and (b) linescan of the magnetic contrast (along the dashed line of (a)), enabling to extract the corresponding magnetization orientation on top of the graph. (adapted from [101])

2.2.2 *Other topological chiral spin textures*

Two-dimensional spin textures are the most studied ones because they are promising for implementation in spintronic devices. Striking examples are the magnetic skyrmion (see Fig. 2.6), and the very similar skyrmionic bubble (see Fig. 2.12, and note 1 for an explanation of the difference with a skyrmion). Here, we quickly show that there exists a plethora of possible magnetic configurations not limited to the $\mid n \mid = 1$ of the skyrmion spin texture. First, to each skyrmion corresponds an antiskyrmion [111] (figure 2.11a), through the transformation $\kappa \rightarrow -\kappa$, where κ is the vorticity number defined in the previous section. Moreover, the biskyrmion [112] is characterized by the merging of two skyrmions with same winding number and is thus characterized by $\mid n \mid = 2$ (see Fig. 2.11b). The biskyrmion has to be distinguished from the skyrmionium [112–114], shown in figure 2.11c, which is the merging of two skyrmions of opposite winding number so that $\mid n \mid =$

0. The skyrmionium is very promising since it is expected to move without skyrmion Hall effect (described in section 2.6), which is detrimental for applications [114].

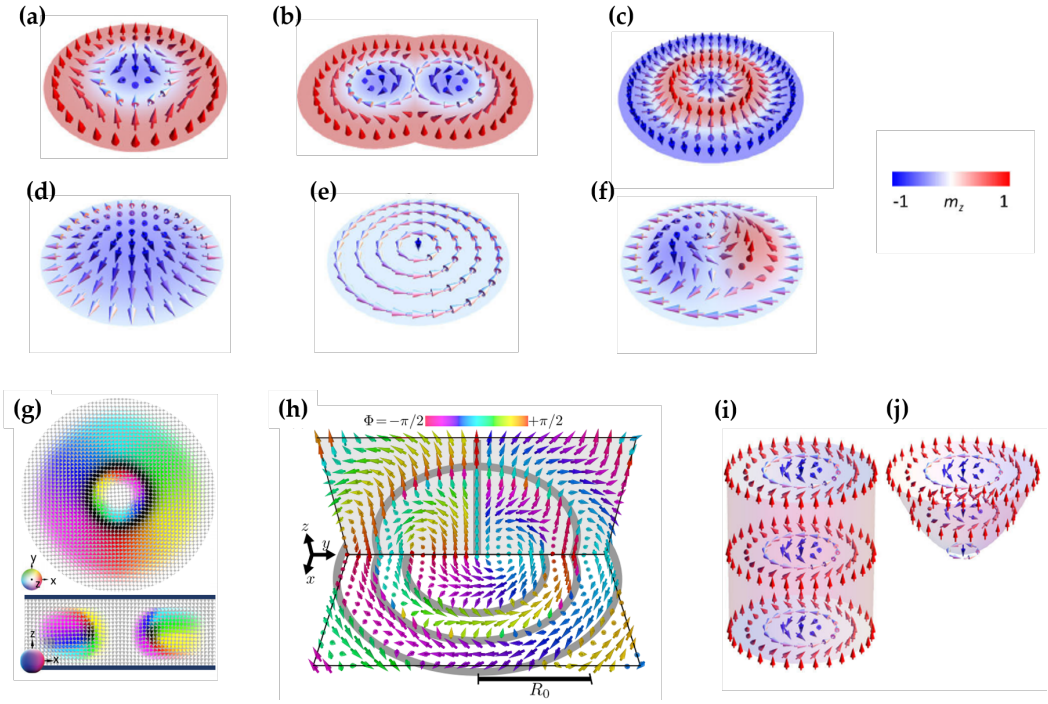

Figure 2.11: **Zoo of topological spin textures:** (a-f) 2D spin textures and (g-j) 3D spin textures, adapted from [102, 115, 116] : (a) Antiskyrmion ($n = 1$), (b) Biskyrmion ($n = -2$), (c) Skyrmionium ($n = 0$), (d) Néel meron ($n = -\frac{1}{2}$), (e) Magnetic vortex ($n = -\frac{1}{2}$), (f) Bimeron ($n = -1$), (g) Upper part is the top view of a hopfions and lower is the cross section view, (h) Three dimensional cut view of a 3D skyrmion, (i) Skyrmion tube and (j) Magnetic robber.

Another important example of 2D spin texture is the magnetic meron [117, 118] (sometimes called radial vortex) which looks like a Néel skyrmion, but with an in plane magnetization at the boundaries (see figure 2.11d). Moreover, the magnetic vortex [119] looks like a Bloch skyrmion, with a very compact core and in plane boundaries, as shown in figure 2.11e. The consequence of these in plane boundaries is that the winding number of a meron or a vortex is half that of the skyrmion, i.e. $\mid n \mid = \frac{1}{2}$. The bimeron [120, 121] shown in Fig. 2.11f is characterized by the merging of two merons with same winding number but opposite polarity. As a consequence, it possesses the same topological charge as the skyrmion but its magnetization configuration differs because of the in plane boundaries.

One can find in the literature some interesting three-dimensional topological spin textures like the so-called "hopfions" [122, 123] (see figure 2.11g), also stabilized by the iDMI, for whom the winding number depends on the iDMI strength, and that can also be displaced with current [123]. The analog of the classical skyrmions also exists in 3D [116] and possesses a much more complex spin texture as depicted on figure 2.11h. Finally, the stacking of several skyrmions can lead to the formation of skyrmion tube (figure 2.11i) or magnetic bobbers (figure 2.11(j)).

Note : Magnetic skyrmion VS skyrmionic bubble

There is a skyrmion look-alike spin texture, called skyrmionic bubble, which can be distinguished from the latter for several reasons. First, the skyrmion is mostly stabilized by the iDMI while the skyrmionic bubble is significantly stabilized by the dipolar energy. The second reason is simply the size: while the skyrmion has a compact nanometer size core (theoretically, only one spin defines the skyrmion center, as shown in Fig. 2.6), the skyrmionic bubble is defined by a circular domain (which is typically about 1μm diameter) surrounded by homochiral DWs.

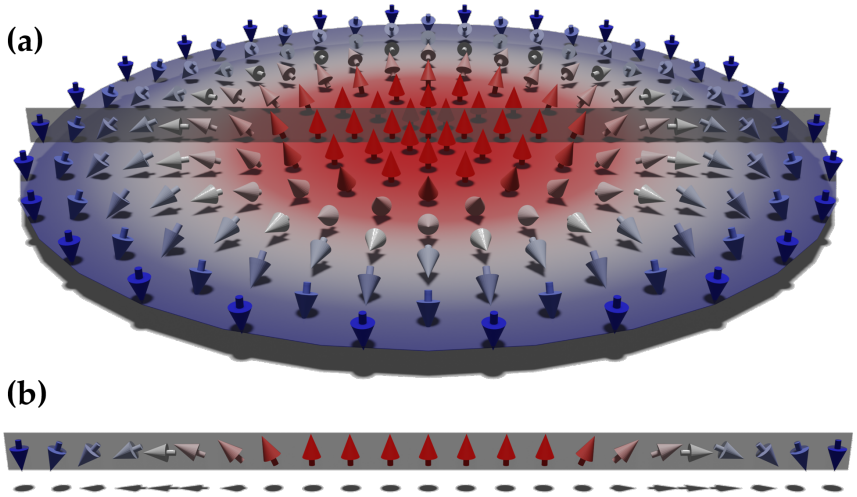

Figure 2.12: **The skyrmionic bubble spin texture:** (a) Schematic representation of a clockwise Néel skyrmionic bubble, that has to be compared to the corresponding skyrmion from Fig. 2.6a. (b) represents a cut section view of (a) across the skyrmionic bubble diameter. It shows the magnetic domain in the center, surrounded by the CW Néel DW.

However, the frontier between these two spin textures can be blurred [124–126], and since they share the same topology (they have the same winding number) and dynamic properties, we will call them both skyrmions in the following.

2.3 THE LANDAU-LIFSCHITZ-GILBERT EQUATION

In the previous chapter we have shown that the balance between magnetic energies, as well as the application of an external magnetic field, governs the equilibrium magnetization configuration. Additionally, they contribute to the establishment of an effective magnetic field:

$$\vec{H}_{eff} = \vec{H}_{exch} + \vec{H}_{dip} + \vec{H}_{anis} + \vec{H}_{DMI} + \vec{H}_{ext} \tag{2.5}$$

where each term is linked to the corresponding magnetic energy through $\vec{H}_i = -\frac{1}{\mu_0 M_S}\frac{\delta E_i}{\delta \vec{m}}$. This effective magnetic field is acting on the magnetization through the Landau-Lifshitz-Gilbert (LLG) equation, which governs magnetization dynamics:

$$\frac{d\vec{m}}{dt} = -\gamma_0 \vec{m} \times \vec{H}_{eff} + \alpha \vec{m} \times \frac{d\vec{m}}{dt} \tag{2.6}$$

where $\vec{m} = \frac{\vec{M}}{M_S}$ is the normalized magnetization vector, $\gamma_0 = \mu_0 \gamma$, with μ_0 the vacuum permeability (in kg·m·s^{-2}·A^{-2}) and $\gamma = \frac{g\mu_B}{\hbar}$ the gyromagnetic ratio (in GHz/T) composed of the Landé factor g, the reduced Planck constant $\hbar$ (in J·s) and the Bohr magneton $\mu_B = \frac{|e|\hbar}{2m_e}$ (in J/T) where e and m_e are respectively the charge (in C) and mass (in kg) of the electron. The LLG equation can be transformed in its equivalent form, the Landau-Lifshitz (LL) equation

$$\frac{d\vec{m}}{dt} = -\frac{\gamma_0}{1+\alpha^2}\vec{m} \times \vec{H}_{eff} - \frac{\alpha}{1+\alpha^2}\vec{m} \times \left(\vec{m} \times \vec{H}_{eff}\right) \tag{2.7}$$

which is more transparent for the understanding of the underlying mechanisms. Let's consider the effective field to be along the z-direction and the normalized magnetization in an arbitrary direction, non-collinear to $\vec{H}_{eff}$, as represented in Fig. 2.13.

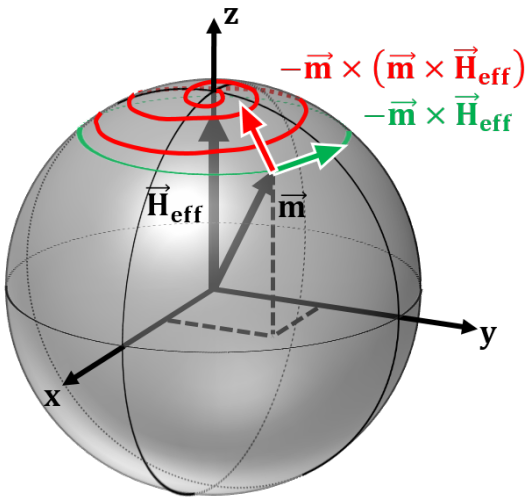

Figure 2.13: **Magnetization dynamics:** According to the Landau-Liftschitz-Gilbert equation, the (normalized) magnetization $\vec{m}$ trajectory is decompoosed in a precession term (green arrow) and a damping term (red arrow). The former corresponds to a conservative magnetization precession (green circle) while the latter induces dissipation that tends to align $\vec{m}$ to $\vec{H}_{eff}$ (red spiral).

Thus, the first term of eq. 2.7 (and of eq. 2.6) corresponds to a precession of the magnetization $\vec{m}$ around the effective field $\vec{H}_{eff}$, as represented by the green arrow in Fig. 2.13. The second term is perpendicular to the precession term, and directed towards $\vec{H}_{eff}$. It corresponds to the damping term, which tends to align $\vec{m}$ along $\vec{H}_{eff}$, and account for the dissipation mechanism. Thus, if considering only the precession term, the magnetization dynamics is conservative and the magnetization describes a cone, whose revolution axis is the effective field (green circle in Fig. 2.13). If including the damping term, dissipation

tends to align $\vec{m}$ to $\vec{H}_{eff}$ (to minimize the corresponding Zeeman energy), as represented by the red spiral in Fig. 2.13.
Moreover, one can see from eq. 2.6 and 2.7 that $\frac{d||\vec{m}||^2}{dt} = 2\vec{m} \cdot \frac{d\vec{m}}{dt} = 0$, and thus that the norm of the magnetization is conserved. Thus, as it is shown in Fig. 2.13, the magnetization direction evolves on the unit sphere, and the precession and damping terms represent a basis with which the whole magnetization trajectory can be described. Generally, for any new source of effective magnetic field $\vec{\Lambda}$, two terms appear in the LL equation, proportional to $\vec{m} \times \vec{\Lambda}$ and $\vec{m} \times (\vec{m} \times \Lambda)$, multiplied by coefficient that contain the physics about it.
If injecting eq. 2.5 in the LL equation 2.7, one can see that each energy term E_i corresponds to a precession torque $\vec{\tau}_i = -\frac{\gamma_0}{1+\alpha^2}\vec{m} \times \vec{H}_i$ and a damping torque $\vec{\tau}_i^{\alpha} = \frac{\alpha}{1+\alpha^2}\vec{m} \times \vec{\tau}_i$. Thus, the dynamics depends on the balance between each torque term and the equilibrium, or steady state is reached when the total torque acting on magnetization is zero

$$\frac{d\vec{m}}{dt} = \vec{0} = \sum_i (\vec{\tau}_i + \vec{\tau}_i^{\alpha}) \tag{2.8}$$

Thinking in terms of these torques gives a good pictures of magnetization dynamics driven by a magnetic field, as it is shown in the next part.

2.4 FIELD-DRIVEN DOMAIN WALL MOTION

In this section, we present a simple model which describes the DW motion under the application of an external magnetic field. The geometry we consider, as described in Fig. 2.14a, consists of an out of plane magnetized sample with a Bloch DW in the middle, which minimizes the volume magnetic charges. The DW is schematically represented by the magnetization in its center. An external magnetic field $\mu_0\vec{H}_{ext}$ is applied in the z-direction.

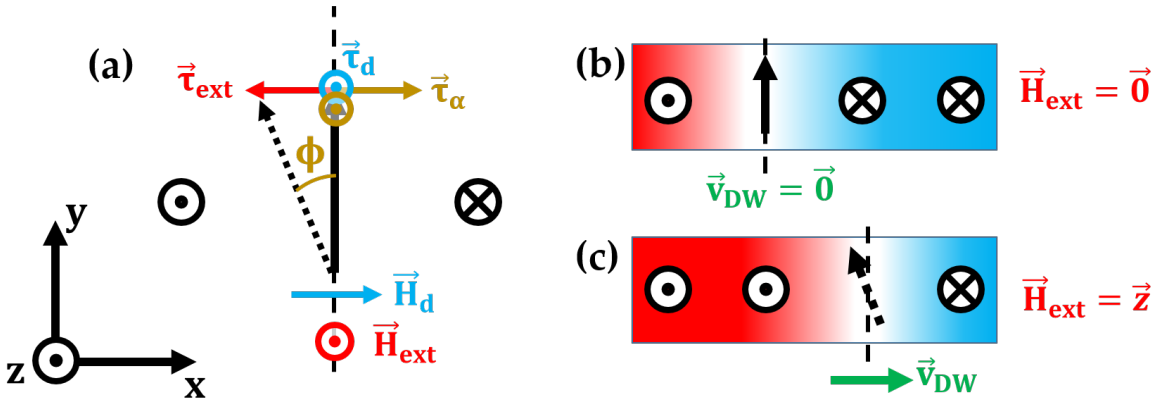

Figure 2.14: **Field-driven domain wall motion:** (a) Schematic representation of the torques responsible for DW propagation under magnetic field. The torque from the external magnetic field is depicted by the red arrow, which induces a dipolar torque, represented by the blue arrow, and finally the response of the damping is represented by gold arrows. (b) Summary : at zero external magnetic, the DW is motionless. By applying an external magnetic field in the z-direction, the DW propagates in the direction of the green arrow, and its internal structure is tilted, as a result of the competition between the torque from the external field and the one from the damping.

As a result, the corresponding torque $\vec{\tau}_{ext} \propto -\vec{m} \times \vec{H}_{ext}$ applies only to the magnetization inside the DW since around, it is collinear to the magnetic field, resulting in $\vec{\tau}_{ext} = \vec{0}$. If we consider that the magnetization inside the DW is along the y-direction, it gives a torque from the external magnetic field $\vec{\tau}_{ext} \propto -\vec{x}$, as depicted by the red arrow in Fig. 2.14a. As a result, volume magnetic charges appear due to the magnetization tilting inside the DW. It creates a dipolar field $\vec{H}_d \propto \vec{x}$ depicted by the blue arrow in the bottom part of Fig. 2.14a. The torque from the dipolar field applies to the tilted magnetization $\vec{m}' \propto \vec{y} - \vec{x}$, and is $\vec{\tau}_d \propto -(\vec{y} - \vec{x}) \times \vec{H}_d = \vec{z}$. It lifts the magnetization inside the DW in the direction of the external field. Finally, the damping is acting on the magnetization inside the DW, slightly tilted in the x-direction and in the z-direction respectively due to the external and dipolar field, $\vec{m}'' \propto \vec{y} - \varepsilon\vec{x} + \varepsilon\vec{z}$. It gives $\vec{\tau}_\alpha \propto \vec{m}'' \times (\vec{\tau}_{ext} + \vec{\tau}_d) = \vec{x} + \vec{z}$, as depicted by gold arrows in Fig. 2.14a. Thus, on the one hand the torque from the damping is compensating the one from the external magnetic field. As a result, the DW is propagating with a steady-state angle ϕ as depicted in Fig. 2.14a. On the other hand, the damping torque is also participating to lift the magnetization out of the plane, in the direction of the external field.
Thus, to summarize this simple model, DW propagation is not directly due to the external magnetic field. It is due to the torque created by the dipolar field which originates from the magnetization tilting inside the DW. Moreover, the magnetization inside the DW remains tilted during the DW propagation, resulting from the competition between $\vec{\tau}_{ext}$ and $\vec{\tau}_\alpha$. In this regime, the DW velocity v_{DW} increases linearly with $\vec{H}_{ext}$, and the DW mobility, $\frac{dv_{DW}}{dH_{ext}}$ is high. Above a certain critical field $\vec{H}_W$, called the Walker field, the damping cannot anymore compensate the torque from the external field and the DW starts to precess while propagating, thus alternating between Bloch and Néel type at high frequency. This precessional regime is known as the Walker regime [127]. It corresponds to a drastic decrease of the DW velocity, as it is shown in Fig. 2.15. In fact in this regime, the DW undergoes back and forth displacement, drastically decreasing its mobility.

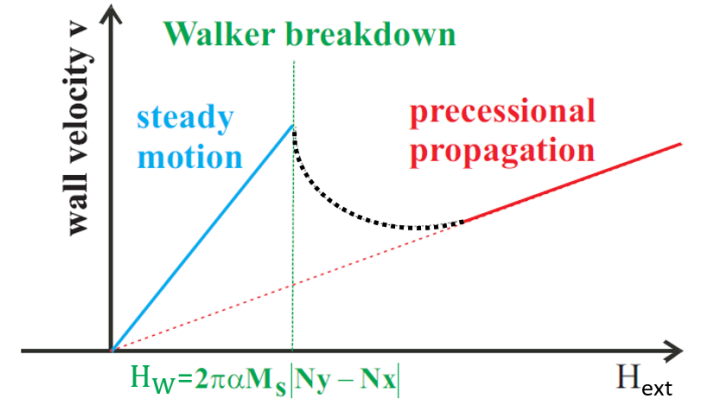

Figure 2.15: **Field-driven domain wall motion: different regimes:** Different DW propagation regimes as a function of the external magnetic field amplitude. Below a critical value called the Walker field, the DW propagates with a steady state tilting angle, and the DW mobility is high (blue line). The Walker breakdown is characterized by a drastic decrease of the DW velocity and mobility, as depicted by the dashed green line. Above the Walker breakdown, the DW is precessing while propagating, called the precessional regime, as depicted by the red line. Extracted from [127].

2.5 CURRENT-DRIVEN DOMAIN WALL MOTION

The main idea behind the control of magnetization with electrical currents is that conducting electrons carry spin momentum that can be transferred to the local magnetization by $s-d$ exchange. There are two main mechanisms that have been widely studied: the spin-transfer torque (STT) and the spin-orbit torque (SOT). The main difference between them is the source of spin polarization: in the former a charge current gets spin-polarized inside a FM layer while in the latter a pure spin current perpendicular to the charge current is produced in an adjacent conductive layer with high spin-orbit interaction.
Although both of these effects can coexist in magnetic materials, the DW and skyrmion dynamics in our HM/FM/MO_x trilayer heterostructure are expected to be dominated by SOT, which in addition provides more efficient effects than STT [128, 129].
Thus, in a first part I briefly present the STT mechanism, without entering into details, and in a second part I present the SOT mechanism that is predominant in our case.

2.5.1 *Spin transfer torque*

As theoretically introduced in 1996 by Berger [130] and Slonczewski [131], the Spin-Transfer Torque (STT) is a transport phenomenon in which a spin-polarized electrical current transfers its angular momentum to the magnetization of a magnetic material. In most of the spintronic devices, the electron current J_e is first spin polarized by passing through a first magnetic layer with fixed magnetization (FM_1), and then interacts with a second magnetic layer whose magnetization is free (FM_2), as shown in Fig. 2.16a. The two magnetic layers are separated by a non-magnetic spacer material, which can be a metal or an insulator ("Spacer" layer in Fig. 2.16a), respectively defining the structure of the so-called spin valve (FM_1/metal/FM_2) and magnetic tunnel junction (FM_1/insulator/FM_2).
The major interest of STT is the possibility to control the magnetization without applying any external magnetic field, enabling down-scaling of spintronic devices. For example, in Magnetic Random-Access Memories (MRAM), STT is used to write information at the nanoscale. The effect of the spin current (polarized in a direction $\vec{p}$) on the magnetization $\vec{m}$ can be described by two additional torques terms in the LLG equation:

$$\vec{\tau}_{STT}^{DL} = -\frac{a_J J}{\hbar M_s}\vec{m}\times(\vec{m}\times\vec{p}) \tag{2.9}$$

$$\vec{\tau}_{STT}^{FL} = -\frac{b_J J}{\hbar M_s}\vec{m}\times\vec{p} \tag{2.10}$$

where a_J and b_J are coefficient related to the strength of the corresponding torque. The first term is called the *damping-like* (DL) STT and the second one is called the *field-like* (FL) STT. The FL-STT, related to magnetization precession, does not participate in the transfer of angular momentum but more to interlayer exchange coupling [132]. The DL-STT is related to magnetization relaxation and thus transfer of angular momentum. Moreover, depending on the sign of J, it can correspond either to a damping term or to an anti-damping term,

which has triggered a huge interest since it allows magnetization reversal without external magnetic field in MRAM devices [133, 134]. Moreover, the anti-damping can be precisely tuned in order to compensate the classical damping, which leads to a purely precessional magnetization dynamics used in well known Spin Torque Nano-Oscillators (STNOs) [135].

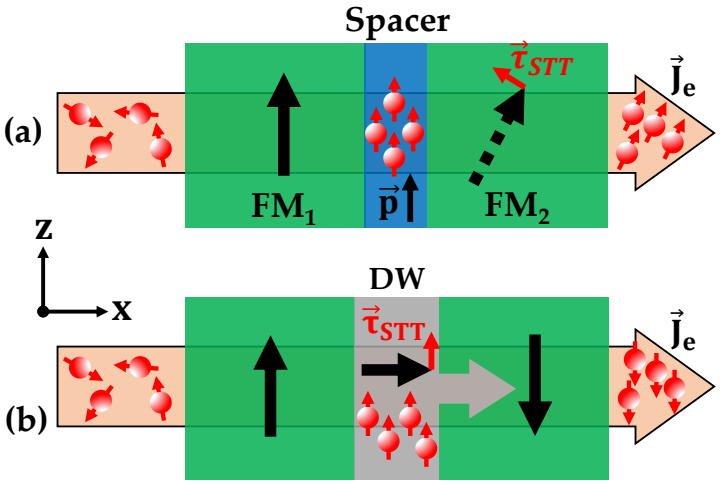

Figure 2.16: **Spin transfer torque:** (a) Typical geometry of a spin valve (spacer = metal) or magnetic tunnel junction (spacer = insulator). Electron flow gets spin polarized in FM_1, which induces a torque on FM_2 (b) Schematic snapshot of a magnetic domain wall (DW) submitted to an electron flow inducing STT-driven DW motion : the electrons get spin polarized in the $+z$ domain on the left, which exerts a torque inside the DW (gray region), resulting in its motion along the electron flow (gray arrow inside the magnetic layer).

The DL-STT can also contribute to the DW motion. Let's consider a DW in a magnetic layer magnetized perpendicular to the sample plane (z direction, see Fig. 2.16b,). The net result of the STT is to drive the DW along the electron flow, regardless of its type (Néel or Bloch) and its helicity. Indeed, just before entering the DW, the electrons are polarized in the direction of the local magnetization, *ie* $\vec{p} = \vec{z}$, as shown in Fig. 2.16b,. Thus, the torque exerted by the spin polarization is maximal inside the DW (gray region in Fig. 2.16b,) and tends to align the magnetization along the $+z$-direction, as depicted by the red $\vec{\tau}_{STT}$ arrow in Fig. 2.16b,. The net result of this phenomenon is the displacement of the DW in the same direction as the electron flow, as shown in 2.16b.
To summarize, in the case of STT, the electron flow gets spin-polarized by going through the FM layer, allowing to manipulate the magnetization with an electrical current. Nonetheless, in our $HM/FM/MO_x$ trilayer, the predominant origin of current driven DW motion stems from another mechanism in which the spin-polarization arises from the adjacent HM layer with large spin orbit interaction. I thus propose to describe it in greater detail below.

2.5.2 *Spin orbit torque*

In this section, I propose to present another mechanism to manipulate the magnetization with an electrical current, which originates from spin-orbit interactions: the spin-orbit

torque (SOT). In a first part we show from symmetry arguments that the SOC applies to systems with broken inversion symmetry. From these symmetry arguments we will show that the SOC results in two different torques, perpendicular to each other.
In a second part, we will present the two physical mechanisms through which the SOC acts in systems with broken inversion symmetry, such as HM/FM/MOx. One is a bulk effect, the so called spin-Hall effect, while the other is an interfacial effect, so called Rashba effect.
Finally, based on the literature we will conclude on the predominant origin of the SOT in our system, providing the proper tools to study the dynamics of our spin textures.

2.5.2.1 *Symmetry considerations for the existence of SOT*

This part is largely inspired by the thesis of Émilie Jué, who worked on the dynamics of DW under STT and SOT [136]

In this part, we use the Curie principle saying that "the symmetries of the causes are to be found in the effects". In others words, we will show that the symmetry of the system imposes the form of the torques that act on the magnetization.

In the following, we will manipulate two kinds of vectors which behave differently under symmetry operations such as mirror symmetry or rotation. On the one hand, there are the true vectors, such as the electric field or electrical current. On the other hand, there are the pseudovectors[6], such as the magnetization, the magnetic field or even the torque exerted by the latter on the former[7]. In Fig. 2.17a we can see that vectors (solid arrows) and pseudovectors (dashed arrows) behave similarly under rotation symmetry. However, as shown in Fig. 2.17b, their behaviour is different when applying a mirror symmetry. This difference of behaviour, associated to the system's symmetries, will give us the allowed torque directions that can exist and that will be applied to the magnetization.

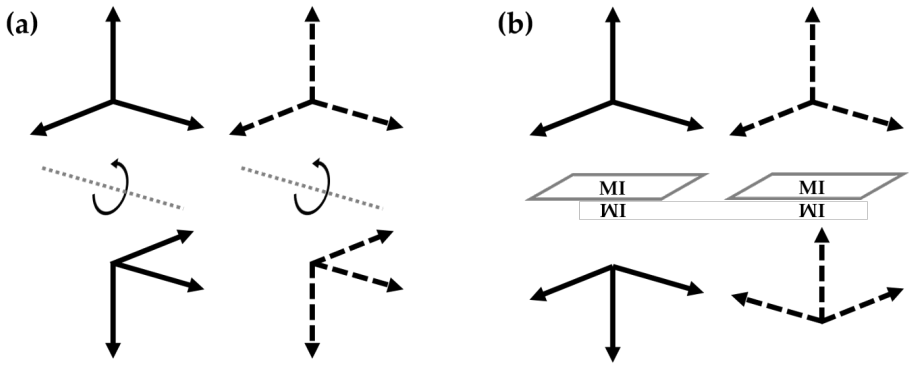

Figure 2.17: **Vectors and pseudovectors:** (a) Vectors (solid arrows) behaves similarly to pseudovectors (dashed arrows) under rotation symmetry (around the y-axis). (b) However, they behave differently under mirror symmetry (mirror in the (x, y) plane).

6 or axial vectors, originating from a vector product of two classical vectors, which leads to different behaviours under symmetry operations
7 The cross product of two pseudovectors is a pseudovector

In the following, we consider an out of plane magnetized domain (along the z-direction), as shown in Fig. 2.18a. Such system is invariant by rotation around the z-axis and by (x,y) mirror symmetry. Spin-orbit torques are non-equilibrium phenomena that take place under current injection. Thus, by injecting it in the x-direction, the rotation symmetry is broken and only the mirror symmetry remains, as shown in Fig. 2.18(b-d). Moreover, a torque being by definition perpendicular to the magnetization, the torque that can exist are oriented along x and y, as depicted respectively by the blue and red arrows[8] in Fig. 2.18e. Here comes an interesting fact, emerging from symmetry argument : since the mirror symmetry remains under current injection, the opposite torque also exist, *ie* in the $-x$ and $-y$ direction, as shown in Fig. 2.18(e,f). In other word, we have proven that current injection in a system with mirror symmetry along the z-axis leads to zero net SOT.

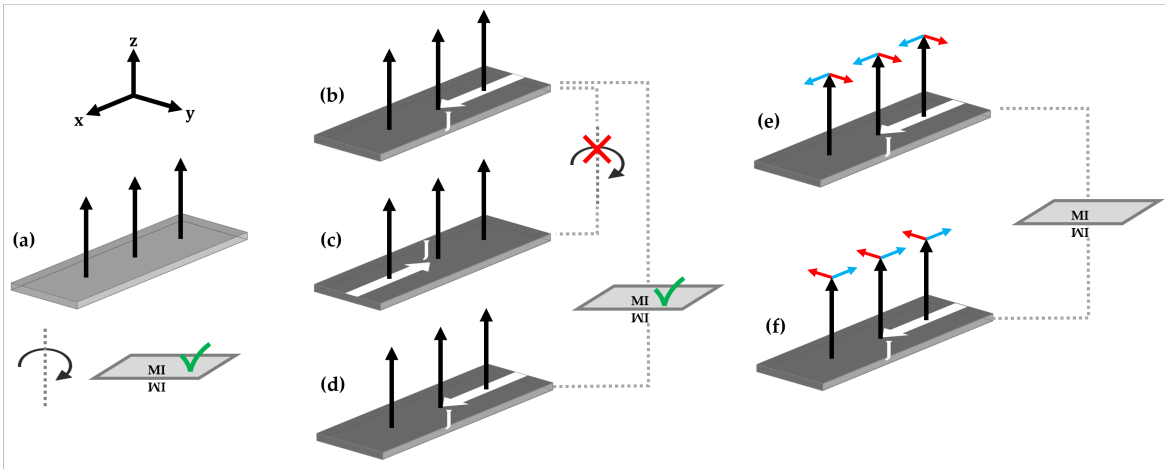

Figure 2.18: **System symmetries without broken inversion symmetry:** (a) In the absence of current flowing in the plane, The system considered here - an out of plane magnetized domain - is invariant under both mirror (in the (x, y) plane) and rotation (around z) symmetry. The magnetization is depicted by the solid black arrows. (b) Under current injection in the plane (white arrow), (c) the rotation symmetry is broken, (d) but not the mirror symmetry, leading to (e-f) a compensation of the SOT (red and blue arrows) by symmetry, inducing zero net SOT.

Now, by introducing an electric field along the z-direction (pink arrow in Fig. 2.19), we break the mirror symmetry with respect to the (x, y) plane, as shown in Fig. 2.19a [9]. Such an electric field can be present in material with broken inversion symmetry. For example, the Rashba effect, which leads to SOT, is due to an electric field along the z-direction originating from the asymmetry of the crystal field (see next section 2.5.2.3). The mirror symmetry can also be broken by an asymmetric stacking, as it is the case for the HM/FM/MO_x trilayer heterostructure studied in this thesis. In addition to the broken mirror symmetry due to the electric field added along the z-direction, the current injection breaks the rotation symmetry, as shown in Fig. 2.19(b-c). In this low-symmetry system, the torques in the x and y direction are no longer compensated by symmetry as shown in Fig. 2.19(e,f). Thus, current injection in systems with broken mirror symmetry leads to

8 These two linearly independent vectors represent a good basis on which any torque can be decomposed
9 By doing so, we anticipate a real physical mechanism in our sample, described in section 2.5.2.3)

torques exerted on the FM magnetization.

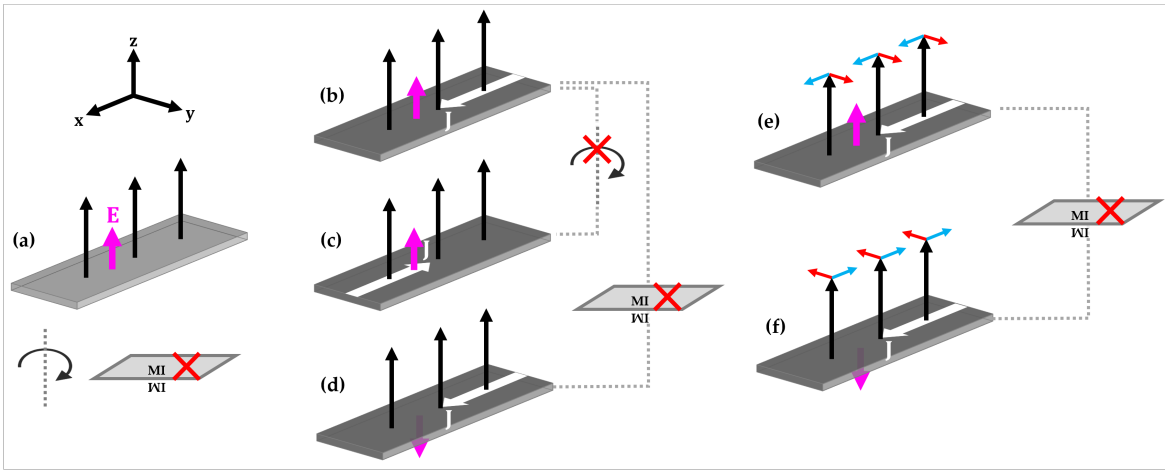

Figure 2.19: **System with broken inversion symmetry:** (a) The mirror symmetry is broken by the addition of the electric field $\vec{E}$ (pink arrow). (b) In the presence of a current (the white arrow), (c) the rotation symmetry and (d) the miror symmetry are broken. (e-f) Thus, in this low symmetry system, the torques (blue and red arrow) are not compensated by any symmetry operation, and can thus act on magnetization.

It is possible to obtain the direction of the torques for all magnetization direction by using symmetry operations. For example, to reverse the magnetization only from $+z$ to $-z$, one need to apply a rotation around the x-axis and a mirror symmetry, as shown in Fig. 2.20(a-c). Thus, we obtain that the torque along y remains along y, and the torque along x is reversed towards $-x$. Now, if we consider a magnetization lying in the plane of the sample (inside the DW), for example in the x direction (Fig. 2.20(d-f)), one obtains a similar result : the torque that was along y remains along y, and the torque along z is reversed towards $-z$. Finally, if the magnetization is along $\pm y$, the system acquires a (x, z) mirror symmetry which leads to zero net SOT (Fig. 2.20(g,h)).

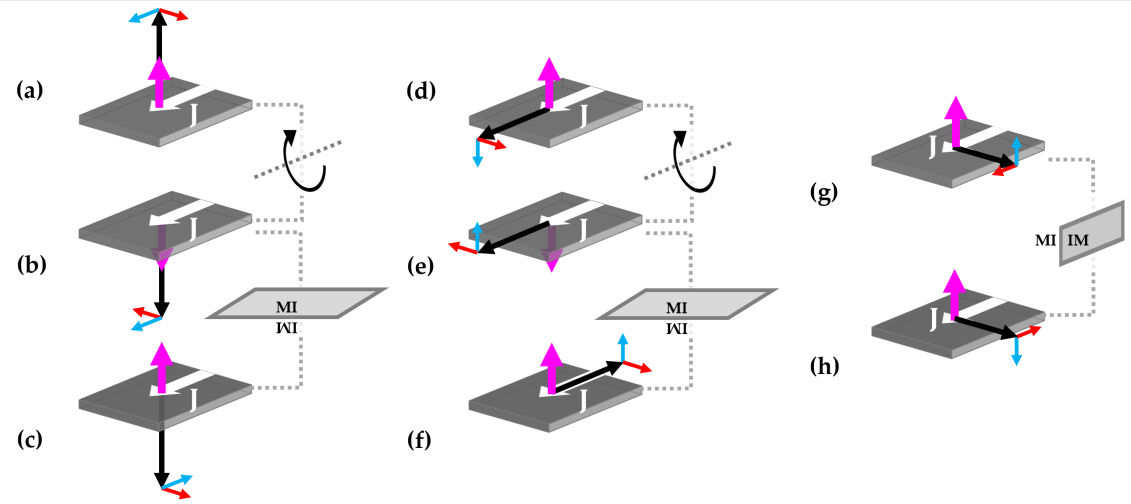

Figure 2.20: **SOT vs magnetization direction:** The torques directions as a function of the magnetization direction can be obtained by using the system symmetries. For an electric field pointing along $+z$, (a) shows the torque directions for magnetization pointing along $+z$, (c) along $-z$, (d) along x, and (f) along $-x$. (b,e) Moreover, using the systems symmetries, the torques directions can also be determined when the electric field points along $-z$. (g,h) If the magnetization is in-plane and perpendicular to the current density (here y axis), the system acquires a (x,z) mirror symmetry which leads to zero net SOT by compensation.

In Fig. 2.21a we summarize these results, by representing schematically the direction of the SOT as a function of the magnetization direction. The torques are called $\vec{\tau}_{DL}$ and $\vec{\tau}_{FL}$ by anticipation of the next paragraph. Moreover, it is often convenient to express torques in terms of their effective magnetic field, *ie* $\vec{\tau}_{DL(FL)} \propto -\vec{m} \times \vec{H_{DL(FL)}}$. Thus in 2.21b and 2.21c we represent $\vec{H}_{DL}$ and $\vec{H}_{FL}$ for the two opposite current directions (respectively $\vec{j} = \vec{x}$ and $\vec{j} = -\vec{x}$) and for the four magnetization directions (since $\vec{m} = \pm\vec{y}$ gives zero net torque by symmetry compensation).

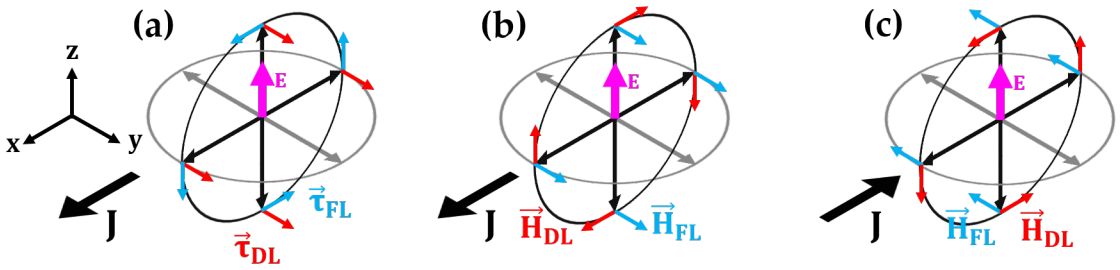

Figure 2.21: **Spin orbit torques direction determined from symmetry consideration in a system lacking inversion symmetry:** (a) Direction of the *field-like* (blue arrows) and *damping-like* (red arrows) torques under $\vec{J} = J\vec{x}$ (black arrow in the bottom left) as a function of magnetization direction. (b) direction of the corresponding effective magnetic field for $\vec{J} = J\vec{x}$ and (c) for $\vec{J} = -J\vec{x}$

To summarize, from symmetry consideration, we have shown that the SOT applies under current injection only if the inversion symmetry is broken, and that its effect can be decomposed into two torques, perpendicular to each other. These two torques depend

on the current direction (called $\vec{j}$) and the direction along which the mirror symmetry is broken (here $\vec{z}$). They are called the *field-like* and *damping-like* torque, and are respectively proportional to (as shown in Fig. 3 of [137]):

$$\vec{\tau}_{FL} \propto -\vec{m} \times \left(\vec{j} \times \vec{z}\right) = -\vec{m} \times \vec{H}_{FL} \quad ; \quad \vec{H}_{FL} = \vec{j} \times \vec{z} \tag{2.11}$$

$$\vec{\tau}_{DL} \propto -\vec{m} \times \left(\vec{m} \times \left(\vec{j} \times \vec{z}\right)\right) = -\vec{m} \times \vec{H}_{DL} \quad ; \quad \vec{H}_{DL} = \vec{m} \times \left(\vec{j} \times \vec{z}\right) \tag{2.12}$$

The existence of SOTs has been predicted and demonstrated experimentally in systems lacking inversion symmetry, such as HM/FM/MO_x trilayers, which are of central interest in this work [138]. The physical origin of SOTs has long been the subject of debate in the scientific community. From years of research, it is now generally considered that SOTs have two origins, which originate either from the HM bulk or from the FM interfaces. They are respectively named the *spin-Hall effect* and the *Rashba effect*, acting jointly under the injection of a current density which breaks the rotational symmetry. In the following, I present these two effects, which will helps us to conclude on the origin of the SOT in our sample, allowing further studies on skyrmions and DW dynamics.

2.5.2.2 *The Spin-Hall effect*

The spin Hall effect (SHE) is a transport phenomenon predicted in the 70's by Russian physicists M. I. Dyakonov and V. I. Perel [139, 140]: a current density (J_{HM}) flowing in the bulk of a conductive material induces a spin accumulation on its lateral boundaries by spin orbit interaction. The direction of spin polarization is transverse to the current density and given by [141–143]

$$\vec{\sigma} = \mathrm{sgn}(\theta_{SH})\vec{j} \times \vec{n} \tag{2.13}$$

where $\vec{j}$ is a unit vector in the direction of the injected current (opposite to the electron flow) and $\vec{n}$ is the normal to the conductor surface. Thus, two opposite lateral surfaces have opposite spin accumulation direction, resulting in a spin current (J_S) generated transversely to the charge current (see Fig. 2.22). The efficiency of this charge-to-spin conversion is called the spin Hall angle $\theta_{SH} = \frac{J_S}{J_{HM}}$ (SHA), and is material-dependent. On the one hand, since the SHE finds its origin in the spin-orbit coupling[10], its efficiency scales as Z^4 [144], with Z the atomic number, as shown in Fig. 2.23c. The SHE is thus more efficient using heavy-metals (HM) instead of standard metals. One the other hand, θ_{SH} can be either positive (Pt, Pd, Ti, Au) or negative (Ta, W, Hf), leading to opposite direction of spin polarization at the lateral boundaries for materials with opposite SHA.

10 via a spin-dependent scattering of electrons on heavy atoms

Note : Symmetry considerations

In the SHE, one can see that the broken inversion symmetry is needed. If considering a HM/FM/HM symmetric structure, the spin accumulation from the top and bottom interface of the FM would compensate, leading *by symmetry* to zero net SOT (see previous part 2.5.2.1).

In Fig. 2.22a (resp. Fig. 2.22b), the SHE is illustrated in a bilayer heterostructure composed of a thin film of FM on top of a thin film of HM with a negative SHA (resp. positive SHA). A current density is flowing in the plane of the HM layer, leading to a vertical spin current whose angular momentum is transferred to the FM magnetization. The resulting SOT can be decomposed in two terms, perpendicular to each other: the *field-like* torque (FL-SOT), $\vec{\tau}_{FL}^{SH} = -\gamma\mu_0 H_{FL}^{SH}\vec{m}\times\vec{\sigma}$ and the *damping-like* torque (DL-SOT) $\vec{\tau}_{DL}^{SH} = -\gamma\mu_0 H_{DL}^{SH}\vec{m}\times(\vec{m}\times\vec{\sigma})$. The coefficients $\mu_0 H_{DL(FL)}^{SH}$ (in T) corresponds to the efficiency of the considered torque. In fact, one can understand the apparition of these two new terms since in the LLG formalism, any new source of effective magnetic field leads to a precession term and a damping term. It corresponds respectively to the *field-like* and *damping-like* torque, with the source being $\vec{\sigma}$ from the SHE. Moreover, the emergence of these two terms can be demonstrated by symmetry, as shown in the previous part 2.5.2.1.

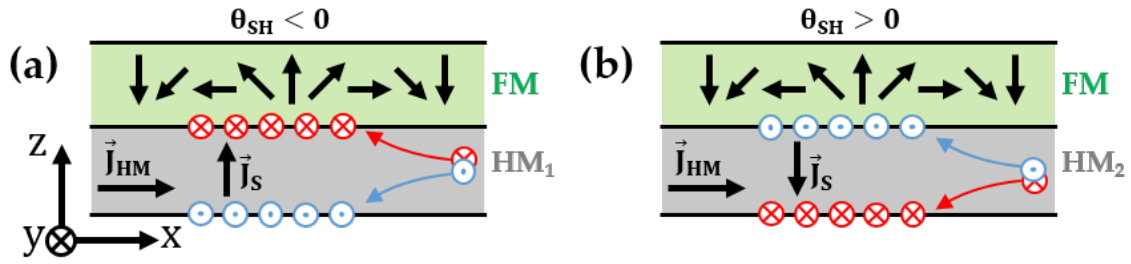

Figure 2.22: **Spin Hall effect in a HM/FM bilayer heterostructure:** (a) (resp. (b)) HM/FM bilayer where a current density $\vec{J}_{HM}$ (horiz. black arrow in HM layer) is flowing in the x-direction in the HM layer with a negative SHA (resp. positive SHA). The resulting spin current $\vec{J}_S$ (vert. black arrow in HM layer) due to electron spin-dependent deflection induces spin accumulation at the HM/FM interface (red and blue arrows), whose angular momentum is transferred to the FM magnetization.

It is often more convenient to write a torque in terms of its effective magnetic field, such that

$$\vec{\tau}_{FL}^{SH} = -\gamma\mu_0\vec{m}\times\vec{H}_{FL}^{SH} \quad ; \quad \vec{H}_{FL}^{SH} = H_{FL}^{SH}\vec{\sigma} \tag{2.14}$$

$$\vec{\tau}_{DL}^{SH} = -\gamma\mu_0\vec{m}\times\vec{H}_{DL}^{SH} \quad ; \quad \vec{H}_{DL}^{SH} = H_{DL}^{SH}\vec{m}\times\vec{\sigma} \tag{2.15}$$

where $\mu_0 H_{DL(FL)}^{SH}$ is the torque efficiency. Thus, $\vec{H}_{FL}^{SH}$ is equivalent to an homogeneous magnetic field in the direction of the spin accumulation $\vec{\sigma}$ while the direction of $\vec{H}_{DL}^{SH}$ depends on the magnetization direction.

The first experimental observation of the spin accumulation due to the SHE has been carried out in GaAs semiconductor using optical Kerr effect technique [145], as shown in Fig. 2.23b. The current was injected along the sample channel (Fig. 2.23c) and the spin polarization near the lateral edges is made clearly visible. It is out of plane and opposite on the two edges of the sample, as expected for the SHE in this configuration.

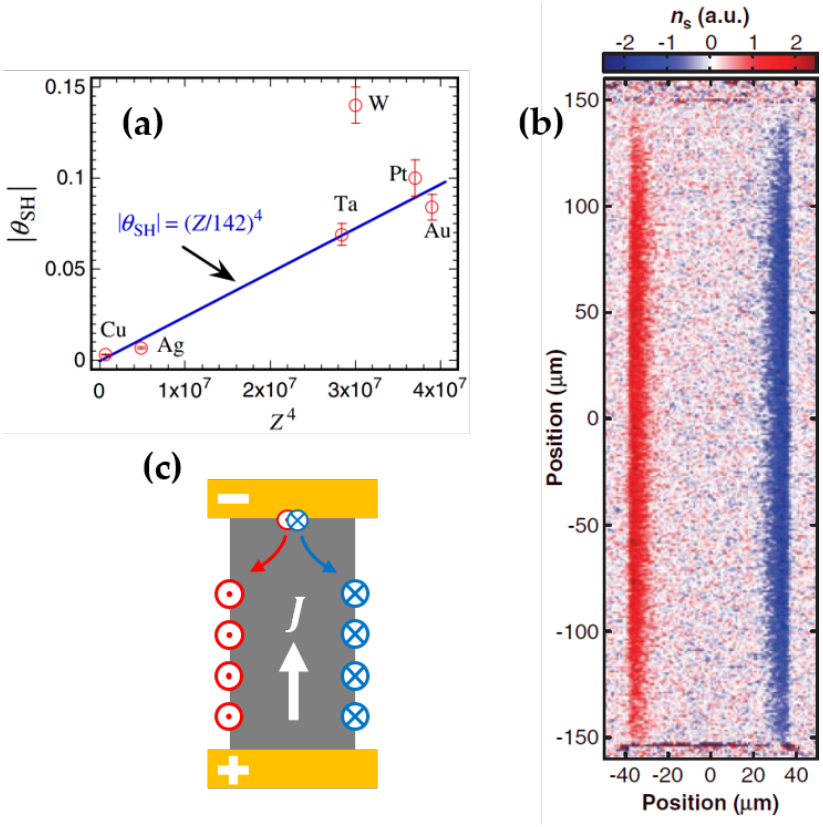

Figure 2.23: **Spin Hall effect - Experimental observation:** (a) Z^4 dependence of the spin Hall angle, showing the link between the SOC and the SHE (extracted from [144]) (b) First experimental observation of the spin accumulation (n_s is related to the spin density) on the lateral boundaries of a GaAs sample using Kerr effect optical technique (adapted from ref [145]). (c) Schematic representation of the result presented in (b). The current density is depicted by the white arrow, and the SHE is illustrated by the separation of opposite spins on opposite track boundaries (the red arrows depict the spins up, and the blue arrows the spins down).

To conclude, it is interesting to mention that the SOT from the SHE, resulting from the injection of a pure spin current vertically in the FM layer, can be seen as equivalent to the STT in which a spin polarized current is injected vertically in a FM layer[11]. The only difference is the source of spin polarization. In the STT, the spins are polarized inside a FM layer while in the SOT, the spins are polarized by spin-orbit interactions in the HM layer. This similarity between SOT and STT is very useful for micromagnetic simulations in which the SOT dynamics is simulated using a vertical spin polarized current (section 6.2.2).

11 But is is important to mention that in the case of STT, a spin polarized charge current is injected in the FM layer, while in the case of SOT it is a pure spin current.

2.5.2.3 *The Rashba effect*

The Rashba effect, or inverse spin-galvanic effect (iSGE) is a pure interfacial effect, where the spins get polarized under current injection due to the presence of an interfacial electric field. In the following we propose a simple picture in order to understand the physical origin and the consequence of the Rashba effect. To start with, we consider a bilayer heterostructure composed of an oxide on top of a conducting layer (Fig. 2.24a). The presence of the interfacial electric field is due to the broken mirror symmetry induced by the interface and by the deformation of the orbitals due to the presence of oxygen atoms. It is vertical and oriented from the conducting layer to the oxide layer, as shown in Fig. 2.24a.

Note : Symmetry considerations

Similarly as the SHE, we can clearly see for the Rashba effect that the broken inversion symmetry is needed. Otherwise the Rashba electric fields from the top and bottom interface of the conducting layer would be opposite, leading *by symmetry* to a compensation and thus to zero net effect, as seen in part 2.5.2.1.

For example, we consider an electron moving in the $-x$-direction as shown in Fig. 2.24b. In the rest frame of the electron, the electric field is equivalent to a magnetic Rashba field given by $\vec{B}_R^{SO} = -\frac{\vec{v}\times\vec{E}_z}{2c^2} \propto -\vec{y}$, thus perpendicular to the electron trajectory (Fig. 2.24b). Generally, this reasoning applies to all electron wavevector: the Rashba effect induces a magnetic field transverse to the electron motion, whose direction is shown in Fig. 2.25b.

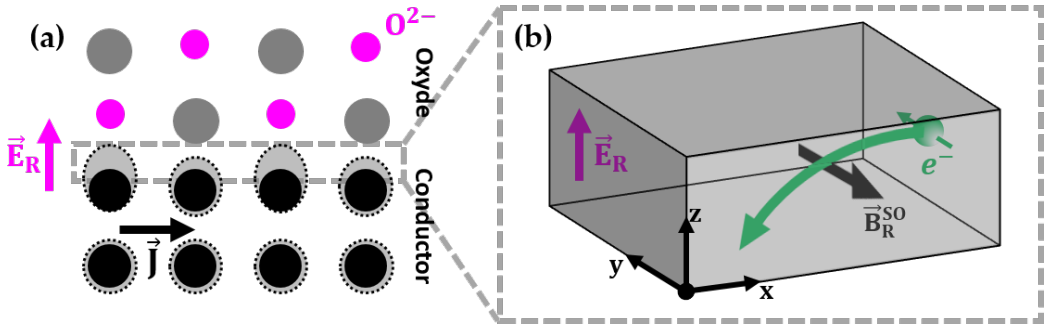

Figure 2.24: **microscopic origin:** (a) Schematic representation of a conductor/oxide interface, where the presence of oxygen leads to an interfacial electric field, called the Rashba eletric field (pink arrow). (b) Zoom-in at the interface, where the Rashba electric field induces a Rashba magnetic field in the rest frame of the electron. This electric field is transverse to the electron motion direction (here we give the example of an electron moving in the $-\vec{x}$ direction, which induces a Rasbha magnetic field along the $-\vec{y}$ direction). The spin of the electron interacts with this magnetic field through a Zeeman coupling, which leads to a Zeeman spin-splitting of the energy levels.

The Zeeman interaction between the electron spin and $\vec{B}_R^{SO}$ which depends on the electron kinetic momentum produces a momentum dependent splitting of the energy bands (so-called spin-momentum locking). This energy splitting is represented schematically in Fig. 2.25(b,c), where the spin up (resp. down) band is represented in blue (resp. red). A cut

at the Fermi level is shown in Fig. 2.25c, evidencing the spin splitting due to the Rashba effect. Thus, for a given direction of electron motion, the Rashba effect consists in a transverse spin polarization and to a lift of the spin degeneracy at the Fermi level (conduction electrons). In absence of current injection, one can see from Fig. 2.25c that there is not net spin accumulation since the Fermi surface is centered. Nonetheless, when injecting a current density in the conducting material (for the example along the x-direction), the Fermi surface is shifted, as shown in Fig. 2.25d. This leads to an uneven occupation of the k and $-k$ momentum state, inducing a spin polarization, given in our case by $\vec{\sigma} = -\frac{m_e^* \alpha_R J}{e\hbar\varepsilon_F}\vec{y}$, with m_e^* the effective electron mass (in kg), J the current density (in A/m²), α_R the Rashba coefficient and ε_F the Fermi energy density (in J/m^3) [146].

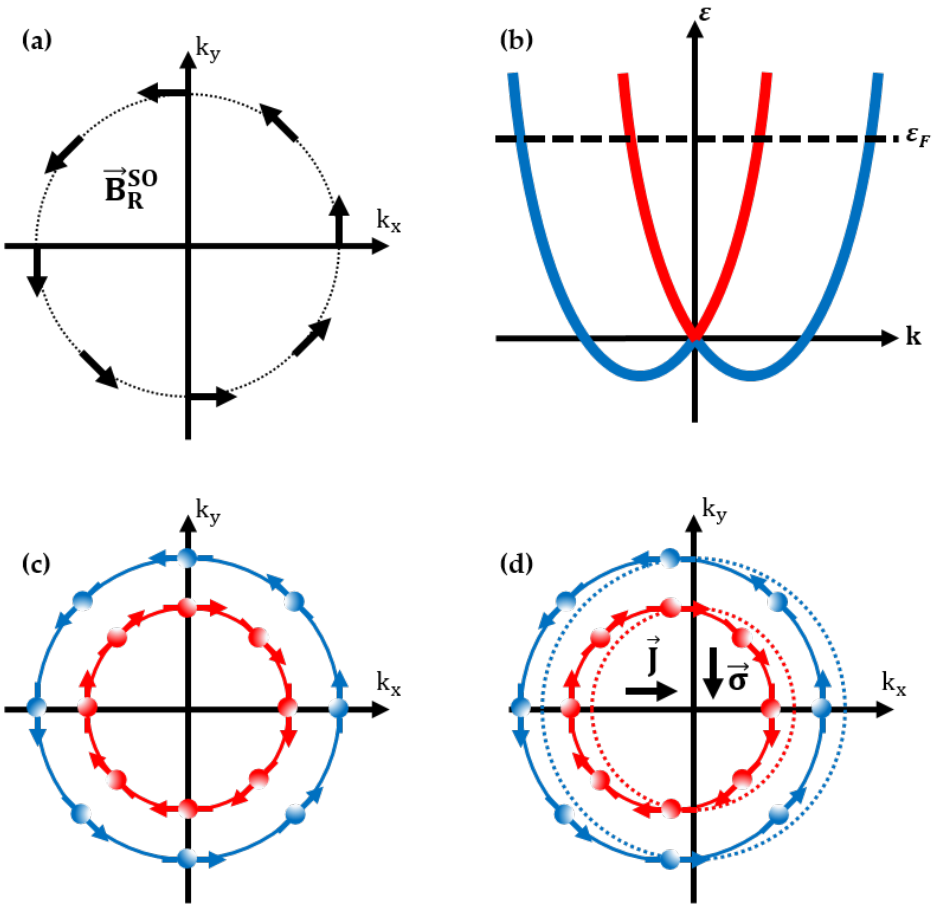

Figure 2.25: **Rashba effect:** (a) Orientation of the Rashba magnetic field, as a function of the electron momentum (generalization of Fig. 2.24) (b) momentum-dependent spin-splitting of the energy bands (c) cut of the energy bands at the Fermi level (dashed line in (b)) and (d) under current injection, there is a shift of the Fermi contour, due to the motion of electron in the direction of the current density $\vec{J}$, which leads to an uneven occupation of the k and $-k$ momentum state, inducing a spin current with a polarization $\vec{\sigma}$ transverse to the current direction.

The effect of this spin accumulation at the interface leads to very similar effect as the SHE, although the physical origin is different. Indeed, the spin accumulation induced by the Rashba effect generates SOT in an adjacent FM layer, that can be decomposed in two contributions which are also called the *field-like* and *damping-like* torque, with

$$\vec{\tau}_{FL}^{R} = -\gamma\mu_0\vec{m}\times\vec{H}_{FL}^{R} \quad ; \quad \vec{H}_{FL}^{R} = H_{FL}^{R}\vec{\sigma} \tag{2.16}$$

$$\vec{\tau}_{DL}^{R} = -\gamma\mu_0\vec{m}\times\vec{H}_{DL}^{R} \quad ; \quad \vec{H}_{DL}^{R} = H_{DL}^{R}\vec{m}\times\vec{\sigma} \tag{2.17}$$

The directions of the torque are the same as in the SHE, but the torque efficiency here is linked to different physical origin, *ie* to the Rashba effect. It is described in terms of Rashba magnetic field, which can be calculated to $H_{FL}^{R} = \frac{\alpha_R JP}{\mu_0\mu_B M_S}$ [147], where α_R is the Rashba coefficient (in J·m), P is the polarization of the charge carriers, and μ_B is the Bohr magneton (in J/T).

2.5.2.4 *Combination of the effects in HM/FM/MO$_x$ trilayer heterostructures*

As it is explained in the previous part, the effect of SOT on FM magnetization can be decomposed in 4 terms, originating from the spin Hall (sec. 2.5.2.2) and the Rashba effects (sec. 2.5.2.3):

$$\vec{\tau}_{FL}^{SH} = -\gamma\mu_0\vec{m}\times\vec{H}_{FL}^{SH} \quad ; \quad \vec{H}_{FL}^{SH} = H_{FL}^{SH}\vec{\sigma} \tag{2.18}$$

$$\vec{\tau}_{DL}^{SH} = -\gamma\mu_0\vec{m}\times\vec{H}_{DL}^{SH} \quad ; \quad \vec{H}_{DL}^{SH} = H_{DL}^{SH}\vec{m}\times\vec{\sigma} \tag{2.19}$$

$$\vec{\tau}_{FL}^{R} = -\gamma\mu_0\vec{m}\times\vec{H}_{FL}^{R} \quad ; \quad \vec{H}_{FL}^{R} = H_{FL}^{R}\vec{\sigma} \tag{2.20}$$

$$\vec{\tau}_{DL}^{R} = -\gamma\mu_0\vec{m}\times\vec{H}_{DL}^{R} \quad ; \quad \vec{H}_{DL}^{R} = H_{DL}^{R}\vec{m}\times\vec{\sigma} \tag{2.21}$$

The relative importance of each of these terms has long been a matter of debate [137], and we propose to show, based on literature, that this complexity can be highly reduced.
First, in a metallic system such as HM/FM/MO$_x$ it has been shown that the effect of SHE can be reduced to the effect of $\vec{\tau}_{DL}^{SH}$, *ie* that $H_{FL}^{SH} \ll H_{DL}^{SH}$ [148].
Second, it has been shown that the torque from the Rashba effect is mainly acting the corresponding a field-like term $\vec{\tau}_{FL}^{R}$ [149].
Thus, in our HM/FM/MO$_x$ systems, it can be considered that the *damping-like* torque originates from the SHE and the *field-like* torque originates from the Rashba effect.
Finally, considering these two torques in a geometry similar to the one considered in this thesis (HM/FM bilayer heterostructure, as shown in Fig. 2.26a), it has been shown that the steady state dynamics is due to $\vec{\tau}_{DL}^{SH}$ [150]. Indeed, as it is shown in 2.26b, $\vec{\tau}_{DL}^{SH}$ induces the DW drift (red curve) while the effect of $\vec{\tau}_{FL}^{R}$ corresponds only to a small initial drift and vanishes in the steady state (blue curve).

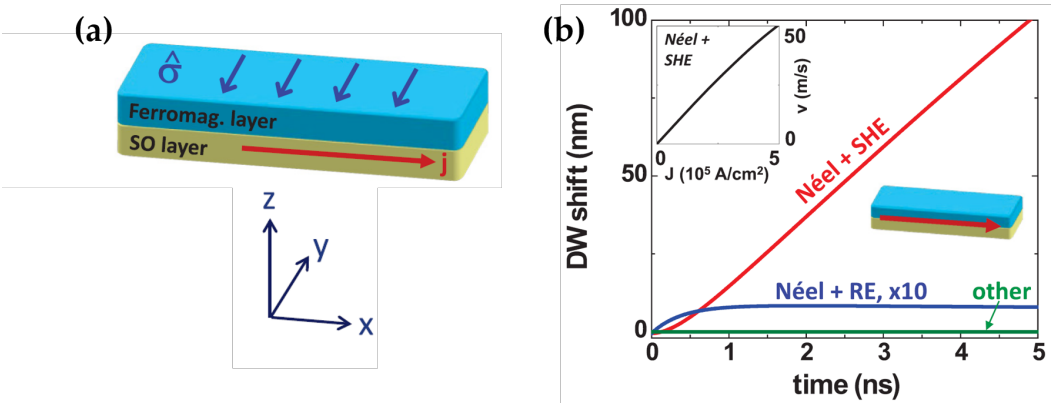

Figure 2.26: **Combination of Rashba ans SHE SOT effects:** (a) Geometry considered for the study of the balance between SHE and Rashba SOT (extracted from [150]) (b) In this geometry, the Rashba effect (RE, blue curve) only contributes to slightly push the DW during a short time, while the spin Hall effect (SHE, red curve) is responsible for the DW motion.

Thus, in samples such as HM/FM/MO_x, the SOT-driven DW dynamics is expected to originate from the spin-Hall effect through the corresponding *damping-like* torque, $\vec{\tau}_{DL}^{SH}$ (eq. 2.19). The LLG equation, that governs magnetization dynamics, is thus extended by this contribution, and reads as:

$$\frac{d\vec{m}}{dt} = -\gamma\mu_0\vec{m}\times\vec{H_{eff}} + \alpha\vec{m}\times\frac{d\vec{m}}{dt} - \gamma\mu_0 H_{DL}^{SH}\vec{m}\times(\vec{m}\times\vec{\sigma}) \tag{2.22}$$

where $\mu_0 H_{DL}^{SH} = \frac{\hbar|\theta_{SH}|J_{HM}}{2|e|M_S t_{FM}}$ is the damping-like torque efficiency[12] with θ_{SH} the spin Hall angle of the HM layer, J_{HM} the current density (in A/m²), e the electric charge (in C), M_S the saturation magnetization of the FM layer (in A/m) and t_{FM} the FM layer thickness (in m) [150]. The effective field $\vec{H_{eff}}$ contains the contribution of the magnetic energies (see section 1.2), while the effect of the SOT is encoded in the last term of the right hand side, corresponding DL-SOT from the SHE.

2.6 SKYRMION DYNAMICS - THIELE EQUATION

In the previous part, we established the LLG equation (eq. 2.22) that governs the magnetization dynamics in our HM/FM/MO_x trilayers under injected current density. It is dominated by SOT, and more precisely by the DL-SOT related to the spin Hall effect.
In the following, we apply this equation to a skyrmion configuration in our HM/FM/MO_x trilayer. We consider a current density flowing in the x-direction in a HM layer with negative spin Hall angle, such as Ta, used in the experimental works of my thesis. We also consider a that the skyrmion configuration is rigid[13] and has a circular symmetry. Under these assumptions, it is demonstrated in Annex 8.5 that the LLG equation can be transformed into the Thiele equation, which governs the dynamics of the skyrmion center [151]. The Thiele equation has the advantage of reducing the complexity of magnetization dynamics to the simple motion of the skyrmion as a point-like object. It is similar to the

12 In the following, $H_{DL}^{SH} \equiv H_{DL}$
13 In other words, considering that the skyrmion keeps the same shape during the SOT driven motion

situation in solid state physics where the motion of a solid object of arbitrary shape is reduced to the motion of its center of mass. Here, the object is the skyrmion (its magnetization configuration) and the equivalent to the center of mass is the position of the center of the skyrmion. This equation represents a force balance on the skyrmion center and in the steady state, its expression reads as

$$\vec{F}_{DL} + \vec{G} \times \vec{v}_{sk} - \alpha \bar{\bar{\mathcal{D}}} \cdot \vec{v}_{sk} = \vec{0} \tag{2.23}$$

where the three terms of the left-hand side represent the three forces acting on the skyrmion center in the presence of a current density flowing in the bottom HM layer.

$$\vec{F_{DL}} = \begin{pmatrix} F_{DL,x} \\ F_{DL,y} \\ 0 \end{pmatrix}, F_{DL,i} = \mu_0 M_S t_{FM} H_{DL} \iint_S \left(m_x \frac{\partial m_z}{\partial x_i} - m_z \frac{\partial m_x}{\partial x_i} \right) dx\, dy \tag{2.24}$$

$$\vec{G} = \begin{pmatrix} 0 \\ 0 \\ G \end{pmatrix}, G = -\frac{M_S t_{FM}}{\gamma} \iint_S \vec{m} \cdot \left(\frac{\partial \vec{m}}{\partial x} \times \frac{\partial \vec{m}}{\partial y} \right) dx\, dy \tag{2.25}$$

$$\bar{\bar{\mathcal{D}}} = \begin{pmatrix} \mathcal{D}_{xx} & \mathcal{D}_{xy} \\ \mathcal{D}_{yx} & \mathcal{D}_{yy} \end{pmatrix}, \mathcal{D}_{ij} = \frac{M_S t_{FM}}{\gamma} \iint_S \left(\frac{\partial \vec{m}}{\partial x_i} \cdot \frac{\partial \vec{m}}{\partial x_j} \right) dx\, dy \tag{2.26}$$

with M_S the saturation magnetization (in A/m), t_{FM} the ferromagnetic thickness (in m) and γ the gyromagnetic ratio (in Hz/T). The first term, $\vec{F}_{DL}$, is the force due to the DL-SOT from the SHE. It is the driving force that shifts a Néel (resp. Bloch) skyrmion along the current direction [152] (resp. perpendicular to it). In addition, a gyromotive force (or gyroforce) $\vec{G} \times \vec{v}_{sk}$ is oriented perpendicular to the skyrmion velocity. Finally, a dissipation force $-\alpha \bar{\bar{\mathcal{D}}} \cdot \vec{v}_{sk}$ originates from the magnetic damping and is oriented against the skyrmion velocity (similar to a viscous force). As a result, the skyrmion is deflected from the direction of the driving force by an angle $\varphi_{SkHE} = \frac{G}{\alpha \mathcal{D}}$, referred to as the skyrmion Hall effect, observed many times in the literature [21, 153–157]. In Fig. 2.27 we show the forces acting on a skyrmion for a current density along the x direction. For both Néel and Bloch skyrmion configuration, we show the direction of the force from the SOT (dashed green arrows), the gyroforce (dash-dotted blue) and the dissipation force (dotted-orange). As a result, the skyrmion velocity (red arrow) takes different direction, depending on the skyrmion structure.

In section 6.2.2, I will use the Thiele equation to develop a model describing skyrmion dynamics in low iDMI systems, and systematically compare to micromagnetic simulations. The forces, and the resulting skyrmion dynamics are precisely described and studied as a function of the skyrmion structural characteristics, such as its helicity, radius or DW width (see Sec. 2.2.1).

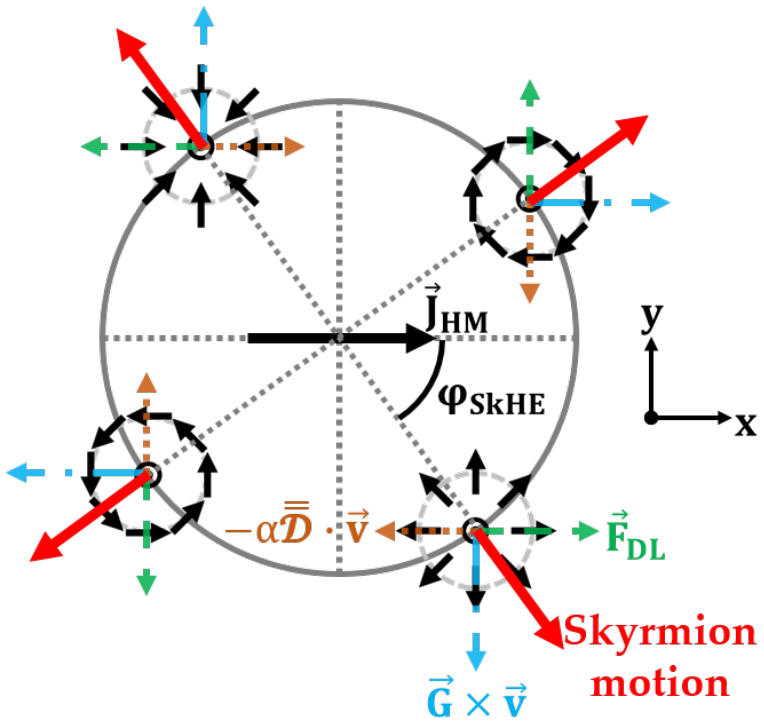

Figure 2.27: **Skyrmion trajectory angle from the Thiele equation:** (a) Decomposition of the forces acting on the skyrmion center for several skyrmion configurations, under an injected current applied in the x-direction (black arrow in the center of the circle). The driving force from the spin orbit torque is depicted by the dashed green arrows, the gyroforce by the dash-dotted blue arrows and the dissipation force by the dotted-orange arrows. The resulting skyrmion motion direction is depicted by the solid red arrow, explaining the existence of the skyrmion Hall effect (φ_{SkHE}) as a result of the force balance acting on the skyrmion center. It is important to notice that the directions of the forces are represented when the skyrmion starts to shift due to $\vec{F}_{DL}$.

To summarize, the LLG equation can be transformed in the Thiele equation under the assumption of a rigid and axisymmetric skyrmion configuration. It tells us that the skyrmion moves under the action of the current density, in a direction that depends mainly on two parameters : the skyrmion helicity ξ and the skyrmion Hall effect, characterized by the skyrmion Hall angle φ_{SkHE}.

2.7 CONCLUSION

In this chapter, we have seen that the competition between magnetic energies are dictating both the equilibrium and dynamic properties of the magnetization. On the one hand, we have introduced the notion of magnetic domain, domain wall and chirality, which allowed to present the magnetic skyrmion spin texture, the object of interest of my PhD thesis. On the other hand, we have introduced and discussed the basics of magnetization dynamics, by presenting the LLG equation and its equivalent for rigid skyrmions: the Thiele equation. These notions are essential for the understanding of the results obtained in my thesis, that concern the stabilization of magnetic skyrmions and their spin-orbit torque driven motion in HM/FM/MO_x magnetic trilayers.

3

EXPERIMENTAL TECHNIQUES

As presented in the previous chapter, we are interested in the properties of magnetic skyrmions in magnetic trilayer heterostructures with a Structural Inversion Asymmetry (SIA), such as heavy-metal/ferromagnet/metal-oxide (HM/FM/MO$_x$). More precisely, the main objective of my PhD was to study the skyrmion properties when applying a gate voltage across the trilayer (see chapter 5). This chapter is dedicated to the description of the main experimental techniques I used during my PhD. It is divided into two parts:

In a first part, I describe step by step the process of fabrication of the sample for voltage control of iDMI. On the one hand, I present the deposition of the magnetic trilayer which hosts skyrmions: Ta/FeCoB/TaO$_x$. One the other hand, I present how we further processed the trilayer for gate voltage application.

In a second part I present the different characterization technique, used to image skyrmion under a gate voltage and to study their properties, namely the Magneto-optical Kerr Effect for skyrmion imaging and the Brillouin Light Scattering for iDMI measurement.

3.1 SAMPLE FABRICATION

3.1.1 *Sample deposition*

For the deposition of the Ta/FeCoB/TaO_x trilayer which hosts magnetic skyrmions, we used DC magnetron sputtering [158]. It is a physical vapor deposition (PVD) technology in which a target (composed of the material to deposit) is bombarded with high energy ions within a plasma which is attracted to the surface of the substrate (in our case, a 4-inches Si/SiO_2 wafer) and condensates to form a thin film. In the deposition chamber, one can find on the one side the substrate on which the material will be deposited (top part in Fig.3.1a), and on the other side the target, composed of the material to deposit (bottom part in Fig.3.1a). The chamber is first put under vacuum (typically 10^{-8} to 10^{-9} mbar) to obtain a good quality of the deposited material. Second, an inert gas composed of Argon (Ar) is injected in the chamber to form the plasma. Then, to initiate the plasma, high voltage is applied between the cathode (at the target location) and the anode (at the substrate location). The electrons present in the sputtering gas are accelerated away from the cathode at high energy which ionize the Ar gas, forming Ar^+ ions. These high-energy ions are accelerated toward the target (cathode), whose atoms are ejected and have sufficient kinetic energy to travel the vacuum environment to reach the substrate. It is called "magnetron" sputtering because it uses a strong magnetic field to confine electrons close to the target surface. On the one hand it improves the deposition rate (by increasing the plasma density) and on the other hand it protects the substrate from direct electron collision, which would damage the deposited thin film.

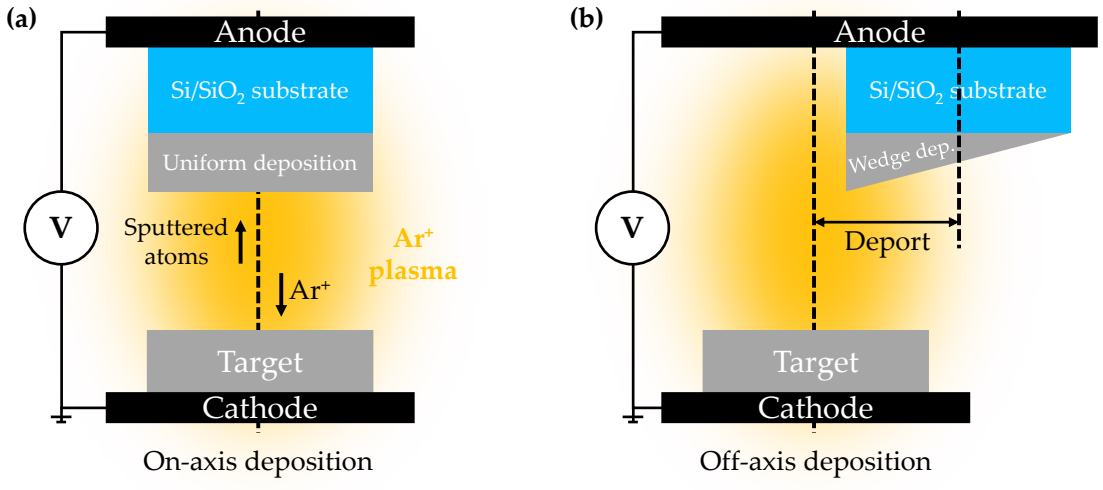

Figure 3.1: **Magnetron Sputtering:** (a) Schematic representation of the working principle of magnetron sputtering, in the on-axis geometry. (b) In the off-axis geometry, the sample is misaligned from the target, leading to a non-uniform deposited thickness

It is also important to mention that there exists different geometries for the deposition in our sputtering machine. On the one hand, the *on-axis* geometry (see Fig 3.1a), the axes of the substrate and the target are aligned, resulting in a uniform thickness of the material deposited on the substrate. On the other hand, in the *off-axis* deposition geometry, we induce a shift between the axes of the target and the substrate, so called the deport (see Fig. 3.1b). Since the deposition rate is larger close the target axis, it leads to a gradual thickness of the deposited material from one edge of the substrate to the other, so called a wedge. This kind of deposition geometry allows a fine control of the material thickness along the wedge. It was very useful for us since skyrmions are stabilized in a very narrow range of material parameter, including for example the ferromagnetic thickness (see chapter 4). We thus used both on-axis and off-axis deposition in the deposition of our Ta/FeCoB/TaO_x trilayer. More precisely, we first deposited on-axis 3 nm of the bottom Ta layer, followed by a crossed double wedge of the FeCoB and the top Ta layer, as shown in Fig. 3.2: The wedge of FeCoB is first deposited, along the x axis. Then, the sample is rotated by 90° and the wedge of the top Ta layer is deposited, perpendicular to the wedge of FeCoB, *ie* along the y-axis. This geometry allows for a precise tuning of the trilayer parameters, since it combines many FeCoB and top Ta thicknesses. It allows on a single sample to ensure skyrmion stabilization (it avoid sample to sample fluctuation), and to study their properties as a function of the material parameters (see chapter 4). The trilayer was further oxidized in a treatment chamber (oxygen pressure 150 mbar for 10 s). Due to the top Ta deposited as a wedge, the oxygen content at the FeCoB/TaO_x interface is gradual from one side of the wedge to the other (see section 4.1 from chapter 4). In order to protect from further oxidation, a 0.5nm layer of Al was deposited and subsequently oxidized at air when taking the sample out of the sputtering machine. Such Al thickness is totally oxidized and thus no metallic Al remains which could be a problem for gate voltage application.

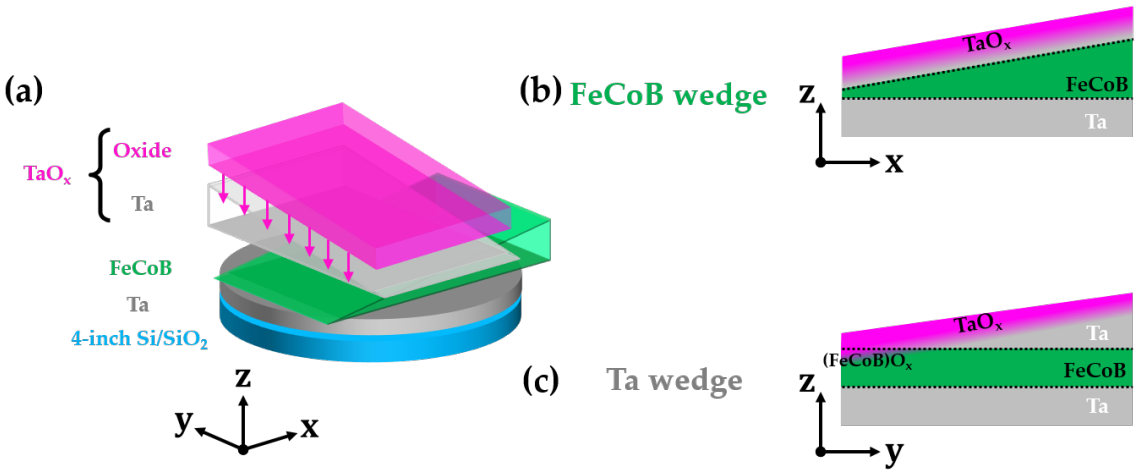

Figure 3.2: **The crossed double wedge deposition:** (a) Schematic representation of the double wedge deposition, where the wedges of FeCoB and top-Ta are deposited perpendicularly the one to the other. (a) Cross section view at a constant top-Ta thickness, varying the FeCoB thickness and (c) cross section view at constant FeCoB, varying the top-Ta thickness.

The final stack thus consists in a Ta(3)/FeCoB(0.8-1.6)/TaO_x(0.5-1)/AlO_x(0.5) (thicknesses in nm) crossed double wedge trilayer heterostructure. Finally, the sample was annealed under high vacuum (typically 10^{-9} mbar) at a temperature of 225°C for 30min. This annealing procedure is the result of an optimization realized during the PhD of Titiksha Srivastava in SPINTEC [159].

The magnetron sputtering deposition of our Ta/FeCoB/TaO_x/AlO_x crossed double wedge sample have been done by Stéphane Auffret, in the Plateforme Technologie Amont (PTA) in SPINTEC, with an Actemium machine.

3.1.2 *Processing the sample for gate voltage application*

In order to study the effect of a gate voltage on the skyrmion properties, the sample has to be further adapted. More precisely we processed the sample for gate voltage application in a capacitor geometry, *ie* the gate voltage is applied to the metallic FeCoB across a dielectric, leading to a an electric field in the $\pm z$ direction. There are two main steps to obtain this capacitor geometry : the deposition of an insulating dielectric layer and the patterning of electrodes, both described in the following. This process was developped at the Néel institute by Anne Bernand Mantel and used during the PhD of Marine Schott [160] and Titiksha Srivastava [159].

Atomic Layer Deposition (ALD) for the dielectric layer

Using Atomic Layer Deposition (ALD) technique [161], we deposited a 20 nm ZrO_x layer, acting as a dielectric layer, and ionic conductor. The ALD is a chemical gas phase deposition method based on alternate saturative surface reaction, allowing layer-by-layer deposition with a very good homogeneity. Layers are formed during reaction cycles by alternately pulsing precursors and reactants and purging with inert gas in between each pulse. In other words, it provides a very good control on the layer thickness ($\AA$ or monolayer control) and a very good layer quality. The thickness of dielectric is the result of an optimization done by Johanna Fischer and myself (not shown in this manuscript). We prepared different sample with dielectric thicknesses[1]: 10, 20, 40 and 70 nm and we studied the $I(V)$ characteristics of the resulting sample. Dielectric breakdown were almost systematically observed for the thinner dielectric layers, while the voltage effect was very small for thicker dielectric layer, the best compromise being a dielectric layer of 20 nm.

We used the ALD setup from Institut Néel, with the help of Laurent Cagnon and Aymen Fassatoui, who teached us how to be autonomous on the machine. Some of the ALD deposition were made by myself and some were done by Johanna Fischer.

1 nominal thicknesses from the ALD were confirmed by X-ray diffraction measurements done by Johanna

Micropatterning of Indium Tin Oxide (ITO) electrodes for gate voltage application

Indium Tin Oxide is the material we used for gate voltage application since as it combines electrical conductivity and optical transparency. It makes it suitable for the study of skyrmion under a gate voltage with optical techniques such as the ones described in Sec. 3.2.1. In order to draw small ITO electrodes on top of our Ta/FeCoB/TaO_x/AlO_x/ZrO_x multilayer, we used a standard LASER lithography process. We start by the deposition of a photoresist layer (AZ1512HS photoresist) on top of the sample, using a spin-coating technique. This technique consists in putting a few drops of the photoresist on the sample and to rotate it at 4000 rpm, which spreads the photoresist by centrifugation, to obtain a thickness of $\simeq$ 1.2 μm (the photoresist corresponds to the yellow layer in Fig. 3.3a). The sample is then put on a hotplate at 100°C during 90s to dry the photoresist. The next step, as shown in Fig. 3.3(a,b), is to locally shine a LASER on the sample, leading to the alteration of the molecular structure of the photoresist where the LASER passed (dark yellow of the photoresist layer in 3.3b). Then, in the development step, the sample is put in a developer, which dissolves targeted regions depending if the resist is negative or positive. For a *positive* resist (resp. *negative*), the regions that have been illuminated by the LASER are dissolved (resp. remain), while the other remain (resp. are dissolved). In Fig. 3.3c we show the result of the development step with a *positive* photoresist such as our AZ1512HS. At this point, the photoresist layer shows holes where the LASER has passed.

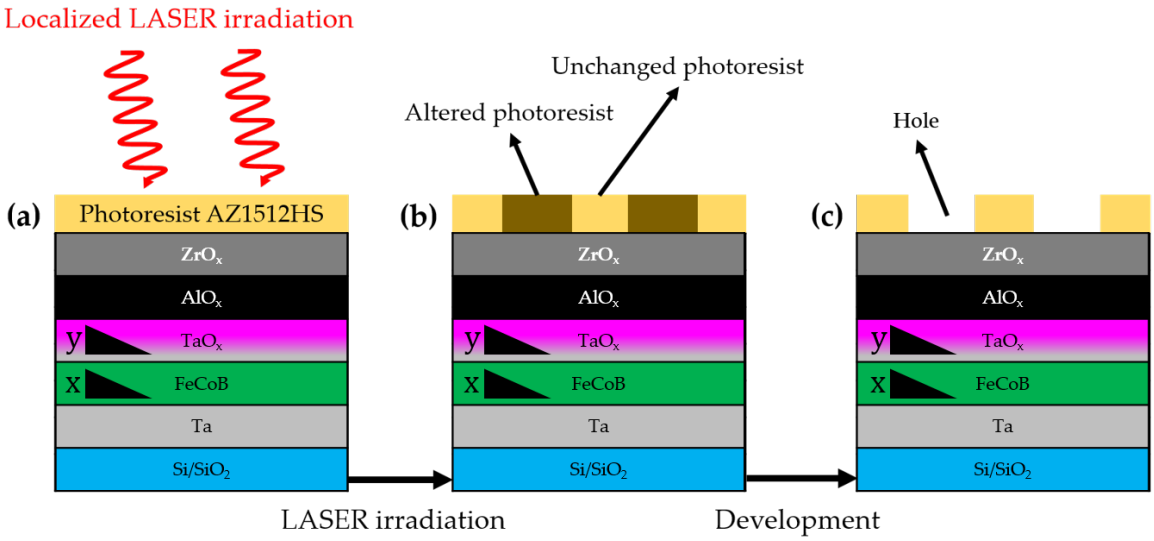

Figure 3.3: **Microppatterning of ITO electrodes by LASER lithography:** (a) Schematic representation of final stack, after the deposition step, with the additional ZrO_x dielectric layer and the photoresist layer. The LASER lithography process consists in local LASER irradiation, (b) which locally alter the molecular structure of the photo resist. (c) Under immersion in a developer, the exposed resist dissolves and leads to the apparition of holes, at the location of the future electrodes.

The ITO is then deposited by magnetron sputtering equally in the holes and on the remaining resist, as shown in Fig. 3.4(a,b). The final step is the lift-off, which consists in immersing the sample in a solution that dissolves all the remaining photoresist. Thus, only the ITO

that is in direct contact with the sample remain. The ITO that is in contact with the sample has the shape given by the regions where the LASER was swept.

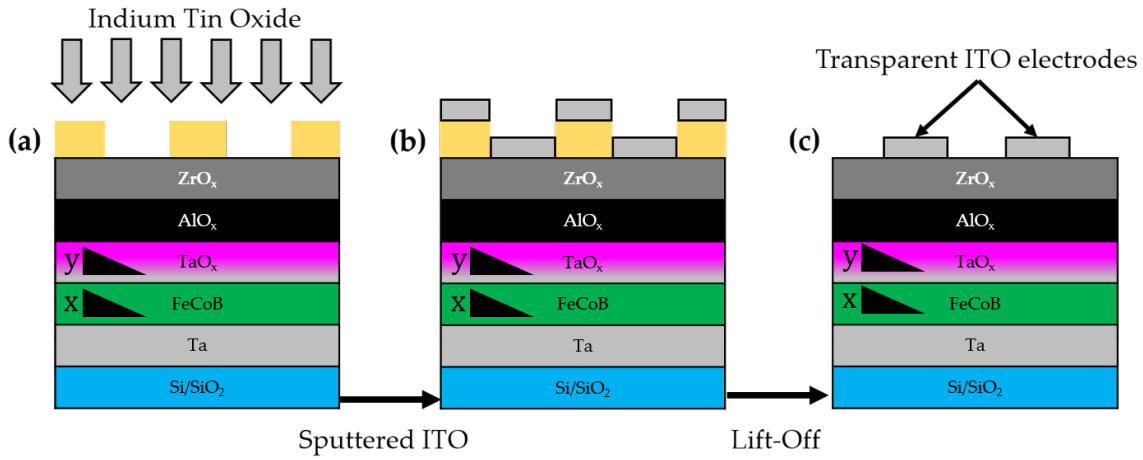

Figure 3.4: **Deposition of the Indium Tin Oxide electrodes for gating:** (a-b) Sputtering of 70 nm of ITO on the sample resulting from Fig. 3.3c, followed by (c) the lift-off. As a result, only the ITO directly in contact with the sample remains, and has the shape of the regions that have been irradiated by the LASER.

The areas in which the LASER is swept is defined on a mask, designed under the Klayout software and shown in Fig. 3.5a. The red-shaded regions correspond to the areas where the LASER will be swept, corresponding to the final shape of the ITO on the sample. We have defined an array of electrodes, of size 800μm$\times$100μm each. The result is shown in Fig. 3.5b, which is an optical image taken under an optical microscope.

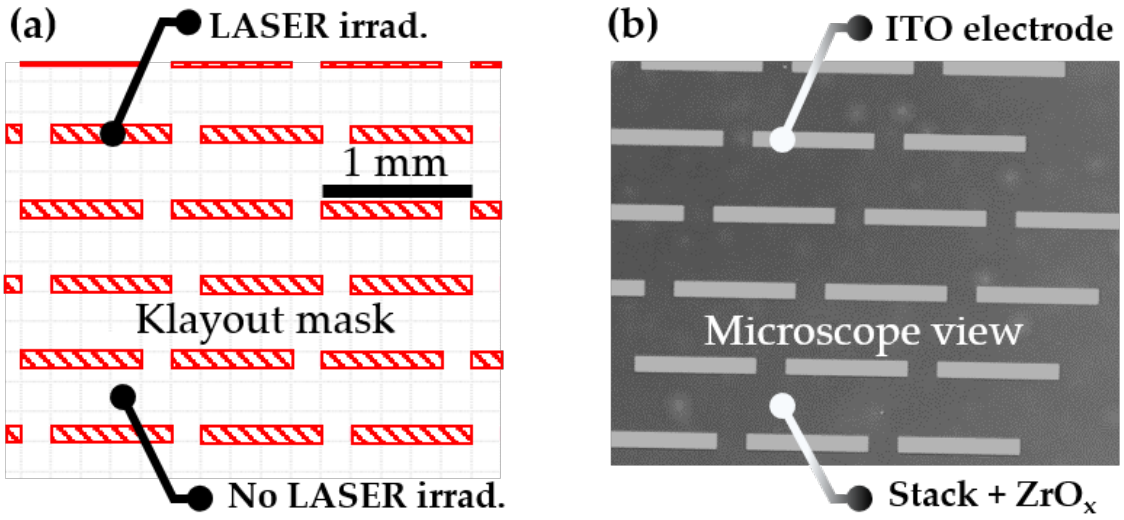

Figure 3.5: **ITO pattern on the sample:** (a) Mask designed under Klayout, where the red-shaded regions correspond to the regions where the LASER is swept, and thus to the shape of the ITO electrode on the sample. (b) Optical image of the sample after the ITO patterning step: the ITO electrodes are the white rectangles, and the dark gray region corresponds to the sample below, composed of the stack, with the additional 20 nm ZrO$_x$ dielectric layer.

The LASER litography process has been done by myself in the Plateforme Technologie amont. The only step that was not done by myself is the ITO deposition by magnetron sputtering, done by Guillaume Gay in the BCAi

Connecting the sample for electrical characterization

At this point, the electrode are patterned on the sample, it only remains to connect them. The sample is first sticked with an insulating glue on a sample holder, that consists in PCB with many copper tracks (as shown in Fig. 3.6(a,b)) It allows multiple connections to current or voltage sources (Keithley 2400 and 2450). In the context of my PhD, we need to connect the sample both for gate voltage application and for current injection in the plane of the bottom Ta layer, to study the skyrmion dynamics under SOT (via the SHE, see Sec. 2.5.2.2).

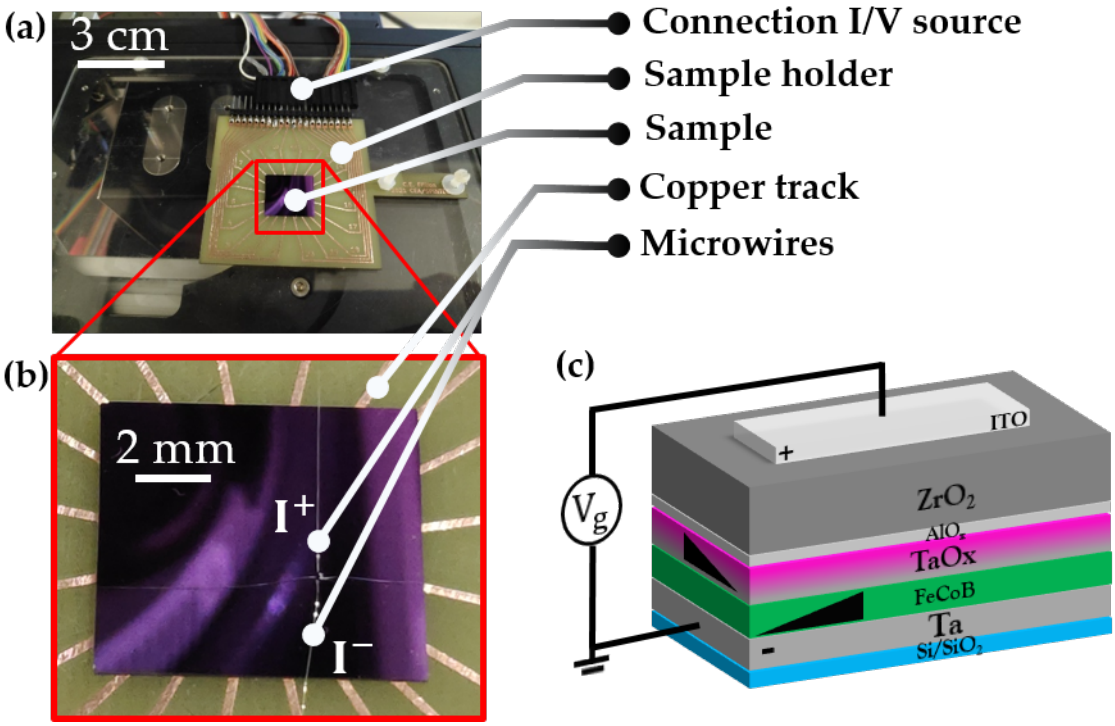

Figure 3.6: **Electrical connection of the sample:** (a) Picture of the sample, mounted on the sample holder with the copper track that are connected to the voltage of current source. (b) A zoom-in view around the sample allows to better distinguish the copper track, but also the microwires, soldered to the sample using a microbonding machine (c) Schematic representation of the sample, on which the gate is applied in a capacitor geometry. The ground voltage electrode is the bottom Ta layer while the positive electrode is the ITO electrode.

On the one hand, the electrical connection for the gate voltage application is realized in a capacitor geometry, as schematically shown in Fig. 3.6c. The ground voltage electrode is the bottom Ta layer while the positive voltage electrode is the ITO. In our experiments, we connected the top ITO electrode by contacting the apex of a conducting tip on the ITO electrode (see chapter 5). The position of the tip can be precisely adjusted using micrometric

regulation screw. The bottom electrode is connected to the voltage source via the sample holder, by soldering micro wires using a microbonding technique. With this technique, it is possible to solder thin wires (25 μm of diameter, visible in Fig. 3.6b) in a precise location. The soldering is done using ultrasonic vibrations, that scratch the multilayer until the bottom Ta layer where the wire is soldered by friction. Thus, on one side the microwire is soldered to the sample, contacting the bottom Ta layer, and on the other side it is contacted to a copper track from the sample holder, itself connected to the voltage source.
On the other hand, the current injection is also realized using microwires soldered using the microbonding device. We solder microwires from the sample to the copper tracks of the sample holder, and the sample holder is connected to the current source, using the electrical connectors visible in the top part of Fig. 3.6a. A view of the microwires soldered on the sample is available at the beginning of chapter 5.

The sample holder has been fabricated by myself. Starting from a PCB fully covered by copper, I used a laser sublimation technique to etch the copper in order to create tracks. The design of the tracks is done under the SOLIDWORKS software, and then the laser sublimation is done in the Y-spot, a building close to SPINTEC proposing such facility.

3.2 CHARACTERIZATION TECHNIQUES

Once the sample is fabricated, it is ready to be studied, using different characterization techniques presented in this section. They allow for the characterization of the magnetic properties of our Ta/FeCoB/TaO_x double wedge. On the one hand it allows for the imaging of skyrmions and the study of their dynamics under current injection (Magneto Optical Kerr Effect), and on the other hand to measure the interfacial Dzayloshinskii-Moriya interaction (iDMI) presented in the previous chapter (by Brillouin Light Scattering).

3.2.1 *Magneto-Optical Kerr effect*

The magneto-optical Kerr effect (MOKE) was discovered by John Kerr in 1878 [162] and is based on the interaction of a light beam with the magnetization of a magnetic sample [163]. A linearly polarized incident LASER beam is sent on the sample with an angle α_i with respect to the normal to the sample plane (see Fig. 3.7a). There exist several configurations for MOKE measurements, depending on the orientation of the magnetization with respect to the incident light beam (see Fig. 3.7(b-d)). In the polar Kerr effect the magnetization lies out of the sample and is parallel to the plane of incidence, as shown in Fig. 3.7b. If the magnetization lies in the sample plane, there is the longitudinal (resp. transverse) Kerr effect in which the magnetization is parallel (resp. perpendicular) to the plane of incidence, as shown in Fig. 3.7c (resp. Fig. 3.7d). After reflection[2] on the magnetic surface (in polar and

2 The analogous effect in transmission is the Faraday effect, discovered earlier, by Michael Faraday in 1845 [164]

longitudinal geometries), the linearly polarized light becomes ellipsoidally polarized and a rotation of the principal polarization axis occurs (see Fig. 3.7a). The rotation of the polarization axis is referred to as Kerr rotation θ_K and is directly related to the magnetization of the material within the probing region of the light. Although it is far from straightforward to obtain the value of the saturation magnetization M_S with the MOKE, it allows to probe locally the magnetization direction (typically over the LASER spot size).

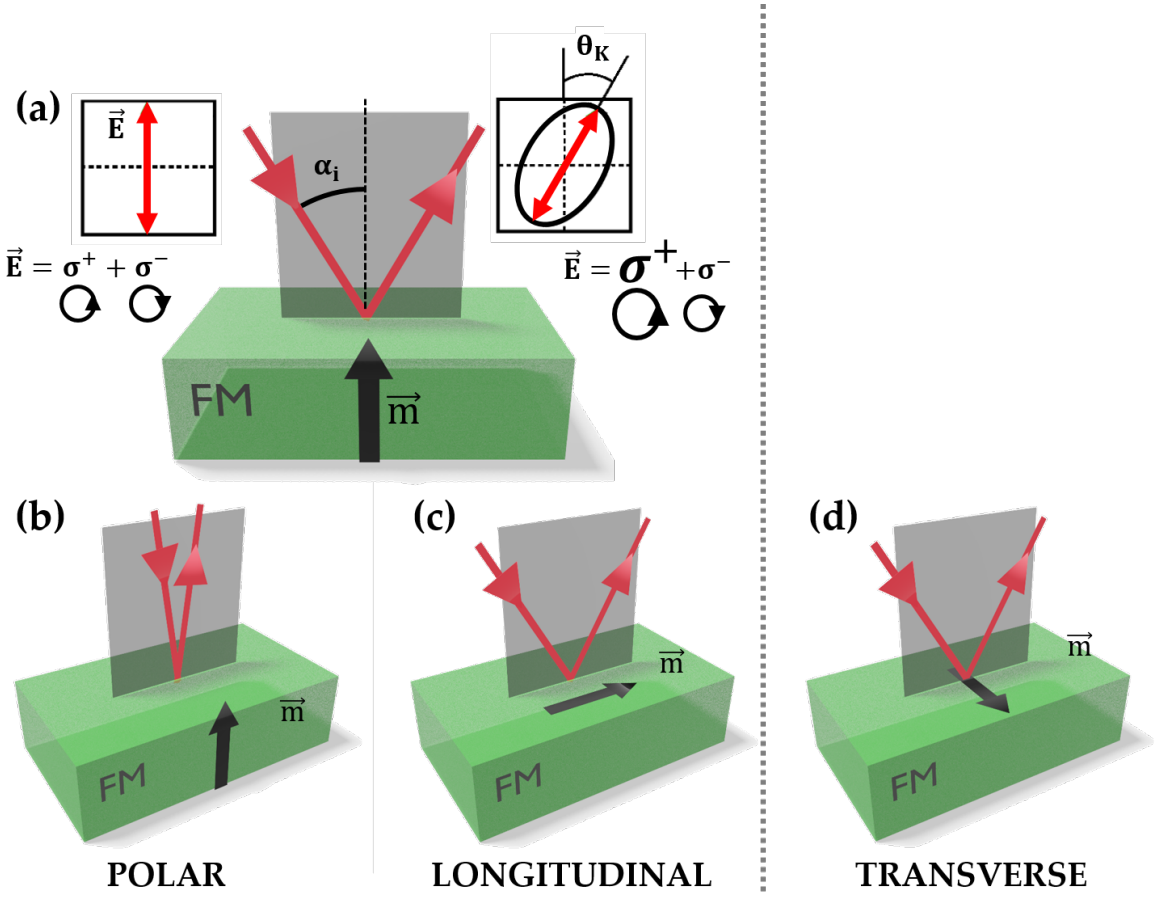

Figure 3.7: **The Magneto-optical Kerr effect:** (a) Working principle of the MOKE: a linearly polarized incident light beam is sent on the sample with an angle α_i with respect to the normal of the sample plane. The interaction between the light and the magnetization results in the rotation of the polarization axis, so called the Kerr rotation, which is a measure of the magnetization direction (b-d) The three configurations for MOKE measurement, respectively the (c) polar, (c) longitudinal and (d) transverse configuration.

At SPINTEC we have two kinds of setups working on the basis of the MOKE, for whom a description is giving in the following.

3.2.1.1 *The NanoMOKE3® magnetometer*

The first device based on the MOKE is the NanoMOKE3® by Durham Magneto Optics Ltd., a fully automated MOKE measuring setup that sends a polarized LASER beam ($\lambda = 500$nm) on the magnetic sample and analyzes the Kerr rotation with the help of an analyzer. The angle of the LASER beam ($\alpha_i = 45°$) provides a sensitivity for all polar, longitudinal and transverse magneto-optical Kerr effect, depending on the magnetization

orientation (see Fig. 3.7(b-d)). The LASER spot size, with a diameter about $300\mu m$ allows for MOKE measurements at a precise location on the sample. The magnetic sample is put on a (x, y) motorised stage which can be controlled by a computer. It allows notably to automatically record hysteresis loops in a list of programmed coordinates. In our case the NanoMOKE3® device is used to record hysteresis loops as a function of the position on the sample, for example every 2mm along x and y, in a square lattice.

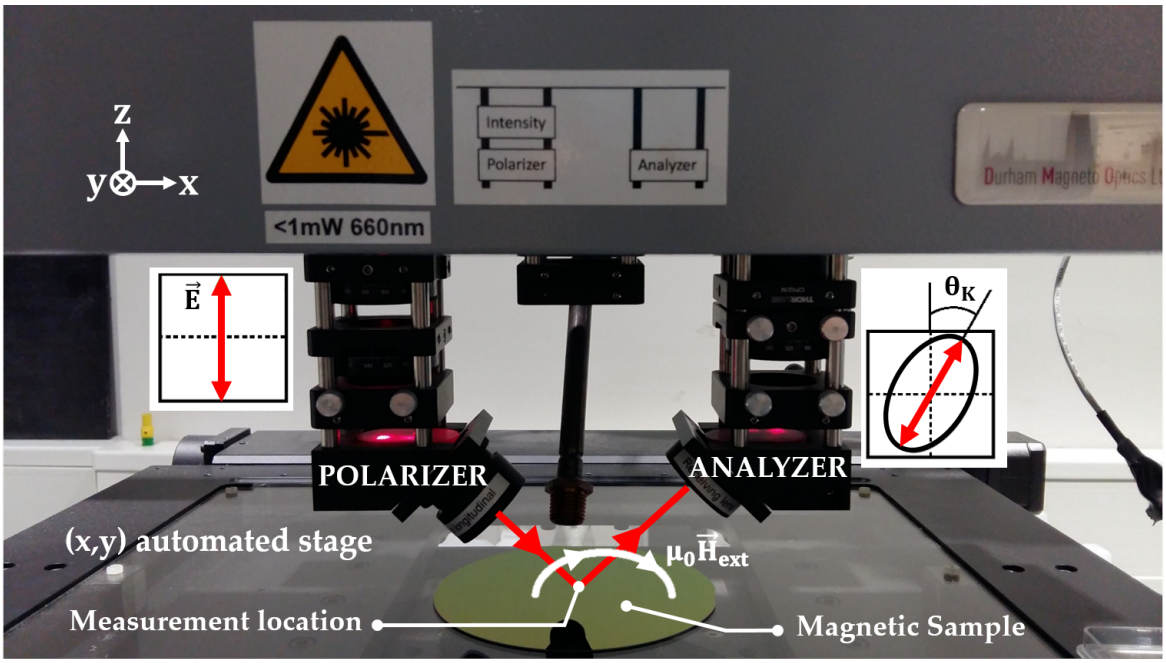

Figure 3.8: **The NanoMOKE3® setup:** In this setup, a linearly polarized red LASER beam is sent from the polarizer to the magnetic sample with an angle $\alpha_i = 45°$. The reflected light passes through the analyzer, which estimates the Kerr rotation θ_K. The sample is put on a (x,y) motorised stage, which allows MOKE measurement at a precise location, as well as automated measurements in programmed locations. An external magnetic field $\mu_0\vec{H}_{ext}$ is applied on the sample, with both an in plane and out of plane component at the measurement location (white curved arrow).

At the measurement location, the external magnetic field (white curved arrow in Fig. 3.8) has both an in plane (along x) and out of plane (along z) component, allowing for a sensitivity to respectively longitudinal and polar Kerr effect (for more detail on the magnetic field geometry, see the note page 72), with a better sensitivity to polar because of the coefficient of the effects. Thus, in this geometry, this setup is sensitive to both out of plane magnetic anisotropy (with the polar Kerr effect) and in-plane magnetic anisotropy (with the longitudinal Kerr effect), with a better sensitivity to the out of plane. In Fig. **??** we show the result from NanoMOKE3® measurements on a sample with a ferromagnetic wedge on which recording an hysteresis loop every 6 mm along the wedge is equivalent to varying the FM thickness of about 0.5 $\AA$. For the thinner FM thickness (around $t_{FM} = 0.6$ nm in Fig. 3.9), a noisy signal without hysteresis is obtained, signature of a paramagnetic state. By increasing progressively the FM thickness, we observe a region magnetized out of the sample plane, characterized by a square hysteresis loop

with an increasing signal/noise ratio (see around $t_{FM} = 0.9$ nm in Fig. 3.9). Increasing further towards thicker ferromagnet, a decrease of the signal/noise ratio, signature of a transition towards in-plane magnetization, since the setup is less sensitive to in-plane anisotropy as explained above. In addition, due to the details of the NanoMOKE3® setup, polar and longitudinal signals have an opposite sign. As a result, hysteresis loops in OOP magnetization region (around $t_{FM} = 0.9$ nm in Fig. 3.9) have a better signal/noise ratio and are reversed compared to the ones in IP regions (around $t_{FM} = 1.3$ nm in Fig. 3.9). In other words, hysteresis loops in OOP magnetization region (resp. IP magnetization region) show a positive (resp. negative) magnetic saturation signal at positive magnetic field.

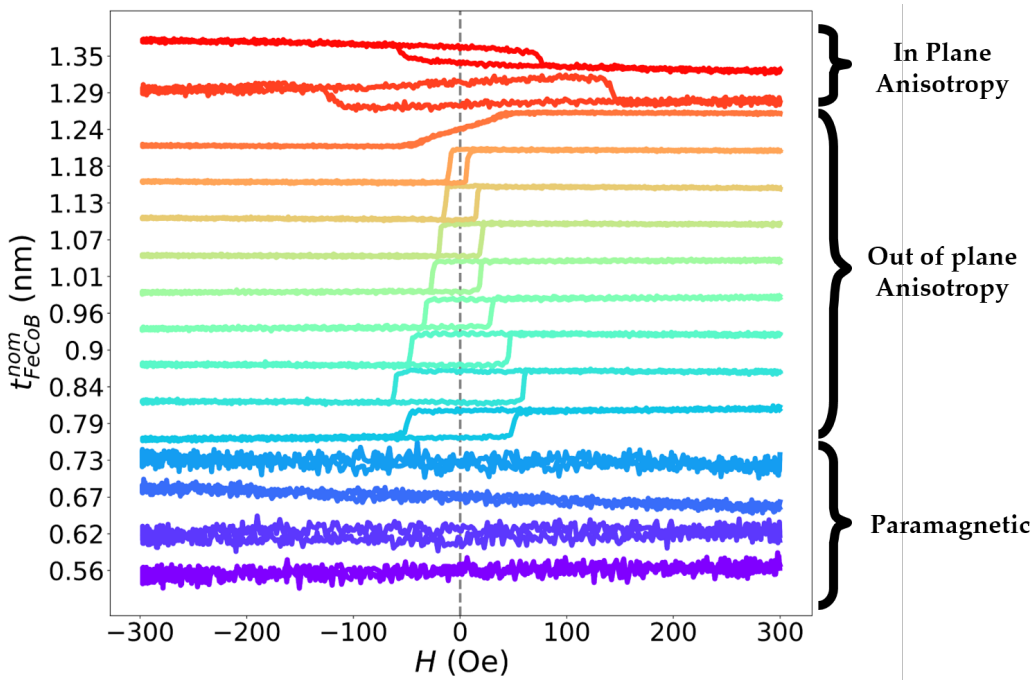

Figure 3.9: **Hysteresis loops under the NanoMOKE3® setup:** Normalized hysteresis loop obtained for varying ferromagnetic thickness (depicted on the y-axis), enabling to extract the magnetization orientation (in-plane or out of plane) with the NanoMOKE3® setup. The sign inversion of the hysteresis between an OOP (around $t_{FM} = 1$ nm) and an IP (around $t_{FM} = 1.3$ nm) region is clearly visible.

Note : Magnetic field geometry

For the MOKE measurements, the magnetic field source is a GMW 5201 electromagnet, which offers the possibility to adjust the out of plane (z) and in plane (x) components of the magnetic field in the region where the measure is done. In Fig. 3.10a, we show the electromagnet and zoom-in around the magnetic poles in Fig. 3.10b, revealing the shape of the magnetic field line (white curved arrows in Fig. 3.10(a,b)). The electromagnet is mounted on a positioning track, which allows to move it along the x-axis and adjust the components of the magnetic field, according to the curve shown in Fig. 3.10c.

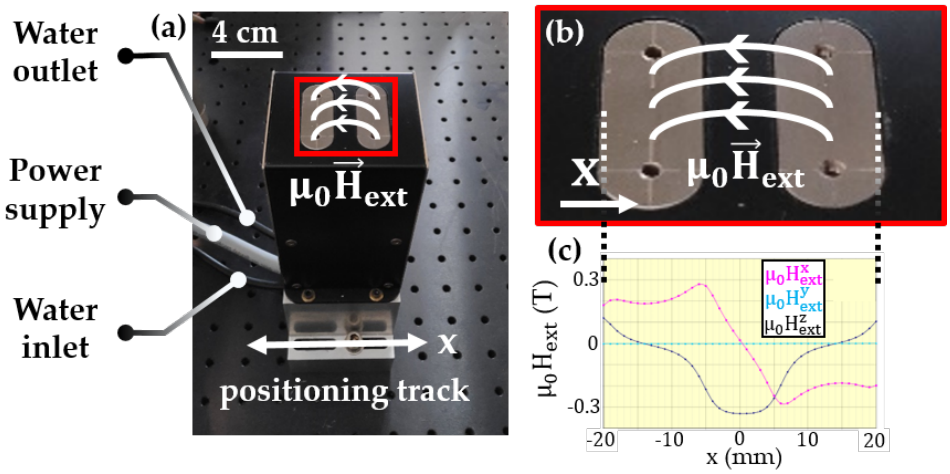

Figure 3.10: **Magnetic field geometry:** (a) The electromagnet GMW 5201, mounted on a positioning track allowing to displace it along the x-axis, thus changing the magnetic field components at the sample position. (b) Zoom-in around the magnetic poles, showing the shape of the magnetic field lines (white curves). (c) Magnetic field components depending on the position along the x-axis.

3.2.1.2 *The MOKE microscope*

The MOKE microscope uses the magneto optical Kerr effect in a classical optical microscope geometry in order to image the magnetic configuration of a magnetic sample. In Fig. 3.11a we describe the light path through the setup, that allows for MOKE measurements. The source of light is a red LED, which first passes through diaphragms to adjust the light intensity. Then, the light passes through the polarizer and a 45° semi-reflecting mirror which redirects the polarized light on the sample, passing through the optical lenses. After reflection on the magnetic sample, light passes through the lenses again and continues straight towards the CMOS camera. Since the incident light is almost vertical ($\alpha_i \simeq 0°$), this setup only measures the polar Kerr effect and is only sensitive to the out of plane magnetization component m_z. The magnetic sample is put on a (x,y) motorised stage, whose position can be remotely adjusted with the (x,y) stage control shown in Fig. 3.11(a,b). At the sample location (under the optical lenses), a magnetic field can be applied using electromagnetic coils. The in-plane and out-of-plane component of the magnetic field can be

adjusted by controlling the position of the magnetic coil under the sample (see note on page 72).

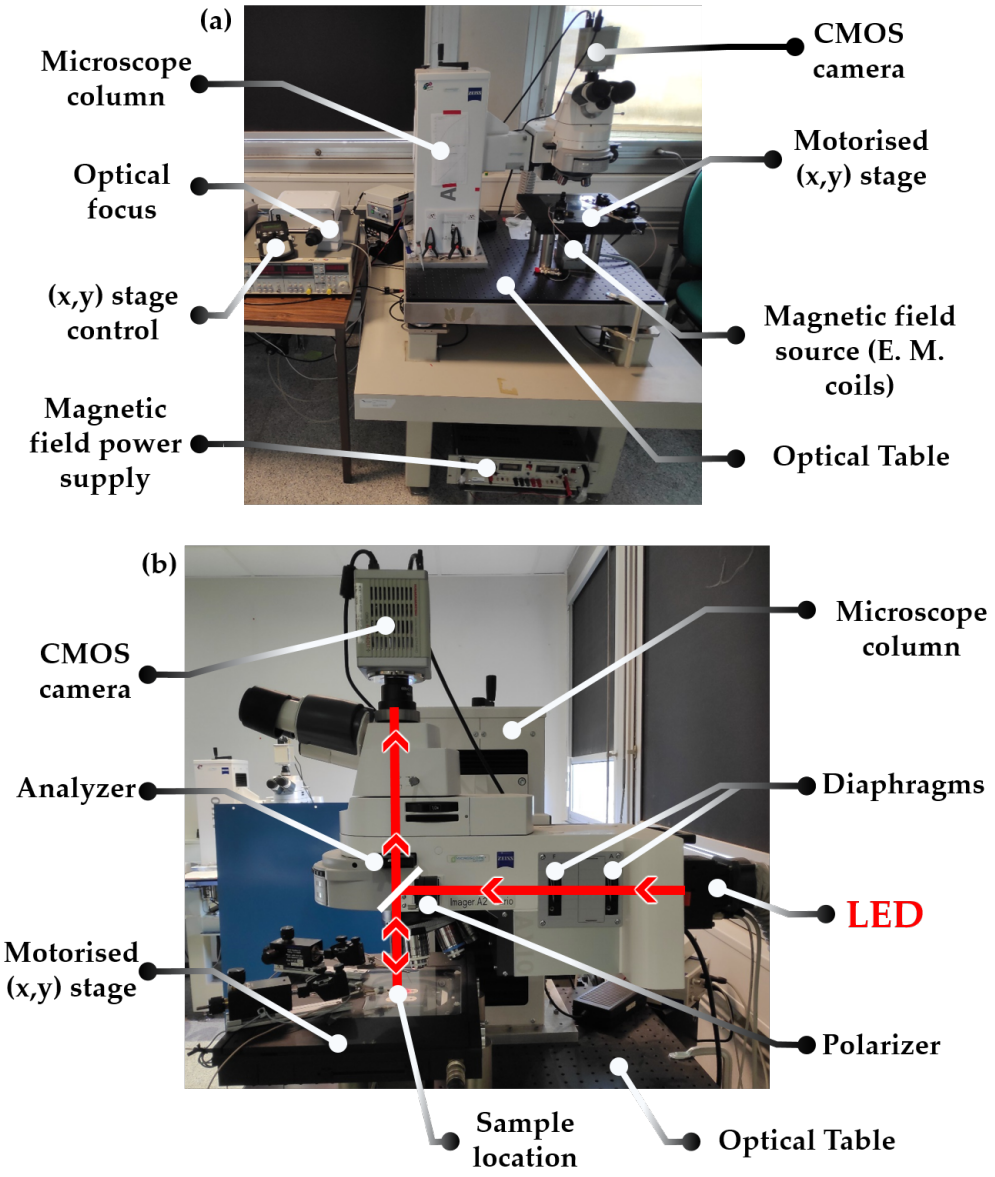

Figure 3.11: **The magneto-optical Kerr effect microscope setup:** (a) Global view of the MOKE microscope setup. (b) Description of the light path (red line) through the setup.

This setup, although working on the same principle as the NanoMOKE3®, is not dedicated to the same kind of measurement. With the MOKE microscope, in addition of recording hysteresis loop locally, there is the possibility to image the magnetic contrast over a region ranging from 5mm (x2.5 zoom) to 50 μm (x100 zoom). Contrary to the NanoMOKE setup (where a narrow LASER is reflected on a single sensor) a thick light beam is reflected on an array of sensors (a CMOS image sensor from the CMOS camera). As a result, in each point, the MOKE microscope gives an imaging of the magnetic domains and their orientation, as shown in Fig. 3.12. The theoretical resolution limit of such a device $r = \frac{\lambda}{2A}$ is limited by the wavelength of the incident light λ and the numerical aperture of the objective lens A. Here,

considering that $\lambda = 600$ nm and $A = 1$, it gives $r \simeq 300$ nm. It is possible to improve the resolution by using objective lens immersion in oil with a high refractive index.

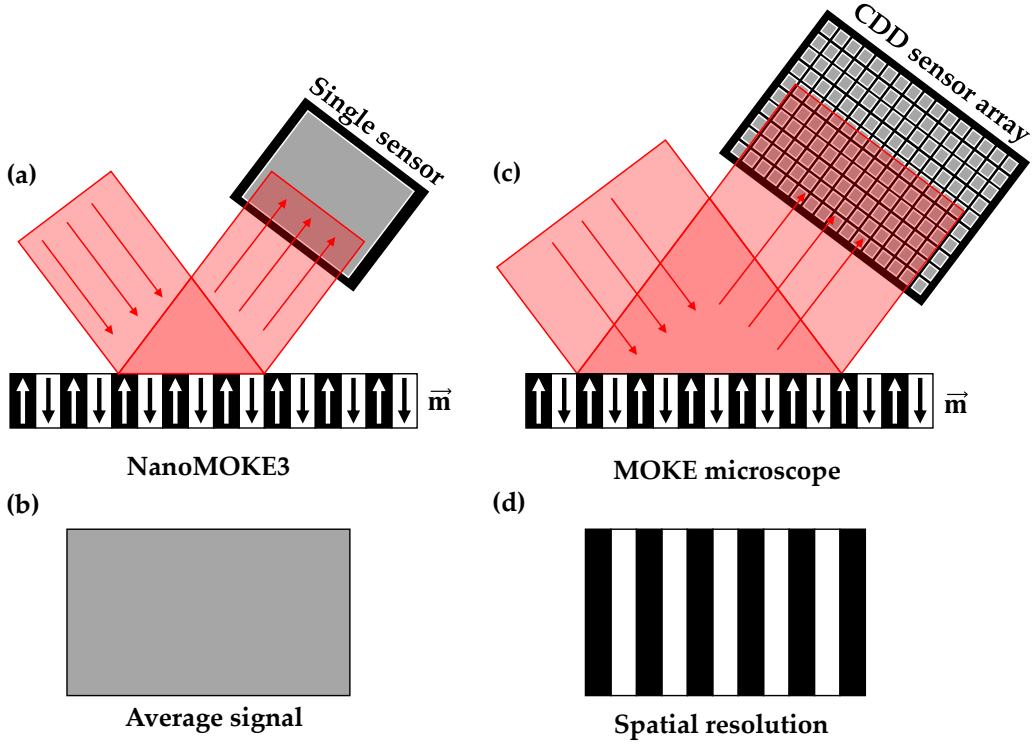

Figure 3.12: **NanoMOKE3® versus MOKE microscope:** (a) In the NanoMOKE3®, a narrow LASER beam ($\simeq 300\mu$m of diameter) is reflected from the magnetic sample to a single sensor, averaging the magnetic signal over the LASER spot size. (b) In the MOKE microscope, a thick red light beam from a LED (up to 5 mm diameter in x2.5 zoom) is reflected from the magnetic surface towards an array of sensors (a CMOS camera), allowing a spatial resolution of the magnetic contrast, *ie* imaging of the micromagnetic domains configuration.

3.2.2 *Brillouin Light Scattering*

Brillouin Light Scattering is named after the physicist Leon Brillouin that predicted this effect in the beginning of the 20th century [165]. It is a general phenomenon that describes the inelastic scattering of light with material vibrations, like phonons (acoustic waves), magnons, polaritons etc. It can also be used to study the vibrations of patterned structures like nanowires arrays. In the context of our work, BLS has been used to determine the iDMI coefficient from the interaction of light with spin waves in our magnetic sample. In the following we briefly describe the working principle of the BLS. A picture of the setup that we used is shown in Fig. 3.13a, where the different elements are described. For clarity, a schematic top view of the setup is shown in Fig. 3.13b.

Principle of BLS: In a BLS measurement, a linearly polarized LASER beam (here green, $\lambda = 532$ nm) is sent on a magnetic sample. More precisely, we have used the Damon-Esbach (DE) configuration in which the magnetization is orthogonal to the plane of incid-

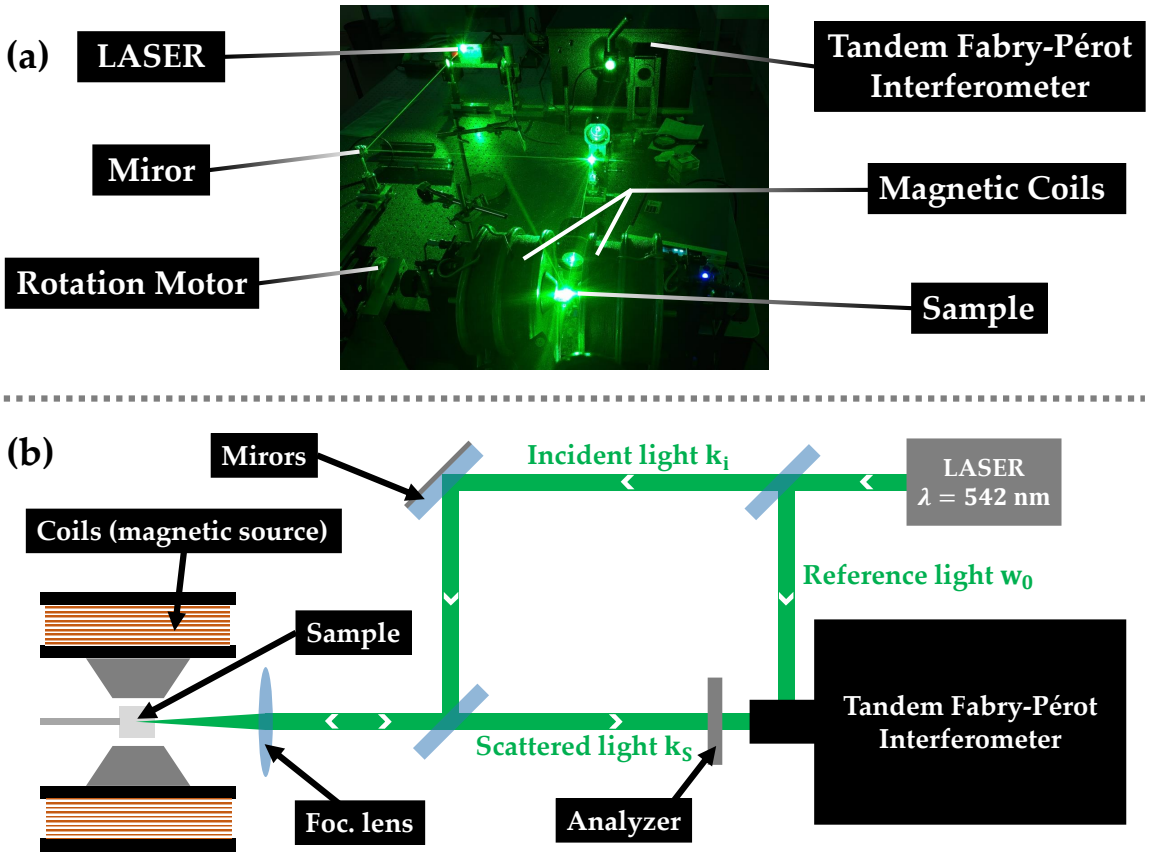

Figure 3.13: **The Brillouin Light Scattering setup from the LSPM, Villetaneuse:** (a) *In situ* picture of the BLS setup, where the different elements are described. (b) Schematic representation of the BLS setup, in a top view. The green LASER ($\lambda = 532$ nm)path is made visible through the setup, as well as the principal constitutive elements of the BLS setup.

ence of light, as shown in Fig. 3.14. In this configuration, the magnetization is saturated along the x direction with an external magnetic field $\mu_0 \vec{H}_{ext}$. The small magnetization precession around the magnetic field induces spin waves to propagate along the $\pm$y direction. The interaction of light with the spin waves can lead to the creation or absorption of a magnon (momentum k_{SW}), respectively called the Stokes and anti-Stokes event. Thus, some of the backscattered photons have a frequency which is slightly increased or decreased depending on the event. The frequency of the backscattered photons in analyzed using a tandem Fabry-Pérot interferometer, whose precise working principle is not described here. In Fig. 3.15a we show a typical BLS spectrum obtained from the Fabry Pérot interferometer. There are two peaks, one corresponding to backscattered photons with a decreased frequency with respect to their frequency (f_S, corresponding to the Stokes events), and the other to photons with an increased frequency (f_{AS}, corresponding to the anti-Stokes events). The key point of BLS measurement is that iDMI induces a frequency shift $\Delta f = |f_S| - |f_{AS}|$ between these two peaks. As demonstrated in Annex 8.6, Δf directly related to the iDMI coefficient through

$$\Delta f = \frac{2\gamma}{\pi M_S} D k_{SW} \tag{3.1}$$

where M_S is the saturation magnetization, γ the gyromagnetic ratio, k_{SW} the wave vector of the spin wave and D the iDMI coefficient. Usually, for more precision Δf is measured as a function of the spin wave momentum k_{SW} and the iDMI is thus extracted from the slope using eq. 3.1, as shown in Fig. 3.15b. The spin wave momentum k_{SW} is changed by varying the incident angle of the LASER beam Θ shown in Fig. 3.14, since $k_{SW} = \frac{4\pi \sin\Theta}{\lambda}$. The typical range for k_{SW} in the setup from the LSPM was 0-20.45 μm^{-1}. The typical uncertainty associated with BLS measurement is about 0.1 GHz, and thus the typical uncertainty on the iDMI coefficient depends on the saturation magnetization M_S. In our case, it gives and error bar about $\Delta D = $ mJ/m². Finally, in order to avoid any offset or discrepancy due to the setup, the measurements are performed for both $\pm\mu_0 \vec{H}_{ext}$, also giving information to calibrate the setup.

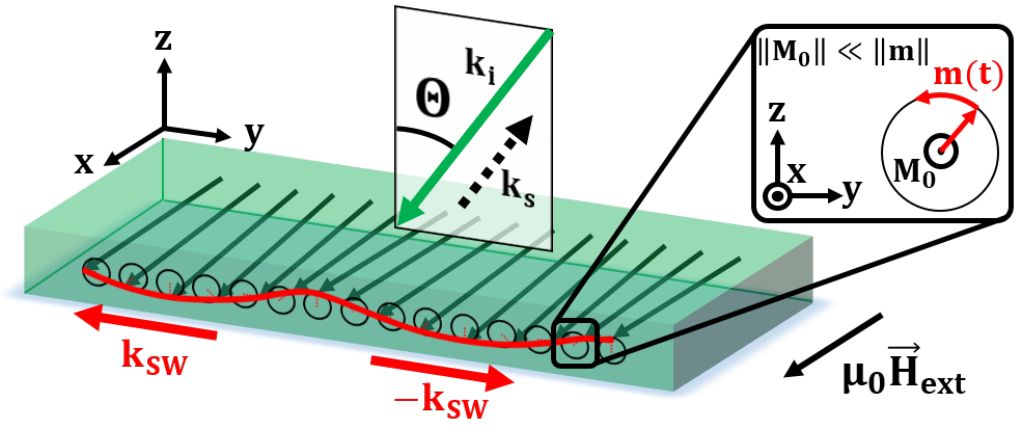

Figure 3.14: **The Damon-Esbach geometry:** (a) In this geometry, the magnetization is saturated along The large magnetic field $\mu_0 \vec{H}_{ext}$, applied along the x axis, leads to a saturated magnetization $\vec{M}_0$ along with a small precessional component $\vec{m}(t)$ around $\mu_0 \vec{H}_{ext}$. Thus the spin waves are propagating along the $\pm$ y direction, as depicted by the $\pm\vec{k}_m$ red arrows.

Brillouin Light Scattering also allows to measure the damping (proportional to the width of the peaks) and the anisotropy (proportional to the average position of the peaks). Thus, BLS is a technique that allows to get a lot of information on the magnetic parameters from only one spectra. However, the acquisition of one spectra is a long experiment (around 10h to accumaulate enough data (40000 photons) to be able to fit with the Lorentzians).

The Brillouin Light Scattering measurements of the iDMI coefficient shown in my thesis work were performed at the Laboratoire des Sciences et des Procédés des Matériaux (LSPM) in Villetaneuse, localized close to Paris. I went on site to realize BLS measurements with the help of Djoudi Ourdani, Mohammed Belmeguenai, Yves Roussigné and Mourad Chérif. The data treatement was partially done by Djoudi Ourdani and by myself.

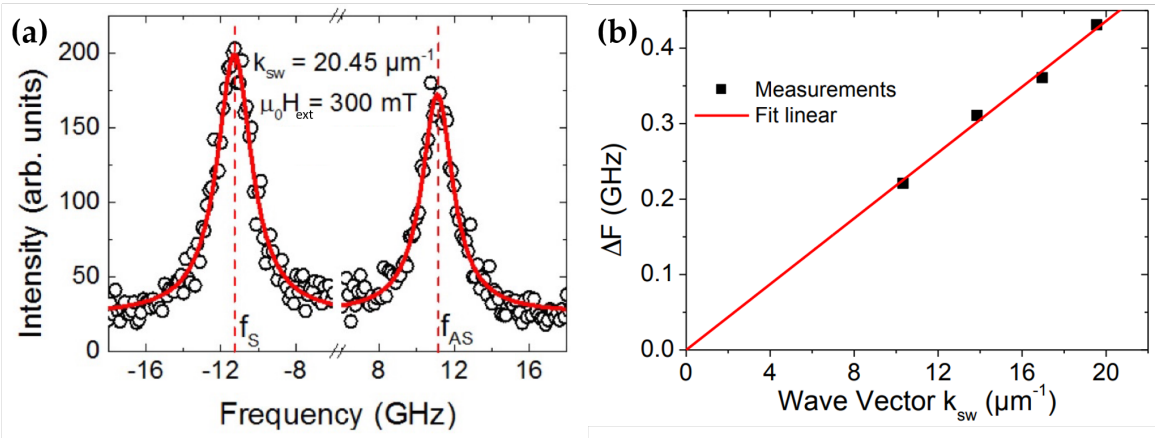

Figure 3.15: **Extracting iDMI from BLS spectra:** (a) Typical BLS spectrum showing the two peaks at frequency f_S for the Stokes events and f_{AS} for the anti-Stokes. The frequency shift $\Delta f = |f_S| - |f_{AS}|$ is a direct measure of the iDMI coefficient via equation 3.1. (b) Frequency shift as a function the spin wave momentum k_{SW}, allowing a more precise iDMI extraction from the slope of the linear regression, using equation 3.1

3.3 CONCLUSION

In this chapter, I gave the step by step procedure of fabrication of our samples, from the deposition of the Ta/FeCoB/TaO_x trilayer that hosts skyrmions to the additional steps dedicated to apply a gate voltage across the structure. In a second section I presented the principal characterization techniques that allowed to obtain the results shown in the next two chapters. Although during my PhD I used other characterization techniques (Vibrating Sample Magnetometer, Lorentz Transmission Electron Miscroscopy, Superconducting Quantum Interferometer Device, etc.), I have chosen to describe the ones useful for the understanding of the results presented in the next chapters.

4

PROPERTIES OF Ta/FeCoB/TaO_x TRILAYERS HETEROSTRUCTURES

In this thesis work, we study the skyrmion properties in a Ta/FeCoB/TaO_x trilayer heterostructure, in the unbiased state and under the influence of a gate voltage. This trilayer is the ideal playground for this work, since it is known to host skyrmions that can be moved by SOT [100], and previous works have shown that the amplitude of the iDMI was tunable with a gate voltage [76]. This chapter is dedicated to the study of the skyrmion properties versus material modulations in the unbiased state, while their properties under a gate voltage are presented in the next chapter.

In a first section, I describe the sample double-wedge deposition which allows for a precise tuning of material parameters in Ta/FeCoB/TaO_x trilayer.

In a second section, we show that it allows for a variety of magnetic properties on a single sample, and notably for the stabilization of magnetic skyrmions in a given range of magnetic and material parameters.

More importantly we show in a third section that we can precisely control the skyrmion properties in this sample through a material-dependent tuning of the interfacial

Dzayloshinskii-Moriya interaction. As a result, we show in particular that the skyrmion chirality can be controlled by the material parameters.

4.1 THE DOUBLE WEDGE SAMPLE

In HM/FM/MO$_x$ trilayers, the adjustment of the skyrmion properties requires the control of the interaction at their origin : the interfacial Dzayloshinskii-Moriya interaction (iDMI, see section 1.2.6). Moreover, stabilizing such small magnetic domains, magnetized out of the sample plane, requires a fine tuning of the uniaxial magnetic anisotropy. Besides, I have shown in Sec. 1.3 that both iDMI and uniaxial anisotropy may be adjusted in by varying the FM thickness, changing the oxidation state at the FM/MO$_x$ interface and changing the type of HM. All of these material modulations can be realized on a unique wafer of the Ta/FeCoB/TaO$_x$ trilayer, deposited in a double wedge geometry as explained below. This technique has been developed during the PhD of Titiksha Srivastava, in which she studied the properties of several double-wedge sample, including Ta/FeCoB/TaO$_x$ [166].

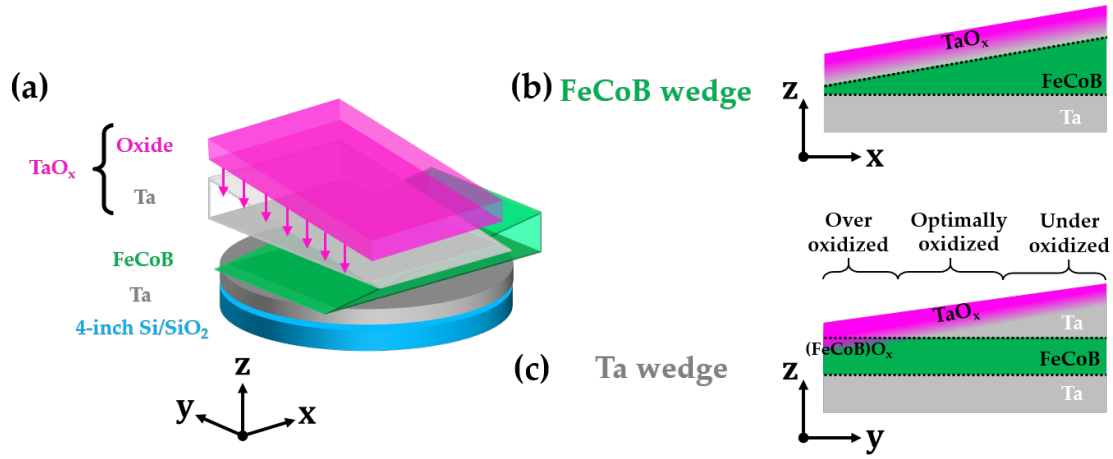

Figure 4.1: **The Ta/FeCoB:TaO$_x$ trilayer heterostructure:** (a) Schematic representation of the double wedge deposition, where the wedges of FeCoB and top-Ta are deposited perpendicularly the one to the other. (a) Cross section view at a constant top-Ta thickness, varying the FeCoB thickness and (c) cross section view at constant FeCoB, varying the top-Ta thickness.

The sample consists in Ta(3)/FeCoB(0.8-1.4)/TaO$_x$(0.5-1) (nominal thicknesses given in nm) deposited on 4-inch Si/SiO$_2$ wafer by magnetron sputtering (see section 3.1.1) in the double wedge geometry (Fig. 4.1a). We first deposited the bottom 3 nm Ta layer in a *on-axis* configuration[1], leading to a constant thickness of Ta over the 4-inch wafer. Then, the deposition of the FeCoB layer is realized in a *off-axis* configuration, leading to a gradient of thickness from one edge of the wafer to the other. In other words, the FeCoB is deposited as a wedge along the x-axis, as shown in Fig. 4.1a,b. The nominal FeCoB thickness varies from $t_{FeCoB}^{nom} = 0.6$ nm on the left of the wafer to $t_{FeCoB}^{nom} = 1.4$ nm on the right of the wafer. Then, a wedge of Ta is deposited on top of the FeCoB one, and perpendicular to it, along the y-axis as shown in Fig. 4.1a,c. The nominal top-Ta thickness varies from

1 For more detail on *on/off-axis* deposition technique, see Sec. 3.1.1

$t_{Ta}^{nom} = 0.5$ nm on the bottom part of the wafer to $t_{Ta}^{nom} = 1$ nm on the top part of the wafer. After deposition the sample is oxidized in a treatment chamber. The top-Ta wedge allows a fine tuning of the oxygen content at the top interface of FeCoB, depending on the top-Ta thickness, as already discussed in section 1.3.1. We can thus define three relevant regions along the top-Ta wedge, depending on the oxidation state of the top interface of FeCoB, as shown in Fig. 4.1c. For the thinnest top-Ta the FeCoB layer is partially oxidized and we name it as an *overoxidized* FeCoB/FeCoBO$_x$/TaO$_x$ interface. As the top-Ta thickness increases, the oxidation state at the top FeCoB interface decreases. Thus we can define the *optimally oxidized* FeCoB/TaO$_x$ interface where the FeCoB layer is not oxidized but the top-Ta is. As explained in section 1.3.1, the optimally oxidized region can be found by searching for the maximum of effective anisotropy along the top-Ta wedge. Finally, when the top-Ta gets thicker, the oxygen content at the top FeCoB interface decreases leading to an *underoxidized* FeCoB/Ta/TaO$_x$ interface.
In order to protect the sample from further oxidation, a 0.5 nm layer of Al was deposited and subsequently oxidized at air when taking the sample out of the sputtering machine. Such Al layer is totally oxidized and passivates the surface. However, after several months and becomes progressively paramagnetic. Finally the sample is annealed at 225°C during 30 min under high vacuum to improve PMA (see section 4.2.4).

As a result, the sample combines various FeCoB thickness and FeCoB/TaO$_x$ interface oxidation states, leading to the presence of several magnetic states on the 4-inch wafer depending on the location on the wafer, including magnetic skyrmions. It is important to notice that skyrmion stabilization can be challenging since they are stable in a very narrow range of magnetic parameters. Even the small variability of the deposition setup does not guarantee their presence in a set of sample with the same nominal parameters. Thus, the double-wedge sample has the combined advantages of granting the presence of magnetic skyrmions and studying there material-dependent properties on a single sample.

4.2 VARIETY OF MAGNETIC CONFIGURATION

After the deposition, the magnetic properties of the sample are measured using the NanoMOKE3® setup from Durham described in section 3.2.1. This setup locally measures hysteresis loops (over a circular area of 300 μm in diameter, corresponding to the LASER spot size) by using the Magneto-Optical Kerr Effect (MOKE), in an hybrid polar/longitudinal geometry. It allows to be sensitive both to out of plane (OOP) and in-plane (IP) magnetic states, and to distinguish between these two with the sign of the hysteresis loop and the signal amplitude (see Sec. 3.2.1). Indeed in this configuration, the polar signal is larger than the longitudinal signal and with a reversed sign. As a result, hysteresis loops in OOP magnetization region (Fig. 4.2b) have a better signal/noise ratio and are reversed compared to the ones in IP regions (Fig. 4.2c).
This setup allows to scan over the sample and to record an hysteresis loop every 2 mm in a square lattice, as shown in Fig. 4.2a (where a 1cm square lattice is instead shown for

clarity). Then, as shown in Fig. 4.2b, from each hysteresis, we extract the magnetization at remanence (magnetization at zero magnetic field, simply called remanence in the following), the coercive field H_C and the amplitude of the Kerr signal, defined as the difference between maximum and minimum signal. It provides us information about the magnetic state/properties as a function of the location (x, y) one the double wedge sample.

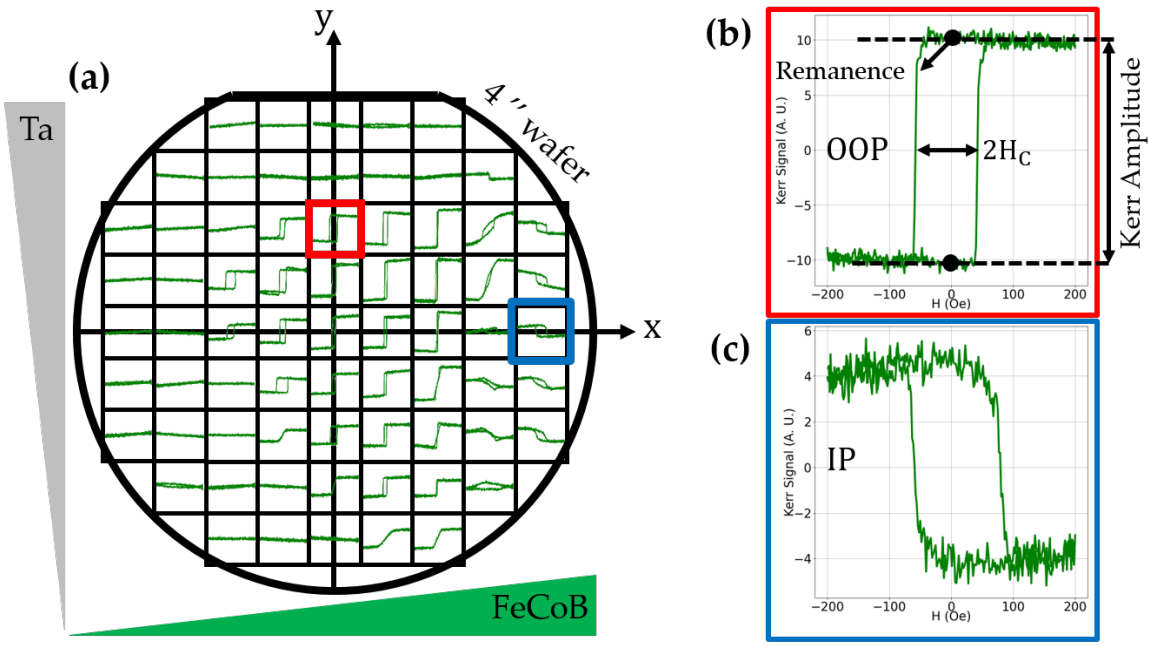

Figure 4.2: **Measurement of magnetic properties with the NanoMOKE3® setup:** (a) Schematic representation of the measurement technique: on the 4" wafer, magnetic hysteresis loops are recorded in a 2 mm square lattice (here 1cm square lattice is shown for clarity) with the NanoMOKE3® setup. (b) Example of hysteresis loop in $(x, y) = (0, 20)$ mm. From this we extract the main magnetic properties such as the remanence (magnetization at zero magnetic field), the coercive field H_C and the amplitude of the Kerr signal.

As a quick reminder, the material is deposited in a double wedge geometry so that moving along x is equivalent to vary the FeCoB thickness and moving along y is equivalent to vary the top-Ta thickness, and thus the oxidation state of the FeCoB/TaO$_x$ interface. Consequently, each (x, y) location corresponds to a couple of thicknesses (t_{FeCoB}, t_{Ta}). It is thus possible to transform the mappings in the (x, y) space into mappings in the (t_{FeCoB}, t_{Ta}) space. Due to the geometry of the deposition (see Sec. 3.1.1), the iso-thickness curves for the FeCoB (green curves in Fig. 4.3a) and for the top-Ta (pink curves in Fig. 4.3a) are circles, centered on the target from the sputtering machine. Thus, the mapping in the (t_{FeCoB}, t_{Ta}) space is distorted compared to the mapping measured experimentally in the (x, y) space, as shown in Fig. 4.3b. The iso-thickness curves of FeCoB and Ta become respectively vertical and horizontal lines, leading to a distorsion of the wafer in the (t_{FeCoB}, t_{Ta}) space. In the following, the experimental mappings of the magnetic properties are shown in the (t_{FeCoB}, t_{Ta}) space.

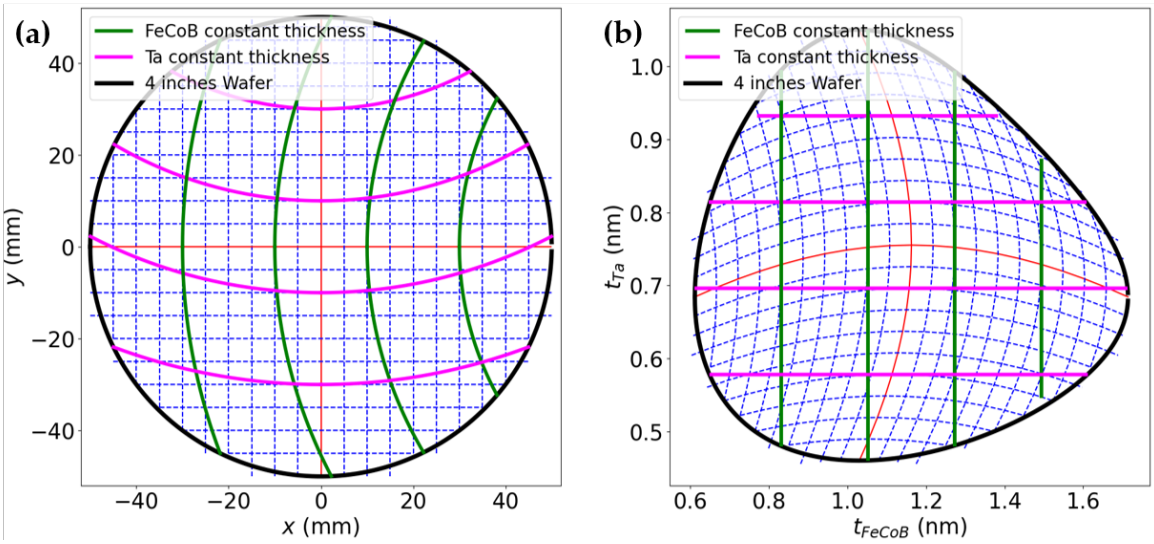

Figure 4.3: **Distortion between NanoMOKE3® mappings:** (a) Schematic representation of the 4" wafer (solid black contour) in the (x, y) space, with dashed blue lattice corresponding to 5 mm scale. Due to the geometry of the sputtering machine, the iso-thickness curves for the FeCoB (green curves) and for the top-Ta (pink curves) are circles, center on the center of the target. (b) Thus, in the (t_{FeCoB}, t_{Ta}) space, the iso-thickness curves of FeCoB and Ta become respectively vertical and horizontal lines, but the wafer is distorted.

Following this method, the magnetic properties of the double wedge sample have been measured with the NanoMOKE3® after the sample annealing (the effect of the annealing is discussed in a dedicated section 4.2.4). We show mappings of the remanence, Kerr signal amplitude and coercive field respectively in Fig. 4.4a, 4.4b and 4.4c. Moreover, for each of these quantity, a cut is shown respectively in Fig. 4.4d, 4.4e and 4.4f. Finally, The hysteresis loops along this cut are shown in Fig. 4.5. From all of these data, we observe three magnetic states, depending on the location on the sample : paramagnetic (PM), out of plane magnetized (OOP) and in-plane magnetized (IP). In the following I describe these regions individually.

4.2.1 *Paramagnetic*

Globally, one can see from Fig. 4.4 that the PM region is located in the thinner FeCoB region, on the left of the mappings. In fact, below a critical thickness called the magnetically dead layer thickness t_{DL}, the Curie temperature is below the room temperature due to size effect (see Sec. 1.3.1). Nevertheless, one can see that the limit of the PM region depends on the oxidation state at the FeCoB/TaO_x interface, as depicted by the dashed-white curve in Fig. 4.4. In fact, in addition to finite size effects, other interface effects contribute to the magnetically dead layer (see note page 86), increasing it and thus pushing the PM limit toward thicker FM layer for both overoxidation or underoxidation of the FeCoB/TaO_x interface (a described in reference [166]). A PM state is characterized by the absence of hysteresis loop and a weak Kerr signal amplitude, as depicted by the red square symbol in Fig. 4.5, which corresponds to the red square location in Fig. 4.4.

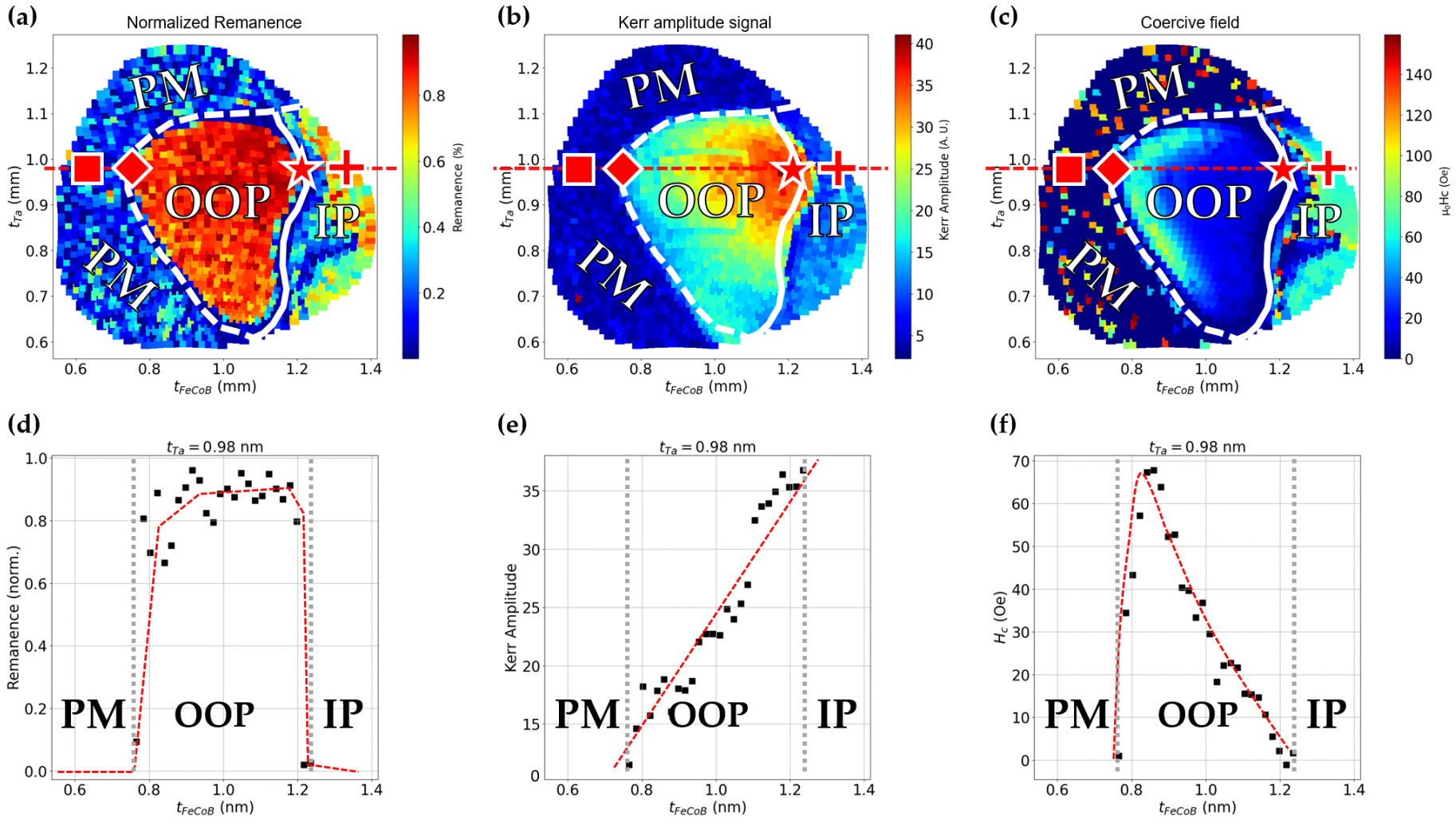

Figure 4.4: **Magnetic properties mapping of the double wedge sample after annealing:** Mappings of the (a) normalized remanence, (b) Kerr amplitude signal and (c) coercive field versus the ferromagnetic thickness and the top-Ta thickness. Each point corresponds to an hysteresis loop, measured by MOKE. (d) Normalized remanence versus the ferromagnetic thickness for an optimally oxidized FeCoB/TaO$_x$ interface. The black squares are those extracted from the hysteresis loops and the red curve is a guide to the eyes. (e) and (f) are similar graph for respectively the Kerr amplitude signal and the coercive field.

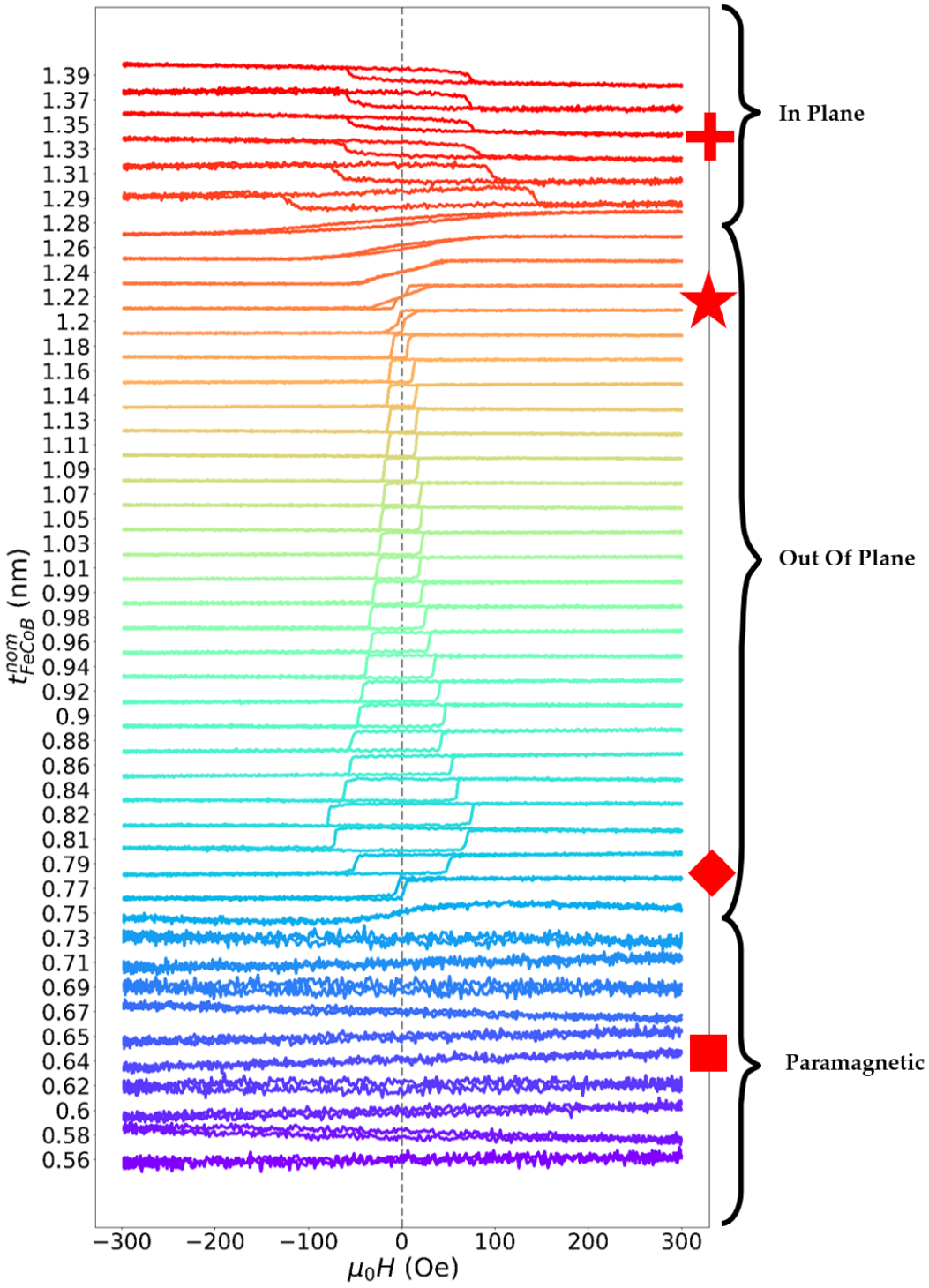

Figure 4.5: **Hysteresis loops versus ferromagnetic thickness after sample annealing:** Normalized hysteresis loops at $t_{Ta} \simeq 0.98$ nm (optimally oxidized FeCoB/TaO_x interface after annealing) for various nominal ferromagnetic thickness, indicated on the y-axis. The symbols corresponds to the different locations indicated in Fig. 4.4a. It allows to distinguish three different magnetic states : the paramagnetic state (bottom part of the graph, square symbol) corresponds to a noisy signal, while square-shaped hysteresis loop are observed in the out of plane region (middle part of the graph, between diamond and star symbols). In the in plane region (top part of the graph, cross symbol), the signal is weaker and the loop is inverted, due to the opposite sign of polar and longitudinal signals in the setup.

4.2.2 *Out Of Plane magnetized*

The out of plane magnetized region is located approximately in the center of the sample. It corresponds to the region where the magnetic hysteresis loop is square-shaped, leading to a normalized remanence close to 1 and a non-zero coercive field (see Fig. 4.5). Thus the contour of the OOP region can be determined with the remanence maps, as shown in Fig. 4.4a. It is surrounded by two kinds of magnetic transition: transition to paramagnetic (dashed-white curve in Fig. 4.4) or transition to in-plane magnetization (solid-white curve in Fig. 4.4). The OOP to PM transition can be obtained by reaching t_{DL}, *ie* by decreasing the FM thickness, or by decreasing (resp. increasing) the top-Ta thickness towards over-oxidation (resp. underoxidation) of the FeCoB/TaO$_x$ interface. The OOP to IP transition can be reached by increasing the ferromagnet thickness to reach the critical thickness t_c at which the shape anisotropy brings the magnetization in the plane (see section 1.2.4). At the transition between OOP and PM or IP, the coercive field and normalized remanence decrease, as depicted by the red diamond and star symbol in Fig. 4.4 and Fig. 4.5. Interestingly, in the OOP to IP transition, we observe "butterfly hysteresis loop", characterized by a zero coercive field and opening at intermediate field, as shown in Fig. 4.5 at the red star location around $t_{FeCoB}^{nom} \simeq 1.2$ nm. This kind of magnetic hysteresis loop is the signature of the presence of demagnetized magnetic stripes and possibly of magnetic skyrmions, as it will be discussed in Sec. 4.2.5.
The behaviour of the coercive field (related to K_{eff} [86]) versus the ferromagnetic thickness shown in Fig. 4.4c,f is in a good agreement with the expectations, presented in Sec. 1.2.4. As we increase the ferromagnetic thickness, we first see a drastic increase of the coercive field around t_{DL}, corresponding to the drastic increase of effective anisotropy shown in Sec. 1.2.4 due to the contribution of the surface anisotropy. Then, we rapidly reach a maximum of coercive field and a slow decrease towards the OOP to IP transition. As an example, in Fig. 4.4f we did a cut of the coercive field values at $t_{Ta} \simeq 0.98$ nm (optimal FeCoB/TaO$_x$ oxidation), which looks similar to Fig. Sec. 1.2.4. Moreover, we can clearly see similar behaviour for other Ta thickness, corresponding to different values of t_{DL} and t_c.

4.2.3 *In Plane magnetized*

The IP region is globally located on the right on the wafer, where the ferromagnet is thicker and K_{eff} becomes negative due to the contribution from the shape anisotropy. In this region, due to the NanoMOKE3® setup (as explained above and in section 3.2.1), we observe a smaller Kerr signal amplitude with a reversed hysteresis loop, as shown in Fig. 4.5 around the red cross symbol, signature of an IP magnetization.

Note : Magnetically dead layer

Because of the stacking geometry and the deposition technique, the thickness of ferromagnet which is really magnetic (t_{FM}) often differs from the nominal thickness (t_{FM}^{nom}), which is the depositited thickness calibrated using deposition rates in the sputtering machine. The difference is called the magnetically dead layer t_{DL} and one has $t_{FM} = t_{FM}^{nom} - t_{DL}$. Here, we give a brief overview of the different origins of t_{DL} and we refer the reader to references [159, 166] for a more extensive study.

The magnetically dead layer can be due to a partial oxidation of the FeCoB layer in the overoxidized region, where the top-Ta is the thinner as shown in Fig. 4.6a. Then, as the top-Ta thickness increases, t_{DL} decreases since the oxygen content inside FeCoB decreases and the minimum of dead layer is reached for the optimally oxidized FeCoB/TaO_x interface (see Fig. 4.6b). In the underoxidized region, the dead layer increases again, with a different origin, as shown in Fig. 4.6c. It has been shown experimentally that the presence of Ta atoms at the interface with FeCoB leads to a decrease of the magnetic moments for Fe atoms next to Ta, leading to a magnetically dead layer [76], which is supported by *ab-initio* calculations [167–169].

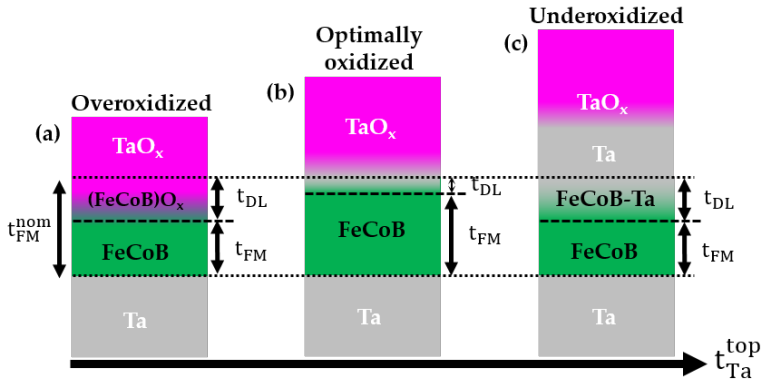

Figure 4.6: **Magnetically dead-layer sources:** (a) Dead layer due to partial oxidation of the FeCoB layer in the overoxidized region (b) The minimum of dead layer is reach in the optimally oxidized region and (c) Dead layer due to intermixing between FeCoB and Ta in the underoxidized region

Ideally, one should separate the magnetically dead layer which is due to interface effect (overoxidation or underoxidation) from the one due to finite size effect [159, 166]. Indeed, in the former, the dead layer is really non magnetic since the magnetic moment per atom is reduced. In the latter, each atom is still magnetic but the decrease of the Curie temperature at room temperature leads to a PM state by the randomization of the magnetic moments orientation. Consequently the former does not depend on temperature while the latter does.

Although we know the complexity of the situation, we have chosen to use a simple picture in which the nominal ferromagnetic thickness is separated into two part: an actual magnetic thickness t_{FM}, with the bulk magnetization value, and a magnetically dead layer t_{DL}, with zero magnetization.

It is possible to experimentally estimate the dead-layer and this is of crucial import-

ance since the real ferromagnetic thickness t_{FM} plays a key role in the estimation of other magnetic parameters.

4.2.4 *Effect of the annealing*

In this section, we show similar mappings of the sample, made with the NanoMOKE3® before subjecting the sample to annealing at 225°C for 30 minutes in a high vacuum chamber. The remanence, Kerr amplitude and coercive field of the double wedge sample before annealing are shown respectively in Fig. 4.7a, 4.7b and 4.7c and after the annealing in Fig. 4.7d, 4.7e and 4.7f.
The main difference provided by the annealing is the extension of the OOP region. Indeed one can see that the effect of the annealing is to increase the size of the OOP region, mainly towards thicker FM and thinner top-Ta. First, annealing improve the quality of the interfaces, increasing the surface anisotropy [170, 171]. Thus, a region which was IP before annealing becomes OOP after, leading to the observed shift of the OOP to IP transition towards thicker FM. Second, annealing leads to the pumping of oxygen from FeCoB layer to Ta layer, which is thermodynamically favoured, as shown by Ellingham diagrams, which shows that the Tantalum oxide energy formation [172, 173] is lower than the one of iron oxide [174]. Thus, regions which were PM because of overoxidation before the annealing become OOP after, explaining the observed shift of the OOP to PM transition towards thinner FM.

4.2.5 *Stabilization and observation of magnetic skyrmions*

In order to search for skyrmions, the magnetization configuration on the double wedge sample is directly imaged using a MOKE microscope in the polar geometry (μ-MOKE) (see Sec. 3.2.1). Although, like the NanoMOKE, it uses the magneto-optical Kerr effect to probe the magnetization, there are two major differences: (i) the μ-MOKE is only sensitive to the out of plane component of the magnetization m_z, contrary to the NanoMOKE3® which is sensitive to both in plane and out of plane component and (ii) here the cross section of the light beam is much larger and light is reflected on a CMOS sensor, allowing for a spatial resolution of the magnetic domains (for more details see section 3.2.1). To summarize, with this setup it is possible to observe the OOP magnetic domain configuration on the sample and in particular to localize regions where magnetic skyrmions can be stabilized. In Fig. 4.8, which is a real-scale view of the sample under the MOKE microscope, each of the small square corresponds to a 5x5mm² region of the 4" wafer (the black circular contour) imaged by μ-MOKE with a x2.5 zoom. More precisely, each image has been taken in a differential imaging mode (see Sec. 3.2.1): the magnetization is first saturated at large magnetic field in order to do the background for the differential imaging, and the magnetic field is decreased to $\mu_0 H_{ext} \simeq 100$ µT, a few second before taking the image (typical time for demagnetization to occur). In differential imaging, a gray contrast corresponds either to magnetization pointing up ($+z$) or in plane, while a black contrast corresponds to mag-

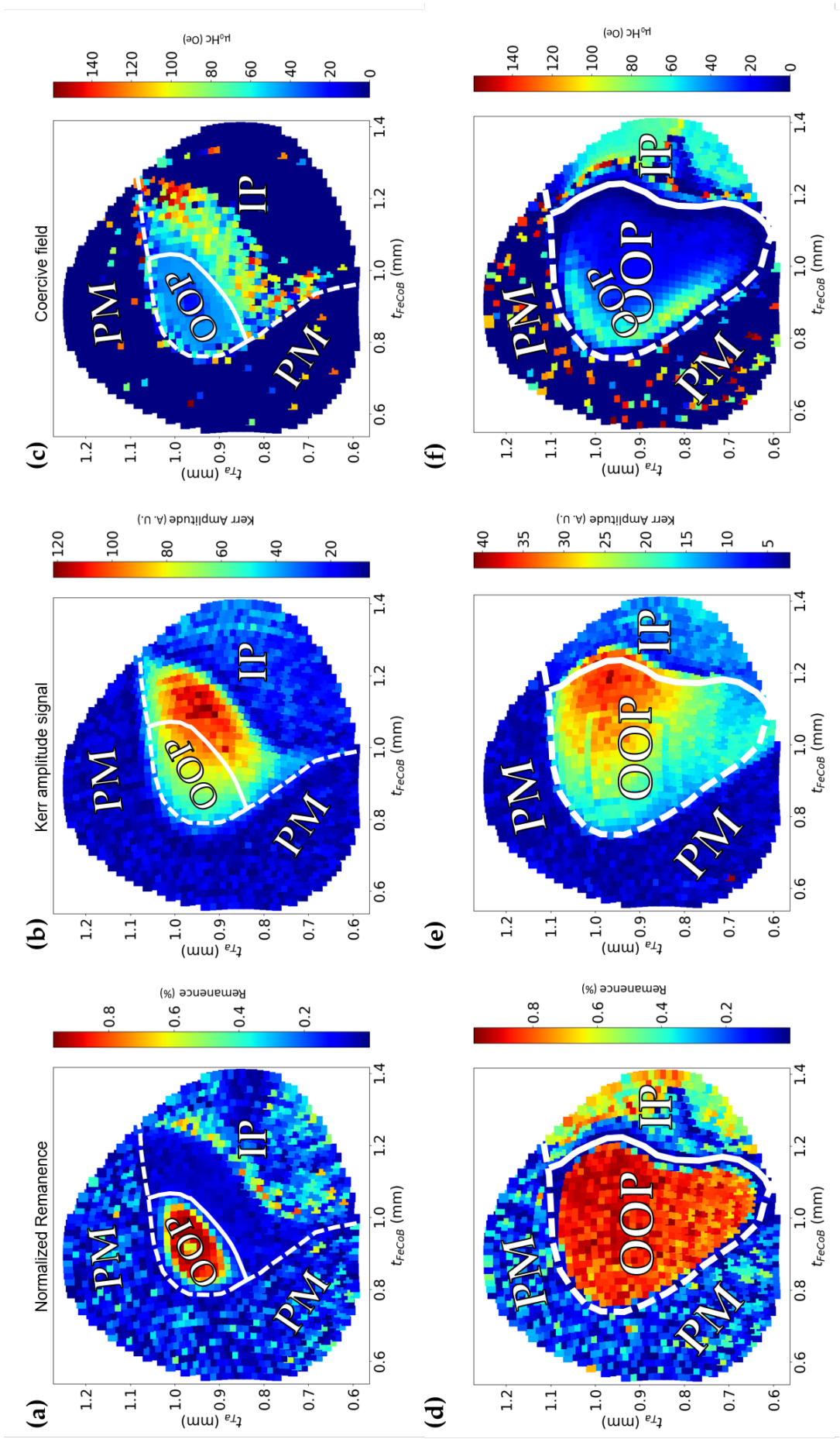

Figure 4.7: **Magnetic properties mapping of the double wedge sample before annealing:** Mappings of the (a) (resp. (d)) normalized remanence, (b) (resp. (e)) Kerr amplitude signal and (c) **(resp. (f))** coercive field versus the ferromagnetic thickness and the top-Ta thickness before the annealing (resp. after). Each point corresponds to an hysteresis loop, measured by MOKE.

netization pointing down ($-z$). Moreover, an in plane region remain gray under magnetic field reversal while an OOP region changes to black, allowing to differentiate between IP and OOP. Also, a small white oval in the centre of most images in Fig. 4.8, which is due to moisture on the lens during measurement. It evolves through the experiment to finally disappear. For more precise measurements on skyrmions we took care to wait sufficiently for the moisture to disappear before starting imaging.

As shown in the previous section, the OOP region corresponds to a normalized remanence close to 1. In other words, at $\mu_0 H_{ext} \simeq 100$ µT, most of this region show a saturated magnetic state, transcribed in the "OOP" gray saturated region in Fig. 4.8. Moreover, as shown in the previous section, the remanence quickly drops to zero on the contour of the OOP region, when going towards OOP to IP or OOP to PM transition. In fact, the magnetization is still pointing out of the sample plane, but the reduction of the effective anisotropy leads to the thermally-activated nucleation of magnetic domains in the opposite direction to the magnetic field. Visually speaking under the μ-MOKE, it corresponds to the drastic change of contrast around the OOP region in Fig. 4.8. The Region Of Interest of this thesis work (the "ROI" dashed-black rectangle in Fig. 4.8a) corresponds to the top part of the wafer, since it is the arena of the most interesting phenomena, as presented in Sec. 4.3 and chapter 5. In Fig. 4.8b, we show the micromagnetic configuration in three regions concentrated in the ROI of the wafer, as depicted by the red diamond (PM to OOP transition), blue triangle (PM to OOP transition) and in the red star location (OOP to IP transition).

One the one hand, at $\mu_0 \vec{H}_{ext} = 0$, we observe a demagnetized domain pattern in each of these region, but with different characteristics. It is made of parallel elongated stripes in the case of PM to OOP transition (see Fig. 4.8e) and labyrinthine domains in the case of OOP to IP transition (see Fig. 4.8g). Such a difference can be explained by the dependence of the effective anisotropy with the FeCoB thickness (see Sec. 1.2.4). In the PM to OOP region, the variation of K_{eff} is much more drastic than in the OOP to IP transition. Then, the domains growth direction is isotropic in regions where the K_{eff}-gradient is small while it is oriented in regions where the K_{eff}-gradient is large. More precisely, the growth is preferentially oriented perpendicular to the K_{eff}-gradient, *ie* along an iso-anisotropy direction.

On the other hand, in each of these region the application of $\mu_0 H_{ext} \simeq 100$ µT leads to the stabilization of magnetic skyrmions of $\simeq 1$ µm diameter[2], as shown in the bottom part of Fig. 4.8.

To summarize, the μ-MOKE performed on our double wedge Ta/FeCoB/TaO$_x$ sample gives all the combinations between FeCoB thickness and FeCoB/TaO$_x$ interface oxidation state for which magnetic skyrmions are stabilized. In fact skyrmions can be stabilized in locations where the effective anisotropy is small, *ie* on the contour of the OOP region, close to PM or IP transition. In these regions, the small effective anisotropy leads to a small DW energy $\sigma_{DW} = 4\sqrt{A_{ex}K_{eff}} - \pi D$, allowing the nucleation and stability of magnetic skyrmions. More precisely, skyrmion can be stabilized when the gain in iDMI energy and dipolar energy overcomes the cost in DW energy [91, 124]. This is achieved when the uniaxial

2 They should thus be called magnetic skyrmion bubbles, but their common topological and dynamical properties (as discussed in note page 41) led us to call them skyrmion in the entirety of this work.

anisotropy $\frac{K_S}{t_{FM}}$ is small, typically corresponding to magnetic phase transition of spin reorientation, *ie* from OOP to either IP or PM transition, as observed in our experiments.

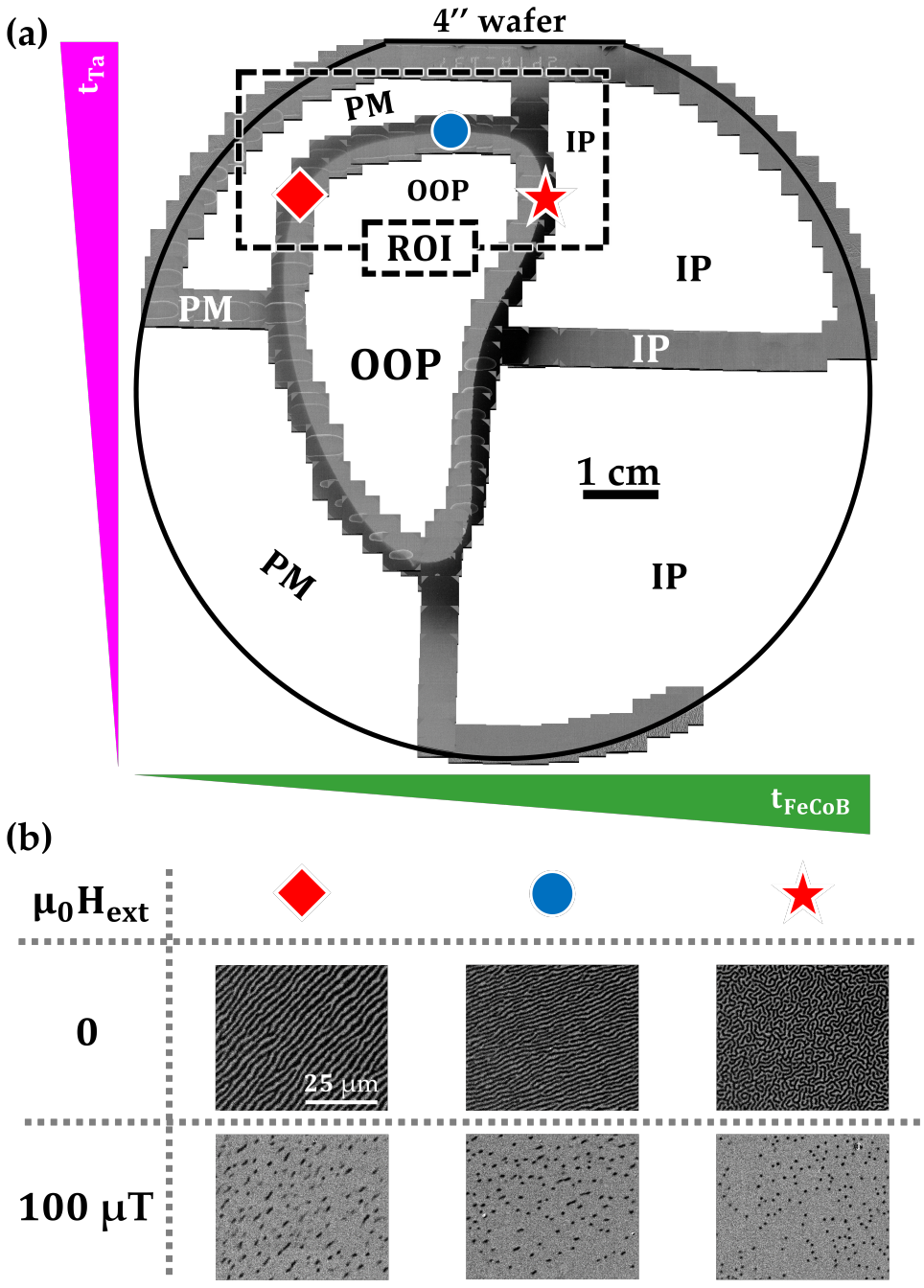

Figure 4.8: **Real-scale reconstructed mapping of the sample from MOKE microscope images:** (a) Recombination of pictures taken under the MOKE microscope in differential imaging mode, under perpendicular magnetic field $\mu_0 H_{ext} \simeq 100$ µT. In the middle, the OOP region is characterized by a saturated magnetic state. Along the contour of this region, magnetic skyrmions can be stabilized with the aforementioned magnetic field. (b) Zoom-in for the red diamond (PM-OOP transition), blue triangle (PM-OOP transition) and red star (OOP-IP transition) location with the MOKE microscope. At zero magnetic field, demagnetized domain configuration is osberved while skyrmions are stabilized at $\mu_0 H_{ext} \simeq 100$ µT.

Note : The narrow range for skyrmion stabilization

From one edge of the 4-inch wafer to the other, *ie* 10 cm, the ferromagnetic thickness varies of about 0.8 nm. In the OOP to IP transition region (red star on Fig. 4.8), skyrmions are observed on a $\simeq$ 3 mm wide region corresponding to a range of FeCoB thickness about 0.24 $\mathring{A}$, which is not even the thickness of an atomic monolayer. It corresponds to a variation of atomic coverage smaller than 10%. This explains the use of thickness gradient, since it is highly difficult to reproducibly obtain the exact good thickness at skyrmions at stabilized with a on-axis deposition.

4.3 MATERIAL-DEPENDENT INVERSION OF THE DZAYLOSHINSKII-MORIYA INTERACTION

The results presented in this section are the object of a paper submitted in Physical Review Applied (currently on ArXiV [175]) in which I am second author. Some part of the text are thus inspired from this article that we wrote.

In HM/FM/MO$_x$, the properties of magnetic skyrmions are driven by the amplitude and the sign of the interfacial Dzayloshinskii-Moriya interaction (iDMI) [91, 124]. An efficient skyrmion manipulation thus requires a precise control of the iDMI coefficient. In the previous section, we have shown that our double wedge sample allows for a fine tuning of material parameters and magnetic properties. In this section we focus on the effect of the FM thickness and the FM/MO$_x$ interface oxidation state on the iDMI amplitude and sign in our Ta/FeCoB/TaO$_x$ trilayer.

Interestingly, a spread of iDMI values and more importantly an inversion of iDMI sign are obtained in the literature for nominally similar trilayers such as Ta/FeCoB/oxide stacks, where relatively small DMI values (several tens of μJ/m^2 typically) are generally found. The reported chirality for various stacks are summarized in Table 4.1, together with the method of measurement. For instance, in similar Ta/FeCoB/MgO stacks, opposite DMI signs and domain wall chiralities are found by different teams [67, 176, 177], and a variation of MgO thickness in Ta/FeCoB/MgO/Pt samples lead to an inversion of DMI sign [178]. Similarly, in Ta/FeCoB/TaOx stacks, either left- of right-handed chiralities have been observed [76, 100, 179, 180] and the insertion of an ultrathin Ta layer at the FeCoB/MgO interface gives a right-handed chirality, as shown in the supplementary materials of reference [181].

Stack	Chirality	Method	Reference
Ta/FeCoB/MgO	CW	FIDWM	[176]
Ta/FeCoB/MgO	CW	CIM	[177]
Ta/FeCoB/MgO	CCW	CIM	[67]
Ta/FeCoB/MgO/Pt	CW/CCW	BLS	[178]
Ta/FeCoB/Ta/MgO	CW	CIM	[181]
Ta/FeCoB/TaO_x	CCW	CIM	[100, 179]
Ta/FeCoB/TaO_x	CW	BLS	[180]
Ta/FeCoB/TaO_x	CW	CIM + BLS	[76, 166]
Ta/FeCoB/TaO_x	CCW/CCW	CIM + BLS	My PhD ([175] and [182])

Table 4.1: **Summary of the chirality obtained for Ta/FeCoB/oxide system with various oxides and overlayers**: CW (resp. CCW) stands for clockwise (resp. counter clockwise). FIDWM stands for field driven domain wall creep motion, BLS stands for Brillouin Light Scattering and CIM stands for current induced motion.

This discrepancy in the sign of iDMI in nominally similar sputter-deposited systems might be attributed to the small and nearly compensating DMI amplitude from top and bottom FeCoB interfaces. The effective iDMI, the sum of both contributions, might thus change sign due to different target compositions, in particular for FeCoB, or to the different machines and deposition details used. For instance, the quality and oxidation level of the FeCoB/oxide interface might play an important role, if the oxide is deposited by RF sputter deposition or using DC sputter deposition of the metal followed by a post-oxidation. The growth rate and sample roughness may also play an important role. However, a clear picture of the iDMI in such Ta/FeCoB/oxide systems is still missing.

In this section, we report on the observation of two iDMI sign crossovers in Ta/FeCoB/TaOx sputtered samples. One is driven by the FeCoB/TaOx top interface oxygen content and the other one occurs when varying the FeCoB thickness. These findings are deduced from Brillouin Light Spectroscopy (BLS) measurements combined with a detailed study of the motion direction of skyrmions under DC current using polar magneto-optical Kerr Effect (p-MOKE) microscopy. These observations may explain the discrepancies observed in literature in this system. Moreover, the possibility to tune DMI sign and amplitude in such trilayer is a tool to optimize the current induced motion of skyrmions, by constructively combining the effects of spin transfer and spin orbit torques. Before presenting the results, I propose to briefly explain how we accessed iDMI sign and amplitude in this section.

Measurement of iDMI with Brillouin Light Scattering

In HM/FM/MO$_x$, the iDMI amplitude and sign can be measured directly with the BLS technique, that we propose to remind quickly here, since it has already been introduced in Sec. 3.2.2. In a BLS measurement, a linearly polarized LASER beam is sent on the magnetic sample put in the Damon-Esbach geometry (see Sec. 3.2.2). The interaction of light with the magnetic material can lead to the absorption or creation of a magnon, respectively called the Stokes and anti-Stokes event, and equivalent to spin waves propagating in opposite directions[3]. Besides, spin waves propagating in opposite direction can be assigned by an opposite chirality [183]. In the absence of iDMI, spin waves propagating in opposite direction are energetically degenerated (*ie* have the same frequency). On the contrary, in the presence of iDMI spin waves, one spin wave chirality is favoured, inducing a lift of the degeneracy. This frequency shift between counter propagating spin waves, called Δf, is related to the iDMI constant through the expression:

$$\Delta f = \frac{2\gamma}{\pi M_S} D k_{SW} \tag{4.1}$$

where γ is the gyromagnetic ratio and k_{SW} the wave vector of the spin wave. Thus, the measurement of the frequency shift between Stokes and anti-Stokes event gives a direct determination of the iDMI coefficient D.

Note : Brillouin Light Scattering measurements

The BLS measurements shown in Fig. 4.10 were done by Djoudi Ourdani and myself in the Laboratoire des Sciences et des Procédés des Matériaux (LSPM) in Villetaneuse, France. Results from Fig. 4.11 and 4.12 are extracted from the reference [175] in which I am second author.

Measurement of iDMI with spin orbit torque driven motion of skyrmions

In this section, the direct iDMI measurements done by BLS are complemented by SOT driven motion of skyrmions, also called current-induced motion (CIM). Indeed, iDMI also plays a key role in the DW dynamics driven by spin-orbit torques [97, 152, 157, 184]. As explained in section 2.5.2.2, a charge current flowing in the HM layer generates a transverse spin current due to the spin Hall effect whose angular momentum is transferred to the FM magnetization [185]. The resulting spin-orbit torque moves DWs and skyrmions in a direction that depends on their helicity, chirality and on the sign of the HM spin Hall angle (SHA). For instance, a HM underlayer with negative SHA, such as Ta [186, 187], induces a motion of CW DWs along the current density whereas CCW DWs move along the electron flow [187]. We used this technique to locally have access to the sign of the iDMI and thus the skyrmion chirality. Technically speaking, we need to inject a charge current

3 In other words BLS is a spectroscopy technique that gives access to the dispersion relation of magnons.

locally (the two current electrodes are typically separated by 100 μm) from a Keithley 2450 current source to the sample. This was done through a sample holder shown in Fig. 4.9a (another example is given in section 3.1.2 from chapter 3). The sample is fixed with insulating glue on one side of the sample holder (on the right in Fig. 4.9a) , and on the other side, several copper tracks are connected to the current source. Then, microwires are connected from the copper tracks to the sample (the thin white wires in Fig. 4.9a) by using the microbonding machine decribed in chapter 3. In Fig. 4.9b we show a x20 zoom-in near the current electrodes on the sample, viewed under the μ-MOKE in differential imaging mode and under an OOP magnetic field $\mu_0 H_{ext} \simeq 80$ µT (in which an electrical current $I = 15$ mA is applied). We can clearly see the two microbonding on the top (I_- current electrode) and bottom part (I_+ current electrode). We can also see the magnetic domains (as well as some skyrmions in the bottom right part), and as in the previous section, a gray contrast means magnetization pointing up while black contrast means that it is pointing down. Interestingly, we can see that the magnetic domains reveal the current lines, which is expected because their orientation and direction of motion is directly linked to the current direction (through the SOT motion due to the SHE).

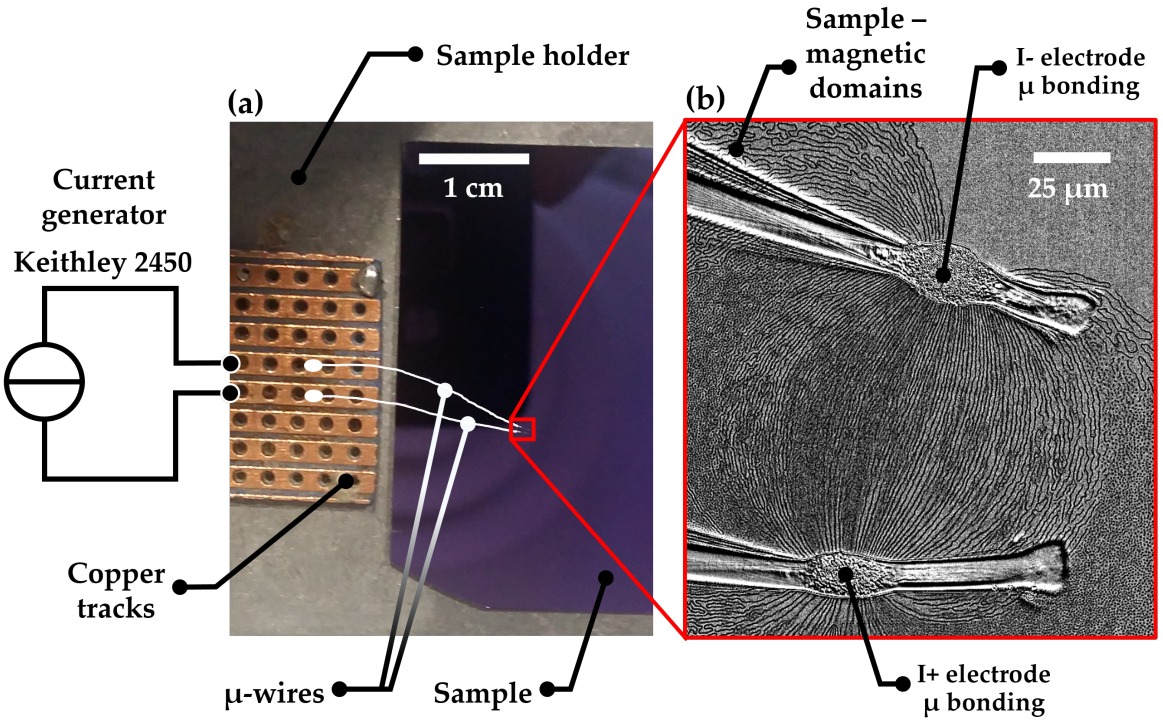

Figure 4.9: **Experimental method for SOT driven motion of skyrmions and DWs:** (a) *In-situ* optical picture of the sample mounted on the sample holder, with the copper tracks that makes the link between the current source (Keithley 2450) and the microwires from the wirebonding machine. (b) Zoom-in near the current electrodes with the MOKE microscope in differential imaging (x20 zoom). The two bonding electrodes are visible on the top and bottom part of the picture. A magnetic field $\mu_0 H_{ext} \simeq 80$ µT is applied out the of sample plane and an electrical current $I = 15$ mA is applied in the sample plane. Magnetic domains are visible, and their direction of elongation reveals the current lines. Some skyrmions are also visible on the right and on the left.

Note : Spin orbit torque driven motion of skyrmions

All electrical connections, current injection and data acquisition for the spin orbit torque driven motion were done by myself at SPINTEC.

In the following I first discuss the variation of iDMI versus the FeCoB/TaO$_x$ interface oxidation state (*ie* versus the top Ta thickness), and then versus the FeCoB thickness. Finally, I discuss a possible effect of the deposition conditions on the interpretation of the results.

4.3.1 *Variation along the top-Ta wedge*

Fig. 4.10 shows results from BLS measurements along the top-Ta wedge, at a nominal ferromagnetic thickness $t_{FeCoB} \simeq 1.2$ nm. The angle of the incident LASER beam is $\theta_{inc} \simeq 60°$, leading to a maximal wave vector for the spin waves $k_{SW} \simeq 20.45\ \mu m^{-1}$ which gives the better sensitivity. Our measurements show that the iDMI amplitude and sign depend on the top-Ta thickness and thus on the FeCoB/TaO$_x$ interface oxidation state. There is an FeCoB/TaO$_x$ interface oxidation state at which the iDMI is zero (dashed-purple line in Fig. 4.10a), and we can interpolate the corresponding top-Ta thickness to $t_{Ta} \simeq 0.93$ nm (dashed-red line in Fig. 4.10b). With respect to this location, a more oxidized (resp. less oxidized) FeCoB/TaO$_x$ interface leads to a negative (resp. positive) iDMI. We also tested the effect of FeCoB/TaO$_x$ interface oxidation state on iDMI with a different deposition technique: in Fig. 4.11 we show results of iDMI measurement by BLS on a set of sample deposited *on-axis* with varying the top-Ta thickness. We deposited 3 samples, one with top-Ta thickness typical of an overoxidized FeCoB/TaO$_x$ interface, one with an optimally oxidized FeCoB/TaO$_x$ interface and another with an underoxidized FeCoB/TaO$_x$ interface. We observe similar results, except that the iDMI sign crossover is shifted towards thinner top-Ta and the values of iDMI are larger, revealing the importance of the deposition technique and thus of the interface quality.

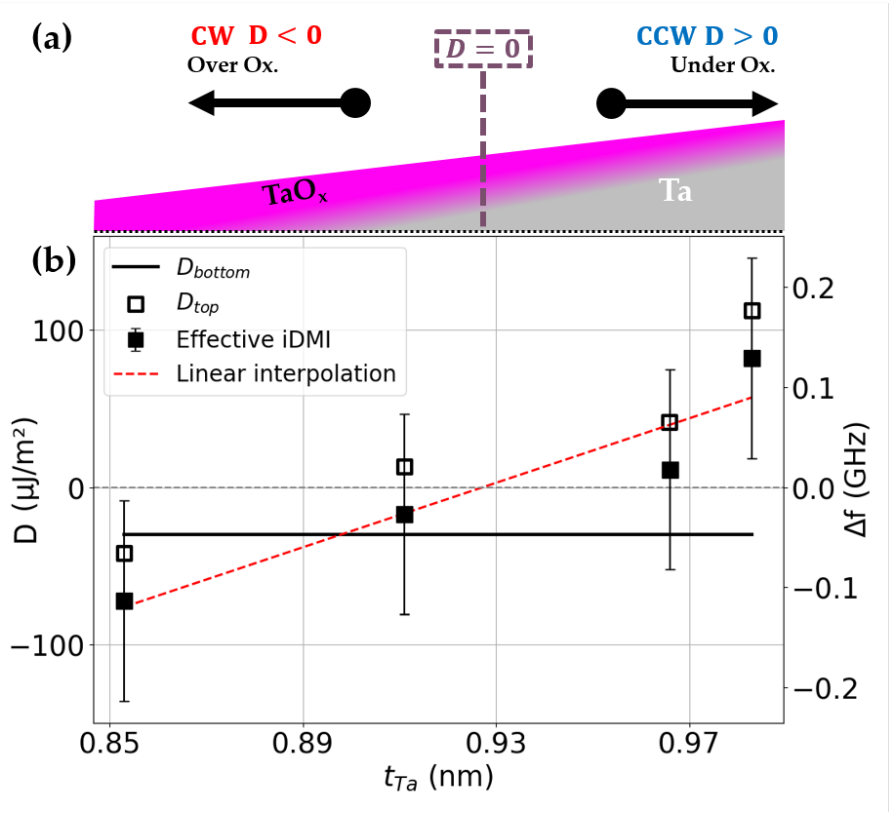

Figure 4.10: **Brillouin Light Scattering measurements of iDMI versus top-Ta thickness (wedge sample):** (a) Schematic representation of the top-Ta wedge, which induces the oxidation gradient and the iDMI sign inversion at a certain FeCoB/TaO_x. (b) Direct iDMI measurement with Brillouin Light Scattering along the top-Ta wedge. The total iDMI (full black squares) can be decomposed in a constant bottom iDMI contribution (black line) and a varying top iDMI contribution (empty black squares). The error bars correspond to $\Delta f = 100$ MHz from the BLS measurement setup.

To go further, we can refine the analysis since the effective iDMI originates from the two FeCoB interfaces in Ta/FeCoB/TaO_x. It can be defined as $D = D_{bottom} + D_{top}$, where D_{bottom} (resp. D_{top}) is the iDMI contribution from the Ta/FeCoB interface (resp. the FeCoB/TaO_x interface).

On the one hand, at the bottom Ta/FeCoB interface, the Fert-Levy mechanism [59] (see section 1.2.6.1) is at the origin of a small, negligible negative iDMI contribution[68, 188] (typically -0.03 mJ/m^2). This contribution is expected to remain constant versus the top-Ta thickness, as depicted by the black line in Fig 4.10b.

On the other hand the origin of iDMI for the top FeCoB/TaO_x interface depends on the oxidation state: (i) In the underoxidized region the *a priori* symetric Ta/FeCoB/Ta stacking is expected to give zero iDMI. Indeed the contribution from Ta/FeCoB and FeCoB/Ta are expected to be the same, with a sign inversion due to the inverted stack, but this is not what we observed. Actually, Ta/FeCoB and FeCoB/Ta are not the same interfaces. Indeed Ta is much heavier than FeCoB, leading to much more intermixing at the top interface, when Ta is sputtered on FeCoB compared to FeCoB sputtered on Ta for the bottom interface. It has been shown that intermixing is likely to enhance the iDMI at the interface [188], which could explain the positive iDMI for Ta/FeCoB/Ta. This kind of results has also been

observed for Pt/Co/Pt, which possesses a small iDMI when it is not supposed to have any due to the *a priori* symmetric stacking [189]. (ii) By gradually oxidizing this interface, we observe a progressive sign inversion of the iDMI. The apparition of an interfacial electric field (due to the presence of an oxide) leads to Rashba effect, at the origin of Rashba iDMI, found to be negative[4] in this system [76] and to depend on the amount of oxygen at the interface [190]. This could explain the progressive sign inversion of the top contribution D_{top}, leading to a sign crossover for the total iDMI. Very recently, an iDMI sign crossover for varying oxidation state at the top interface has been observed in a similar stack [64].

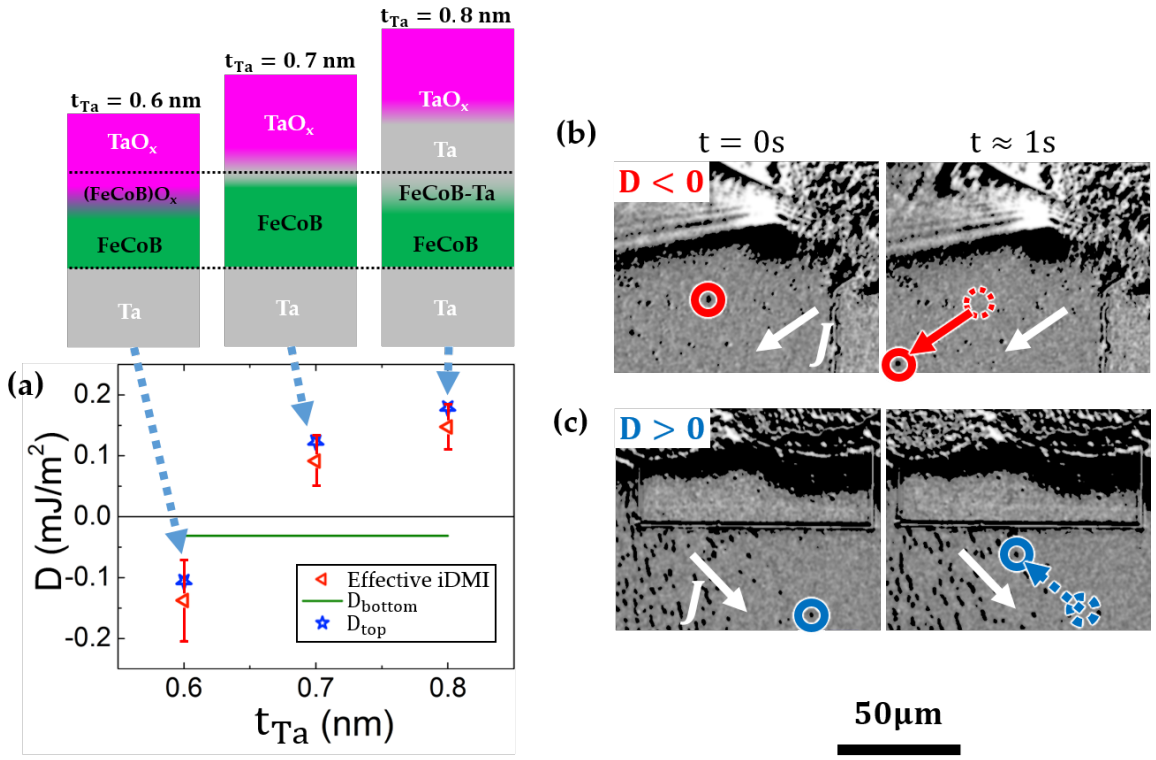

Figure 4.11: **iDMI and skyrmion chirality versus top-Ta thickness in *on-axis* samples:** (a) Direct iDMI measurement with BLS varying the top Ta layer thickness in three samples deposited *on-axis*, whose schematic representation can be found at the top part. The results from BLS are similar to the one from Fig. 4.10 observed in a wedge sample. (b) (resp. (c)) Snapshots of the skyrmions CIM in the negative (resp. positive) iDMI region as measured by BLS, at two different times separated by 1s. The current direction is depicted by the white arrow while the skyrmion motion is depicted by the red (resp. blue) arrow that links its two positions at 1s interval surrounded by red (resp. blue) circles.

In addition to direct iDMI measurement with the BLS, we performed spin-orbit torque driven motion in order to correlate the iDMI sign with the preferred chirality of the spin textures in the magnetic material. Results of skyrmion CIM measured under MOKE microscope for a positive and a negative value of iDMI are shown respectively in Fig. 4.11c and 4.11d. Skyrmion motion is evidenced by circles around its position at two times separated by 1 s, in addition to an arrow which gives the direction of motion. A solid red arrow means that the skyrmion moves along the current density (depicted by the white arrow)

4 In reference [76], the convention for iDMI sign is opposite to the one used in the present work

and a dashed blue arrow means that it moves in the opposite direction. Hence, we can deduce from these CIM measurement that the skyrmion adopt a CW chirality in region where $D < 0$, while a CCW chirality is preferred in regions where for $D > 0$. These results also confirm the iDMI sign crossover for the BLS measurement along the top-Ta wedge.
To summarize, variation of iDMI versus the top-Ta thickness is due to the fact that the contribution from the top FeCoB/TaO_x interface depends on the oxidation state. There is a progressive change in the iDMI origin, from positive Fert-Levy contribution at underoxidized interface to negative Rashba iDMI for optimally oxidized to overoxidized interface.

4.3.2 *Variation along the FeCoB wedge*

In this section, we show direct iDMI measurements done by BLS on samples with varying FeCoB nominal thickness. Using a *on-axis* deposition technique, we deposited a set of samples with varying FeCoB nominal thickness, and a fixed nominal top-Ta thickness $t_{Ta} \simeq 0.95$ nm, close to the one leading to an optimal FeCoB/TaO_x interface oxidation. As it is shown in Fig. 4.12 we cannot conclude on an iDMI sign inversion along the FeCoB wedge from the BLS measurements because of the errorbars. Although BLS measurements were inconclusive, the study of the SOT driven motion of skyrmions revealed an actual inversion of the CIM direction along the FeCoB wedge. In the thinner FeCoB region the skyrmions move along the current density (Fig. 4.12c), while they move in the opposite direction in the thicker region (Fig. 4.12d for positive iDMI.). It means that they have a CW chirality in the thinner region, associated to the negative iDMI coefficient, and a CCW chirality in the thicker FeCoB, associated to the positive iDMI coefficient.
The underlying mechanism under such an iDMI sign crossover as a function of the ferromagnet thickness is still unclear. It could be due to the fact that the interfaces become coupled for very thin ferromagnet [95, 190]. Also, the reduction of the dimensionality could induce modifications in the energy levels of the conduction electrons and hence in the band structure. The roughness could also play a role, but further experiments will be necessary in order to understand this observation.

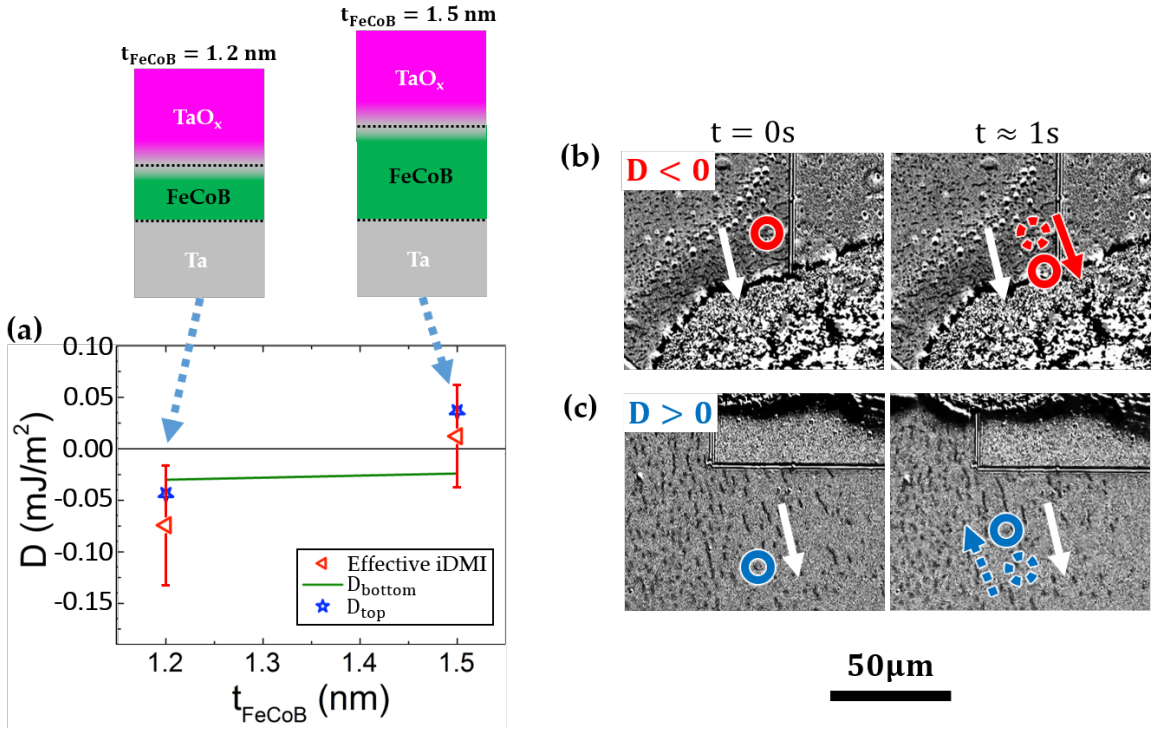

Figure 4.12: **iDMI and skyrmion chirality versus FeCoB thickness in *on-axis* samples:** (a) Direct iDMI measurement with BLS varying the top FeCoB thickness in two samples deposited *on-axis*, whose schematic representation can be found at the top part. (b) (resp. (c)) Snapshots of the skyrmions CIM in the negative (resp. positive) iDMI region as measured by BLS, at two different times separated by 1s. The current direction is depicted by the white arrow while the skyrmion motion is depicted by the red (resp. blue) arrow that link its two positions at 1s interval surrounded by red (resp. blue) circles.

4.3.3 *Possible influence of the deposition geometry?*

In Fig. 4.13a, we recall the reconstructed mapping from the μ-MOKE images, on which we superimposed a real-scale representation of the iso-thickness curves for the FeCoB (green curves) and the top-Ta (pink curves). In Fig. 4.13(b,c,d), we show results from skyrmion CIM in three different locations. It shows both the iDMI sign inversion driven by the FeCoB/TaO$_x$ interface oxidation state (CIM inversion between the blue triangle and the red star) and by the FeCoB thickness (CIM inversion between the blue triangle and the red diamond). Since the blue triangle and the red diamond are horizontally separated on the double wedge sample, it was expected to vary t_{FeCoB} at a constant FeCoB/TaO$_x$ interface oxidation state. But let us recall that, on a double wedge deposited sample, the iso-thickness curves are not horizontal and vertical lines but circles, centered on the target of the sputtering machine (see the green (iso-t_{FeCoB}) and pink (iso-t_{top-Ta}) curves on Fig. 4.13a). Thus, even if the two regions where the CIM was measured are horizontally separated, the FeCoB/TaO$_x$ interface oxidation state slightly varies, which could be the origin of this inversion of the chirality. Thus, in this hypothesis, the mechanism of iDMI sign crossover is mainly induced by the variation of the FeCoB/TaO$_x$ interface oxidation

state, and thus the iDMI sign crossover would stand on a circle of constant FeCoB/TaO$_x$ oxidation state, depicted by the dashed pink circle in Fig. 4.13a.

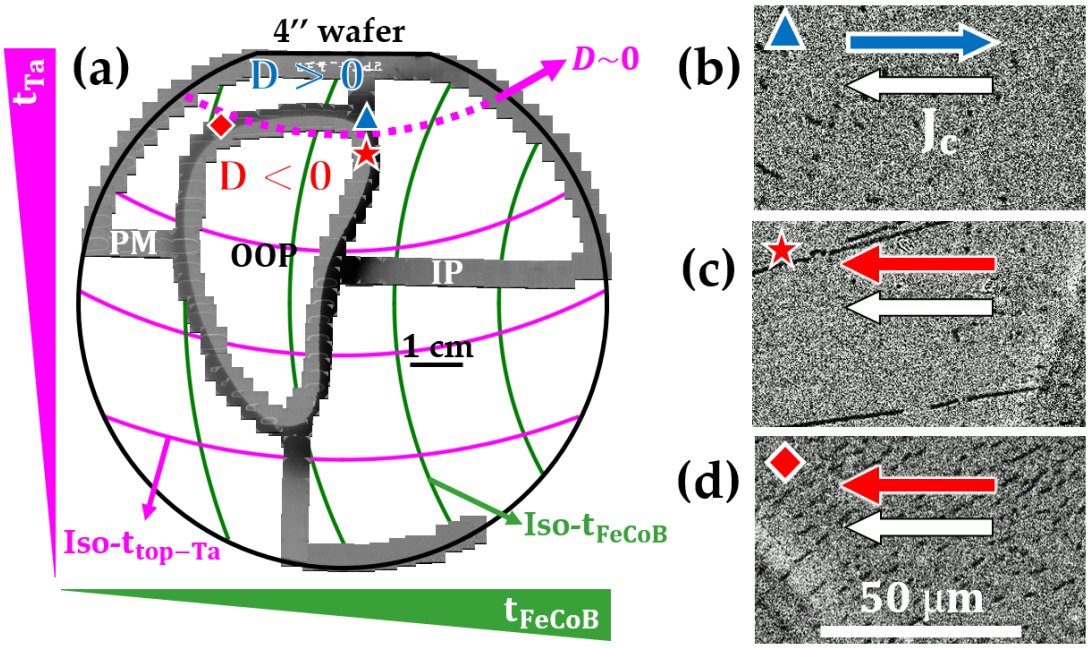

Figure 4.13: **Possible influence of the deposition geometry:** (a) Real scale representation of the iso-thickness curves on the sample. The $D = 0$ curve could correspond to an iso-thickness of the top-Ta layer which could explain our observation of iDMI and CIM inversion by moving horizontally. (b)-(c)-(d) CIM measurements.

However, recently this hypothesis has been invalidated by further experiments performed by Capucine Guéneau during her Master 2 internship[5]. In these experiments, a systematic study of the CIM of DW as a function of the position on the 4" inches wafer revealed that the $D \simeq 0$ curve is not a circle following an iso-oxidation state of the FeCoB/TaO$_x$ interface. This is clear when representing the data in the (t_{FeCoB}, t_{Ta}) space, as shown in Fig. 4.14. Each point corresponds to a measurement of CIM direction of DWs, indicating their chirality. These results confirm that the FeCoB thickness has an influence of the iDMI amplitude and sign, and further experiment combined with *ab-initio* calculations are on-going in order to unveil the underlying mechanism.

5 She is now working as a PhD in SPINTEC, on the following of my PhD work

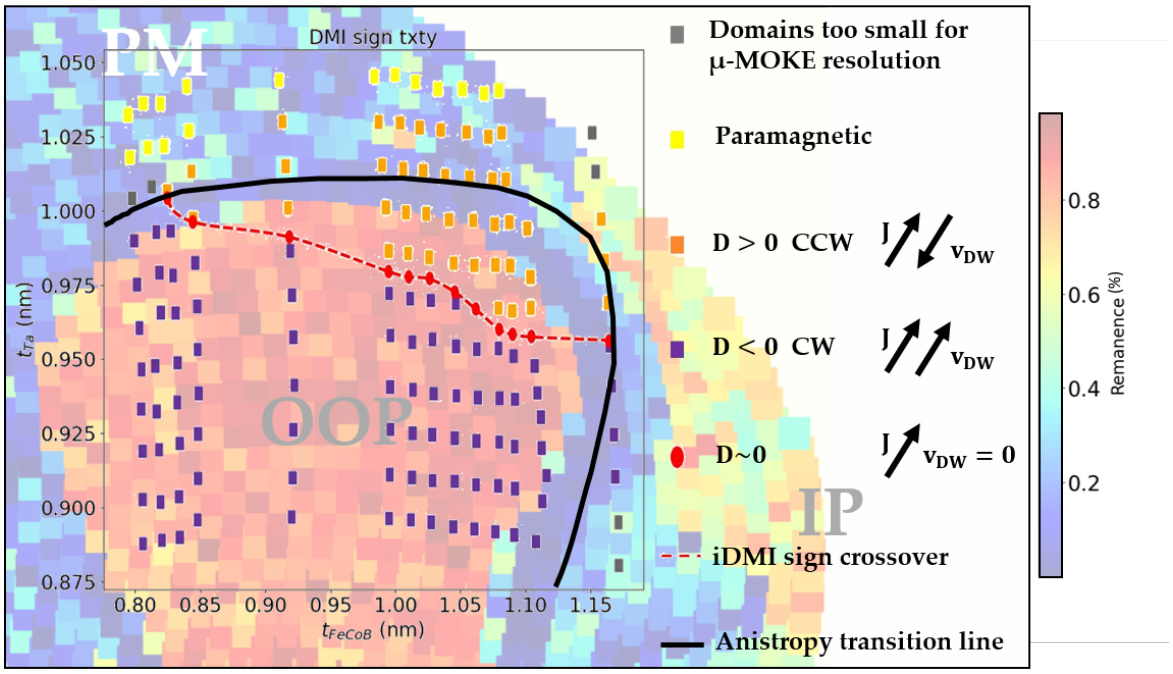

Figure 4.14: **Mapping of the iDMI sign by SOT driven motion of DWs:** (Courtesy Capucine Guéneau) Mapping of the SOT driven motion direction of DWs as a function of the FeCoB and top-Ta layer thicknesses, superimposed in transparency on the NanoMOKE normalized remanence mapping. An orange color means that DWs move opposite to the current direction, while purple means that DWs move along to the current. The transition between these two cases is depicted by the red color, where nearly no motion of DWs is observed. The iDMI sign crossover is thus depicted as a guide to the eyes, by the dashed-red curve. Moreover, in some points of the sample, the domains where too small to be imaged (gray dots) or it was paramagnetic (yellow dots). The boundary of the OOP region is represented by a thin solid black line.

4.3.4 *Combination of spin-orbit and spin transfer torques for an efficient skyrmion motion*

Finally, we have studied more thoroughly the influence of iDMI sign on skyrmion velocity along the FeCoB wedge that presents the unexpected chirality inversion. The current density where we extracted the skyrmion velocity was estimated to $J_{HM} \simeq 1.3 \times 10^9$ A/m² following the method presented in Annex 8.7. The different locations in which the skyrmion velocity has been measured (from #1 to #5 as the FeCoB thickness is increased) are represented on the normalized remanence map of the sample in the thicknesses space shown in Fig. 4.15a. The average skyrmion velocity v_{sk} is estimated by dividing the displacement (δ) by a typical time (τ) such that skyrmion passes a few pinning sites (typical time of a few seconds). The velocity is then averaged over the moving skyrmions (typically 5 to 10 skyrmions).

Fig. 4.15b shows the evolution of skyrmion velocity under $J_{HM} \simeq 1.3 \times 10^9$ A/m² in the negative iDMI region (#1-2 red digits), in the iDMI sign crossover region (#3 green digit) and in the positive iDMI region (#4-5 blue digits). With our convention, a positive velocity corresponds to a motion along the injected current direction, thus to a right-handed/CW chirality. When crossing the boundary where iDMI changes sign and skyrmion chirality

is inverted, the sign of skyrmion velocity is inverted as well. Interestingly, the typical velocities at location #5 ($D > 0$) is around -53 μm/s, whereas it is only about +10 μm/s at location #1 ($D < 0$), similar to the results of other teams on this system [100], for equivalent current densities. Besides, the left-handed/CCW chirality skyrmions ($D > 0$ region) can be moved with a current density as small as 2.6×10^8 A/m^2, which confirms a significantly larger mobility and lower pinning of these skyrmions with left-handed/CCW chirality. In this case, the spin orbit torque (SOT) favors a motion along the electron flow, similarly to a Zhang and Li spin transfer torque (STT) [191] and we may thus wonder about their relative contributions. By using the tabulated resistivities of Ta, Fe and Co ($\rho_{Ta} \simeq 44\ \Omega$/nm and $\rho_{Fe_{0.9}Co_{0.1}} \simeq 95\ \Omega$/nm) and the thicknesses of our sample, we roughly estimate that one third of the current flows through the FeCoB and two thirds in the Ta underlayer. Spin transfer torque within the FeCoB might thus play a non-negligible role in skyrmion motion. Hence, in the left-handed/CCW case, both torques act together to accelerate skyrmions. By contrast, if the chirality is inverted, STT is now opposite to SOT, which thus slows down skyrmion motion. This addition of STT for left-handed/CCW skyrmions might thus explain that, in this negative iDMI region, skyrmions can be moved with a ten times lower current as compared to the positive iDMI region. We note here that to explain the different speeds of CW and CCW skyrmions, we cannot exclude a small contribution from possible different pinning strength due to the slightly different growth conditions along the wedges. The left-handed/CCW skyrmions with large mobility and low pinning are thus more promising for applications. Finally, it is important to notice that the region in which no motion is observed for DWs and skyrmion do might not exactly correspond to the $D = 0$ region. Indeed, this is expected for a pure SOT motion, but if considering the additional STT contribution, this region can be shifted where the STT compensates exactly the SOT contribution to motion. Finally it is noteworthy that at the boundary between regions of positive and negative iDMI (for region #3 where zero iDMI is attributed) we observed a high density of bubbles that has nearly no motion under current (see inset of Fig. 4.15b, where the white scale bar corresponds to 20μm). They just show usual Brownian motion, expected for 300K experiments. In the case of zero iDMI, skyrmions with Bloch domain wall may be stabilized. The driving force is perpendicular to the current, either in one direction or in the other depending on the chirality of the Bloch domain wall. As there is no preferred chirality for a Bloch domain wall, we interpret the absence of motion as the effect of repulsive interactions between the closely packed bubbles. The interplay of STT and SOT for efficient chiral DW motion has been studied in previous works for large K_{eff} [67].

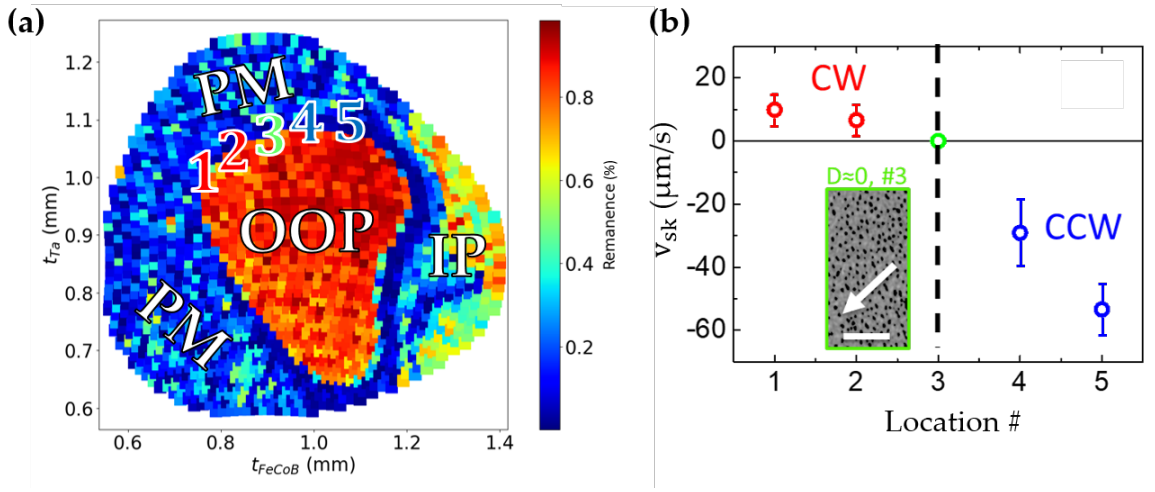

Figure 4.15: **Skyrmion motion velocity versus location along the FeCoB wedge:** (a) Sketch of the different locations (from #1 to #5) in which the velocity was extracted from the skyrmion motion. Regions #1,2 correspond to negative iDMI, #3 to the iDMI sign crossover and #4,5 to positive iDMI. (b) Skyrmion velocity under $J_{HM} \simeq 1.3 \times 10^9$ A/m², measured at locations #1 to #5. A positive velocity corresponds to a motion of skyrmions along the injected current direction. The error bars mainly come from the statistical dispersion of velocities measured on several skyrmions. Inset: p-MOKE microscopy image in region #3 of the iDMI sign crossover ($D \simeq 0$), no detectable displacement of bubbles is observed under the same injected current, except usual Brownian motion.

4.4 CONCLUSION

In this chapter, I have presented the magnetic properties of our Ta(3)/FeCoB(0.8-1.4)/TaO$_x$(0.5-1) trilayer heterostructure (thicknesses given in nanometer). In particular I have shown that the double wedge deposition technique ensures the presence and stabilization of magnetic skyrmions, in the transition region between paramagnetic and out-of-plane anisotropy, or between out of plane and in-plane anisotropies.

More importantly, I have highlighted the possibility to realize a fine material-dependent tuning of the iDMI. With direct BLS measurements and indirect spin-orbit driven skyrmion dynamic study, I have shown that the amplitude and the sign of the iDMI could be tuned both by tuning the FeCoB/TaO$_x$ interface oxidation state or the FeCoB thickness.

5

GATE CONTROL OF SKYRMION AND DOMAIN WALL CHIRALITY

The results presented in this section are the object of a publication in Nature Communications in which I am the first author [182]. The main text of this section is thus largely inspired from this paper.

In the previous chapter I have presented the magnetic properties of Ta/FeCoB/TaO_x trilayer crossed double wedge. Notably, we have shown that the amplitude and the sign of the iDMI could be adjusted with the oxidation state at the top FeCoB/TaO_x interface. However, such material tuning induces that the iDMI is fixed by the sample deposition and cannot be further adjusted.

In this section, I propose to go beyond this limitation and show use the possibility to tune iDMI locally and dynamically, after deposition, using a gate voltage. Recently, it has been shown that using chemisorption of hydrogen on the FM layer can invert the iDMI sign locally and reversibly [66]. However, this technique for controlling iDMI and thus DW chirality necessitates complex experimental setups, such as ultrahigh vacuum or low energy electron microscopy to monitor the hydrogen coverage. As presented in section 1.3.2, gate voltage emerged as a promising, low power and versatile technique to achieve both a local and dynamical control of interfacial magnetism [73, 74, 77], notably of iDMI. The possibility to electrically reverse the sign of the iDMI would provide a versatile and reversible control of skyrmion chirality, which could considerably improve

their all-electrical, individual and low power manipulation.

In a first section, I demonstrate experimentally that a gate voltage induces a local and dynamical reversal of skyrmion chirality in a Ta/FeCoB/TaO_x trilayer.
In a second section, I show a similar effect on chiral DWs in a labyrinthine magnetic state, confirming our findings on magnetic skyrmions. Regardless of the initial DW chirality, which is controlled by the initial oxidation level at the FeCoB/TaO_x interface, a gate voltage with appropriate polarity is able to switch chirality back and forth in a persistent way. This reversal is attributed to ionic migration, and thus oxidation or reduction of the FeCoB/TaO_x interface, by the gate voltage, which results in the inversion of iDMI sign.
Finally, using an analytical model I predict that the skyrmion can remain stable during the chirality inversion.

5.1 EXPERIMENTAL OBSERVATIONS

5.1.1 *Skyrmion Chirality Reversal with Gate Voltage*

This study is carried out in a Ta(3)/FeCoB(1.2)/TaO_x(0.85-1) (thicknesses in nm) trilayer. The magnetic properties of this sample have been presented in section 4.3. Here, the only difference is that we restrict ourselves to a constant ferromagnetic thickness ($t_{FeCoB} \simeq 1.2$ nm), thus simplifying the sample to a single top Ta wedge, as shown in Fig. 5.1a.

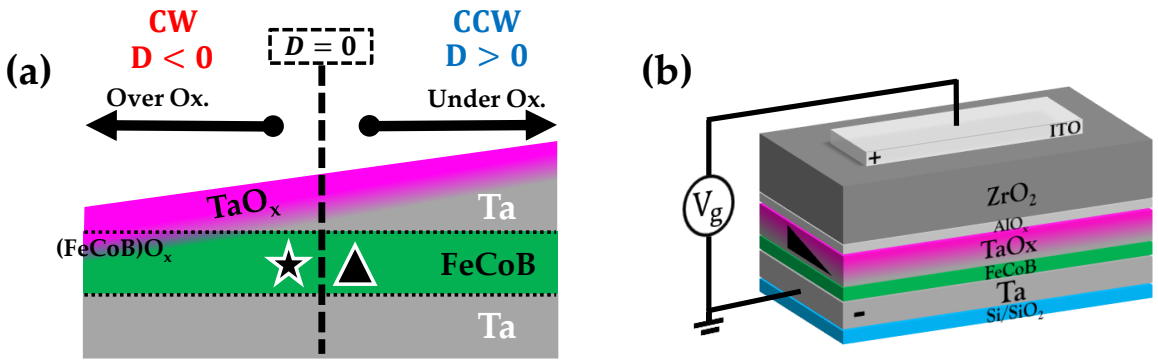

Figure 5.1: **Sample adapted for gate voltage application:** (a) Schematic cross section of the trilayer: the top-Ta wedge induces an oxidation gradient at the top interface, leading to a iDMI sign crossover as directly measured by BLS vs top-Ta thickness (see section 4.3). The star and triangle location correspond to the location of the experiments in respectively Fig. 5.5, 5.3, 5.4, 5.6 and Fig. 5.7, 5.8, 5.9. (b) Schematic representation of the Ta/FeCoB/TaO_x trilayer with thin AlO_x capping, additional ZrO_2 oxide and transparent ITO electrode for gate voltage application.

As we already know from section 4.3, the top Ta wedge induces an iDMI sign crossover close to the optimally oxidized FeCoB/TaO_x interface, schematically represented by a dashed line in Fig. 5.1a. For an underoxidized (resp. overoxidized) FeCoB/TaO_x interface, the iDMI coefficient D is positive (resp. negative), corresponding to DW with a CCW (resp. CW) chirality. Then, we adapted the sample for gate voltage application: in addition

to the 0.5 nm AlO_x capping layer deposited *in-situ* by sputtering, a 20 nm ZrO_2 oxide layer was deposited *ex-situ* by Atomic Layer Deposition (section 3.1.2) on top of the trilayer. It acts as a dielectric layer for the gate voltage application. Moreover, it is known to be a good ionic conductor, which will play a key role in the following. Finally, I patterned 70 nm transparent Indium Tin Oxide (ITO) electrodes by laser lithography for gating, leading to a capacitor geometry for the gate voltage application (see Sec. 3.1.2). The size of the electrodes was 100×800 μm^2. A schematic representation of the resulting Ta(3)/FeCoB(1.2)/TaO_x(0.85-1) trilayer (nominal thicknesses in nm), with 20 nm ZrO_2 oxide and transparent ITO electrode is shown in Fig. 5.1b.

The experiment then consists in probing the skyrmion chirality by analyzing their SOT driven motion direction (see also Sec. 2.6). Here, a current density is injected in the bottom Ta layer via micro-bonded wires (explained in more detail in chapter 4), which generates the source of SOT via the SHE. It is done in the initial as-grown state (*ie* before gate voltage application) and under or after the application of a gate voltage. The iDMI amplitude and sign being adjustable with the oxidation level at the FeCoB/TaO_x interface, the wedge sample geometry shown in Fig. 5.1a allowed us to prepare an initial skyrmion with a desired chirality.

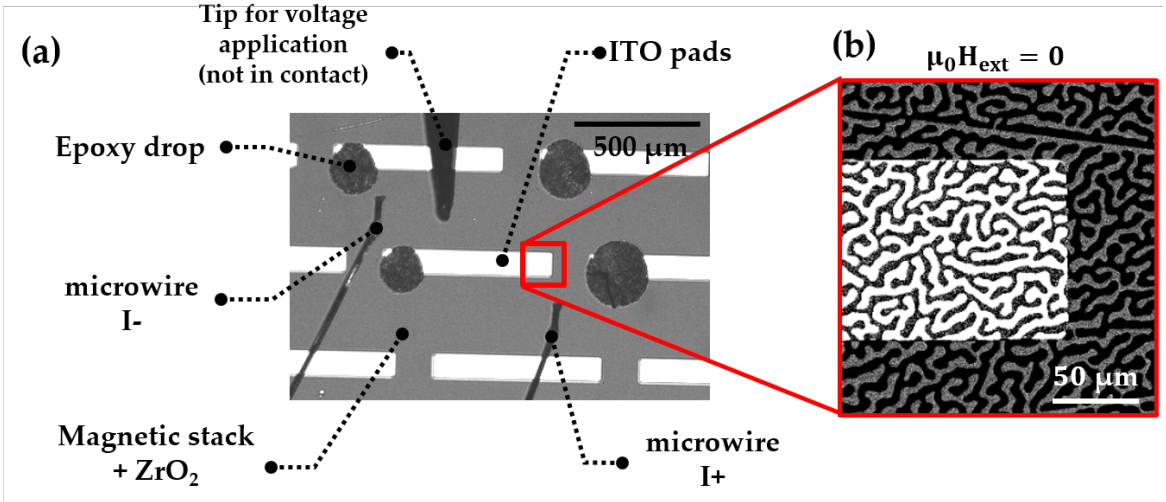

Figure 5.2: **Description of the experiment:** (a) Optical top view of the multilayer with patterned ITO electrodes (white rectangles), microbonded wires for current injection, and tip for voltage application (which is further put on epoxy drops to avoid ITO damage). (b) A zoomed view of the extremity of an ITO electrode, taken under the MOKE microscope, revealing the demagnetized configuration in zero external magnetic field. The magnetization is visible both below (white/gray contrast region) and around the ITO (black/gray contrast region).

In Fig. 5.2a we show an optical microscope top view of the sample with the patterned ITO electrodes (the white rectangles) and the microbonded wires for current injection (the I+ and I- wires). The ground voltage electrode (not visible in Fig. 5.2a) is chosen to be the bottom Ta layer while the positive voltage electrode is the ITO (Fig. 5.1b), patterned on top of the multilayer, on which a tip is carefully contacted using micromanipulators (the tip is not in contact with the ITO in Fig. 5.2a). In order to avoid ITO damage and thus potential shortcut, the tip is contacted on a conductive epoxy drop, that is first deposited on the

ITO and subsequently dried[1]. The current, flowing from the source (I+) to the sink (I-), induces SOT at the bottom Ta/FeCoB interface. As a reminder, a HM underlayer with negative SHA, such as Ta [186, 187], induces a motion of CW DWs along the current density whereas CCW DWs move along the electron flow [187]. Thus, the use of the MOKE microscope through transparent electrodes allows us to directly observe the current-induced motion (CIM) direction and its inversion during or after the application of a gate voltage.
In Fig. 5.2b, the micromagnetic configuration is clearly visible under the ITO electrode, allowing to probe its dynamics under a gate voltage. Differential imaging is used in order to improve the contrast (the reference is the saturated magnetic state). Under zero applied magnetic field, demagnetization of the sample occurs and labyrinthine domains are formed. Below ITO (resp. around it), black (resp. grey) regions correspond to magnetization pointing up, and white (resp. black) regions to magnetization pointing down. This variation of contrast between below and around ITO might be explained by anti-reflecting effect from the ITO electrodes.
In the area close to the iDMI sign crossover (star location in Fig. 5.1a), an external out of plane magnetic field $\mu_0 H_{ext} \simeq 80$ μT stabilizes magnetic skyrmions of $\simeq 1$ μm diameter (white dots under ITO in Fig. 5.3(a,b)). When a current is applied, skyrmions drift undistorted all in the same direction confirming their skyrmionic nature and their homochirality. We call them skyrmions in the following, since they share the same topology [124]. Due to the low injected current density[2], about $J \simeq 5 \times 10^9$ A.m^{-2}, some skyrmions remain motionless as they are probably pinned by defects. The trajectory of each skyrmion is represented as a colored line between a starting point (surrounded by a circle) and a ending point (surrounding by a star). In Fig. 5.3(a-b) the trajectories are superimposed to the first frame of the MOKE microscope movie, on which we can see a skyrmion in each circle. For a better visualization, the trajectories are represented alone on a graph below the MOKE image (see Fig. 5.3(c,d)). The ITO electrode contour is depicted by a gray line, and the direction of the current density by a black arrow.
In the initial state ($V_g = 0$), the mobile skyrmions move along the current direction (speed $v_{0V} = 13.5 \pm 2$ μm.s^{-1} at $J \simeq 5 \times 10^9$ A.m^{-2}) which is expected for a Néel DW with a CW chirality (see Fig. 5.3(a,c)). The average velocity ($v = \frac{\delta}{\tau}$) is estimated by dividing the displacement (δ) by a typical time (τ) such that skyrmion passes a few pinning sites (typical time of 4 seconds in Fig. 5.3). The velocity is then averaged over the moving skyrmions. It is noteworthy that the effect of the thickness gradient on the skyrmion motion is negligible, indicating that current is the driving force (See Annex XX). Besides, skyrmion Hall effect is expected to be negligible due to the small velocities in this regime of low current densities [153, 154, 156]. Furthermore, the continuous motion of skyrmions when crossing the edges of the ITO electrode shows that the magnetic configuration is the same below and around the electrode.

Skyrmion CIM is then measured while applying a positive gate voltage on the electrode. We observe a progressive change: skyrmion speed first decreases, then the motion direc-

1 90°C during 15 minutes on a hotplate. Note that in Fig. 5.2a the voltage tip is not in contact with the epoxy.
2 For more details on the estimation of the current density, see Annex 8.7

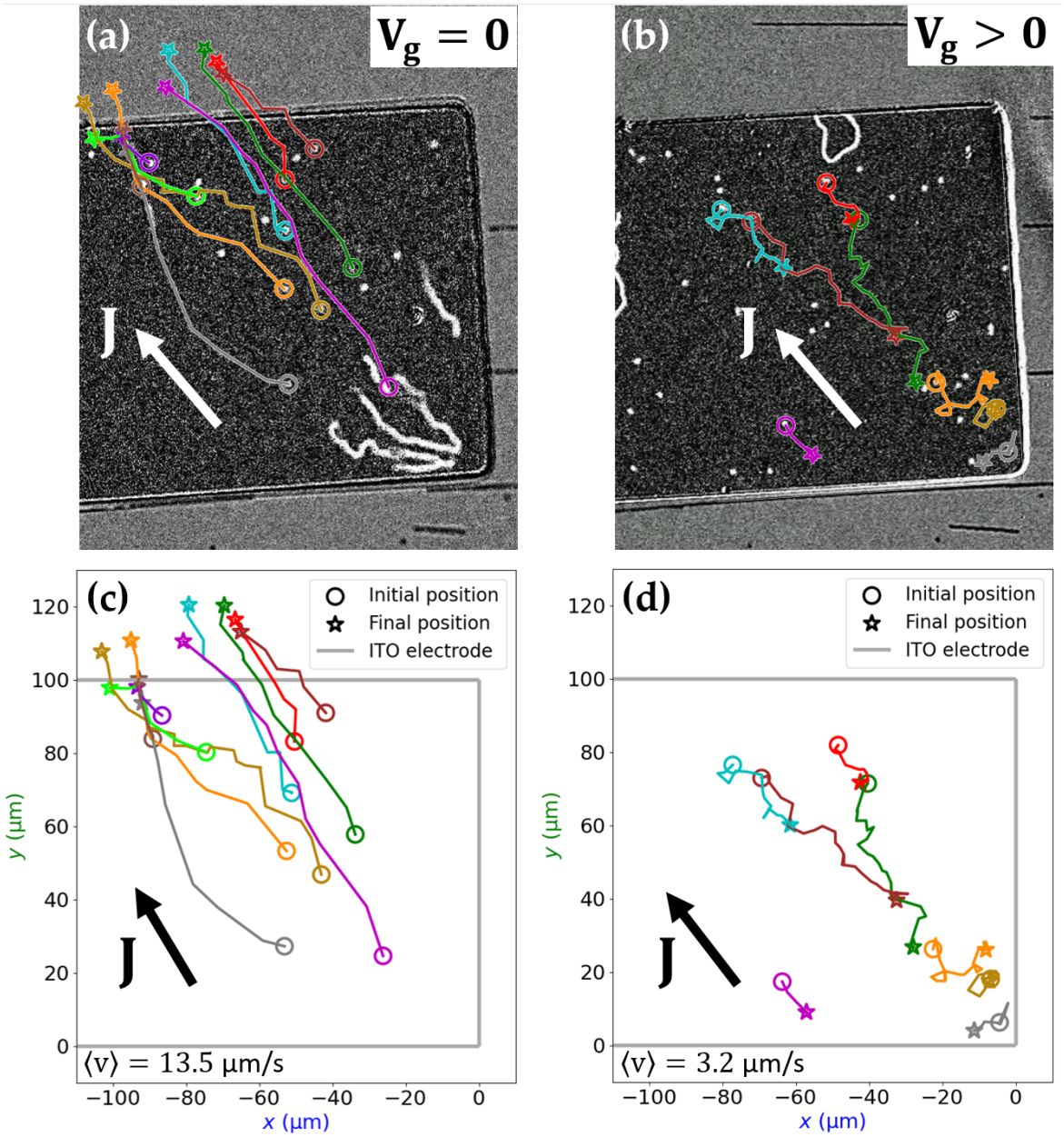

Figure 5.3: **Skyrmion chirality reversal with a gate voltage:** (a,c) Skyrmion CIM monitored during 4 s under p-MOKE microscope at the star location shown on Fig. 5.1a for zero gate voltage and (b,d) for $V_g = +3.5$V, applied on ITO (the dark rectangular region). An out of plane magnetic field $\mu_0 H_{ext} \simeq 80$ μT is applied, as well as an in plane current density $J \simeq 5 \times 10^9$ A.m^{-2}. In (a) (resp. (b)), the trajectories are superimposed to MOKE microscope image of the initial position of each skyrmion (surrounded by circles). For clarity, the trajectories are represented alone in (c) (resp. (d)), where the gray rectangle corresponds to the ITO contour and the black arrow to the current density.

tion inverts, typically after 90 s, and speed further increases and saturates. The CIM is now along the electron flow with $v_{+3.5V} = -3.2 \pm 2$ μm.s^{-1} at $J \simeq 5 \times 10^9$ A.m^{-2} (see Fig. 5.3(b,d)). However, some skyrmions remain totally pinned and some of them are hopping around in the bottom right corner of the ITO electrode. This might be explained by the anisotropy difference induced by the gate voltage between under and around the ITO: skyrmions are submitted to a force, acting in the vicinity of the ITO edges and directed

from the high anisotropy region (around ITO) to the low anisotropy region (under ITO) [192].

The observed inversion of skyrmion motion direction is a signature of a transition from CW to CCW chirality, induced by an inversion of iDMI sign due to the gate voltage. As expected, this CIM reversal is observed only below the ITO electrode, where the FeCoB/TaO_x interface properties are modified by the gate voltage. This effect is reversible: switching the gate voltage to zero allows recovering the as-grown CW skyrmion chirality, on the time scale of several minutes. Moreover, the chirality inversion is reproducible: skyrmions in Fig. 5.3 have previously undergone several chirality reversals.

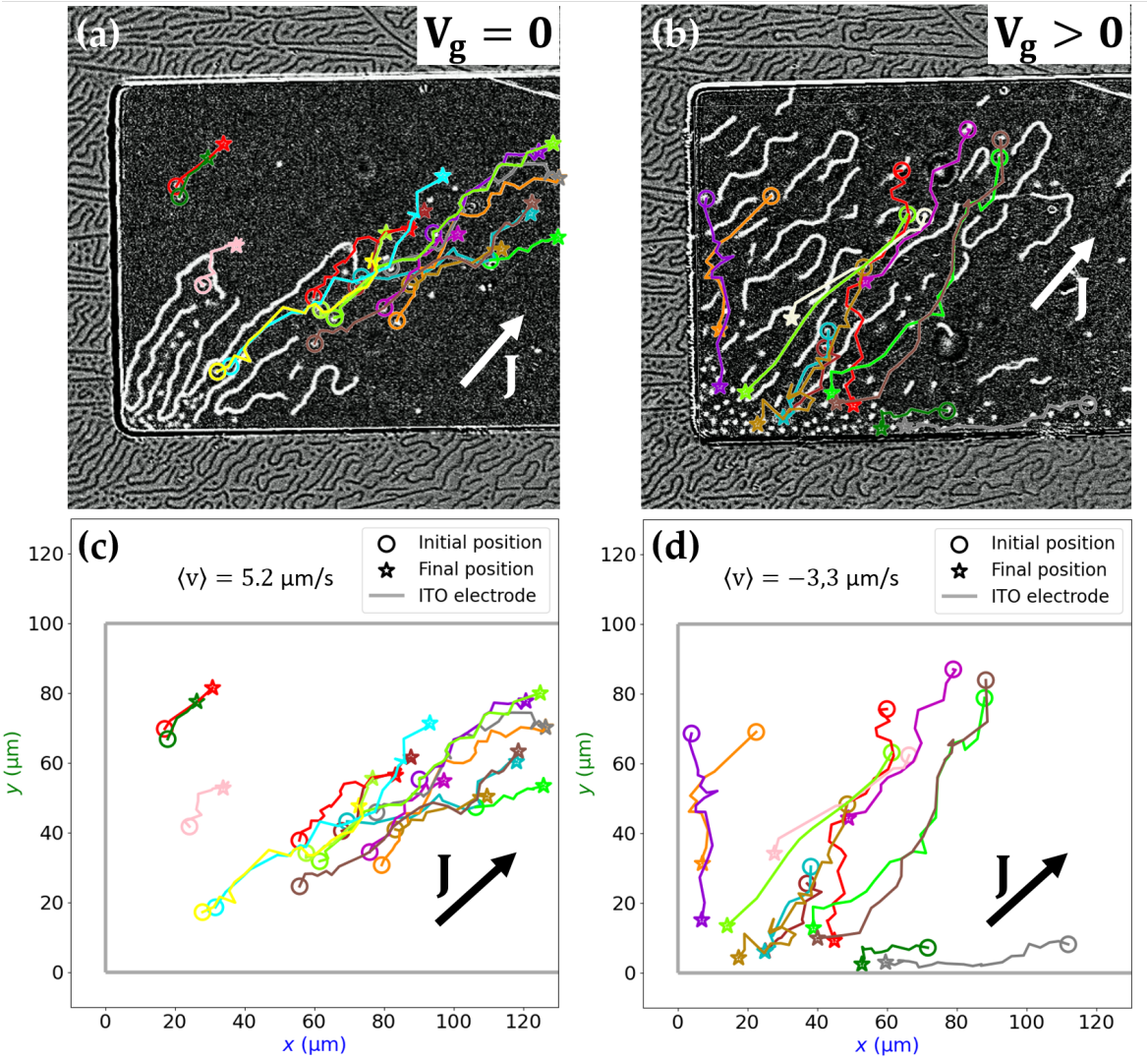

Figure 5.4: **Skyrmion chirality reversal:** (a,c) (resp. (b,d)) Trajectory of magnetic skyrmions under another electrode with more skyrmions, under zero gate voltage (resp positive gate voltage). In (a) (resp. (b)), the trajectories are superimposed to MOKE microscope image of the initial position of each skyrmion (surrounded by circles). For clarity, the trajectories are represented alone in (c) (resp. (d)), where the gray rectangle corresponds to the ITO contour and the black arrow to the current density.

In addition, in Fig. 5.4, we propose to show results of a similar experiment on another electrode nearby the one of Fig 5.3. The larger number of skyrmions in this experiment allows for more statistics and confidence in the effect. Similarly to the experiment presen-

ted above, the initial chirality is CW both below and around the ITO, since skyrmions are moving along the current density in these two regions (see Fig. 5.4(a,c)). However, there is a small difference in the magnetic state below the ITO electrode and around it due to a previous small voltage application on the ITO electrode. Once again, the application of a positive gate voltage leads to the inversion of the current induced motion under the ITO, signature of the inversion of the skyrmions chirality (see Fig. 5.4(b,d)). The skyrmions close to the ITO border are repelled and move along the edge. We observe a convergent motion of skyrmions in the bottom left corner of the ITO, leading to an accumulation of skyrmions (see Fig. 5.4b). It is interesting to notice that some skyrmions have common parts of trajectories. It can be explained by the presence of a local pinning or low anisotropy site in which the skyrmions passing nearby are attracted.

5.1.1.1 *Intermediate conclusion*

Our experimental observations show that the gate voltage produces the same effect as a displacement along the Ta wedge from the region with $D < 0$ (star in Fig. 5.1a) to the region with $D > 0$ (triangle in Fig. 5.1a): starting from the region where skyrmions have CW chirality (schematic representation of a CW skyrmion in the left part of Fig. 5.5), a positive gate-voltage leads to a reversal to CCW chirality (schematic representation of a CCW skyrmion in the right part of Fig. 5.5).

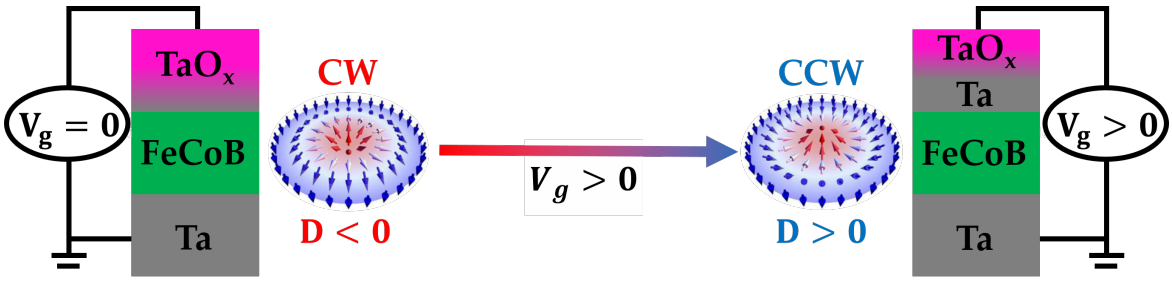

Figure 5.5: **Ionic migration as a tool to control the skyrmion chirality with a gate voltage:** Mechanism underlying our experimental observation. In our geometry, $V_g > 0$ reduces the FeCoB/TaO_x interface, inducing an inversion of the iDMI sign, and thus of the skyrmion chirality, as schematically represented.

Thus, a positive gate-voltage induces interfacial magnetic properties similar to those of a less oxidized interface. We may interpret this result either as a charge effect or as a migration of oxygen ions away from the interface. The former should produce an immediate effect whereas the latter is expected to be slower and possibly persistent. Since our measurements show that the reversal of the skyrmion motion occurs with a certain latency, we propose that the driving mechanism is ion migration. The positive gate voltage acts as a local reduction of the FeCoB/TaO_x interface that triggers the chirality reversal, as schematically represented in Fig. 5.5. Moreover, the observed recovery of the initial chirality when switching-off the gate voltage ($V_g = 0$) is consistent with the spontaneous re-oxidation of the FM/MO_x interface observed in similar materials with an equivalent timescale [86].

5.1.2 *Persistent and Reversible Control of Chirality with Gate Voltage*

Hereafter, we explore the chirality reversal process on labyrinthine domains (see Fig. 5.6) obtained by decreasing the external magnetic field to 30 μT in a region of the sample similar to the one of Fig. 5.5a-d. This magnetic configuration is more robust than skyrmions to small changes of magnetic parameters and magnetic field [184]. Here, we focus on the persistent effect of gate voltage on DW chirality. Thus, the current injection experiments, to probe the chirality, were performed after turning off the gate voltage.

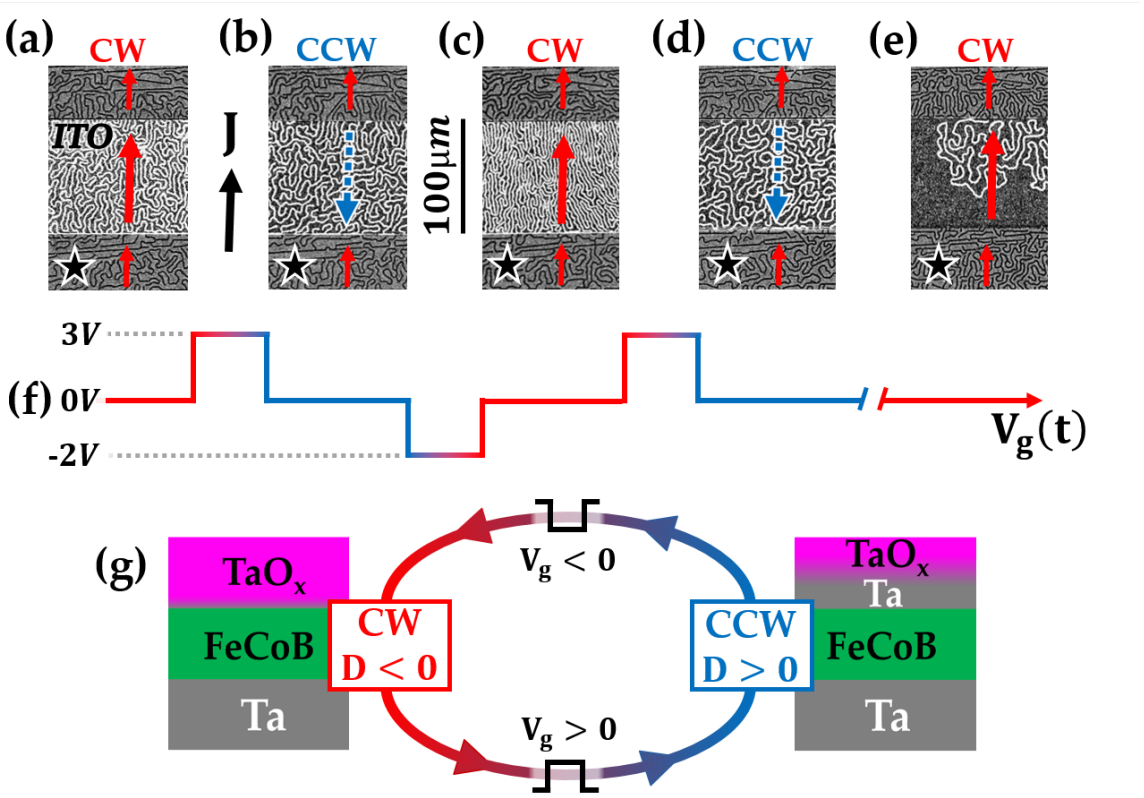

Figure 5.6: **Persistent and reversible chirality switch:** In the region close to iDMI sign inversion (star in Fig. 5.1a), the current density J (black arrow) induces a motion of DWs (red/blue arrows for a motion along/opposite to the current density), as observed by p-MOKE microscopy after switching off the gate voltage. (a-e) observation of DW motion under zero gate voltage and $\mu_0 H_{ext} \simeq 30$ μT, after sequential 90s-long voltage pulses. (f) Schematic representation of the applied voltage as a function of time. Initially (a) DW have CW chirality; after a positive gate voltage pulse (b), chirality is reversed to CCW under the ITO electrode; after a negative gate voltage pulse (c), CW chirality is recovered ; after a positive gate voltage pulse (d), chirality has switched again to CCW; (e) after waiting ~2 hours with zero gate voltage applied, the initial CW chirality is recovered. (g) Schematics of the effect of gate voltage pulses on interface oxidation, DW chirality and iDMI.

Fig. 5.6a shows the initial nearly demagnetized state with labyrinthine domains. The pattern of the labyrinthine domains is identical and continuous below and around the electrode. In the initial state, before gate voltage application, the DWs move in the same direction as the current, which is an indication of their CW chirality (red arrow in Fig. 5.6a). After the application of a 90 s positive gate voltage pulse ($V_g = 3$ V), the CIM of the DWs

below the electrode is reversed (dashed blue arrow in Fig. 5.6b), indicating a CCW chirality, which is due to an inversion of iDMI sign. This result is similar to the one obtained for skyrmions, except that the domain wall chirality is now probed at electric remanence, *ie.* $\simeq 5$ s after the gate voltage has been set to zero.

We further observed that a 90 s negative gate voltage pulse ($V_g = -2$ V) restores the initial CW chirality (Fig. 5.6c). A subsequent 90 s positive gate voltage pulse ($V_g = 3$ V) once again switches towards CCW chirality (Fig. 5.6d). Thus, chirality can be reversibly controlled by gate voltage and in a persistent way. It is reversed from CW to CCW (resp. from CCW to CW) with a positive (resp. negative) gate voltage, which we attribute to reduction (resp. oxidation) of the FeCoB/TaO_x interface (see Fig. 5.6g). Moreover, this local and dynamical control of the chirality is realized with voltages compatible with applications ($|V_g| \simeq 2-3$ V).

Finally, the reversed CCW DWs of Fig. 5.6d recover their initial CW chirality after about two hours (Fig. 5.6e), which is longer than for skyrmions (see previous section). In this experiment, contrary to previous section, negative voltages were applied to the FM/MO_x interface (oxidation of the interface), which is known to induce a certain degree of irreversibility [87, 96] and that may be at the origin of a slower recovery of magnetic properties. We suggest that the positive gate voltage drives oxygen ions from their equilibrium position into a metastable less oxidized state, in which they remain after the gate voltage has been turned off. The existence of such a metastable state has been theoretically demonstrated at Fe/MgO interface, in the opposite case, ie. when interfacial oxygen is migrated towards the first Fe layer [193]. The slow recovery of the initial state, also reported in other studies [194, 195], corresponds to a return to equilibrium. The time scale of this process is consistent with our hypothesis of ion migration, which is known to occur in TaO_x and ZrO_x [196].

Until now, the experiments were done in the star location in Fig. 5.1a, where the chirality is CW before gate voltage application. In this region, we showed for both skyrmions (see Fig. 5.3 and 5.4) and labyrinthine domains (see Fig. 5.6) that the application of a positive gate voltage can lead to the transition from CW to CCW chirality under the ITO electrode. This is evidenced by the inversion of the CIM direction of the DWs under the ITO.

Here, we show the converse effect starting from labyrinthine domains with a CCW chirality before gate voltage application, corresponding to the triangle location in Fig. 5.1a. The external magnetic field is switched off ($\mu_0 H_{ext} = 0$) in order to get the fully demagnetized magnetic configuration shown in Fig. 5.7.

The initial CCW chirality is evidenced by the CIM direction along the electron flow before applying any gate voltage on ITO electrode (dashed blue arrow on Fig. 5.7a). This time, the CIM direction under the ITO electrode is reversed (red arrow) after the application of a negative gate voltage, as shown in Fig. 5.7b. It is now along the current density, indicating a CW chirality under the ITO electrode. The domains are more densely packed due to the effect of Voltage Control of Magnetic Anisotropy (VCMA), discussed in section 5.2. The decrease of anisotropy due to the voltage application leads to a decrease in the DW energy and thus of the typical domain width [76, 91].

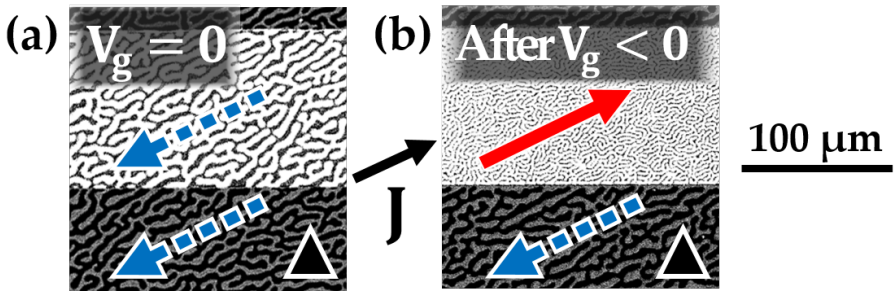

Figure 5.7: **Voltage Control of DW Chirality:** p-MOKE images of the labyrinthine configuration, under zero magnetic field. (a) Starting from a CCW chirality (triangle location in Fig. 5.1a), (b) the application of a negative gate voltage on ITO can lead to a transition towards CW chirality.

5.1.2.1 *Intermediate conclusion*

From each side of the iDMI crossover line (the dashed line on Fig. 5.1a), it is possible to reverse the chirality by applying a gate voltage of appropriate polarity, as schematically represented in Fig. 5.6g. Chirality is switched from CW to CCW (resp. from CCW to CW) with a positive (resp. negative) gate voltage, attributed to reduction (resp. oxidation) of the FeCoB/TaO_x interface. Furthermore, we observed that the reduction of the interface is persistent but reversible whereas the oxidation of the interface is an irreversible effect.

5.1.3 *Fine control of DW chirality*

In the previous section, a gate voltage is applied homogeneously on the ITO electrode, leading to a uniform effective voltage V_{eff} under the ITO, equal to the applied gate voltage, as schematically represented in Fig. 5.8a for a negative gate voltage. As a consequence, the oxidation is homogeneously altered under the ITO, as shown in Fig. 5.8b with the example of a negative gate voltage leading to oxidation of the FeCoB/TaO_x interface[3]. Thus, the iDMI sign is homogeneously reversed leading to the uniform opposite CIM direction under the ITO as shown in Fig. 5.8c. In fact, in the previous section, the current was either applied when the voltage is turned-off (the case of Fig. 5.6 and 5.7) or during a few seconds ($\simeq$ 10 s in Fig. 5.3 and 5.4) in order to determine the chirality of the DWs by recording their CIM direction. Such duration of current pulse is not sufficient to have an effect on the ionic migration induced by the gate voltage.

However, if the current is continuously applied, an additional in-plane gradient of potential will be induced by the voltage from the current source $V_I(x)$. Thus, the bottom electrode presents a gradient of potential and then, the effective voltage accross the sample is gradual from one ITO edge to the other, as shown in Fig. 5.8d. Thus, by judiciously choosing the current and voltage polarities, this highly-tunable configuration allows one to create a iDMI gradient along to the current lines. In Fig. 5.8d-e, we show the example of a negative voltage polarity applied on the ITO together with a positive

3 For clarity we voluntary omit to represent the AlO_x and ZrO_2 layers.

(resp. negative) current polarity on the right (resp. on the left). As a results, there is a larger negative effective voltage on the right part of the ITO than on the left part (see Fig. 5.8d). Then, the FeCoB/TaO_x interface oxidizes faster on the right part than on the left part (see Fig. 5.8e) and the iDMI sign first reverses on the right part, as experimentally observed in 5.8f. Another consequence is the appearance of a $D \simeq 0$ frontier (purple region in Fig. 5.8f), which moves with time depending on the voltage amplitude and polarity.

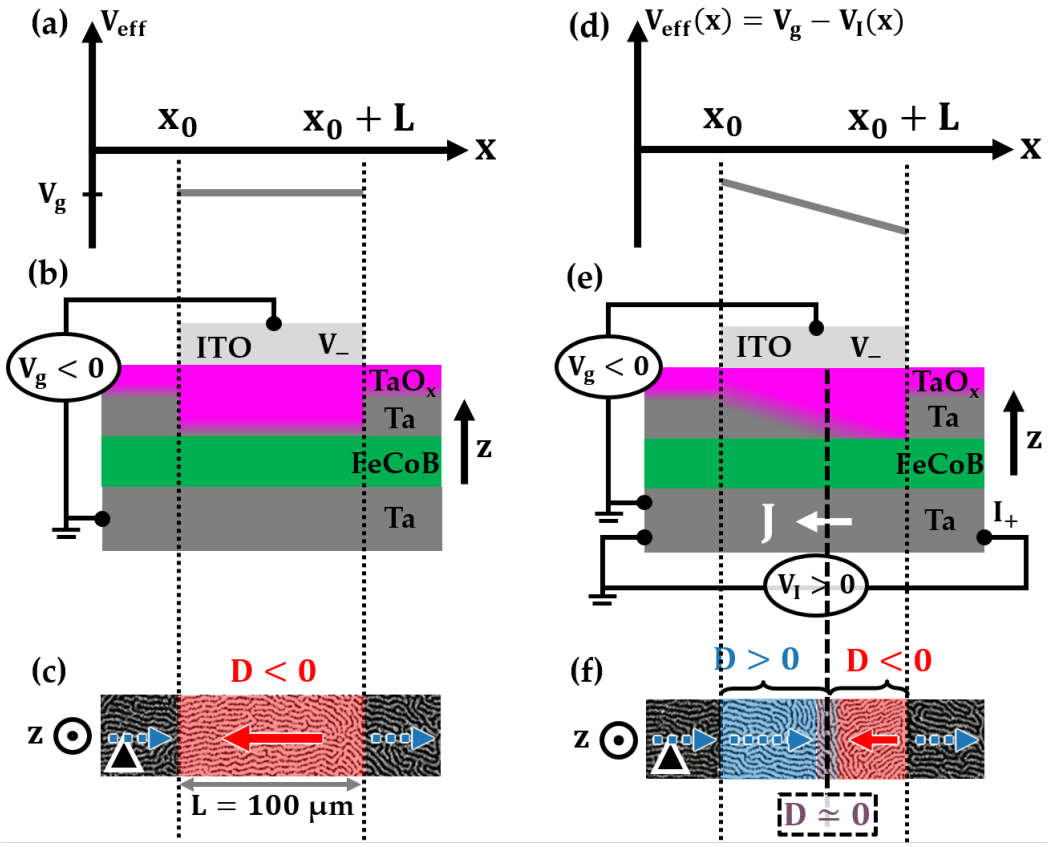

Figure 5.8: **Fine control of DW Chirality:** (a-c) Homogeneous gate voltage application: (a) effective voltage under the ITO electrode for a negative gate voltage. (b) it leads to an homogeneous alteration of the oxidation state under the ITO, (c) inducing the observed uniform inversion of the DWs chirality under the ITO. (d-f) Inhomogeneous gate voltage application: (a) gradual effective voltage under the ITO electrode due to the negative applied gate voltage in addition to the current applied from the right to the left. (b) it leads to an inhomogeneous alteration of the oxidation state under the ITO, (c) inducing the a non-uniform inversion of the DWs chirality under the ITO.

In Fig. 5.9 we show a more complete experiment where the two current electrodes are visible. The ground (resp. the positive) current electrode is in the top left (resp. bottom right) of each p-MOKE images, and the ITO is the rectangular shape in the middle of each image. In this region of the sample, the as-grown iDMI is negative, leading to a motion of DW against the current density as depicted by the dashed blue arrows (same conventions and color code as in the previous sections). Moreover, we can see that the DW motion reveal the current lines, since their motion direction is set by the current direction and the two microbonded wires are visible on these p-MOKE images.

In the initial state, the DWs below and around the ITO move in the same direction, without discontinuity at the electrode edge (Fig. 5.9a). Then, similarly as in Fig. 5.8, we apply a negative gate voltage and a current is continuously applied. We then observe a progressive change, which happens first close to the positive currrent electrode I_+ as shown in Fig. 5.9b. At this location, after 90s of negative gate voltage application, the DWs stop their motion, as represented by a purple color. After 300s of negative gate voltage application, the DW motion direction is reversed as depicted by the red color in Fig. 5.9c. Thus, looking locally, we observe very similar results as in the previous sections 5.1.1 and 5.1.2. However this time, since the voltage is not homogeneous under the ITO, what happens locally do not happens globally.

If we look globally at the entire ITO electrode, we first see the apparition of a region where the DW motion is stopped, located close to the I_+ current electrode as depicted by the purple region in Fig. 5.9b. Then, this region grows and, after 300 s of negative gate voltage application on ITO, we see the apparition of a region where the DW motion is opposite to the initial one, as represented in red in Fig. 5.9c. If we keep applying negative gate voltage, this red region is growing and the purple $D \simeq 0$ frontier propagates perpendicular to the current lines, from the I_+ electrode to the I_- electrode, as shown in Fig. 5.9c-d. Keeping applying negative gate voltage leads to the reversal of the entire electrode. We also observed that the subsequent application of a positive gate voltage leads to the propagation of the purple $D \simeq 0$ frontier in the opposite direction with respect to the negative gate voltage, showing that the effect is partially reversible. However, the purple $D \simeq 0$ frontier stopped at a certain position close to the I_+ current electrode as shown in Fig. 5.9e, and is not evolving further when keeping applying $V_g > 0$. In this region, the negative effective voltage was probably too strong and applied during too much time ($\simeq$ 420 s), leading to irreversibility due to overoxidation. This experiment thus clearly shows that negative gate voltage induces irreversibility in some conditions, depending on the voltage amplitude and the application time. It also confirms some features from the previous section. Notably, in section 5.1.2, we have shown that negative gate voltage induced irreversibility. In addition to the irreversibility, we also observe a modification of the domain size, which we explained in terms of voltage induced modification of magnetic anisotropy (as measured in next section).

It is noteworthy that the position and orientation of the $D \simeq 0$ frontier can be adjusted respectively by the voltage amplitude and the current electrode position. We observed that it is always perpendicular to the current lines and moves in a direction that depends on the voltage polarity.

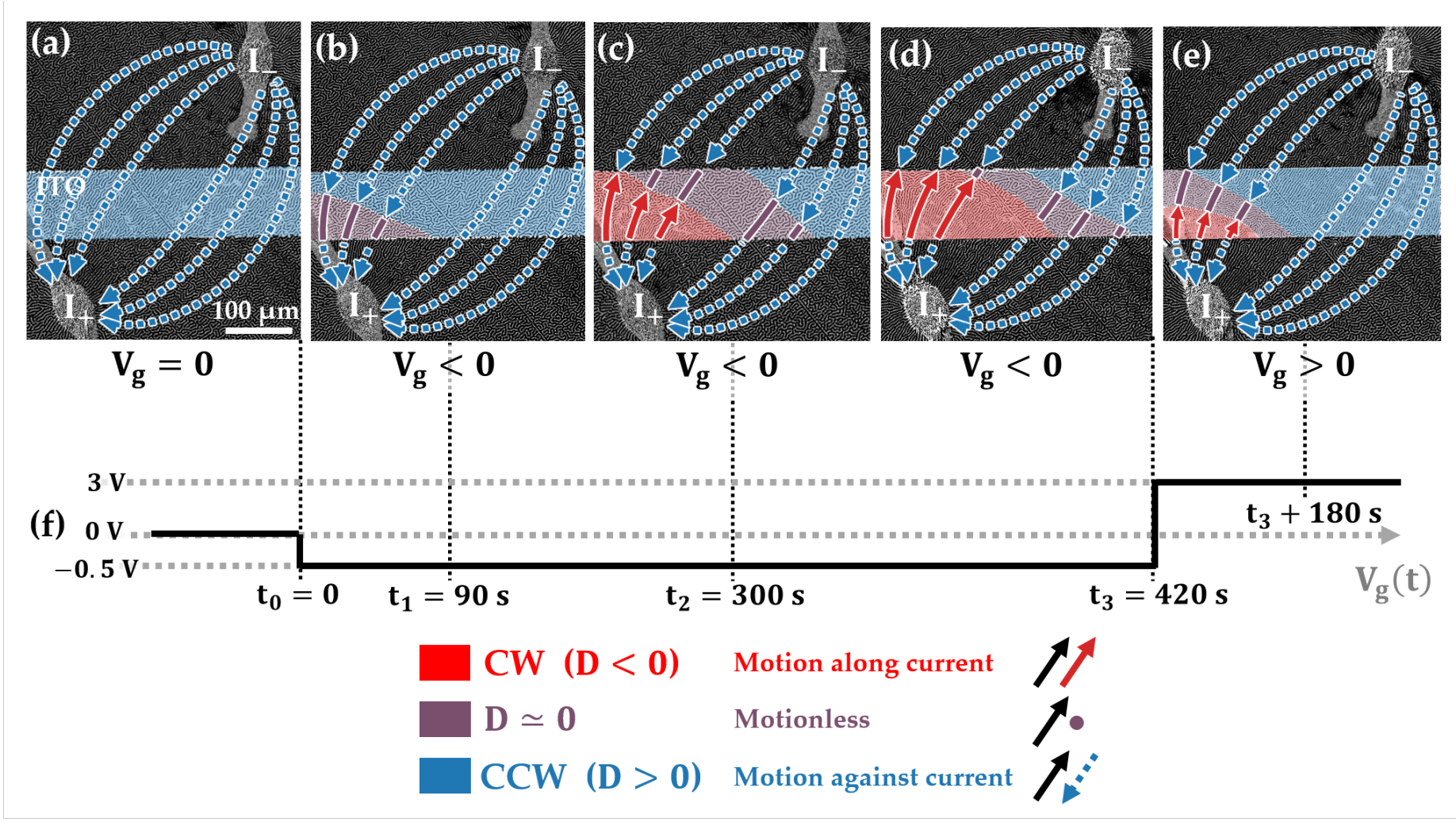

Figure 5.9: **Fine control of DW Chirality:** (a-e) p-MOKE images of labyrinthine micromagnetic configuration, under zero applied magnetic field. In each image, the ITO electrode is the horizontal colored strip in the middle, and the color indicates locally the chirality of the DWs below. The current electrodes are visible at the bottom left (I_+) and at the top right (I_-). The colored arrows follow the current lines, and their color indicates the local chirality : dashed blue means a CCW chirality, solid red means CW chirality. Purple lines means that the DWs are motionless and thus no preferred chirality can be assigned. (a) In the initial state (under $V_g = 0$ V), the DWs are homogeneously CCW under the ITO, while when applying a $V_g < 0$, we observe the progressive apparition of a CW region close to the I_+ electrode, separated from the CCW one by a $D \simeq 0$ frontier in purple. (b)-(d) This frontier can be move, either to the right with $V_g < 0$ or (e) to the left with $V_g > 0$. (f) Schematic timeline of the voltage value.

5.1.4 *Discussion on the chirality reversal induced by gate voltage*

Small iDMI and internal structure of DW

In the previous chapter, we explained the two-fold origin of iDMI from the two FeCoB interfaces of Ta/FeCoB/TaO_x trilayer. In this section, our experiments are done in the region where the contributions from the two interfaces almost cancel each other. Then, iDMI values are very small ($|D| \simeq 10\ \mu J/m^2$) and should result in hybrid Bloch-Néel domain walls, so called intermediate walls (see section 6.1). However, the observed CIM aligned with the current lines is the expected behaviour of Néel DWs. In this regime of low current density, also called pinning regime, the trajectory is highly dependent of the energy landscape. Thus, a skyrmion could move in a direction that is not the one dictated by the SOT, simply because the energy landscape prevents it from doing so and forces it to move through energy valleys. Moreover, we observed in micromagnetic simulations (see chapter 6) that under too high current density, even non Néel type skyrmion can exhibit the trajectory of Néel type skyrmions. Also, there are two opposite Bloch component in non Néel type skyrmion which are energetically degenerated and thermal activation could induced a fast transition between these two component, resulting in a averaged trajectory in which the Bloch contribution vanishes. However, further work is necessary to clearly define what is a "high" current density. In any case, an inversion of the iDMI sign leads to the inversion of the Néel component of the DW, which similarly leads to an inversion of the CIM direction.

Gate voltage application : Ionic migration versus interface charging effect

It has been demonstrated that the perpendicular magnetic anisotropy and the iDMI have common origins, and are thus both sensitive to voltage [95] and oxidation [62]. Then, similarly to voltage control of magnetic anisotropy (VCMA) [85], an applied gate voltage can produce instantaneous reversible charge effects on iDMI [76] or persistent ones linked to ionic migration (see supplementary of reference [76]). In the case of charge effects, the short screening length in metals (shorter than the FeCoB film thickness) would mainly modify charge distribution at the interface with the oxide. The addition of the applied electric field to the Rashba-field could reverse the total interfacial electric field, possibly inducing an inversion of iDMI sign.
Nevertheless, here we have shown that the effect of the gate voltage produces a similar effect as a displacement along the oxidation gradient. This is consistent with ion migration affecting the top FeCoB/TaO_x interface. This ion migration induced by gate voltage may lead to a transition between negative Rashba and positive Fert-Levy contribution to iDMI. As we observed persistent effect on the time scale of minutes, we propose that ionic migration is the dominant mechanism observed in our study. Oxygen ions are most probably the migrating ions, as they are the mobile species in ZrO_2. However, we cannot

exclude the possibility of cation or proton migration [194].

On the applicability of the gate-controlled chirality

Since iDMI may also be tuned by charge effects [76] that occur as sub-nanosecond time scale [197], we may envision an ultra fast switch of skyrmion chirality through a transient Bloch state. Furthermore, contrary to a current polarity inversion, which would invert similarly the motion direction of all skyrmions in the track, a gate voltage would provide a simple and local method to individually control skyrmions. Besides, very recently, design of logic gates based on local chirality control have been proposed [19]. It shows that by controlling locally the skyrmion chirality, it is possible to realize AND, OR, NOT, NAND, NOR, XOR, and XNOR skyrmion-based logic gate devices. Thus, being able to control chirality with a gate voltage offers a new degree of freedom which could be used in reversible and (re)programmable logic gates. In addition, their individual motion tuning can be fully exploited in race logic where information is stored in propagation time [198, 199].
Eventually, due to the persistency of the effect, we may envision their use in artificial neural networks based on cross bar geometries [200] with multiple gates to dynamically and reversibly control the exact path of each input skyrmion. Besides, skyrmion motion along a track could be stopped by a Néel to Bloch transition using a gate voltage. This would enable an alternative realization of a skyrmion transistor hitherto proposed using VCMA [20, 21].

5.2 STABILITY OF SKYRMIONS UNDER CHIRALITY REVERSAL: ANALYTICAL MODEL

As discussed in section 5.1.1, the observed inversion of the skyrmion CIM under the application of a gate voltage is the signature of a transition between CW and CCW Néel skyrmions, which results from a iDMI sign inversion. In principle, this transition is possible without unravelling the spin texture since CW Néel, CCW Néel and the expected intermediate Bloch skyrmion at zero iDMI share the same topology (same skyrmion number, see chapter 1). However, even if this transformation is topologically allowed, it may affect the energetic stability of the skyrmion, in particular the stability of the Bloch skyrmion at zero iDMI. In the absence of stabilization by iDMI energy in thin films, only dipolar energy and out of plane external magnetic field may stabilize Bloch skyrmions [201].
To evaluate the stability of skyrmions during the application of a gate voltage, we have considered an analytical model[4] describing the energy difference between an isolated skyrmion bubble and the uniform magnetic state [91], written as

$$\Delta E_{sb} = 2\pi R t_{FM}\sigma_{DW} + 2\pi R^2 t_{FM}\mu_0 M_S H_{ext} - \pi t_{FM}^3 \mu_0 M_S^2 I(d) \tag{5.1}$$

where σ_{DW} is the domain wall energy, t_{FM} is the ferromagnetic layer thickness, R is the bubble radius, M_S is the saturation magnetization, $\mu_0 H_{ext}$ is the applied magnetic field and $I(d)$ is defined as

4 Developped by Anne Bernand-Mantel and Laurent Ranno from Néel institute.

$$I(d) = -\frac{2}{3\pi} d \left[d^2 + (1-d^2)\,\frac{E(u^2)}{u} - \frac{K(u^2)}{u} \right]$$

where $d = \frac{2R}{t_{FM}}$, $u = \frac{d^2}{1+d^2}$ and $E(u)$, $K(u)$ are elliptic integral defined as

$$E(u) = \int_0^{\pi/2} \sqrt{1 - u\sin^2(\alpha)}\, d\alpha$$
$$K(u) = \int_0^{\pi/2} \frac{d\alpha}{\sqrt{1 - u\sin^2(\alpha)}}$$

In eq. 5.1, the first term is the domain wall energy cost, which contains exchange, anisotropy and iDMI energy energies contributions in $\sigma_{DW} = 4\sqrt{A_{ex}K_{eff}} - \pi D$. The second term corresponds to the Zeeman energy and the last one is the dipolar energy.

5.2.1 *Extraction of the Ta/FeCoB/TaO$_x$ magnetic parameters*

In the following, we first present how we determined the parameters to inject in the model, and we present the corresponding prediction from the analytical model.

Saturation magnetization and magnetically dead-layer thickness:

Due to interface effects, it is common that a part of the nominal ferromagnetic thickness t_{FM}^{nom} is not magnetic (see section 4.2). Thus, the real ferromagnetic thickness is given by $t_{FM} = t_{FM}^{nom} - t_{DL}$ where t_{DL} is the magnetically dead-layer. This parameter, such as the saturation magnetization were extracted via magnetometry (both Superconducting QUantum Interference Device and Vibrating Sample Magnetometers). We consider a magnetic thin film of nominal thickness t_{FM}^{nom}, decomposed in a dead layer of thickness t_{DL} with zero magnetization and a ferromagnetic layer of thickness t_{FM} with magnetization M_S. In this case, the surface magnetic moment is expected to vary as $m_{surf} = M_S(t_{FM}^{nom} - t_{DL})$. Thus, measuring the surface magnetic moment m_{surf} versus t_{FM}^{nom}, gives both the M_S (corresponding to the slope) and the t_{DL} (corresponding to the thickness at which the surface magnetization drops to zero). By doing so we extracted $t_{DL} = 0.61 \pm 0.03$ and $M_S = 1.48 \pm 0.06$ MA.m^{-1}, as shown in Fig. 5.10. In the model we thus injected the measured M_S and since our nominal ferromagnetic thickness is $t_{FM}^{nom} = 1.2$ nm, we considered a ferromagnetic thickness of $t_{FM} = 0.59$ nm to take into account the magnetically dead layer.

Note : Magnetically dead layer and saturation magnetization measurement

These parameters were measured by Hélène Béa at SPINTEC (with VSM) and by Johanna Fischer in Munich (with VSM-SQUID). Both measurements gave very similar results.

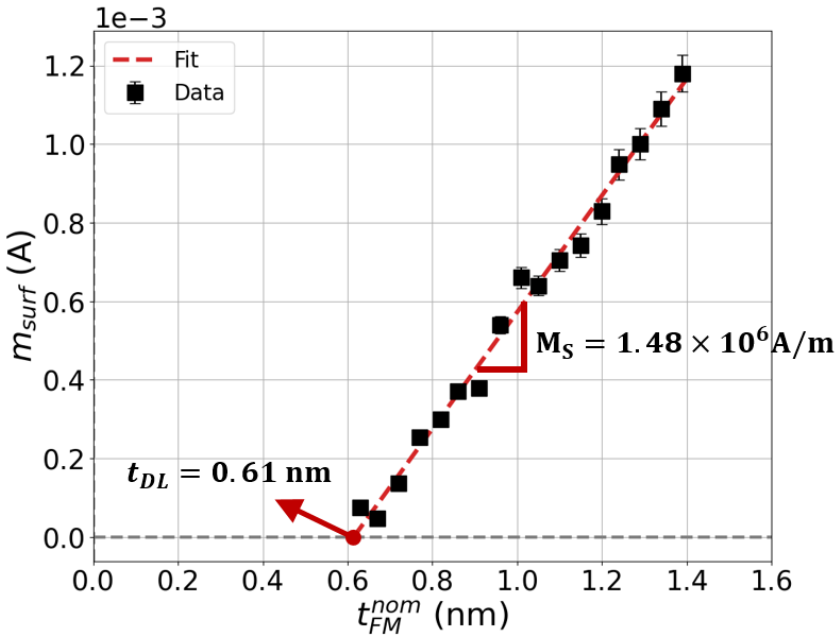

Figure 5.10: **Magnetization and magnetically dead-layer estimation:** Surface magnetic moment versus nominal FeCoB thickness. The slope corresponds to the saturation magnetization and the intercept with the horizontal axis to the magnetically dead layer thickness

Determination of iDMI coefficient:

In section 4.3 we showed that the iDMI depends on the location along the top-Ta wedge. The interpolation of BLS measurement in the region where the chirality inversion has been observed ($t_{Ta} \simeq 0.92$ nm corresponding to the star location in Fig. 5.1a) leads to a typical order of magnitude for the iDMI coefficient $|D| \simeq 10$ μJ/m^2. Thus, in our calculation, the iDMI sign is inverted from -10 to 10 μJ/m^2, through a transient $D = 0$ step that is interesting to take into account for the study of the skyrmion stability.

Anistropy measurements:

The effective magnetic anisotropy and its variation under a gate voltage were measured through hard axis hysteresis loop with the p-MOKE microscope. The data were fitted to a model in which we consider an applied magnetic field H_{ext} inclined by an angle Ψ with respect to the magnetic layer plane, which is the magnetization hard-plane (see Fig. 5.11a). Thus, the magnetic energy density can be written as :

$$E = K_{eff} \sin^2\theta - \mu_0 H_{ext} M_S \sin(\theta + \Psi)$$

The first term corresponds to the uniaxial anisotropy energy and the second to the Zeeman energy. The parameter $K_{eff} = \frac{K_s}{t_{FM}} - K_d$ is the effective anisotropy constant, where K_S is the interface anisotropy constant and $K_d = \frac{1}{2}\mu_0 M_S^2$ is the shape anisotropy constant. $\mu_0 H_{ext}$ is the applied field and θ the angle between the magnetization and the easy axis (see Fig.

5.11a). Then, we can obtain the equilibrium position by differentiating with respect to θ. Finally, as the MOKE microscope in the polar geometry is only sensitive to $m_z = \cos\theta$ (z-component of the normalized magnetization vector $\frac{\vec{M}}{M_S}$), we can write the sine and cosine in terms of m_z, leading to

$$\mu_0 H_{ext} = \mu_0 H_K \frac{m_z\sqrt{1-m_z^2}}{m_z\cos\alpha - \sin\alpha\sqrt{1-m_z^2}} \tag{5.2}$$

where $\mu_0 H_K = \frac{2K_{eff}}{M_S}$ is the anisotropy field which can be extracted by fitting this implicit equation to the experimental hard axis hysteresis curves, in their implicit form $\mu_0 H_{ext}(m_z)$. Examples of such fit are given in Fig. 5.11(c,d).

Skyrmions are observed for ferromagnetic thickness close to a spin reorientation from PMA to IPA. In this region, the zero remanent magnetization, induced by the weak effective anisotropy, makes it difficult to use this model directly for skyrmions. However, we can take advantage of the wedge of ferromagnet to extrapolate from a region where this model is valid. For thinner ferromagnetic thickness the effective anisotropy increases since we move away from the PMA-IPA transition, and the model becomes valid when remanent magnetization is not zero.

We thus did a series of measurements on ITO electrodes, for both zero and positive gate voltages, as a function of the FeCoB thickness in order to extrapolate the value of H_K to the FM thickness where skyrmions are observed 5.11b. Typical raw data and their fits with the model are shown for thinner and thicker FeCoB (resp. Fig. 5.11c and Fig. 5.11d).

A linear behaviour of H_K versus t_{FeCoB}^{nom} is observed for both $V_g = 0$ and $V_g > 0$, which allowed us to extrapolate the anisotropy fields and VCMA to the thickness at which we observe skyrmions (as shown in Fig. 5.11e). The presence of errobars on $\mu_0 H_K$ induces a variability on the fit slopes, and we have considered the largest VCMA for skyrmions in the calculations. This is the least favorable case in terms of skyrmion stability and this upper limit ensures their stability even for large anisotropy variation. Thus, for skyrmions in our trilayer, the anisotropy field varies from 40 to 24 mT, when applying a positive gate voltage ($V_g = 6$ V), corresponding to a decrease of about $\mu_0 \Delta H_K = 16$ mT. It leads to a weak 1% variation of K_S from 0.83 to 0.82 mJ/m^2. Moreover, the magnetization variation under gate voltage can be determined with the Kerr signal amplitude variation. In Fig. 5.11c and 5.11d, the Kerr signal is represented on a normalized scale on the left part and on a non normalized scale on the right part. Thus, we can see that the amplitude of the hysteresis loop is not altered by the gate voltage application. Consequently, in the model we neglected the variation of the saturation magnetization. Finally, the exchange stiffness was fixed to $A_{ex} = 12$ pJ/m [76] and an external magnetic field $\mu_0 H_{ext} = -750$ μT was set in a direction opposite to the magnetization in the core of the skyrmion (destabilizing field).

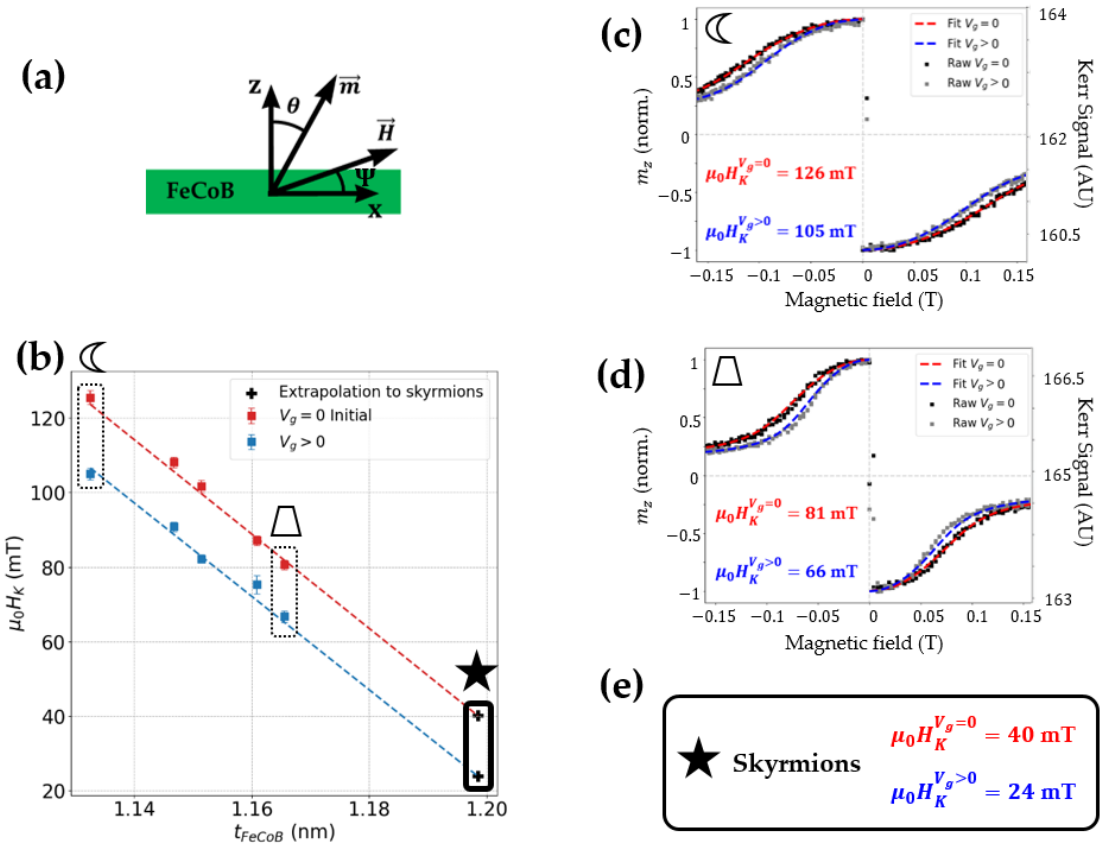

Figure 5.11: **Variation of the magnetic anisotropy under gate voltage:** (a) Geometry considered in our energetic model. (b) Anisotropy fields measured at $V_g = 0$ (red data points) and $V_g > 0$ (blue data points). It is possible to extrapolate values for skyrmions, as depicted by the dashed lines and the "+" symbols. (c,d) Raw data and their fit respectively for thinner and thicker FeCoB thickness. (e) An extrapolation at the FeCoB thickness at which skyrmions are observed allows to extract the values of anisotropy field and its variation under gate voltage in the region of interest.

5.2.2 *Model prediction*

Then, we injected these parameters and their variation under gate voltage (see Fig. 5.12a) in the analytical model, resulting in the three curves shown in Fig. 5.12b, where equation 5.1 is plotted versus the skyrmion radius. Indeed, the chirality inversion due to the gate voltage can be simulated as the transition between an initial state with $D < 0$ to a final state with $D > 0$ via a transient state at $D = 0$. In addition, the anisotropy is varied linearly with respect to the iDMI value, *ie* starting from the initial $\mu_0 H_K = 40$ mT at $D < 0$, we decrease the anisotropy by $\frac{\mu_0 \Delta H_K}{2}$ at $D = 0$ and by $\mu_0 \Delta H_K$ at $D > 0$, as it is summarized in Fig. 5.11b. The solid red, dashed purple and dash-dotted blue curves correspond respectively to the model prediction in the initial, transient and final state as defined in Fig. 5.11a.

(a)

M_S (A/m)		1.48×10^6
t_{DL} (nm)		0.61
$t_{FM} = t_{FM}^{nom} - t_{DL}$ (nm)		0.59
A_{ex} (pJ/m)		12
$\mu_0 H_{ext}^z$ (μT)		−750
$\mu_0 \Delta H_K$ (mT)		16
ΔK_S (μJ/m²)		10
D (μJ/m²)	★	−10
	✖	0
	▲	10
$\mu_0 H_K$ (mT)	★	40
	✖	$40 - \frac{\mu_0 \Delta H_K}{2}$
	▲	$40 - \mu_0 \Delta H_K$
K_S (mJ/m²)	★	0.83
	✖	$0.83 - \frac{\Delta K_S}{2}$
	▲	$0.83 - \Delta K_S$

(b)

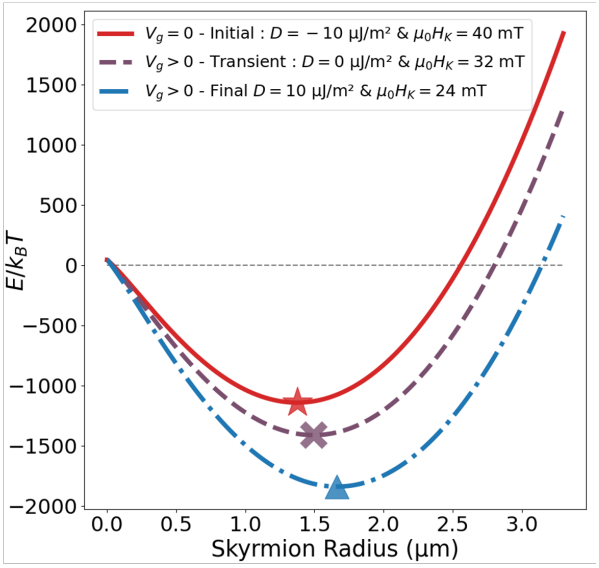

Figure 5.12: **Analytical model[91]: stability of skyrmions in FeCoB during iDMI inversion induced by the gate voltage:** Analytical calculation of energy difference (in units of $k_B T_{300K}$) between skyrmion and uniform state for FeCoB as a function of skyrmion radius. Solid red, dashed purple and dash-dotted blue curves correspond respectively to negative, zero and positive iDMI, associated to a progressive anisotropy variation under gate voltage, as experimentally measured. Due to the small iDMI value in FeCoB, the slight change of equilibrium radius (depicted by symbols) is mostly due to the anisotropy variation.

The model predicts that for both non-zero and zero iDMI, a skyrmion is stable for diameters around 1.5 μm, close to the experimental values (see Fig. 5.12). Only a slight change of equilibrium diameter is expected, mostly due to the anisotropy variations under gate voltage, since our relatively small iDMI values contribute little to the total energy of the skyrmion. According to the model, it should be possible to reverse the chirality of a single skyrmion without annihilating it.

Discussion

One must notice that this model is valid for $Q = \frac{K_u}{K_d} > 1$, where $K_u = \frac{K_s}{t_{FM}}$ is the uniaxial anistropy and $K_d = \frac{1}{2}\mu_0 M_s^2$ is the shape anisotropy constant. In our case, we can extract from experimental parameters $Q = 1.02$, lying in the area of validity of the model.
We also considered the case of an increase of anisotropy by the amount ΔH_K (not shown here). This time the radius is decreasing, which is still mostly due to the anisotropy variation. Finally, we computed the case where only the iDMI varies from -10 to 10 μJ/m^2 with no anisotropy variation. In this case the three curves almost superimpose the one on the other, showing that such small iDMI does not contribute consequently to the total energy of the skyrmion.

5.3 CONCLUSION

We have demonstrated a gate-voltage induced reversal of skyrmion chirality in Ta/FeCoB/TaO_x system through the inversion of their current induced motion direction. Besides, we also observed a local, persistent and reversible chirality reversal of labyrinthine chiral domain walls by gate voltage. On the one hand we have shown that the application of an homogeneous gate voltage leads to a uniform chirality reversal under the electrode. On the other hand, by applying a gradient of electric field under the electrode we were able to create a gradient of iDMI under the electrode, enabling a very fine control of the DW motion at a given position. These reversals are due to an inversion of the iDMI sign and explained by the gate-controlled modification of the oxidation state at the ferromagnet/oxide interface (see Fig. 5.13). Analytical calculations support the feasibility of a chirality reversal for skyrmions without annihilation. Such local and dynamical degree of freedom at the nanometer scale would lay the foundations for efficient and multifunctional architectures involving magnetic skyrmions as information carriers [179].

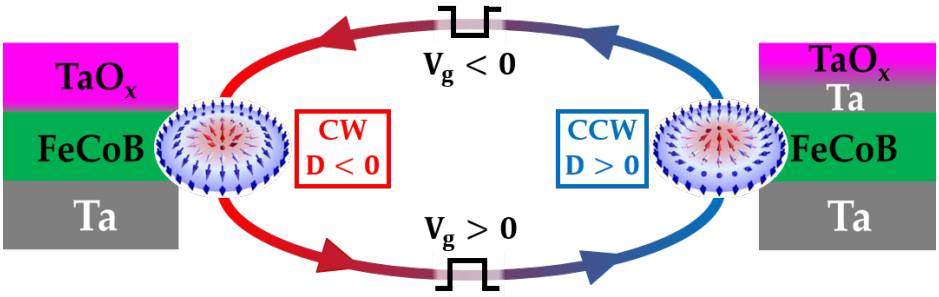

Figure 5.13: **Gate-controlled chirality:** Summary of the experimental observation. Regardless of the initial chirality, it can be reversed by a gate voltage with the appropriate polarity. It is explained in terms of interface oxidation ($V_g < 0$) or reduction ($V_g > 0$) which induces an inversion of the iDMI sign.

Our experimental observations motivated a deeper study of the skyrmion chirality inversion. We have seen that a control of the iDMI sign enables to control the chirality of domain wall and thus their direction of motion driven by SOT. We may wonder what happens to the skyrmion DW internal structure and its SOT driven motion if we refine the control to the iDMI amplitude. In the next chapter, we propose a more thorough study of the static and dynamic properties of skyrmions as a function of the iDMI amplitude and sign.

6

STATIC AND DYNAMIC PROPERTIES OF SKYRMIONS IN LOW IDMI SYSTEMS

In the previous section we have shown experimentally the close relationship between the static and dynamic properties of skyrmions and chiral DW in our low iDMI systems. We have shown that material parameters and gate voltage can invert the iDMI sign and DW chirality. To show this, we used the link between the DW chirality and their motion and their motion driven by spin-orbit torques. These experiments show the link between the internal structure of the DW and the dynamics of the spin texture. In this chapter, I study this link more thoroughly with a numerical and analytical study of the static and dynamic properties of skyrmions under a very fine tuning of iDMI.

In a first section, I show that a fine control of the iDMI amplitude and sign enables a fine tuning of the DW internal structure. I unveil the role of iDMI versus magnetic volume charges in the stabilization of the DW structure through a simple analytical model based on the DW energy.

In a second section, I show that such fine tuning of DW internal structure enables a precise control of the skyrmion trajectory under spin orbit torques. The developed model, based on Thiele equation, shows a good agreement with the micromagnetic simulations.

6.1 EQUILIBRIUM DOMAIN WALL HELICITY IN LOW IDMI SYSTEMS

In the absence of iDMI in magnetic thin films with PMA, the minimization of volume magnetic charges leads to the stabilization of non-homochiral Bloch-type DWs. As in the previous chapter, we define the helicity ξ as the angle between the normal to the DW and the magnetic moments inside it (see Fig. 6.1). Thus, the internal structure of a Bloch DW is defined by an helicity $\xi = \pm\frac{\pi}{2}$, as shown in Fig. 6.1a. On the other hand, it is generally considered that adding iDMI in these systems stabilizes homochiral Néel DWs whose chirality is given by the sign of the iDMI coefficient D. Néel DWs are defined by $\xi = 0$ if the chirality is CW ($D < 0$) or $\xi = \pi$ if the chirality is CCW ($D > 0$). In Fig. 6.1c we give the example of a DW with a CW chirality.

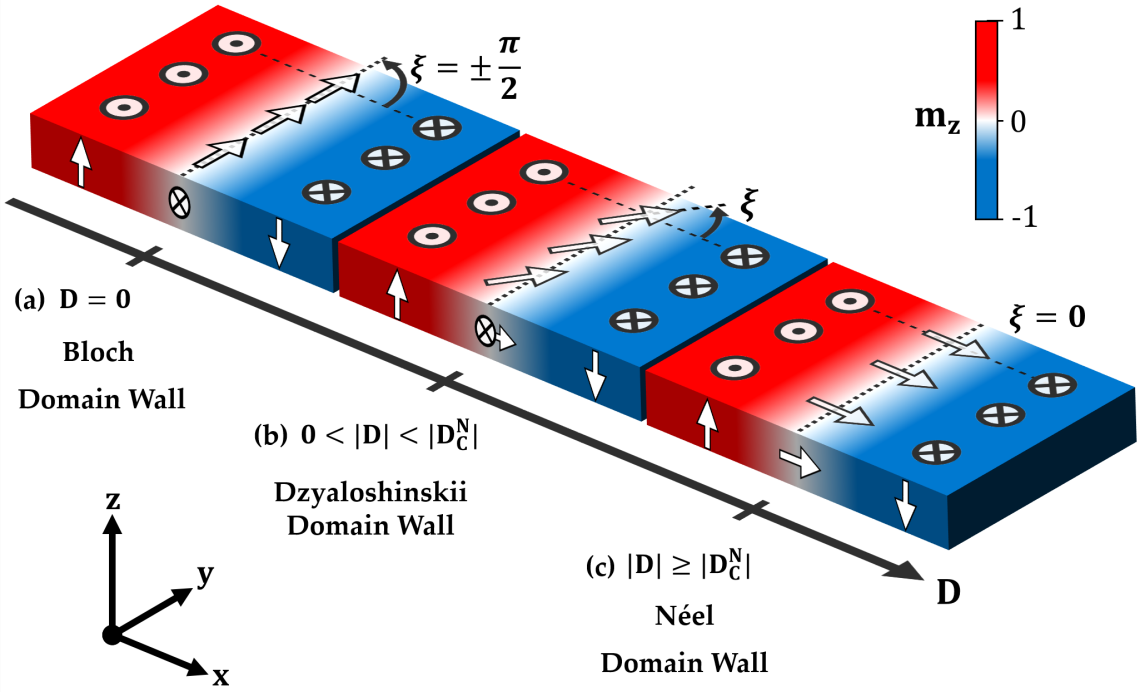

Figure 6.1: **Magnetic domain wall in the presence of iDMI:** (a) In the absence of iDMI, non-homochiral Bloch DW are stabilized, defined by an helicity $\xi = \pm\frac{\pi}{2}$ (b) for low iDMI coefficient, intermediate DW internal structure are stabilized, so called Dzyaloshinskii DW and (c) at a certain critical iDMI value, D_C^N, the DW are purely Néel type.

However it is important to remember that pure Néel DWs are stabilized only if the amplitude of the iDMI coefficient overcomes a critical value, that we call D_C^N in the following. For iDMI coefficient smaller than D_C^N, intermediate DW internal structure is stabilized, between Bloch and Néel configuration, known as Dzyaloshinskii wall [97] (Fig. 6.1b). In the following, we define the "low iDMI" as the range $|D| < |D_C^N|$, where DW with intermediate helicities are more favorable[1]. More especially, skyrmions with hybrid Néel-Bloch DWs, also called "twisted skyrmions" [202–204] can be stabilized, as experimentally observed at

1 which is probably the case in our sample in which the iDMI coefficient, measured by BLS, are very small, about $|D| = 10\ \mu J/m^2$

the surface of helimagnet with bulk-DMI [202] and in Pt/Co/Ir- and Pt/Co/AlO_x-based multilayers with PMA and interfacial DMI [205]. In this chapter, I propose a theoretical study of their static and dynamic properties, through micromagnetic simulations and analytical model.

6.1.1 *Micromagnetic simulations*

Using micromagnetic simulations under the Mumax[3] software package, we propose to show in this section the effect of iDMI tuning on the skyrmion spin texture. More precisely, we describe the skyrmion by its structural characteristics, *i.e.* by its radius R, its DW width δ_{DW} , and helicity ξ. The magnetic parameters chosen for these simulations allow to stabilize nanometer size magnetic skyrmions, more relevant for application and more adapted to micromagnetic simulations since they require a reasonable number of cells. More precisely, we optimized Co-based magnetic parameters (extracted from reference [153]) in order to stabilize a Bloch skyrmion at $D = 0$. We found that Bloch skyrmion stabilization is possible with a fine tuning of the uniaxial anisotropy K_u, in order to decrease the cost in DW energy when the iDMI goes to zero. Thus, Bloch skyrmions can be stabilized for quality factor $Q = \frac{K_u}{K_d} \simeq 1$, *i.e.* close to an in-plane spin reorientation. In our simulations, the quality factor is about $Q = 1.0024$. It is also possible to stabilize the Bloch skyrmion with larger Q factors with the counterpart of a decrease in the size of the skyrmion, requiring to refine the mesh and thus increasing the computation time. We thus used optimized Co-based parameters, enabling to stabilize a Bloch skyrmion at zero iDMI, not too small in order to gain in computation time. The value of the damping parameter $\alpha = 0.5$ has also been chosen in order to optimize the convergence time. The simulation region is a 512 nm square, with a mesh size of 1 nm $\times$ 1 nm $\times$ 0.9 nm. We have used Periodic Boundary Condition (PBC) in order to anticipate current injection and to consider the presence of magnetic material around the simulation region. The 10 repetitions for the periodic boundary conditions have been shown to be the best compromise between computation time and proper consideration of the dipolar effects [206]. A summary of the parameters used in the simulation can be found in table 6.1.

Number of Cells	(N_x, N_y, N_z)	$(512, 512, 1)$ cells
Size	(L_x, L_y, t)	$(512, 512, 0.9)$ nm
Periodic Boundary Conditions	(N_x, N_y, N_z)	$(10, 10, 0)$
Temperature	T	0 K
Magnetic damping	α	0.5
External magnetic field	$\mu_0 H_{ext}$	-6 mT
Magnetization	M_S	1.42×10^6 A/m
Exchange stiffness	A_{ex}	1.6×10^{-11} J/m
Uniaxial Anisotropy	K_u	1.27×10^6 J/m^3
Interfacial DMI	D	$\in [-0.5; 0.5]$ mJ/m^2

Table 6.1: Co-based material parameters [153] used in the micromagnetic simulations

For a set of iDMI coefficients in the range $D \in [-0.5; 0.5]$ mJ/m^2, we stabilized a skyrmion spin texture and we extracted from its structural characteristics (R, δ_{DW}, ξ).
Before starting the analysis of the simulation result, let us quickly present how the data is organized in this section. One the one hand, Fig. 6.2 presents the analysis of the simulation data, and shows the skyrmion helicity (Fig. 6.2a), radius (Fig. 6.2b) and DW width (Fig. 6.2c) as a function of the iDMI value. On the other hand, for clarity and in order to easily visualize the results, we show in Fig. 6.3 the skyrmion micromagnetic configuration corresponding to some data points from from Fig. 6.2, surrounded by colored symbol. More details about the extraction of skyrmion structural parameters are given in note page 131.

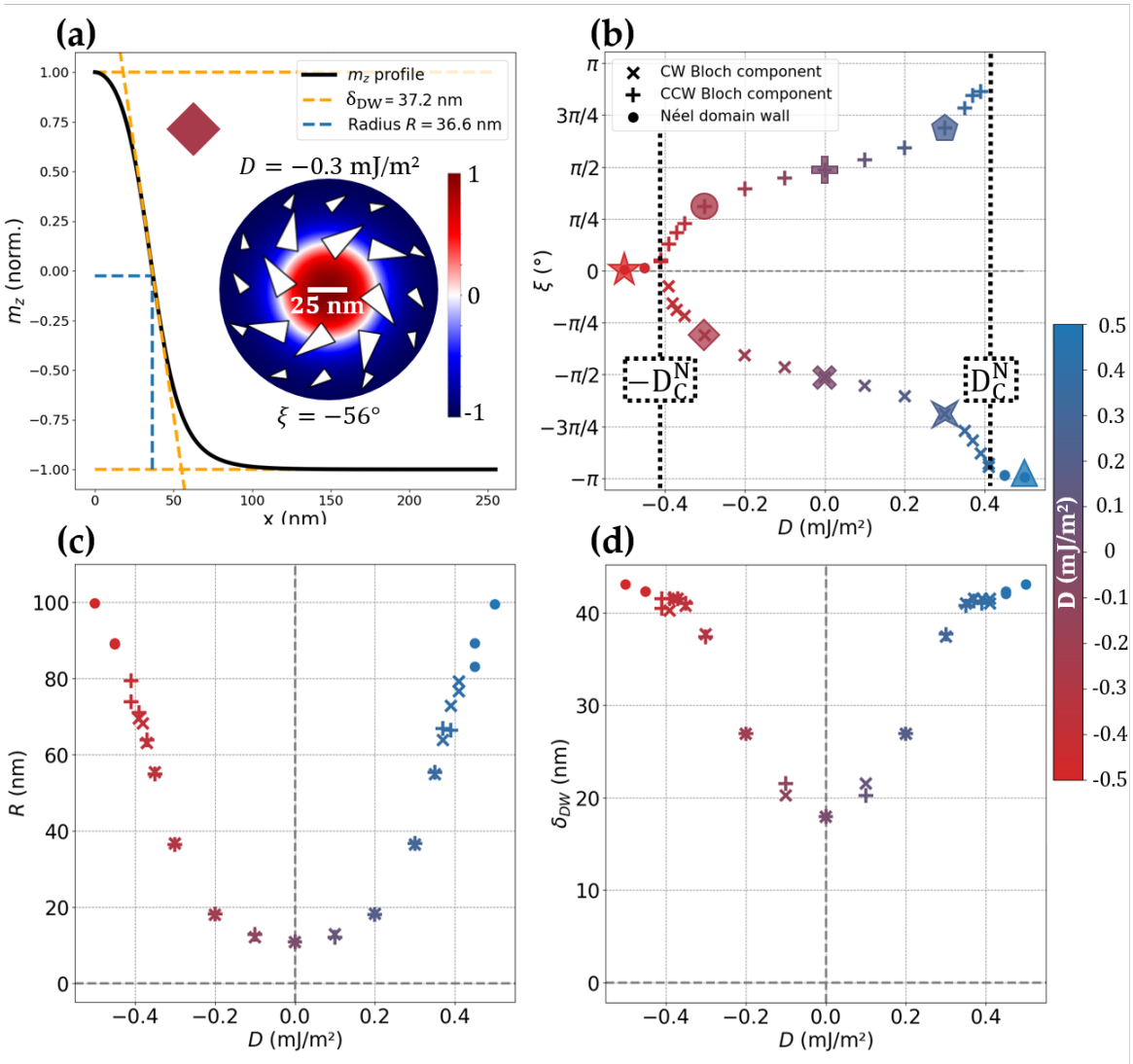

Figure 6.2: **Skyrmion structural characteristics as a function of the iDMI value - Simulations:** Evolution of the skyrmion (a) helicity, (b) radius and (c) DW width as a function of the iDMI coefficient. (d) m_z profile and magnetic configuration (inset) of the skyrmion corresponding to the burgundy diamond in (a). The radius is taken where $m_z = 0$ (dashed blue line) and the DW width determined by the tangent method (dashed yellow lines).

Note : Extraction of skyrmion structural characteristics

The skyrmion structural parameters are extracted from the micromagnetic configurations resulting from simulations. In Fig. 6.2a, we show an example of skyrmion m_z profile (depicted by the black curve), corresponding to the data point surrounded by the diamond symbol in Fig. 6.2b. The m_z profile is taken from the skyrmion center in $x = 0$ to the border of the simulation region in $x = 256$ nm. The radius R is extracted from the point at which $m_z = 0$ (dashed blue lines) and δ_{DW} from the tangent method (dashed yellow lines). Finally, the helicity is extracted via the in plane component (m_x, m_y) in the middle of the DW (white arrow in the inset of Fig. 6.2a).

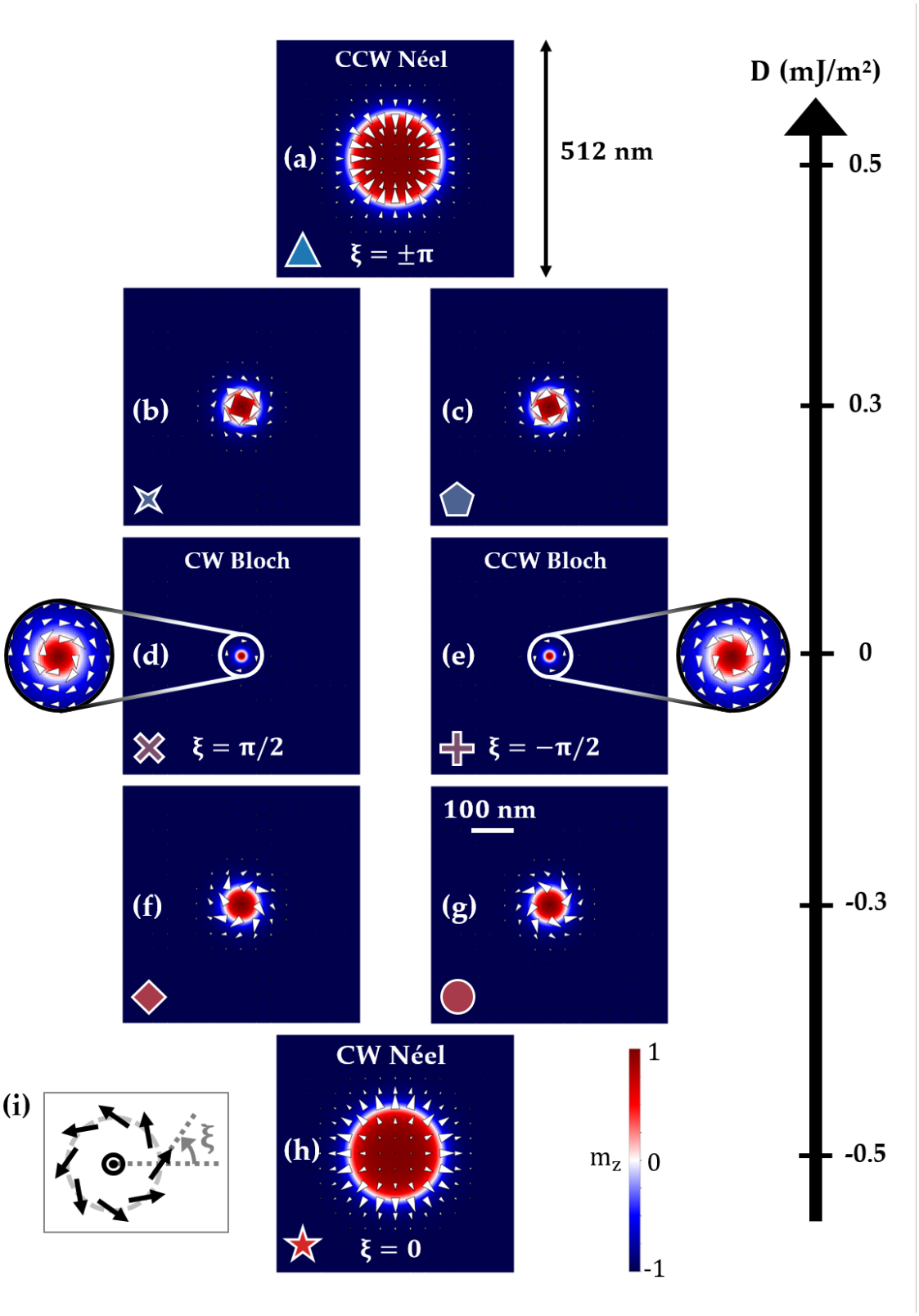

Figure 6.3: **Skyrmion spin texture versus iDMI value:** (a-h) Skyrmion micromagnetic configuration extracted from simulations for some relevant iDMI values (m_z mappings in which the in-plane moments are represented by white arrows). The continuous transformation between CW and CCW Néel skyrmion can follow two degenerate routes. The spin texture evolution is accompanied by a significant radius variation. (i) Definition of the helicity: angle between the magnetic moments in the DW and the normal to the DW.

First we discuss the effect of an iDMI modulation on the skyrmion helicity shown in Fig. 6.2b with some corresponding spin textures in Fig. 6.3(a-h). As explained previously, Néel DWs and thus Néel skyrmions are stabilized only at large iDMI, as shown in 6.2b. The Néel skyrmion is CCW for positive iDMI value, thus characterized by[2] $\xi = \pm\pi$ (blue triangle in Fig. 6.2b corresponding to Fig. 6.3a), and CW for negative iDMI value, characterized by $\xi = 0$ (red star in Fig. 6.2b corresponding to Fig. 6.3h). These Néel skyrmions are observed for iDMI value larger than an critical iDMI value $|D_C^N| \simeq 0.41$ mJ/m². Thus two regimes clearly appears, separated by D_C^N, one being called in the following the "large iDMI regime" (described above) for $|D| > |D_C^N|$ and the other the "low iDMI regime" for $|D| < |D_C^N|$, that we describe below.
In the low iDMI regime, for $|D| < |D_C^N|$, the DW is of intermediate type, so-called Dzyaloshinskii walls and leading to twisted skyrmions. In other words, it has a Néel component fixed by the iDMI sign, in addition to a Bloch component, which can be either CW (characterized by $\xi < 0$ and "$\times$" symbols in Fig. 6.2, and corresponding to the left column in Fig. 6.3), or CCW (characterized by $\xi > 0$ and "+" symbols in Fig. 6.2 and corresponding to the right column in Fig. 6.3). Two skyrmions, stabilized with the same material parameters and having opposite Bloch components (for example Fig. 6.3(b,c) or Fig. 6.3(d,e) or Fig. 6.3(f,g)) are energetically degenerated. The iDMI sets the Néel component but nothing favors one Bloch component over the opposite one. Consequently, the transition between CW Néel and CCW Néel due to a progressive iDMI change is a continuous transformation in which (i) the skyrmion is conserved and (ii) the helicity evolves continuously from $\xi = 0$ to $\xi = \pm\pi$, following two possible channels, that are energetically degenerated : either the DW has a CW Bloch component, either it has a CCW Bloch component when the iDMI is decreased. It is noteworthy to notice that even at zero iDMI, a nanometer size Bloch skyrmion can be stabilized. In absence of stabilization by iDMI energy, stabilizing such a small spin texture only by dipolar energy is far from straightforward [201].

A fine tuning of the iDMI not only affects the skyrmion helicity. We also observed significant change in the skyrmion radius of about one order of magnitude, as shown in Fig. 6.3 and shown in Fig. 6.2c. It is around $R \simeq 100$ nm for $D = \pm 0.5$ mJ/m² while it decreases to $R \simeq 10$ nm for $D = 0$. Such drastic variation of the skyrmion radius versus iDMI coefficient can be explained by the contribution to iDMI to the DW energy (as shown in the model in the next section and explained in Sec. 2.1 from chapter 2). At large iDMI the radius evolves roughly linearly with respect to D, which is predicted in the literature [124]. Finally, the small deviation from linearity at large iDMI might be due to edge effect since the skyrmion size becomes significant compared to the simulation region. The skyrmion is not isolated anymore and starts thus to interact with the neighbouring one (let's remind that we have 10 repetition in the (x,y) plane due to the PBC), limiting its growth.

2 It is noteworthy that our definition of the helicity is appropriate to skyrmions with a polarity $p = 1$, *i.e.* with a core magnetization pointing in the $+z$ direction. Indeed, for a given helicity, inverting the polarity inverts the chirality of the skyrmion. If $p = -1$, one has to add π to the helicity defined here to keep the same conventions. In our simulations, the polarity remains $p = 1$ so that our definition of the helicity remains valid.

Similar changes in the DW width were observed in the simulations as shown in 6.2d. It decreases by more than a factor of 2 when the iDMI is decreased down to zero. The variation of the DW width is linked to the variation of volume magnetic charges when ξ is varying, although a clear picture of this behaviour still needs to be found. Moreover, it seems that for $|D| > |D_C^N|$, the DW width reaches a plateau or, at least, evolves much more slowly with respect to D.

6.1.2 *Analytical model*

In this part, I develop a model based on the DW energy which allows to understand the underlying physics of what was observed in the simulations.
First, let us establish the expression of the DW surface energy density. In the absence of iDMI, the energy of the Bloch DW is given in the limit of ultrathin films[3] by $\sigma_{DW} = 4\sqrt{A_{ex}K_0}$, where $K_0 = K_u - K_d$ with K_u the uniaxial anisotropy and $K_d = \frac{1}{2}\mu_0 M_S^2$ the contribution from the dipolar energy. Adding iDMI to the systems leads to the addition of two competing terms in the surface energy density, that will set the equilibrium DW helicity.
On the one hand, the iDMI favors non collinear spins with Néel rotation and thus changes σ_{DW} by an amount $\pi D \cos\xi$ (see Annex 8.3). Thus, if we consider only the iDMI contribution, the minimization of $\sigma_{DW} = 4\sqrt{A_{ex}K_0} + \pi D \cos\xi$ would always lead to Néel type DW, *i.e.* $\xi = 0 + n\pi$ ($n \in \mathbb{Z}$), whatever the amplitude of the iDMI coefficient, which is not the case in low iDMI systems, as shown in the simulations of the previous section.
On the other hand, magnetic volume charges are created by the Néel component of the DW, and are very often neglected in the literature [124], which is no longer possible for the low iDMI systems. These magnetic volume charges act as an additional anisotropy term which favors Bloch DW type. Their contribution to the effective anisotropy can be estimated to $K_d^V \cos^2\xi$ [207], where $K_d^V = \frac{1}{2}\mu_0 N_{xx} M_S^2$ with N_{xx} the demagnetizing factor, estimated to $\frac{t \ln 2}{\delta_{DW}}$ in thin films geometry [208].
Thus, with this model, the equilibrium helicity of the DW is the result of the competition between iDMI and magnetic volume charges in the DW surface energy density :

$$\sigma_{DW} = 4\sqrt{A_{ex}\left(K_0 + K_d^V \cos^2\xi\right)} + \pi D \cos\xi \tag{6.1}$$

where we can define $K_{eff} = K_0 + K_d^V \cos^2\xi$ as the effective anisotropy in the presence of iDMI. Minimization with respect to ξ gives the expression of the equilibrium helicity versus the iDMI value, as well as the critical iDMI value at which the DW is pure Néel

$$\xi(D) = \pm\cos^{-1}\left(-\pi D\sqrt{\frac{K_0/K_d^V}{16A_{ex}K_d^V - \pi^2 D^2}}\right) \tag{6.2}$$

$$\xi(D_C^N) = 0 + n\pi \iff |D_C^N| = \frac{4}{\pi}\sqrt{\frac{A_{ex}K_d^V}{1 + K_0/K_d^V}} \tag{6.3}$$

3 $t \ll \delta_{DW}$, where t is the film thickness and δ_{DW} is the DW width, see Annex 8.3

The "±" sign in eq. 6.2 stands for the two degenerate Bloch component in the low iDMI regime ("-" corresponds to CW Bloch component and "+" to CCW Bloch component). This expression is plotted in Fig. 6.4a as a function of the reduced iDMI coefficient D/D_C^N. By integrating σ_{DW} over the skyrmion surface, it is possible to compare it to the the thermal energy k_BT. For this, we considered a skyrmion of intermediate radius $R = 50$ nm, and we define $\sigma = \sigma_{DW} * 2\pi R t_{FM}$ where $2\pi R t_{FM}$ is the DW surface. In Fig. 6.4b we show σ/k_BT for some relevant reduced iDMI coefficient. The symbols on the curves in Fig. 6.4a correspond to the energy minima in Fig. 6.4b and for each of them, the corresponding skyrmion configuration is given in Fig. 6.4c. It is important to notice that in the model, contrary to the simulations, we do not take into account the variation of the skyrmion size when varying iDMI and thus the helicity, which is an ongoing work not presented here.

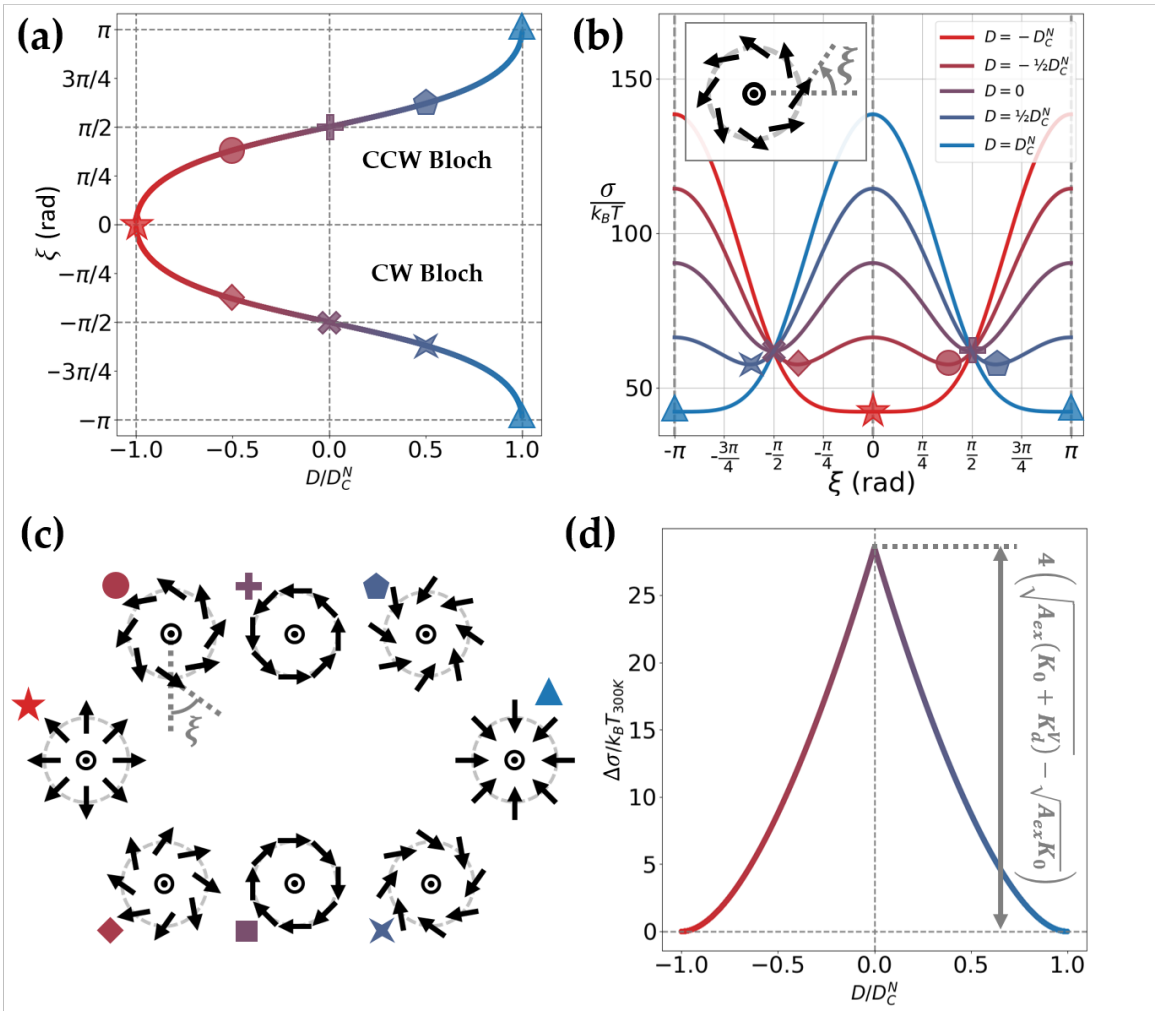

Figure 6.4: **Skyrmion structural characteristics as a function of the iDMI value - Analytical model:** (a) Domain wall energy versus helicity for several values of iDMI coefficient, in units of D_C^N. (b) Helicity versus iDMI coefficient, obtained from the minimization of σ_{DW} with respect to ξ. For $|D| \geq |D_C^N|$ a unique helicity, set by the sign of D, is solution. For $|D| < |D_C^N|$, two solutions are energetically degenerate, corresponding to the two Bloch chiralities defined by $\pm\xi$, as schematically represented (d). (c) Energy barrier (in units of k_BT) between the two degenerate Bloch states for $|D| < |D_C^N|$.

From Fig. 6.4, two regimes appear, as a function of the iDMI amplitude: On the one hand, for $|D| \geq |D_C^N|$, the iDMI contribution in σ_{DW} overcomes the magnetic volume charges and there is only one minimum, which corresponds to the unique Néel chirality favored by the iDMI sign. For example for $|D| \geq |D_C^N|$ and $D < 0$, the minimum is in $\xi = 0$ which corresponds to Néel with a CW chirality (red star in Fig. 6.4(a,b)), while for $D > 0$, the minima is in $\xi = \pm\pi$ which corresponds to a Néel with a CCW chirality (blue triangle in Fig. 6.4(a,b)).
On other hand, if $|D| < |D_C^N|$, the iDMI contribution in σ_{DW} is no longer greater than the volume magnetic charges and a Bloch component appears on the magnetic moments inside the DW, leading to intermediate helicities. Moreover in this case there are two energetically degenerated energy minima, as shown in Fig. 6.4a. In fact, the iDMI sign sets a preferred Néel component for the DW but nothing favors one Bloch component over its opposite, so that the two Bloch chiralities, of helicity $\pm\xi$ are energetically degenerated. This is due to the interfacial nature of this iDMI which favors Néel type DW. Moreover, each energy minimum is surrounded by two maxima and the smaller minimum conserves the Néel component favored by the iDMI sign. The value of this energy barrier conserving the Néel component is plotted in Fig. 6.4d as a function of the reduced iDMI coefficient. It is maximum at $D = 0$ where it is proportional to the volume charges $\Delta\sigma_{DW} = 4\left(\sqrt{A_{ex}\left(K_0 + K_d^V\right)} - \sqrt{A_{ex}K_0}\right)$. Then, increasing the iDMI decreases the energy barrier which finally vanishes for $|D| = |D_C^N|$ where the two opposite Bloch component "collapse" to result in a DW of pure Néel type.

In Fig. 6.5, the expression 6.2 from the analytical model (dashed green curve) is superimposed to the data from the simulations. Since the critical iDMI coefficient that is predicted by the model ($D_{C,m}^N \simeq 0.21$ mJ/m²) is different from the one extracted from the simulations ($D_{C,s}^N \simeq 0.41$ mJ/m²), we observe a mismatch between the simulations and the model prediction. In fact, in our model we underestimate the magnetic volume charges [209], which leads to an underestimation of the critical iDMI value D_C^N. It might be due to the fact that this model is based on an approximation for the dipolar energy in the DW, which consist in transforming the long range and local dipolar interaction in a anisotropy term, making the calculation analytically feasible [124]. Nevertheless, in Fig. 6.5, both the model and the simulation data have been plotted with the appropriate D_C^N, and in this case the model and the simulations show a very good agreement. Thus, on the one hand the simulations can provide an accurate computation of the magnetic volume charges, and the analytical model can predict the equilibrium DW helicity for a given iDMI coefficient. Moreover the model clearly unveils the role of iDMI versus magnetic volume charge in the stabilization of the DW helicity, in agreement with previous works in the literature [210].

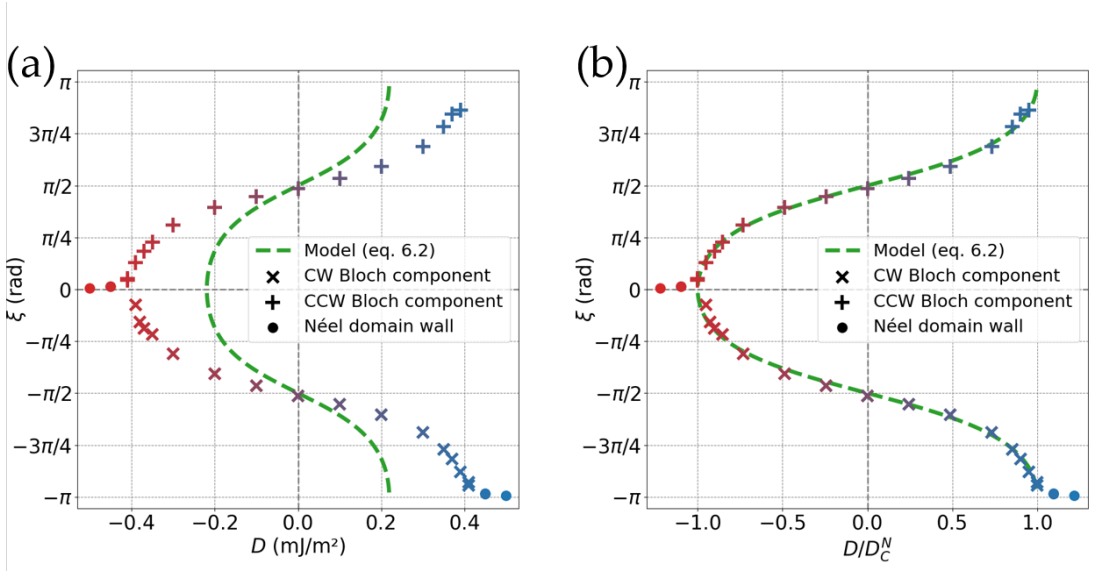

Figure 6.5: **Skyrmion statics: Comparison Model / Simulations:** (a) DW helicity versus iDMI value : DW energy model (green curve, corresponding to equation 6.2) superimposed to the simulation data and (b) same graph plotted in reduced units of D.

It is interesting to notice that by inserting eq. 6.2 in eq. 6.1, one can get the behaviour of the domain wall energy as a function of the iDMI coefficient in the low iDMI regime:

$$\sigma_{DW} = 4\sqrt{A_{ex}K_0\left(1+\frac{1}{\left(\frac{4\sqrt{A_{ex}K_d^V}}{\pi D}\right)^2-1}\right)} - \pi D\sqrt{\frac{K_0/K_d^V}{\left(\frac{4\sqrt{A_{ex}K_d^V}}{\pi D}\right)^2-1}} \tag{6.4}$$

In Fig. 6.6 we plotted the variation of helicity (gray curve) and DW energy (black curve) versus the iDMI coefficient. It summarizes the main feature of the analytical model : starting from $D = 0$, Bloch type magnetic skyrmions are stable and the cost in DW energy is the maximum. Then, increasing the iDMI leads on the one hand to the decrease of the DW energy, and to the progressive variation of the helicity, until reaching the critical iDMI coefficient D_C^N at which the skyrmion is purely Néel. If one continues increasing the iDMI coefficient, for $|D| > |D_C^N|$, the DW energy varies linearly with the iDMI coefficient since one has $\xi = 0 \pm n\pi$ and thus $\sigma_{DW} = 4\sqrt{A_{ex}\left(K_0 + K_d^V\right)} \pm \pi D$. The helicity thus is fixed to the Néel one but the DW energy continues to decrease until a critical iDMI value D_C^{SS} which corresponds to the transition towards spin spiral magnetic configuration [211–213], where it is favorable to form as many DWs as possible. Equation 6.4 allows to extract the expression of this critical iDMI coefficient, $D_C^{SS} = \frac{4}{\pi}\sqrt{A_{ex}\left(K_0 + K_d^V\right)}$. Since $\left|\frac{D_C^{SS}}{D_C^N}\right| = \frac{K_0+K_d^V}{K_d^V}$ one has always $|D_C^{SS}| \geq |D_C^N|$, *i.e.* a spin-spiral configuration is always composed of pure Néel DW. The limiting case, where $D_C^N = D_C^{SS}$ happens at the spin reorientation, when $K_0 = 0$ corresponding to the transition between PMA and IP magnetic state. The spin-spiral configuration, although it is not the focus of this chapter, has also been stabilized in the simulations for large iDMI value, as shown in the top-left of Fig. 6.6. This variety of

DW types gives an idea of the richness of the iDMI-induced physics but in the following we will restrict ourselves to the study of skyrmions in the low iDMI range.

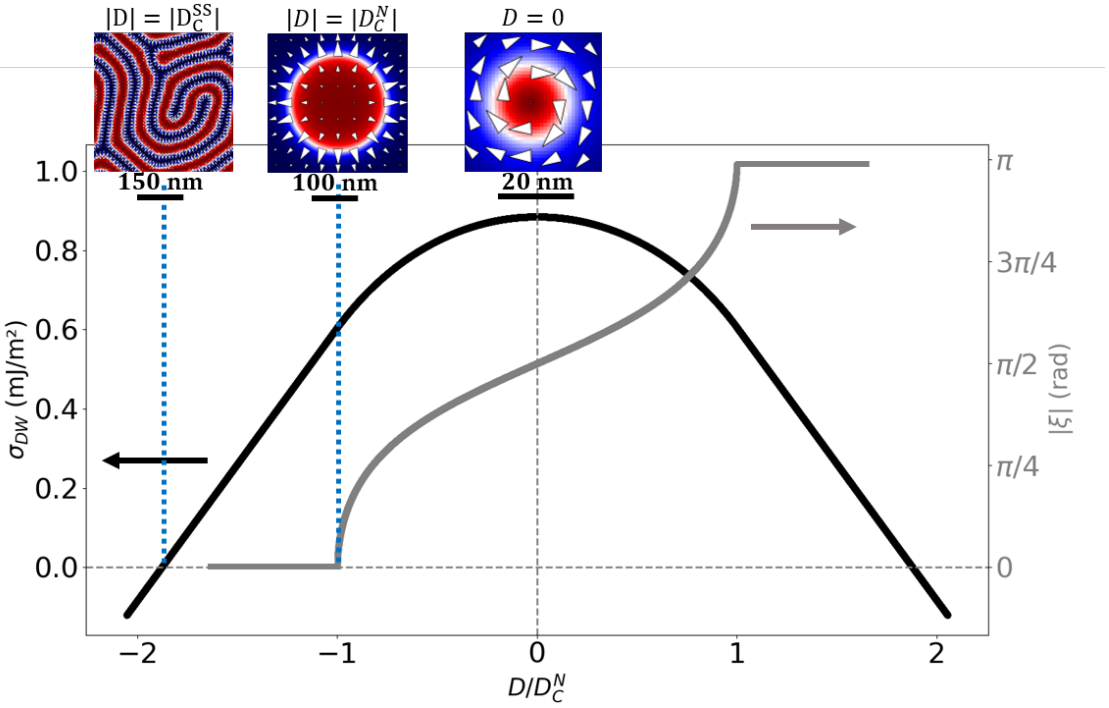

Figure 6.6: **Helicity and domain wall energy as a function of iDMI value:** The helicity (gray curve) and the domain wall energy (black curve) are plotted as a function of the iDMI value, in units of D_C^N. Starting from $D = 0$ at which a Bloch skyrmion is stabilized, increasing the iDMI value leads to the continuous transformation towards a Néel skyrmion at $D = D_C^N$. By further increasing iDMI value, the domain wall energy becomes negative and a spin-spiral state is stabilized.

6.1.3 *Deterministic choice of the Bloch component inside the domain wall*

As shown in the previous section, two skyrmions stabilized with the same D and having a DW with an opposite Bloch component are energetically degenerated (Fig. 6.4b) and these two states are separated by an energy barrier (Fig. 6.4b,d). In this section use the effect of a nanosecond magnetic field pulses to choose the Bloch component inside the DW, and to switch between the two Bloch chiralities in a deterministic way.

The magnetic parameters used in these simulations are the same as in the previous section. We start by stabilizing a skyrmion with intermediate DW internal structure, defined by $\xi \simeq 51°$ (CCW Bloch component) at $D = -0.3$ mJ/m² (corresponding to the red[4] circle in Fig. 6.2, Fig. 6.3 and Fig. 6.7). For these parameters, the DW energy as a function of the skyrmion helicity is plotted in Fig. 6.7. We can see the two degenerated energy minima, and our initial CCW Bloch skyrmion state corresponds to the minima on the right, depicted by the red circle. The corresponding spin texture is reminded in Fig. 6.8b. Here, the radius of the skyrmion stabilized at $D = -0.3$ mJ/m² is slightly higher compared to the one in the

4 In this section, the "red" color corresponds in fact to a red-purple color, but for simplicity it is called red in the following.

previous section (see Fig. 6.3 and Fig. 6.3) because the applied magnetic is slightly smaller. Here the skyrmion radius is $R \simeq 100$ nm at $\mu_0 H_{ext} = -0.5$ mT while in the previous section it was $R \simeq 37$ at $\mu_0 H_{ext} = -6$ mT.

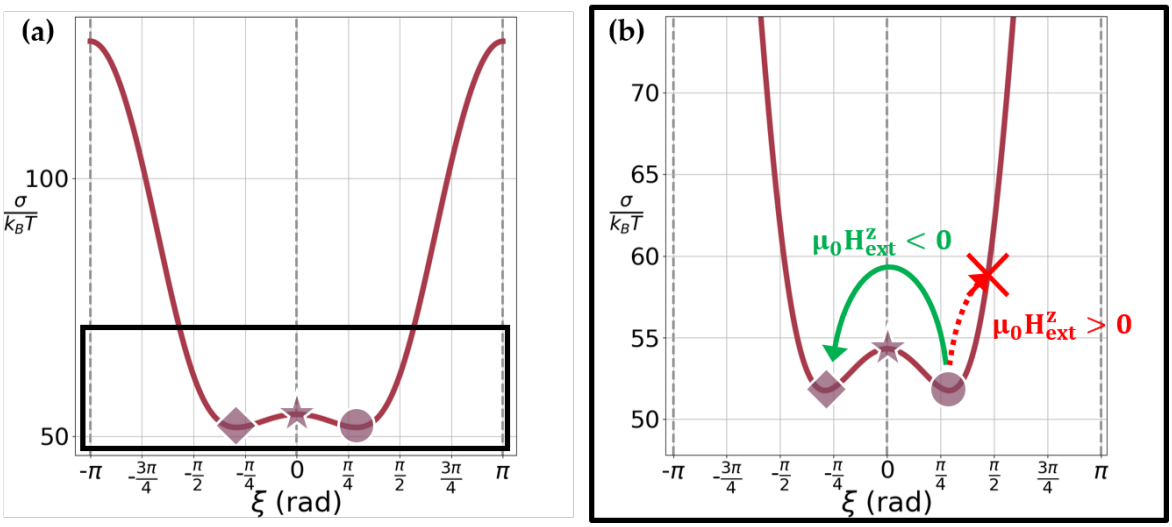

Figure 6.7: **Energy barrier between two skyrmions having opposite Bloch component:** (a) Domain wall energy as a function of the helicity at $D/D_C^N = 0.75$, corresponding to the red circle in Fig. 6.2, Fig. 6.3 and Fig. 6.7. (b) Zoom-in,e evidencing the two energetically degenerated minima, separated by an energy barrier. Starting from the minimum on the right, a negative magnetic field pulse can induce a transition towards the one on the left (green arrow), while a positive magnetic field pulse has not effect on the equilibrium helicity (dashed red arrow)

In Fig. 6.8a, we reported the evolution of the skyrmion helicity (initially depicted by the red circle) as a function of time, when applying magnetic field pulses. At $t = 0$, a 1 ns pulse of a 10 mT magnetic field is applied in a direction opposite to the skyrmion core magnetization ($-z$ direction, see the black curve in Fig. 6.8a). It has two consequences on the skyrmion: (i) a decrease of the skyrmion radius (see Fig. 6.8c), since the magnetic is applied in the opposite direction to its core, magnetized in the $+z$ direction and (ii) the torque exerted by this magnetic field on the in plane magnetic moments in the DW leads to their precession around the applied field. As result, after $\delta t \simeq 0.7ns$, a transient Néel DW is obtained (see Fig. 6.8c, which energetically corresponds to the summit of the energy barrier shown in Fig. 6.7b). After 1 ns, the external magnetic field is put back to the initial value and the skyrmion relaxes with an opposite helicity as in the initial state, *i.e.* with a CW Bloch component (see Fig. 6.8e and corresponding purple diamond location in Fig. 6.8a). We further observed that the application of a subsequent magnetic field pulse with an opposite direction ($+z$ direction) allows to recover the initial CCW Bloch component, as it is shown in Fig. 6.8a. This time, the skyrmion radius slightly increases because of the positive magnetic field pulse (see the transient Néel state in Fig. 6.8d) Moreover, by reproducing this manipulation, it is possible to go back and forth between the two Bloch components, by applying a magnetic field in the appropriate direction.

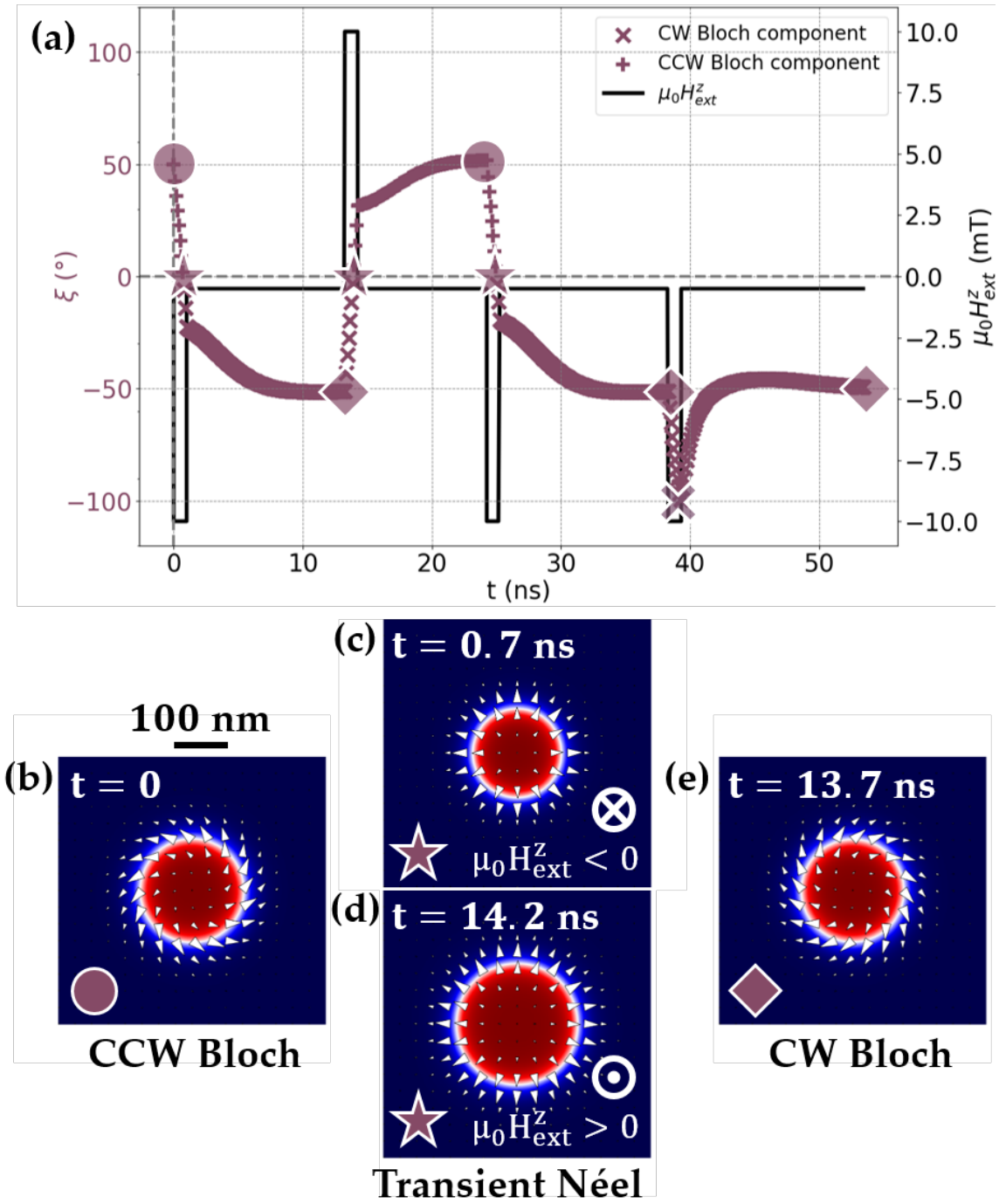

Figure 6.8: **Deterministic choice of skyrmion Bloch chirality:** (a) DW helicity (purple data points) and magnetic field (black curve) as a function of time. A negative (resp. positive) magnetic field pulse induces the transition from CCW to CW (resp. CW to CCW) Bloch component in the skyrmion DW, through a transient Néel skyrmion state. (b) Skyrmion with a CCW Bloch component in the DW (c) (resp (d)) Transient Néel skyrmion for negative magnetic field pulse (resp. positive) (e) Skyrmion with a CW Bloch component in the DW.

If the magnetic field is not applied in the appropriate direction, no helicity inversion is observed, as shown around $t \simeq 40$ ns in Fig. 6.8a. Indeed, as explained in the previous section, each energy minimum is surrounded by two energy barriers : the smaller one

conserves the Néel component favored by the iDMI sign while the other does not. In our case, the CW skyrmion at $t \simeq 40$ ns is surrounded by a small energy barrier in $\xi = 0$ (favoured by $D < 0$) and by a large barrier in $\xi = \pm\pi$ (not favoured by $D < 0$) (see Fig. 6.7). Consequently, a positive magnetic field pulse induces a precession that leads to a transient CW Néel skyrmion, favoured by the iDMI sign, and thus allowing the Bloch chirality inversion as seen above. However, the application of a negative magnetic field pulse would lead to a precession in the opposite direction, towards the high energy barrier *i.e.* a transient CCW Néel skyrmion, which is not favoured by iDMI. Thus, we observed that in this case, the helicity stopped varying around $\xi = -100°$ (see Fig. 6.8a), corresponding to a very small CCW Néel component. To summarize, the energetically favourable path to go from one minima to the other is logically the path that conserves the Néel component imposed by the iDMI sign.

6.1.4 *Conclusion*

In this section, we have shown using micromagnetic simulations that a fine tuning of the iDMI allows controlling the static skyrmion characteristics such as the DW helicity, the radius or the DW width. We used a model based on the DW energy in order to understand the physical origin of the simulation results. It unveiled the key role of the competition between iDMI and magnetic volume charges in the stabilization of the DW internal structure, in agreement with previous works in the literature [210]. We further showed that the Bloch component in the DW of twisted skyrmions can be controlled using pulses of magnetic field applied in the appropriate direction.

6.2 SKYRMION MOTION UNDER SPIN-ORBIT TORQUE VERSUS DW HELICITY

In this section we are interested in the dynamics of magnetic skyrmions under injected current as a function of their magnetic configuration, which can be adjusted by controlling the iDMI (see previous section).
More precisely, in a first part I show simulations of the SOT-driven motion of skyrmions, as a function of their structural parameters. The main parameter is the DW helicity ξ, but we will see that the skyrmion radius R and DW width δ_{DW} also play a role in the dynamic properties. Then, as a function of these parameters, I extracted the trajectory angle φ_{traj} and the skyrmion velocity v_{sk}.
In a second part, I establish an analytical model which explains the behaviour observed in the simulations, and gives the skyrmion trajectory and velocity as a function of the parameters (ξ, R, δ_{DW}).

6.2.1 *Micromagnetic simulations*

In this part, I study the SOT-driven motion of magnetic skyrmions in a HM/FM bilayer system similar to the one of our experiments. We thus consider a HM layer with negative

spin Hall angle such as Ta [186], and a current density J_{HM} flowing inside it in the $\vec{x}$ direction (Fig. 6.9a). Due to the spin Hall effect (see section 2.5.2.2) in the HM layer, a vertical spin current appears, polarized in the $\vec{\sigma} = \vec{y}$ direction (yellow arrows in Fig. 6.9a). This spin current induces spin orbit torques on the FM magnetization, notably on skyrmions, which will be set in motion. More precisely, the torque responsible for skyrmion motion is called the damping like torque (see section 2.5.2.4). In order to mimic this situation in the micromagnetic simulations with Mumax3, we injected in the FM layer a vertical current density J with a spin polarization ($P = 0.1$) in the $\vec{y}$ direction [214], as depicted by the yellow arrows in Fig. 6.9b. The current density is chosen to $J = 10^{10}$ A/m² to avoid skyrmion deformation due to high current densities, which simplifies the interpretation of the results in the next part and allows to use the model to fit the simulation data.

The material parameters (see table 6.1 in page 130), as well as the size of the simulation region ($512 \times 512 \times 0.9$ nm), remain the same as in the previous section. The presence of Periodic Boundary Conditions allows to avoid edge effect for skyrmions moving towards the simulation region borders. The initial stable skyrmion states (*i.e.* before current injection) consists in all the skyrmions in Fig. 6.2, characterized by their helicity ξ, radius R and DW width δ_{DW}. Then, the simulation consists in injecting the current density to record the dynamic properties such as the trajectory angle, or the skyrmion velocity.

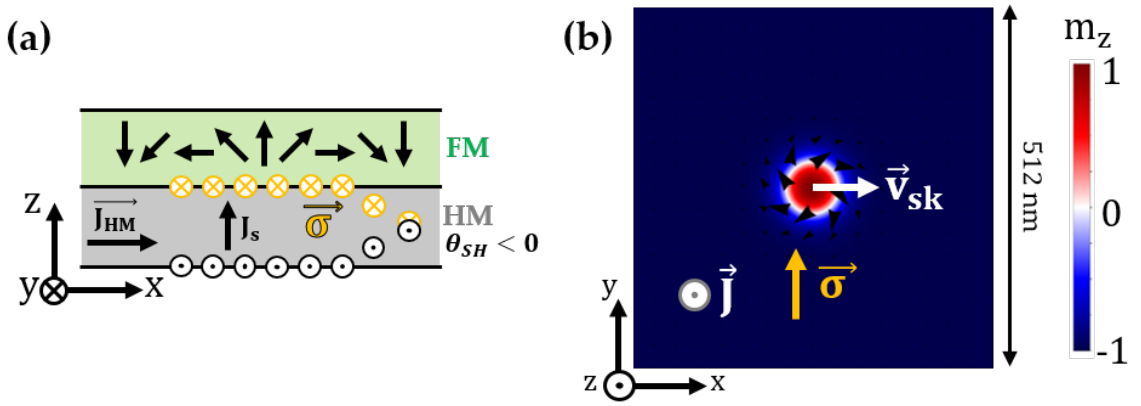

Figure 6.9: **Current injection geometry in Mumax3:** Experimentally, the motion of skyrmion is due to the SHE from the current flowing in the X direction in a HM layer with negative spin Hall angle. In the micromagnetic simulations, the equivalent situation is obtained by injecting a vertical current density $\vec{J}$ which is spin polarized in the $\vec{y}$ direction (yellow arrow) [214].

The current density is injected during $t = 200$ ns and the skyrmions start to drift without deformation in a direction that depends on its helicity. The trajectory of skyrmions in the (x, y) plane is plotted in Fig. 6.10a, where the direction of the current density is depicted by the black arrow. The color code and symbols shape have the same signification as in the previous section. As a guide to the eyes, some trajectories are accompanied by a schematic illustration of the corresponding skyrmion configuration. The main feature is that for a given direction of current density, skyrmions can be driven in any direction

depending on their DW helicity ξ. In particular we see that skyrmions with opposite chiralities ($\xi \rightarrow \xi + \pi$) have trajectories pointing in opposite directions. The helicity can be finely tuned by adjusting the iDMI value, as shown in the previous section. Moreover, it is clear both from Fig. 6.10a and Fig. 6.10b that the skyrmion velocity[5] depends on its helicity. It is maximum for Néel skyrmion and minimum for Bloch skyrmion, with a factor of 5 between them. In the literature, iDMI is known to improve DW motion (refs), which is thus in agreement with our results.

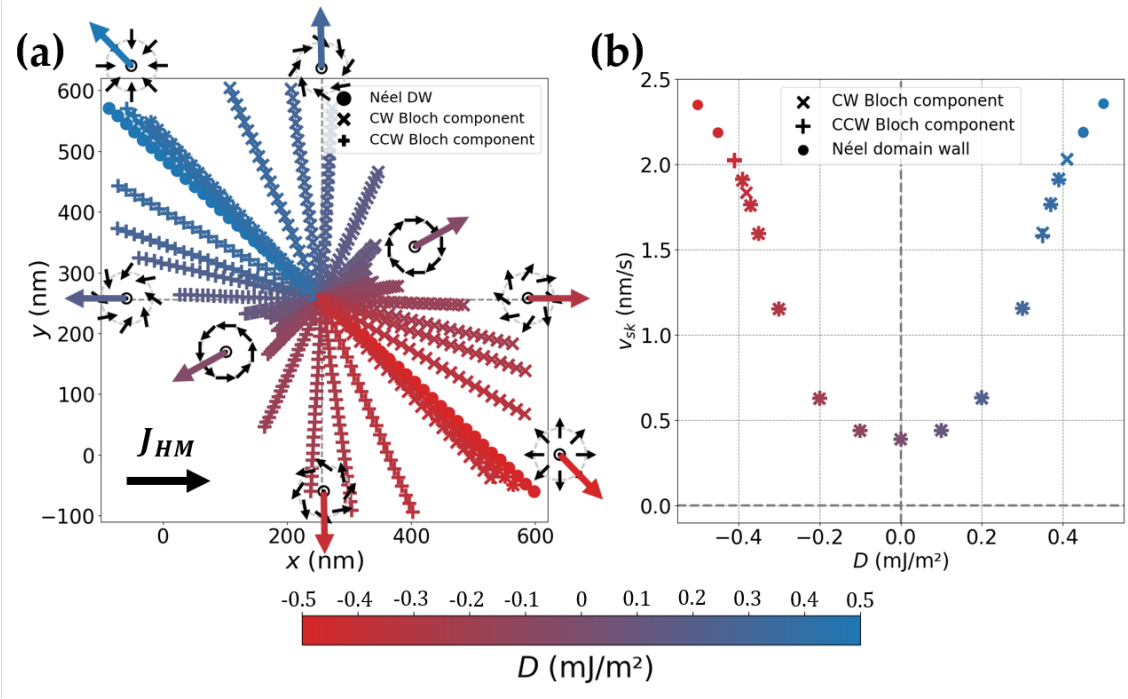

Figure 6.10: **Trajectories of skyrmions driven by spin orbit torque:** (a) Trajectories of skyrmions with different helicities, under the current density $\vec{J}_{HM}$ depicted by the black arrow. For some trajectories, the corresponding skyrmion configuration is represented right next to it. (b) Velocity of skyrmion as a function of the iDMI coefficient.

For clarity, Fig. 6.10a can be simplified by extracting the parameters of interest, namely the DW helicity and the trajectory angle φ_{traj}, defined as the angle between the skyrmion's center trajectory and the x-axis (see Fig. 6.11b). The result is plotted in Fig. 6.11a, where the symbols shape and the color keep the same signification as before.

Thus, for a given direction of the current density, skyrmions can be moved in every directions within the plane of the FM layer as a function of their helicity. In first approximation, we observe a linear dependence of $\varphi_{traj}(\xi)$ with the helicity ξ, with a vertical offset, about $\simeq -42°$. It corresponds to the well known skyrmion Hall effect (SkHE) [154, 155]: it is known to deflect Néel skyrmions from the current direction, along which the force from the direction of the force from the SOT (see section 2.6 from chapter 2). The SkHE is detrimental for applications, more especially is skyrmion racetracks where the skyrmions do not follow the track but deflect towards the edges where it can be slowed-down or even expelled [215]. In fact, this deflection applies to all skyrmions, in addition to the effect of

5 obtained from the ratio between the covered distance L and the current injection time $v_{sk} = \frac{L}{t}$

the helicity, which is the main effect. Thus, the slope of $\varphi_{traj}(\xi)$ corresponds to the dependence of φ_{traj} on the helicity and the intercept is given, in first approximation, by the SkHE, and is called the skyrmion Hall angle φ_{SkHE} (SkHA). It is noteworthy to see that, due to the quasi linear behaviour, $\xi \to \xi + \pi$ implies $\varphi_{traj} \to \varphi_{traj} + \pi$, generalizing the fact that two skyrmions of opposite chiralities move in opposite directions.

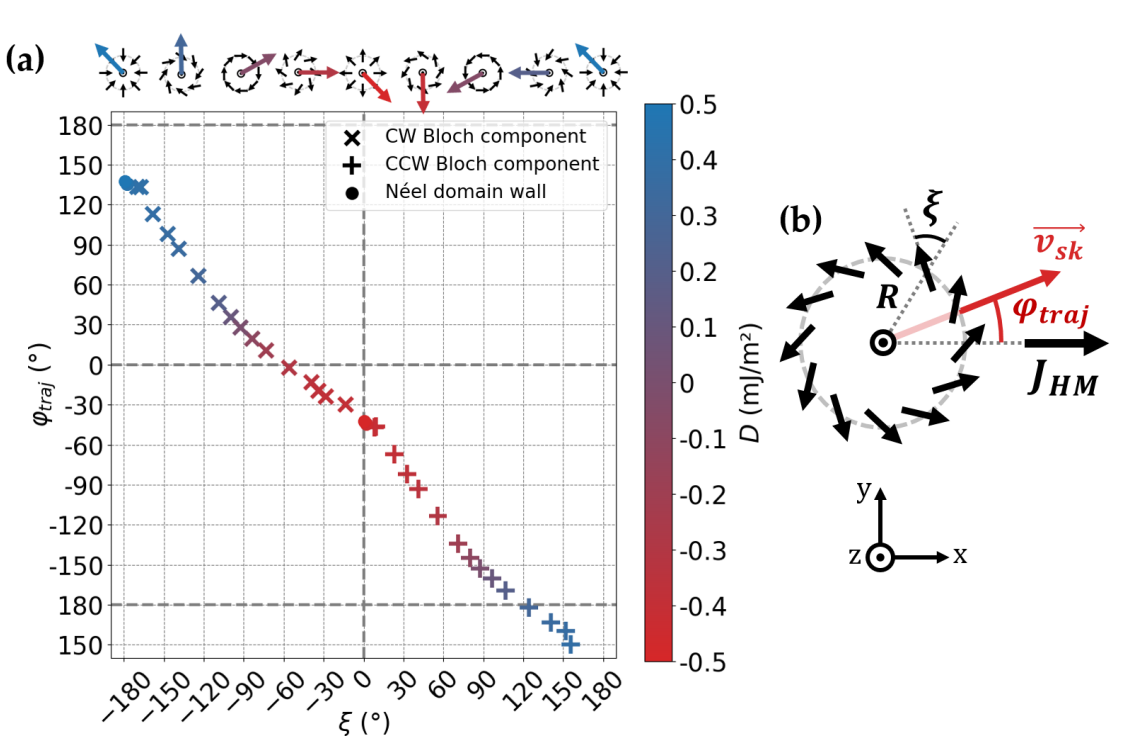

Figure 6.11: **Skyrmion trajectory angle versus DW helicity:** (a) Angle between the skyrmion velocity and the current density flowing in the bottom HM layer, versus the skyrmion helicity. (b) Definition of the trajectory angle φ_{traj}, and the helicity.

In Fig. 6.11a, two data points are of particular interest. Indeed, the skyrmion defined by $\xi = -54°$ move along the current density, without any deflection from the current direction and thus without SkHA. Similarly, the skyrmion defined by $\xi = 126°$ move in the opposite direction, still without any deflection from the current direction. Such a feature is of high interest for skyrmions dynamics in racetrack geometries, since very often the skyrmion deflects from the track due to the skyrmion Hall Effect. It can lead to skyrmion expulsion from the track [215], skyrmion annihilation on the edges of the track, or to skyrmion slowdown due to friction from the edges. Thus, being able to suppress the skHE with such precise DW control represents a very interesting degree of freedom for skyrmions dynamics in general, and even more for skyrmion racetrack memories.

There are already several ways to suppress the SkHE, as can be found in the literature. First, in synthetic antiferromagnet, the antiferromagnetic coupling between adjacent magnetic layer stabilizes adjecent skyrmions with opposite core polarities, and thus leads to zero net SkHE by compensation [28, 216, 217]. Similarly, the skyrmion Hall effect can be reduced in ferrimagnets [218] or even suppressed in antiferromagnets [30, 219]. Second, suppressing the SkHE with a tuning of the DW internal structure has already been shown

using micromagnetic simulations by tuning the ratio between a bulk DMI and an interfacial DMI [220, 221], or by tuning interfacial iDMI in magnetic multilayers coupled the one to the other [210]. Here, we directly tune an interfacial iDMI in a single magnetic layer system to suppress the SkHE, which can be achieved experimentally using a gate voltage, as shown by our experimental results in HM/FM/MO_x trilayer heterostructure.

6.2.2 *Analytical model*

In Fig. 6.11a we observe a slight deviation from the linear behaviour around $\xi = \pm\pi/2$. We may wonder if such deviation could be due to size effect since this region of the graph corresponds to the smaller skyrmions. This observation motivated the need to establish an analytical model in order to understand the behaviour observed in the micromagnetic simulations. Here, I propose a model based on the derivation of a modified Thiele equation which explains both the linear behaviour and the small non-linearity observed in the simulations.

6.2.2.1 *Modified Thiele equation*

The geometry that is considered for the model is the same as for our experiments, and is thus similar to the micromagnetic simulations: we consider a skyrmion spin texture in a thin FM layer, characterized by its radius R, DW width δ_{DW} and helicity ξ, as defined in Fig. 6.12. The FM layer is put on top of a HM layer with a negative spin Hall angle in which a current density $\vec{J}_{HM}$ is flowing in the $\vec{x}$ direction. From the SHE, it induces a spin accumulation $\vec{\sigma} = -\vec{j} \times \vec{z} = \vec{y}$ at the HM/FM interface (see eq. 2.13 from chapter 2). It is at the origin of SOT on the FM magnetization, and notably we consider in the following the effect of the DL-SOT from the SHE, which is at the origin of skyrmion motion (see section 2.5.2.4). More specifically, the model presented here computes the trajectory angle φ_{traj} between the current direction $\vec{J}_{HM}$ and the skyrmion core velocity $\vec{v}_{sk}$ (see Fig. 6.12b). Thus, here the magnetization dynamics is governed by the LLG equation with an additional term from the DL-SOT (as introduced in eq. 2.22 from chapter 2):

$$\frac{d\vec{m}}{dt} = -\gamma\mu_0\vec{m} \times \vec{H_{eff}} + \alpha\vec{m} \times \frac{d\vec{m}}{dt} - \gamma\mu_0 H_{DL}\vec{m} \times (\vec{m} \times \vec{y}) \tag{6.5}$$

where $\vec{m} = \frac{\vec{M}}{M_S}$ is the normalized magnetization, γ the gyromagnetic ratio (in rad·Hz/T), μ_0 the vacuum permeability (in T·m/A), α the magnetic damping and the effective field is defined as $\vec{H_{eff}} = -\frac{1}{\mu_0 M_S}\frac{\delta\mathcal{E}}{\delta\vec{m}}$ with $\mathcal{E}$ the magnetic energy density (in J/m^3). The last term corresponds to the DL-SOT term, where $H_{DL} = \frac{\hbar|\theta_{SH}|J_{HM}}{2|e|\mu_0 M_S t_{FM}}$ is the torque efficiency with θ_{SH} the spin Hall angle of the HM layer, J_{HM} the current density (in A/m²), e the electron charge (in C), M_S the saturation magnetization of the FM layer (in A/m) and t_{FM} the FM layer thickness (in m).

Solving skyrmion dynamics by directly using the LLG equation is a complex task, that cannot be performed analytically. In the following, we propose to overcome this limitation by introducing the Thiele formalism and the Thiele equation, which governs skyrmion

dynamics driven by SOT.

Initially, *i.e.* before current injection, we assume that the skyrmion configuration is axisymmetric with respect its center. Thus, it is convenient to locate each spin in the cylindrical coordinates (r, φ, z), whose origin is taken at the skyrmion center (Fig. 6.12a)

$$\begin{pmatrix} x \\ y \\ z \end{pmatrix} \rightarrow \begin{pmatrix} x(r,\varphi) \\ y(r,\varphi) \\ z \end{pmatrix} = \begin{pmatrix} r\cos\varphi \\ r\sin\varphi \\ z \end{pmatrix} \tag{6.6}$$

We also assume that the helicity ξ does not depends on the radial direction of the skyrmion. At any location (r, φ, z), the magnetization direction is described in spherical coordinates $(1, \theta_0(r,\varphi), \phi_0(r,\varphi))$, as shown in Fig. 6.12b. Because of this skyrmion symmetry, one has $\theta_0(r,\varphi) \rightarrow \theta_0(r)$ and $\phi_0(r,\varphi) \rightarrow \phi_0(\varphi)$ so that initially, the skyrmion magnetization configuration is:

$$\vec{m}_0 = \begin{pmatrix} \sin\theta_0(r)\cos\phi_0(\varphi) \\ \sin\theta_0(r)\sin\phi_0(\varphi) \\ \cos\theta_0(r) \end{pmatrix} \tag{6.7}$$

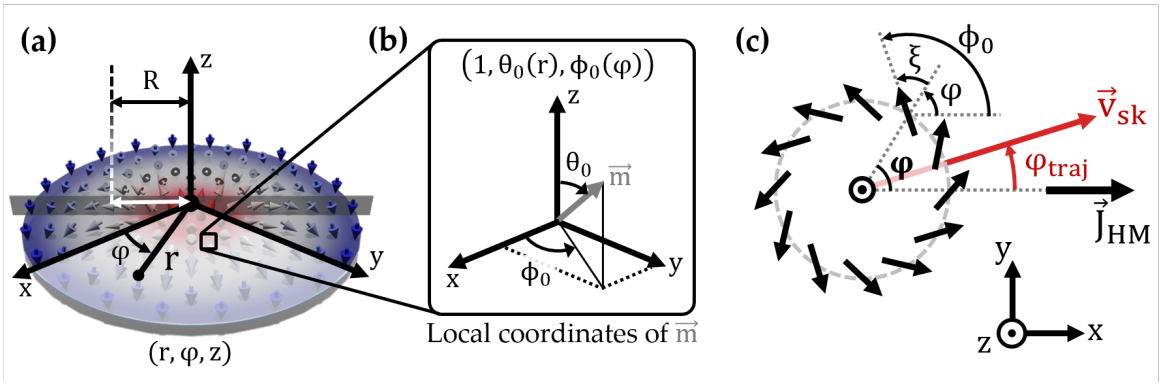

Figure 6.12: **Coordinate system for the analytical model:** Coordinate system used to describe the skyrmion spin texture and to derive the different terms of the Thiele equation. (a) Sketch of a Néel-type skyrmion, on which a given spin is located in cylindrical coordinates (r, φ, z). (b) Locally the orientation of each spin is described using spherical angles $(1, \theta(r), \phi(\varphi))$. The angle ϕ_0 is the sum of the cylindrical angle φ and the helicity ξ, as shown in (c) which is a top view of a Dzyaloshinskii skyrmion. The trajectory angle φ_{traj} is defined as the angle between the current density $\vec{J}_{HM}$ (black arrow) and the skyrmion velocity vector $\vec{v}_{sk}$ (red arrow).

Then, under current injection, the skyrmion drifts in one direction due to the effect of the DL-SOT. The key of the Thiele formalism is the hypothesis of a rigid skyrmion: the skyrmion is assumed to move without any deformation due to the current density. Moreover, the skyrmion is assumed to be a point-like object, located at the coordinate of its center, similarly as point mechanics. It allows to describe the magnetization configuration $\vec{m}$ at any time, only knowing the initial configuration $\vec{m}_0$ and the position of the skyrmion center $\vec{X}_c$ in the cylindrical coordinates:

$$\vec{m}(\vec{X},t) = \vec{m_0}(\vec{X} - \vec{X_c}(t)) \longleftrightarrow \begin{cases} \theta(\vec{X},t) = \theta_0(\vec{X} - \vec{X_c}(t)) \\ \phi(\vec{X},t) = \phi_0(\vec{X} - \vec{X_c}(t)) \end{cases} \tag{6.8}$$

where $\vec{X} = (r, \varphi, z$ is a position in the cylindrical coordinate system. The meaning of eq. 6.8 is that the assumption of rigid skyrmion is equivalent to keep the origin of the cylindrical coordinate system at the skyrmion center although it is moving.
Using this formalism, the LLG equation can be transformed into an equation which represents the force balance applied at the skyrmion center (see Annex 8.5). This equation is called the Thiele equation and governs the skyrmion dynamics driven by SOT (see Sec. 2.6):

$$\vec{F}_{DL} + \vec{G} \times \vec{v}_{sk} - \alpha \bar{\bar{\mathcal{D}}} \cdot \vec{v}_{sk} = \vec{0} \tag{6.9}$$

where the expression of these forces can be written in the coordinate system descibed in Fig. 6.12 (demonstration in Annex 8.5):

$$\vec{F}_{DL} = \mu_0 M_S t_{FM} H_{DL} \int_S \left(\sigma_\phi \vec{\nabla}\theta - \sin\theta \sigma_\theta \vec{\nabla}\phi \right) d^2\vec{r} \tag{6.10}$$

$$\vec{G} = \frac{M_S t_{FM}}{\gamma} \int_S \sin\theta \left(\vec{\nabla}\theta \times \vec{\nabla}\phi \right) d^2\vec{r} \tag{6.11}$$

$$\bar{\bar{\mathcal{D}}} = \frac{M_S t_{FM}}{\gamma} \int_S \left(\left(\vec{\nabla}\theta \right)^2 + \sin^2\theta \left(\vec{\nabla}\phi \right)^2 \right) d^2\vec{r} \tag{6.12}$$

where the gradient is in the cylindrical coordinate system $\vec{\nabla} = (\frac{\partial}{\partial r}, \frac{1}{r}\frac{\partial}{\partial \varphi}, \partial z)$ as well as the integration $\int_S d^2\vec{r} = \int_S r dr d\varphi$. In annex 8.5 we derive the expressions of these three terms and we change of basis to express them in the Cartesian coordinate system, which is more convenient to study the trajectory of the skyrmion in the (x,y) plane.
The first term $\vec{F}_{DL}$ is the force due to the DL-SOT originating from the current density flowing in the HM layer below the FM layer. The second term $\vec{G} \times \vec{v}_{sk}$ is the gyroforce, where $\vec{G}$ is called the gyrovector. It is always perpendicular to the skyrmion velocity, $\vec{v}_{sk}$. The last term $-\alpha \bar{\bar{\mathcal{D}}} \cdot \vec{v}_{sk}$ is the dissipation force, similar to a viscous force acting on the skyrmion. All these three terms are forces (in N), and the magnetic damping α is the same as in the LLG equation 6.5.
First, one can notice that the gyrovector $\vec{G}$ is a function of the winding number $n = p \cdot W$ (defined in eq 8.65 from section 2.2.1), and reads as $G = -4\pi \frac{M_S t_{FM}}{\gamma} n$. Let us remind that the number p is the skyrmion polarity ($p = \pm 1$ if the magnetization at the skyrmion center is along $\pm z$), and $W = \frac{[\phi(\varphi)]_{\varphi=0}^{2\pi}}{2\pi}$ describes the behaviour of the magnetization along the skyrmion perimeter. Moreover, for a skyrmion spin texture, one has $\phi(\varphi) = \varphi + \xi$ (see Fig. 6.12b), leading to $W = 1$ and thus $n = p$. Consequently, the gyrovector reads as $G = -4\pi \frac{M_S t_{FM}}{\gamma} p$ and the transversal force $\vec{G} \times \vec{v}_{sk}$ depends on the skyrmion polarity and velocity, as experimentally observed in the literature [153].

Second, the dissipative tensor $\bar{\bar{\mathcal{D}}}$ becomes diagonal due to the axial skyrmion symmetry, *i.e.* $\mathcal{D}_{xy} = \mathcal{D}_{yx} = 0$ and $\mathcal{D}_{xx} = \mathcal{D}_{yy} = \mathcal{D}$, where $\mathcal{D}$ is given from eq. 6.12 :

$$\begin{aligned}\mathcal{D} &= \frac{M_S t_{FM}}{\gamma}\pi \int_{r=0}^{+\infty} \left[r\left(\frac{\partial\theta}{\partial r}\right)^2 + \frac{\sin^2\theta}{r}\right] dr \\ &= \frac{M_S t_{FM}}{\gamma}\beta_0 \end{aligned} \tag{6.13}$$

where β_0 is a dimensionless coefficient given by

$$\beta_0 = \pi \int_{r=0}^{+\infty} \left[r\left(\frac{\partial\theta}{\partial r}\right)^2 + \frac{\sin^2\theta}{r}\right] dr \tag{6.14}$$

It is interesting to notice that it corresponds to the exchange integral of the micromagnetic exchange energy. The first term in the integrand corresponds to the usual exchange term while the second one is a curvature exchange term that become predominant for small skyrmion, corresponding to additional exchange due to the small skyrmion size [124] because the DW can no longer be considered flat.
Thus, both the gyroforce term $\vec{G} \times \vec{v}_{sk}$ and the dissipative term $-\alpha\bar{\bar{\mathcal{D}}} \cdot \vec{v}_{sk}$ are helicity-independent. The dependence on the helicity ξ arises through the last terms to be derived, the force due to the DL-SoT, $\vec{F}_{DL}$. According to equation 6.10, one can get

$$\vec{F}_{DL} = \begin{pmatrix} F_{DL,x}(\xi) \\ F_{DL,y}(\xi) \\ 0 \end{pmatrix} = \mu_0 M_S t_{FM} H_{DL} \left(\beta_1 + \beta_2\right) \begin{pmatrix} \cos\xi \\ -\sin\xi \\ 0 \end{pmatrix} \tag{6.15}$$

where β_1 and β_2 are given by

$$\beta_1 = \pi \int_{r=0}^{+\infty} r\left(\frac{\partial\theta}{\partial r}\right) dr \tag{6.16}$$

$$\beta_2 = \pi \int_{r=0}^{+\infty} \sin\theta(r)\cos\theta(r)\, dr \tag{6.17}$$

At this point, $\vec{F}_{DL}$, $\vec{G}$ and $\bar{\bar{\mathcal{D}}}$ being calculated, one can extract from the Thiele equation the expressions for the longitudinal (v_x) and transverse (v_y) velocities of the skyrmion:

$$v_x(\xi) = \frac{\alpha\mathcal{D}F_{DL,x}(\xi) - GF_{DL,y}(\xi)}{G^2 + \alpha^2\mathcal{D}^2} \tag{6.18}$$

$$v_y(\xi) = \frac{\alpha\mathcal{D}F_{DL,y}(\xi) + GF_{DL,x}(\xi)}{G^2 + \alpha^2\mathcal{D}^2} \tag{6.19}$$

6.2.2.2 *Extraction of the skyrmion trajectory angle*

It is then possible to extract the angle of the skyrmion trajectory

$$\begin{aligned}\varphi_{traj}(\xi) &= \arctan\left(\frac{v_y(\xi)}{v_x(\xi)}\right)\\ &= \arctan\left(\frac{\frac{G}{\alpha\mathcal{D}}F_{DL,x}(\xi)+F_{DL,y}(\xi)}{F_{DL,x}(\xi)-\frac{G}{\alpha\mathcal{D}}F_{DL,y}(\xi)}\right)\\ &= \arctan\left(\frac{\frac{G}{\alpha\mathcal{D}}\cos\xi-\sin\xi}{\frac{G}{\alpha\mathcal{D}}\sin\xi+\cos\xi}\right)\end{aligned} \tag{6.20}$$

Replacing G and $\mathcal{D}$ by their respective expressions leads to $\frac{G}{\alpha\mathcal{D}} = \frac{-4\pi p}{\alpha\beta_0}$. Finally, using basic trigonometric properties, one can show that equation 6.20 is equivalent to

$$\varphi_{traj}(\beta_0,\xi) = \arctan\left(\frac{-4\pi p}{\alpha\beta_0}\right) - \xi = \varphi_{SkHE}(\beta_0) - \xi \tag{6.21}$$

where $\varphi_{SkHE} = \arctan\left(\frac{-4\pi p}{\alpha\beta_0}\right) = \arctan\left(\frac{G}{\alpha\mathcal{D}}\right)$ is the usual skyrmion Hall angle (SkHA) [153], arising from the skyrmion Hall effect (SkHE). As explained previously, for smaller skyrmions, an additional curvature exchange term is expected to give different β_0, thus leading to a SkHE that depends on the skyrmion size, and more especially on the ratio $\frac{R}{\delta_{DW}}$, as we will show in the following. Thus, we have $\varphi_{traj}\left(\frac{R}{\delta_{DW}},\xi\right) = \varphi_{SkHE}\left(\frac{R}{\delta_{DW}}\right) - \xi$ where the dependence on the skyrmion size is due to the coeffcient β_0.

6.2.2.3 *Influence of the domain wall profile*

A first look to expression 6.21 predicts a linear dependence of φ_{traj} with the helicity, with an offset φ_{SkHE} that corresponds to the skyrmion Hall effect. Such a behaviour is close to what is observed in the simulations, but does not explain the slight deviations from the linearity around $\xi = \pm\frac{\pi}{2}$ (see fig. 6.11a). In fact, the exact model prediction requires to specify a DW profile, for the calculation of the coefficient β_0 (see eq. 8.71). In a first attempt, we used the expression of a Bloch DW profile, given by

$$\theta(r) = 2\arctan\left(e^{\frac{2(r-R)}{\delta_{DW}}}\right) \tag{6.22}$$

For a given radius R and DW width δ_{DW}, this expression allows the computation of φ_{SkHE}. To compare the model with the simulation, we want to compute φ_{traj} for each value of $\xi \in [0, \pm\pi]$, and thus we need to consider possible variation of radius and/or DW width with the helicity. We have seen in Fig. 6.2 that the helicity ξ, radius R, and the DW width δ_{DW} depend differently on the iDMI coefficient. It is thus possible to plot R and δ_{DW} as a function of ξ, as shown respectively in Fig. 6.13a and 6.13b. These indirect dependencies are crucial for the model, since it gives a value of R and δ_{DW}, and thus a DW profile for each helicity. In other words, for each value of ξ, the profile was taken to eq. 6.22 with R and δ_{DW} extracted from the simulations. More precisely, the interpolated $R(\xi)$ and

$\delta_{DW}(\xi)$ (dashed black curves in Fig. 6.13) are used to compute β_0 (with the profile from 6.22 injected in eq. 8.71) to finally compute the skyrmion trajectory with eq. 6.21.

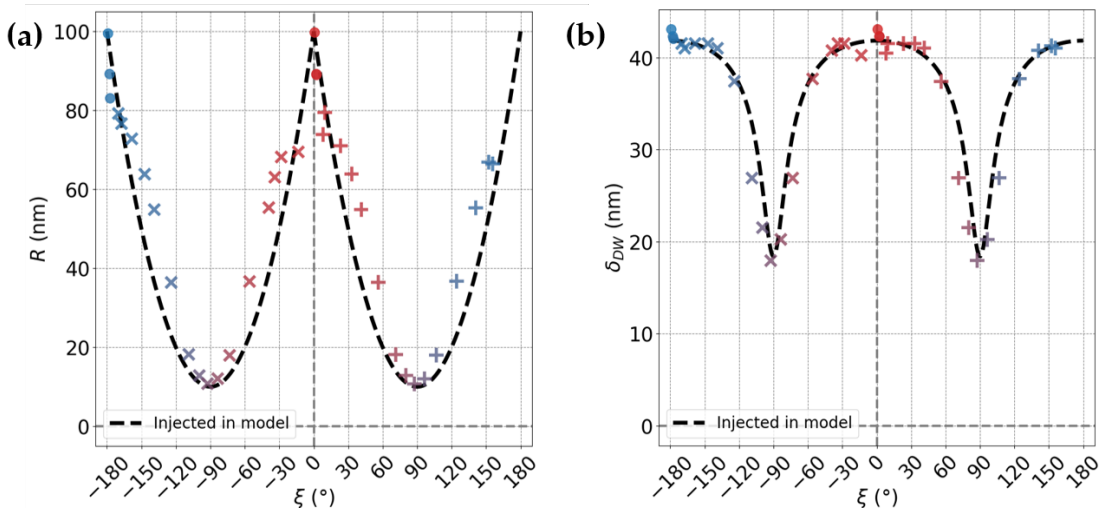

Figure 6.13: **Skyrmion structural parameters as a function of helicity:** (a) Skyrmion radius and (b) DW width as a function of the skyrmion helicity. The data points correspond to the parameters extracted from the simulations and the dashed black curve to the parameters injected in the model for fitting.

In Fig. 6.14 we show the comparison between the micromagnetic simulations (data points) and the model predictions (green curve). The model shows a good agreement with the simulations around $\xi = 0$ and $\xi = \pm\pi$, but there is a mismatch around $\xi = \pm\frac{\pi}{2}$. In fact, the region in which the model does not match the simulation corresponds to the region where the skyrmion is small, ie where $\frac{R}{\delta_{DW}} \simeq 1$. The reason behind this is that the Bloch profile as expressed in eq. 6.22 is not adapted for small skyrmions, and gives non-physical results. More precisely, one can see in Fig. 6.14b that when the skyrmion is large enough $\frac{R}{\delta_{DW}} \leq 2$, there is a good agreement between the profile extracted from the simulations (black curve, that corresponds to the extracted profile from the CW Néel skyrmion[6] shown in Fig. 6.3h) and the profile from eq. 6.22. However, as shown in Fig. 6.14c for smaller skyrmions (corresponding the CCW Bloch skyrmion at $D = 0$ shown in Fig. 6.3e), the Bloch DW profile does not describe correctly the skyrmion spin texture, since it gives $\theta(r = 0) \neq 0$, which is not possible for a skyrmion spin texture. By using such a profile, the polarity $p = \frac{[\cos\theta(r)]_{r=0}^{+\infty}}{2}$ (defined in section 2.2.1) is not correctly calculated and so does φ_{SkHE}.

6 We can notice that the profile extracted from the simulation have a slightly more extended tail. In fact, contrary to a Bloch DW, a Néel DW contains volume magnetic charges which leads to this extension at its boundary.

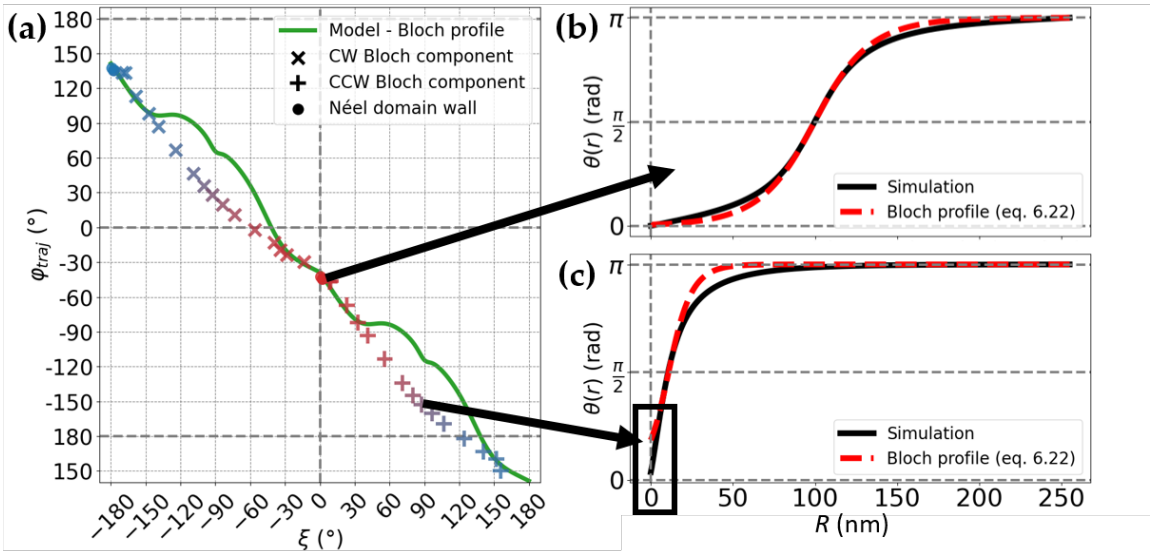

Figure 6.14: **Skyrmion trajectory angle versus helicity - comparison model / simulations:** (a) Comparison between the simulation data point and the model prediction (green curve) for the Bloch DW profile from eq. 6.22. (b) (resp. (c)) Comparison of the DW profile extracted from simulations (black curve) and the Bloch profile (dashed read curve) for the data point at $\xi \simeq 0$ (resp. $\xi \simeq \frac{\pi}{2}$). As surrounded in black in (c), the Bloch DW profile from eq. 6.22 is not convenient for small skyrmion, since it predicts $\theta(r = 0) \neq 0$.

This observation led us to introduce a Bloch-type DW profile which respect the main feature of a skyrmion, *i.e.* $\theta(r = 0) = 0$ and $\theta(r = \infty) = \pi$ even for small skyrmions (*i.e.* two DWs close to each other). These conditions are satisfied with

$$\theta(r) = 2\pi \frac{\arctan\left(e^{\frac{2(r-R)}{\delta_{DW}}}\right) - \arctan\left(e^{-\frac{2R}{\delta_{DW}}}\right)}{\pi - 2\arctan\left(e^{-\frac{2R}{\delta_{DW}}}\right)} \tag{6.23}$$

As shown in Fig. 6.15b, this DW profile reduces to the classical Bloch DW profile (shown in 6.14b) for large $\frac{R}{\delta_{DW}}$ ratio. Moreover, as shown in Fig. 6.15c, the boundary conditions $\theta(r = 0) = 0$ and $\theta(r = \infty) = \pi$ are now respected, at the expense of a small shift in the radius for the smaller skyrmions, which drops quickly to zero with the R/δ_{DW} ratio.
Using this expression and thus correcting small skyrmions profile, we can see in Fig. 6.15a that the model shows an excellent agreement with the micromagnetic simulations. The linear behaviour, as well as the non-linearity around $\xi = \pm\frac{\pi}{2}$ are nicely reproduced. The black dotted line corresponds to the case in which the skyrmion radius and DW width are fixed to their value at $\xi = 0$ and considered constant as a function of the helicity, leading to a constant φ_{SkHE} which thus represents only an offset to the linear behaviour.

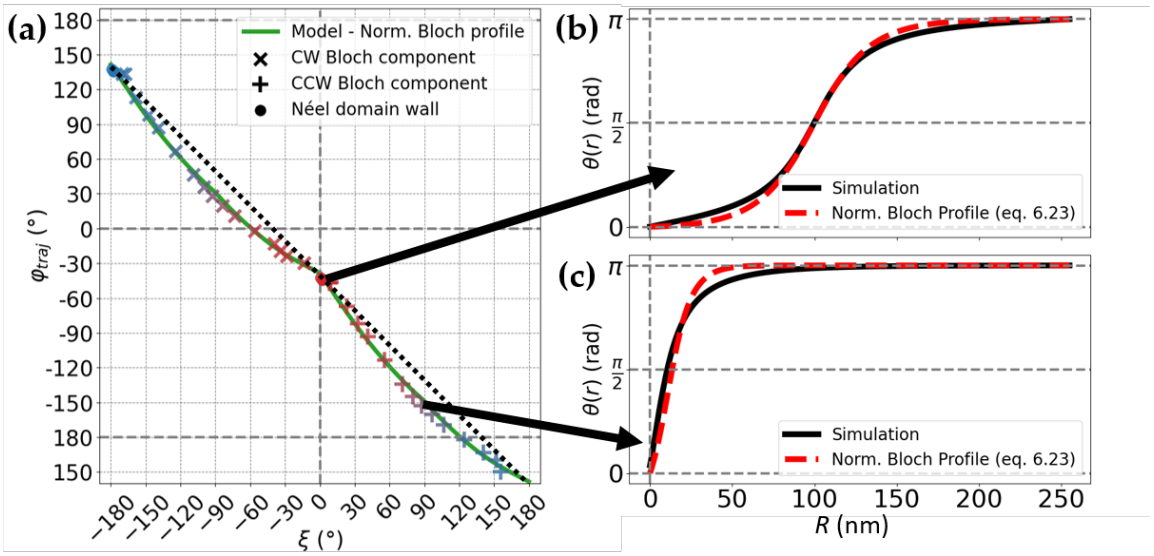

Figure 6.15: **Skyrmion trajectory angle versus helicity - comparison model / simulations:** (a) Comparison between the simulation data point and the model prediction (green curve) for the adjusted Bloch DW profile from eq. 6.22. (b) (resp. (c)) Comparison of the DW profile extracted from simulations (black curve) and the Bloch profile (dashed read curve) for the data point at $\xi \simeq 0$ (resp. $\xi \simeq \frac{\pi}{2}$). In this case (c), the adjusted Bloch DW profile from eq. 6.23 is convenient for small skyrmion, since it respects $\theta(r = 0) = 0$.

The deviation to linearity can be now explained by considering the variation of φ_{SkHE} with the $\frac{R}{\delta_{DW}}$ ratio. In Fig. 6.16, we substracted the linear contribution from the simulation data in order to consider only the SkHE. It is then compared to the SkHE predicted by the model, corresponding to the green curve. Globally, both the simulations and the model predict an increase of the absolute value of the SkHE when the skyrmion becomes smaller, *i.e.* around $\xi = \pm\frac{\pi}{2}$, when $D = 0$, with a maximal mismatch between them about 10% around $\xi = \pm\frac{\pi}{2}$. Further improvement of the DW profile might improve the agreement between the model prediction and the simulations.

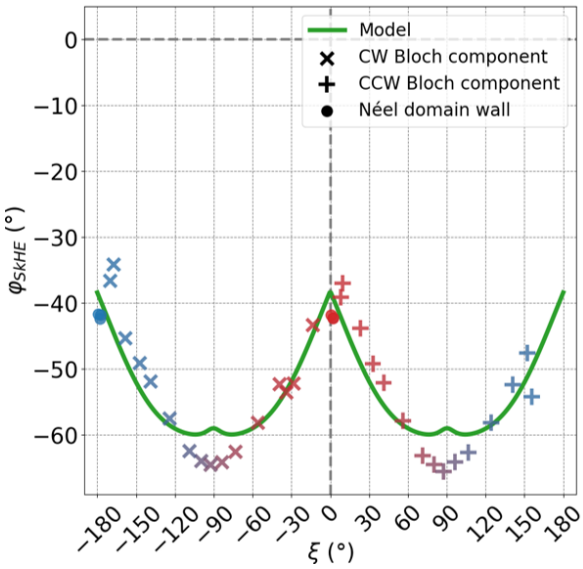

Figure 6.16: **Skyrmion Hall effect - comparison model / simulations:** Both the simulations (data points) and the model (green curve) predict an increase of the SkHE when the skyrmion becomes smaller, *i.e.* around $\xi = \pm\frac{\pi}{2}$, or when $D = 0$.

6.2.2.4 *Large skyrmion approximation*

In the following, we consider "large skyrmions", *i.e.* typically when $\frac{R}{\delta_{DW}} > 2$. In this case, β_0 can be approximated to $4\pi\frac{R}{\delta_{DW}}$ (in agreement with the supplementary informations of reference [222]) as shown in Fig. 6.17a, where β_0 (solid black curve) and the approximation (dashed black line) are plotted as a function of the $\frac{R}{\delta_{DW}}$ ratio. Thus, in the approximation of large skyrmion, the skyrmion trajectory angle reads as [153]

$$\varphi_{traj}^{R>\delta_{DW}}\left(\frac{R}{\delta_{DW}},\xi\right) = \arctan\left(\frac{-p\delta_{DW}}{\alpha R}\right) - \xi \tag{6.24}$$

Consequently, φ_{SkHE} can also be approximated as shown in Fig. 6.17b, where the model prediction for φ_{SkHE} (solid black curve) and the approximation (dashed black curve) are plotted as a function of the $\frac{R}{\delta_{DW}}$ ratio. The error on φ_{SkHE} associated to this approximation depends on the $\frac{R}{\delta_{DW}}$ ratio and is plotted in the inset of Fig. 6.17b for the damping coefficient $\alpha = 0.5$ considered in our simulations. For different values of damping parameter, we refer the reader to annex 8.5.

Thus, considering large skyrmion, equation 6.24 is 'ready to use', since the complex integral that defines β_0 is replaced by a simple term linear in $\frac{R}{\delta_{DW}}$. The skyrmion trajectory becomes accessible by specifying the skyrmion configuration, completely defined by the 4 parameters (R, δ_{DW}, ξ,p), in addition to the magnetic damping α.

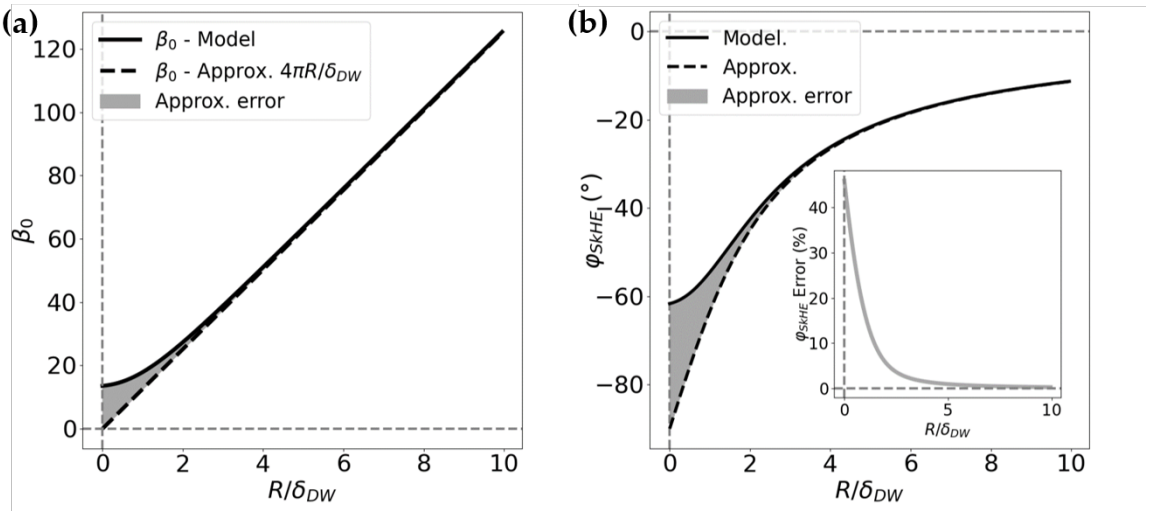

Figure 6.17: **Large skyrmion size approximation:** (a) The black curve represents the variation of β_0 coefficient versus the $\frac{R}{\delta_{DW}}$ ratio. For skyrmion whose radius is larger than the DW width (typically $R > 2\delta_{DW}$), it reduces to a simple linear behavior (dashed black line). (b) The solid black curve represents the variation of skyrmion Hall angle φ_{SkHE} versus the $\frac{R}{\delta_{DW}}$ ratio for a damping coefficient $\alpha = 0.5$. The dashed black line corresponds to the approximation for large skyrmion. The error associated to this approximation is plotted in the inset of (b) versus the $\frac{R}{\delta_{DW}}$ ratio.

Moreover, as shown in Fig. 6.18a, for large skyrmions the coefficient β_2 is always smaller than β_1 and rapidly goes to zero (solid gray curve) and β_1 (solid black curve) can be approximated to $\pi^2 R$ [222, 223] (plotted as a dashed black line). With these simplifications, we can recover the usual expression of the velocity for a CW Néel skyrmion at $\xi = 0$ [153]

$$v_x = \frac{\alpha \mathcal{D} F_{DL,x}}{G^2 + \alpha^2 \mathcal{D}^2} \tag{6.25}$$

$$v_y = \frac{G F_{DL,x}}{G^2 + \alpha^2 \mathcal{D}^2} \tag{6.26}$$

and thus, replacing β_0 by $4\pi\frac{R}{\delta_{DW}}$ and $(\beta_1 + \beta_2)$ by $\pi^2 R$ one can get

$$v_{sk} = \sqrt{v_{sk,x}^2 + v_{sk,y}^2} = \frac{\gamma \pi}{4} \frac{H_{DL}}{\sqrt{1 + \left(\frac{\alpha R}{\delta_{DW}}\right)^2}} \tag{6.27}$$

It shows one the one hand that the skyrmion velocity scales linearly with the current (since $H_{DL} \propto J$) and also that it also depends on the skyrmion size via the dependence in $\frac{R}{\delta_{DW}}$ at the denominator.

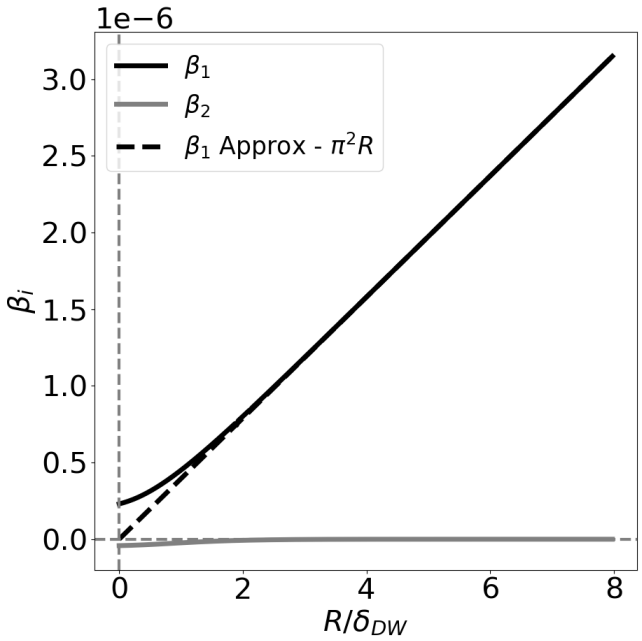

Figure 6.18: **Large skyrmion size approximation for $\beta_1 + \beta_2$:** (a) The solid black curve (resp. gray) represents the variation of β_1 (resp. β_2) coefficient versus the $\frac{R}{\delta_{DW}}$ ratio. For skyrmion whose radius is larger than the DW width (typically $R > 2\delta_{DW}$), the coefficient β_2 goes to zero and $\beta_1 \simeq \pi^2 R$ (dashed black curve).

6.2.2.5 *Large current regime*

We also tested to inject larger current density to see the effect on the skyrmion dynamics. We have injected a current one order of magnitude larger than in the previous sections, *i.e.* $J = 10^{11}$ A/m² during $\delta t = 30$ ns.

The trajectory of skyrmions in the (x, y) plane is plotted in Fig. 6.19a, where the direction of the current density is depicted by the black arrow. The color code and symbols shape have the same signification as in the previous section. As a guide to the eyes, some trajectories are accompanied by a schematic illustration of the corresponding initial skyrmion configuration. Similarly as in the previous section, we see that a skyrmion can be driven in any direction depending on its initial helicity, but here the trajectories are significantly different from previously.

On the one hand, the trajectories of Bloch and Néel skyrmions remain linear, with a small difference in the SkHE, which is known to depend on the skyrmion velocity [153] (for example, the SkHE for the Néel skyrmion is now about $-48°$, while it was $-42°$ at $J = 10^{10}$ A/m²). On the other hand, the main feature that we can observe is the curvature of the trajectory of some skyrmions. More precisely, there is threshold in the iDMI value above which the trajectory is curved: here, skyrmions stabilized with iDMI coefficient above $|D| = 0.27$ mJ/m² (thus about 66% of D_C^N) have a curved trajectory. For some skyrmion which have a curved trajectory, we injected the current for a longer time, about $\delta t = 100$ ns in order to reach an eventual trajectory stabilization. The trajectory of these skyrmion are plotted in black in Fig. 6.19b. We have observed that the curved trajectory is a transitory

regime, which finally stabilizes (in what we called a steady trajectory in the following). For these curved trajectories, the skyrmion steady trajectory is along the same direction as a Néel skyrmion (as a CW Néel skyrmion in Fig. 6.19b but the same happens for the opposite chirality).

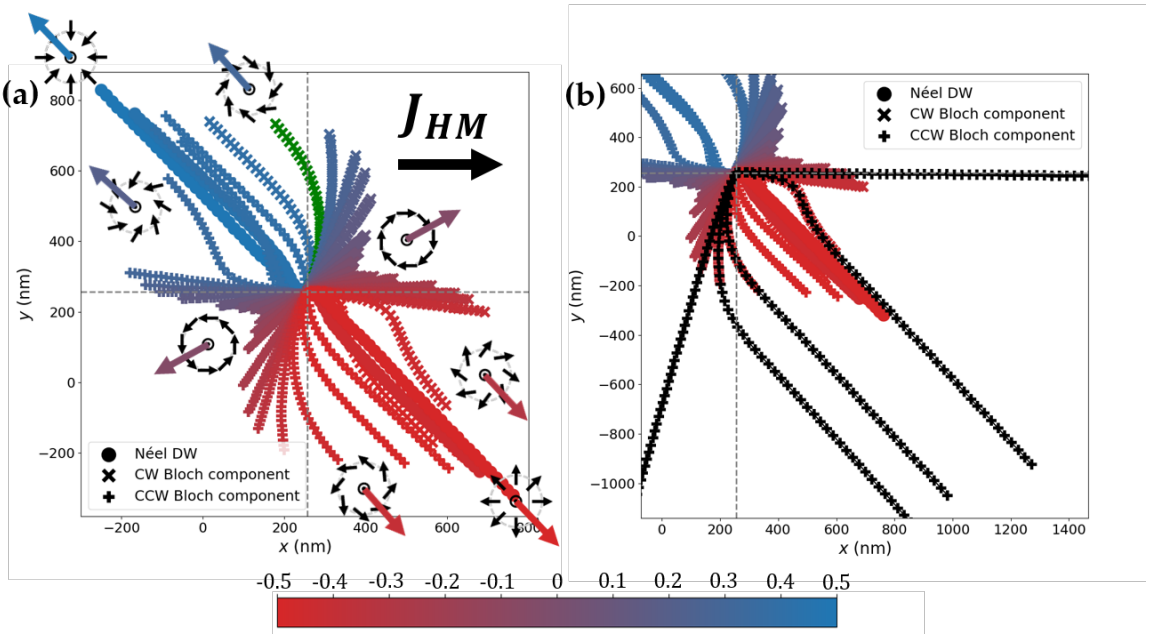

Figure 6.19: **Trajectories of skyrmions driven by spin orbit torque under high current density:** (a) Trajectories of skyrmions with different initial helicities, under the current density $\vec{J}_{HM}$ depicted by the black arrow. For some trajectories, the corresponding initial skyrmion configuration is represented right next to it. The green trajectories corresponds to the one shown in the zoom-in in Fig. 6.20a. (b) Zoomed out view of (a) with the trajectory of some skyrmion under a longer current injection time (black trajectories). After a transitory regime, curved trajectory stabilizes in the same direction as the trajectory of Néel skyrmions.

Since the computation time were long we applied the current during 30 ns for most of the simulation points, and only some of the data points (located around the threshold) are those from the longer current injection time. It decreases the computation time, with the counterpart that some skyrmions have not reached the steady trajectory. In Fig. 6.20b we show a zoom-in of the trajectory plotted in green in Fig. 6.19a: since it is curved, we have three possibilities to define the trajectory angle: (i) either we consider the tangent at the end of the trajectory (black dashed line), so called φ_{traj}^{end}, (ii) either we consider the tangent to the trajectory in the initial position (solid black line), so called φ_{traj}^{init} (iii) or we consider the angle formed by the line between the initial and final skyrmion position (dotted black line), so called φ_{traj}. The result from these three extraction methods are represented respectively in Fig. 6.20b, Fig. 6.20d and Fig. 6.20c. We suggest that the most relevant method of extraction consists in extracting the angle at the end of the trajectory, since it would describe the steady trajectory of skyrmion. Thus, in the following we focus on Fig. 6.20b. In this graph, the iDMI threshold after which skyrmions have the same steady trajectory as a Néel skyrmion corresponds to the plateau observed around $\xi = 0$ and $\xi = \pm\pi$ (depicted by a green dashed line).

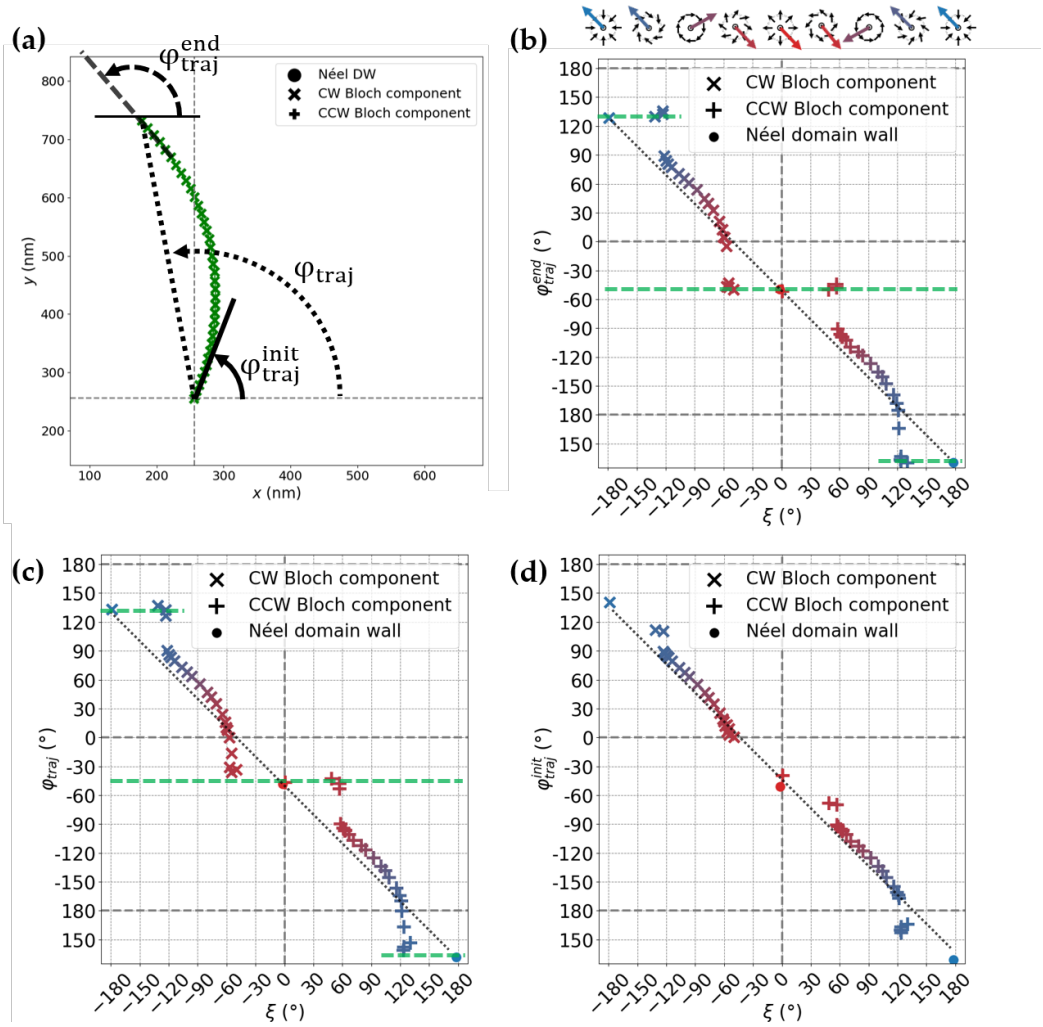

Figure 6.20: **Skyrmion trajectory angle versus DW helicity under high current density:** (a) Zoom in view of the trajectory shown in Fig. 6.19a, in order to define the three possibilities to define a trajectory angle : φ_{traj}^{end} (black dashed line), φ_{traj}^{init} (solid dashed line) and φ_{traj} (dotted dashed line). (b) Results for $\varphi_{traj}^{end}(\xi)$, (c) for $\varphi_{traj}(\xi)$ and (d) for $\varphi_{traj}^{init}(\xi)$

Here, it is important to notice that our analytical model, based on the Thiele equation, is no longer valid since we observed significant skyrmion deformation during the motion. Further studies are still necessary for a better understanding of these results; *e.g.* understanding the skyrmion deformation and the influence on the dynamics, define what is a high current density more quantitatively and elaborate a model that could reproduce these observations, and notably the observed threshold at which skyrmion are deflected towards the trajectory of a Néel skyrmion.

6.3 CONCLUSION

In this chapter I investigated the effects of an iDMI modulation on the skyrmion properties, and provided tools to predicts both the static and dynamic properties of the spin texture.

On the one hand, I showed in a first section that the equilibrium skyrmion configuration can be accurately tuned by a precise control of the iDMI. In particular, using micromagnetic simulation, I showed that the skyrmion helicity, radius and DW width can be adjusted by the iDMI coefficient. Moreover, by developing an analytical model, I unveiled the role of the competition between the iDMI and the magnetic volume charges in setting the equilibrium DW helicity. Although there is a discrepancy between the predicted an simulated iDMI value a which the DW is purely Néel, the model shows a good agreement with the simulations, as reminded in Fig. 6.21a.

On the other hand, I showed that this fine tuning of the skyrmion helicity can be used to realize a fine tuning of the skyrmion trajectory driven by spin orbit torque. Using micromagnetic simulations, I showed that the trajectory angle of the skyrmion can be adjusted by the helicity, and thus (indirectly) by the iDMI coefficient. Based on the Thiele equation, I developed an analytical model that predicts skyrmion trajectory as a function of its structural characteristics, completely defined by the 4 parameters (R, δ_{DW}, ξ,p), in addition to the magnetic damping α. The model shows an excellent agreement with the simulations, as reminded in Fig. 6.21b. We further observed in a regime of large current densities that non-Néel skyrmion can exhibit the same trajectory as Néel skyrmion. It could explain the Néel like motion experimentally observed in our sample although we measured very small iDMI coefficient ($|D| \simeq 10$ μJ/m²). This large current regime is still an ongoing work that has to be further studied.

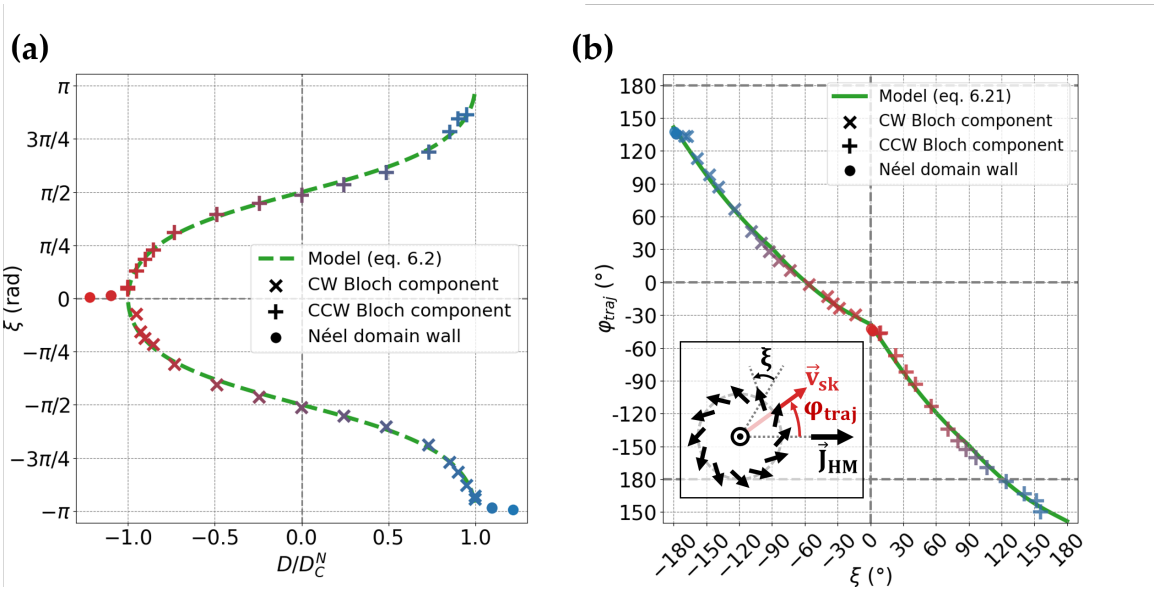

Figure 6.21: **Summary - Static and dynamic properties of skyrmion in low iDMI systems:** A fine tuning of the iDMI enables a fine control of both (a) the skyrmion equilibrium properties and (b) the skyrmion dynamics. In each case, we performed micromagnetic simulations (data points) that were compared to analytical model that we developed (green curve).

To summarize I have evidenced the crucial importance of a precise iDMI control, which sets both static and dynamics properties of skyrmion. In addition to the experimental work done in this thesis, the precise control of individual skyrmion properties becomes accessible and paves the way for highly-tunable skyrmion-based logic devices.

7

CONCLUSION AND PERSPECTIVES

This short chapter is dedicated to remind the main results obtained in this work and the perspectives of this project.

7.1 GENERAL CONCLUSION

In this thesis, I handled experimentally, analytically and numerically the properties of magnetic skyrmions and chiral domain walls in heavy-metal/ferromagnet/metal-oxide ($HM/FM/MO_x$) ultrathin trilayers.
After reminding the state of the art and the different experimental methods used, I presented in chapter 4 the magnetic sample and its properties: a crossed double wedge $Ta/FeCoB/TaO_x$ trilayer, in which the FeCoB and top Ta layers are two wedges perpendicular to each other. It combines many FeCoB thicknesses and oxidation levels of the $FeCoB/TaO_x$ interface, at the origin of a variety of magnetic configurations on the same sample, as a function of the position, namely paramagnetic (PM), out of plane magnetized (OOP) and in plane magnetized (IP). More importantly, we observed magnetic skyrmions in the OOP to PM and OOP to IP transition regions. It allows, on a single sample, to ensure the presence of magnetic skyrmions and to study their properties as a function of relevant parameters such as the FeCoB thickness and the $FeCoB/TaO_x$ interface oxidation level. Notably, I have highlighted the possibility to realize a fine material-dependent tuning of the iDMI. With direct BLS measurements and indirect spin-orbit driven skyrmion dynamic study, I have shown that not only the amplitude but also the sign of the iDMI could be tuned both by tuning the $FeCoB/TaO_x$ interface oxidation state or the FeCoB thickness.
In chapter 5, we have demonstrated experimentally a gate-voltage induced reversal of skyrmion chirality through the inversion of their current induced motion direction. Besides, we also observed a local, persistent and reversible chirality reversal of labyrinthine chiral domain walls by gate voltage. On the one hand, we have shown that the application of an homogeneous gate voltage leads to a uniform chirality reversal under the electrode. On the other hand, by applying a gradient of electric field under the electrode we were able to create a gradient of iDMI under the electrode, enabling a very fine control of the DW motion at a given position. We attributed this effect to the oxygen migration due to the gate voltage, associated to the dependence of the iDMI sign on the oxidation level of the $FeCoB/TaO_x$ interface. Indeed, in our capacitor geometry, the application of a positive (resp. negative) gate voltage leads to the reduction (resp. oxidation) of the $FeCoB/TaO_x$ in-

terface. Starting from a negative (resp. positive) iDMI for an oxidized (resp. underoxidized) interface, the application of a positive (resp. negative) gate voltage induces an inversion of the iDMI sign. Moreover, analytical calculations support the feasibility of a chirality reversal for skyrmions without annihilation since, for some material parameters, they can be stabilized by dipolar energy at zero iDMI.
Our experimental observations motivated a deeper study of the skyrmion chirality inversion under a fine control of iDMI amplitude and sign. In chapter 6, I investigated analytically and numerically the effects of an iDMI modulation on the skyrmion properties, and provided tools to predicts both the static and dynamic properties of these spin textures. On the one hand, I showed that the equilibrium skyrmion configuration can be accurately tuned by a precise control of the iDMI. In particular, using micromagnetic simulations, I showed that the skyrmion helicity, radius and DW width can be adjusted by the iDMI coefficient. Moreover, by developing an analytical model, I unveiled the role of the competition between the iDMI and the magnetic volume charges in setting the equilibrium DW helicity. On the other hand, I showed that this fine tuning of the skyrmion helicity can be used to realize a fine tuning of the skyrmion trajectory driven by spin orbit torque. Using micromagnetic simulations, I showed that the trajectory angle of the skyrmion can be adjusted by the helicity, and thus (indirectly) by the iDMI coefficient. Based on the Thiele equation, I developed an analytical model that predicts skyrmion trajectory as a function of its structural characteristics (radius, domain wall width, helicity and polarity), in addition to the magnetic damping.
In conclusion, this thesis work shows that the properties of magnetic skyrmions can be tuned locally and dynamically with a gate voltage, which has the other major advantage to be power efficient. Additionally, theoretical study through micromagnetic simulations and analytical model shows that it should be possible to realize a fine tuning of the skyrmion static and dynamic properties, without skyrmion annihilation when the iDMI goes to zero. The combination of our experimental, theoretical and numerical works provides tools for a potential precise control of individual skyrmion properties, thus paving the way for highly-tunable skyrmion-based logic devices.

7.2 PERSPECTIVES

In addition to answering many of the questions initially posed, this work has provided additional ones that bear interesting physics for further study.

All electrical, individual skyrmion manipulation and detection

In ongoing works, we are currently trying to reproduce the observations from the simulations, *i.e.* the individual and all-electrical skyrmion control. In that way, we are now studying the skyrmions dynamics in crossbar geometry as shown in Fig. 7.1. The width of the magnetic track (yellow contour in Fig. 7.1) was optimised to 5 μm by Johanna Fischer. It allows to isolate skyrmions and to move them individually in the horizontal track

by current injection (white arrow in Fig. 7.1). The aim is to obtain a unique skyrmion in the center of the crossbar, which is covered by an ITO electrode (dashed red contour). On the one hand, the crossbar geometry allows for the detection of individual skyrmion via anomalous Hall effect, which could enable to do the experiments on smaller and faster skyrmions. On the other hand, the ITO electrode aims at controlling the skyrmion structure in order to tune its dynamics by inverting its chirality and by controlling finely its internal structure. Notably, the major is to study more precisely the chirality inversion observed in my PhD work. Thus, it consists in isolating a unique skyrmion in the crossbar under the ITO and to invert its chirality with the gate voltage without its annihilation (let us remind that the skyrmion was lost during gate voltage application in the experiments I performed during my PhD). The ITO could also be used to stop skyrmion flow on demand, allowing to realize skyrmion-based synaptic devices. Such project is currently handled by Capucine Guéneau, who did her Master 2 internship at SPINTEC and is now starting her PhD in our team, working on the continuity of my PhD project.

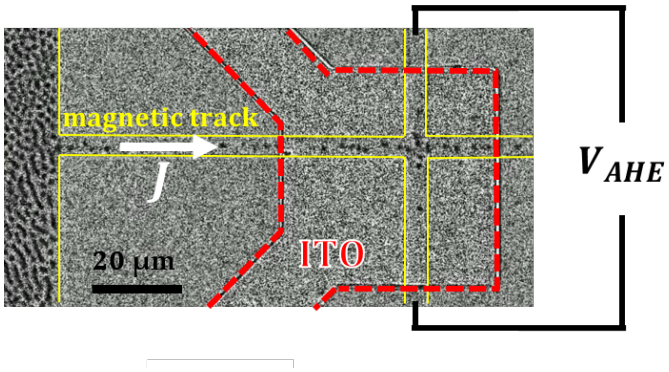

Figure 7.1: **Perspectives: Individual skyrmion detection in magnetic tracks:**

Logic gates based on the inversion of the chirality

In very recent work, it has been shown that skyrmion-based logic gates including AND, OR, NOT, NAND, NOR, XOR, and XNOR can be implemented and reconstructed by locally controlling the iDMI sign on a racetrack memory [19], as shown in Fig 7.2. Such result, associated to our experimental observation of gate control iDMI sign, would allow highly tunable, reconfigurable logic gates for efficient and small skyrmion-based logic devices.

Figure 7.2: **Perspectives: logic gates using the local control of skyrmion chirality:** (a) XOR (b) OR and (c) NOR logic gates, realized with spatial modulation of the iDMI sign on skyrmion based racetrack memory (extracted from [19])

Very sensitive magnetic sensors

As explained in chapter 4, the crossed double wedge Ta/FeCoB/TaO_x trilayer offers many different magnetic states on a single sample. Notably, in some regions where magnetic skyrmions are stabilized, the shape of the hysteresis loop shows a high sensitivity to external magnetic field (see Fig. 7.3a), making them promising for sensitive magnetic sensors. Using the anomalous Hall effect in the crossbar geometry (see Fig. 7.1), the magnetization is transcribed in an electric signal, which is thus very sensitive to the external magnetic field. In a second step, the skyrmionic layer will be integrated in a magnetic tunnel junction, for which we can expect a sensitivity up to 1000 %/mT and a detectivity as low as 0.5-3 nT/$\sqrt{\text{Hz}}$. This possibility to use skyrmions in very sensitive magnetic sensors will be handled by Johanna Fischer, newly hired as a CNRS researcher.

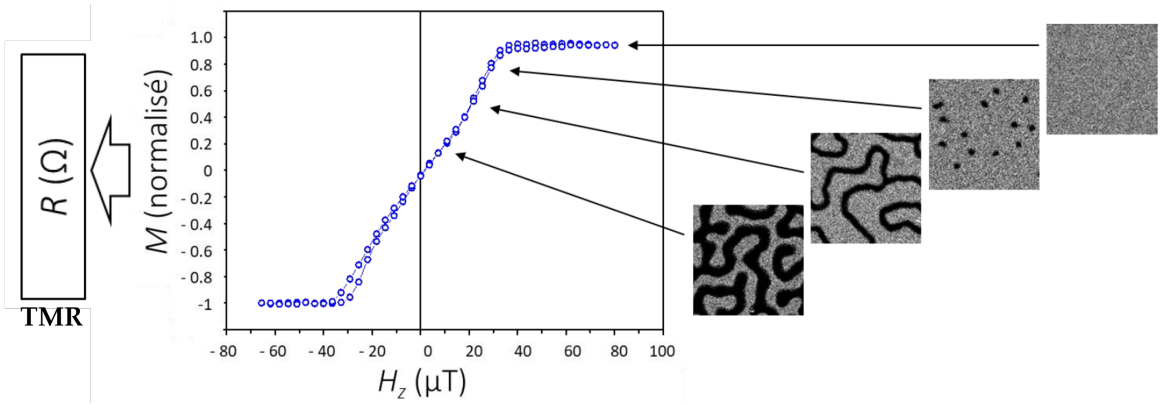

Figure 7.3: **Perspectives: highly sensitive and integrated magnetic skyrmion based sensor:** (Figure extracted from the project of Johanna Fischer) Typical hysteresis loop in some region of the sample where skyrmion are stabilized under a very small magnetic field. As a result, the magnetic state is very sensitive to small magnetic field, which could be implemented in new highly sensitive magnetic sensors via TMR measurements.

8

ANNEXES

8.1 ANNEX 1: MAGNETIC ENERGIES IN THE MICROMAGNETIC FRAMEWORK

In this section we derive the expression of the micromagnetic energies given in section **??**, using a simple cubic lattice of parameter a, as shown in Fig. 8.1. The method remains the same for each interaction: the energy at the atomic site i is computed and then summed over all the sites of the magnetic material.

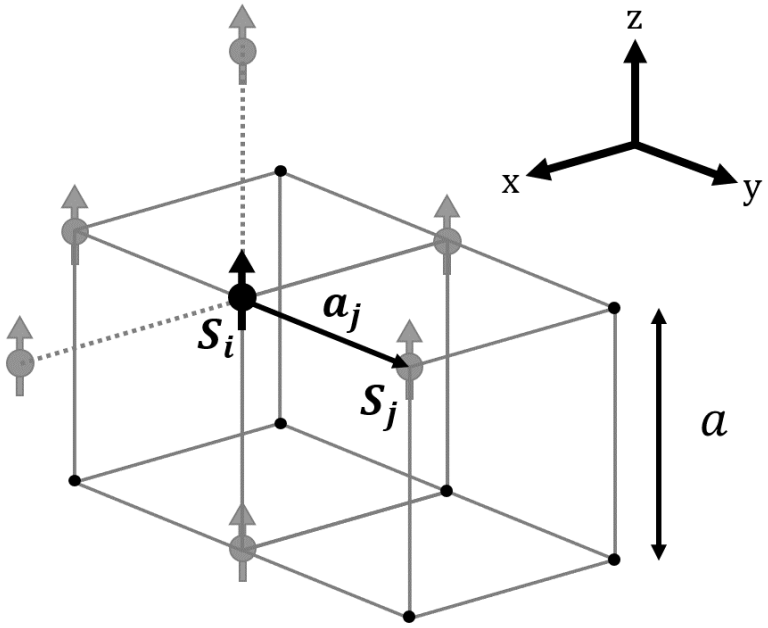

Figure 8.1: Simple cubic lattice considered for the calculation of the energies in the micromagnetic framework.

8.1.1 *The exchange energy*

Let's consider a simple cubic lattice as shown in Fig. 8.1 The exchange energy of a unit cell is obtained by summing the atomistic echange energy (defined in eq. 1.2 from chapter 1) over the 6 first neighbouring spins:

$$\epsilon^i_{exch} = -\sum_{j=1}^{6} J_{ij}\vec{S}_i \cdot \vec{S}_j \tag{8.1}$$

In the micromagnetic framework we introduce a continuous magnetization field $\vec{m}$ and we set $\vec{S}_i = \vec{m}(x_i) = \vec{m}_i$ and $\vec{S}_j = \vec{m}(x_i + \vec{a}_j)$. A Taylor expansion around site i gives:

$$\vec{m}(x_i + \vec{a}_j) = \vec{m}_i + a_j\frac{d\vec{m}_i}{dx} + b_j\frac{d\vec{m}_i}{dy} + c_j\frac{d\vec{m}_i}{dz} + \frac{1}{2}\left(a_j^2\frac{d^2\vec{m}_i}{dx^2} + b_j^2\frac{d^2\vec{m}_i}{dy^2} + c_j^2\frac{d^2\vec{m}_i}{dz^2}\right) + \mathcal{O}(a^3) \tag{8.2}$$

where $\vec{a}_j = \left(a_j, b_j, c_j\right)^T$ is the vector connecting sites in $\vec{x}_i$ and $\vec{x}_i + \vec{a}_j$. In this simple cubic model, only the first neighbouring spins are considered and thus $\vec{a}_j$ takes the value $\vec{a}_j = \left(\pm a_j, 0, 0\right)^T$, $\vec{a}_j = \left(0, \pm b_j, 0\right)^T$ or $\vec{a}_j = \left(0, 0, \pm c_j\right)^T$ where $|a_j| = |b_j| = |c_j| = a$. Thus, in this model for all vector $\vec{a}_j$ there exist a vector $-\vec{a}_j$ so that the first order terms in 8.2 vanish after summation. Thus, in the next expression, only remains the quadratic terms and the constant term $\vec{m}_i \cdot \vec{m}_i$ is neglected as it represents only an offset. Considering an homogeneous and isotropic sample, *ie* $J_{ij} = J\forall(i,j)$, one gets the exchange energy for a unit cell

$$\epsilon^i_{exch} = -2JS^2a^2\vec{m}_i \cdot \left(\frac{d^2\vec{m}_i}{dx^2} + \frac{d^2\vec{m}_i}{dy^2} + \frac{d^2\vec{m}_i}{dz^2}\right) \tag{8.3}$$

where $|\vec{S}_i| = |\vec{S}_j| = S$. By differentiating $\vec{m} \cdot \vec{m} = 1$ twice with respect to x, one can get

$$\vec{m} \cdot \frac{d\vec{m}}{dx} = -\left(\frac{d\vec{m}}{dx}\right)^2 \tag{8.4}$$

so that

$$\epsilon^i_{exch} = 2JS^2a^2\left[\left(\frac{d\vec{m}_i}{dx}\right)^2 + \left(\frac{d\vec{m}_i}{dy}\right)^2 + \left(\frac{d\vec{m}_i}{dz}\right)^2\right] \tag{8.5}$$

The exchange energy is obtained by summation over the unit cells, and dividing by two to avoid counting twice each pair of atoms

$$E_{exch} = \sum_i \epsilon^i_{exch} = \frac{JS^2}{a}\sum_i a^3\left[\left(\frac{d\vec{m}_i}{dx}\right)^2 + \left(\frac{d\vec{m}_i}{dy}\right)^2 + \left(\frac{d\vec{m}_i}{dz}\right)^2\right] \tag{8.6}$$

In the continuous approach of micromagnetism, the summation is replaced by an integral over the volume of magnetic material so that the exchange energy reads like

$$E_{exch} = A_{ex}\int_V \left[\left(\frac{d\vec{m}}{dx}\right)^2 + \left(\frac{d\vec{m}}{dy}\right)^2 + \left(\frac{d\vec{m}}{dz}\right)^2\right] dV \tag{8.7}$$

where $A_{ex} = \frac{JS^2}{a}n$ (in J/m) is the exchange stiffness constant, with n the number of atoms per unit cell. Finally, expanding the integrand and rearranging it gives the expression of the exchange energy in the micromagnetic framework:

$$E_{exch} = A_{ex}\int_V \left[\left(\vec{\nabla}m_x\right)^2 + \left(\vec{\nabla}m_y\right)^2 + \left(\vec{\nabla}m_z\right)^2\right] dV \tag{8.8}$$

8.1.2 *The interfacial Dzyaloshinskii-Moriya energy*

To determine the expression of the iDMI interaction in the micromagnetic framework, the technique is the same as in the previous section about the exchange energy. The energy of a unit cell is given by summing the atomistic iDMI energy defined in eq. 1.14 from chapter 1 over the first neighbours:

$$\epsilon^i_{iDMI} = \sum_{j=1}^{6} \vec{d}_{ij} \cdot \left(\vec{S}_i \times \vec{S}_j\right) \tag{8.9}$$

with $\vec{d}_{ij} = d(\vec{z} \times \vec{r}_{ij})$, where $\vec{z}$ is the outward normal to the film plane and $\vec{r}_{ij}$ the normalized vector connecting atomic sites i and j. Thus, the orientation of $\vec{d}_{ij}$ depends on the neighbouring spin that is considered, and on the sign of the atomistic iDMI constant

d. It important to notice that $\vec{d_{ij}} = \vec{0}$ for $\vec{r_{ij}} = \pm\vec{z}$, so that it is sufficient to restrict ourselves to the (x, y) plane.
In this (x, y) plane one has $\vec{d_{ij}} = (0, \pm d)^T$ for $\vec{a_j} = (\pm a_j, 0)^T$ and $\vec{d_{ij}} = (\pm d, 0)^T$ for $\vec{a_j} = (0, \mp b_j)^T$. The iDMI vectors are depicted in Fig. 8.2a for $d > 0$ (blue arrows) and in Fig. 8.2b for $d < 0$ (dotted red arrows). The four neighbouring spins of atomic site i are represented in each case, and they are oriented so that it minimizes the iDMI interaction of the considered pair. It is very interesting to notice that, even with these simple calculations, an homochiral spin texture appears and looks like Néel skyrmion, CW for $d > 0$ (Fig. 8.2a) and CCW for $d < 0$ (Fig. 8.2b).

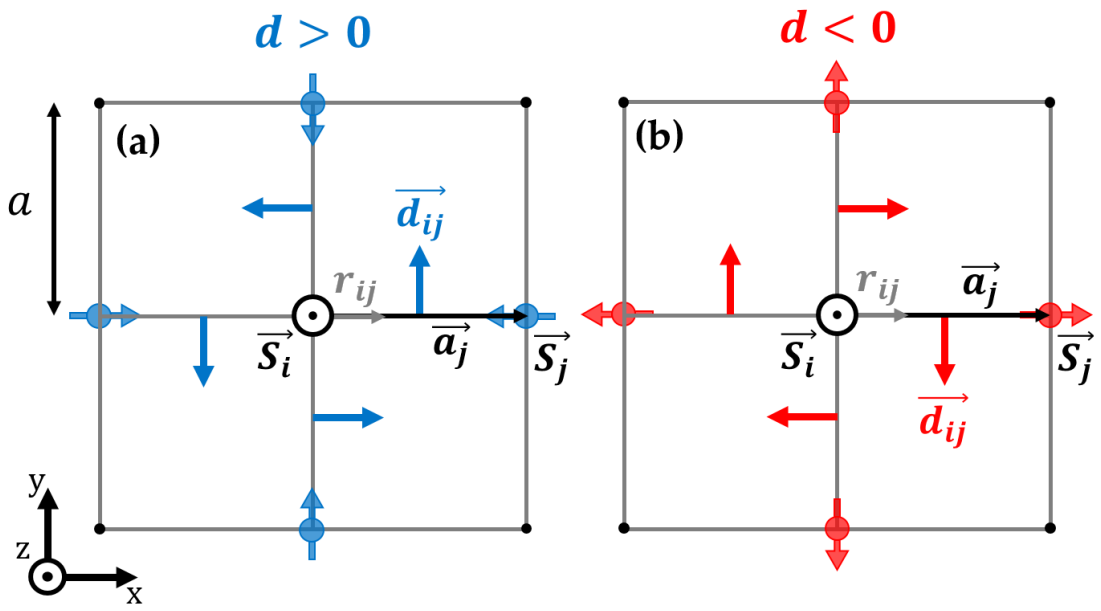

Figure 8.2: Square Lattice for calculation of the micromagnetic iDMI energy

Since the direction of $\vec{d_{ij}}$ depends of the neigbours, as explained above, the quadratic terms in the Taylor expansion vanish during the summation and the iDMI energy for a unit cell is equal to

$$\epsilon^i_{iDMI} = 2adS^2 \left[\vec{y} \cdot \left(\vec{m}_i \times \frac{d\vec{m}_i}{dx} \right) - \vec{x} \cdot \left(\vec{m}_i \times \frac{d\vec{m}_i}{dy} \right) \right] \tag{8.10}$$

Thus the total iDMI energy can be obtained by summing over the unit cell

$$E_{iDMI} = \sum_i \epsilon^i_{iDMI} = \frac{2dS^2}{at_{FM}} \sum_i a^2 t_{FM} \left[\vec{y} \cdot \left(\vec{m}_i \times \frac{d\vec{m}_i}{dx} \right) - \vec{x} \cdot \left(\vec{m}_i \times \frac{d\vec{m}_i}{dy} \right) \right] \tag{8.11}$$

where t_{FM} is the film thickness. In the continuous framework of micromagnetism it gives

$$E_{iDMI} = D \int_V \left[\vec{y} \cdot \left(\vec{m} \times \frac{d\vec{m}}{dx} \right) - \vec{x} \cdot \left(\vec{m} \times \frac{d\vec{m}}{dy} \right) \right] dV \tag{8.12}$$

where $D = \frac{dS^2}{at_{FM}} n$ the iDMI constant. If one defines $\vec{m}_\perp = (m_x, m_y)^T$, then expanding and rearranging the integrand of eq. 8.12 leads to

$$E_{iDMI} = D \int_V \left(m_z(\vec{\nabla} \cdot \vec{m_\perp}) - (\vec{m_\perp} \cdot \vec{\nabla}) m_z \right) dV \tag{8.13}$$

8.1.3 *One dimensionnal model*

Here we demonstrate the energy terms that will allow to determine the magnetic domain wall profile and energy in section 8.3.2.
In the following we consider a simple $1D$-model of a DW in which the magnetization rotates from $+\vec{z}$ to $-\vec{z}$ along the $\vec{x}$ direction (see Fig. 8.3). The magnetization inside the DW can be tilted by an angle ξ, called the helicity, defined in section 2.1 from chapter 2, and shown in Fig. 8.3(b,c). As a reminder, a Bloch DW is defined by $\xi = \pm\frac{\pi}{2}$ (Fig. 8.3c) while a Néel DW is defined by $\xi = 0$ (CW) (Fig. 8.3a) or $\xi = \pm\pi$ (CCW). The intermediate helicities define what is called a Dzyaloshinskii wall (Fig. 8.3b), as explained in section section 2.1 from chapter 2.

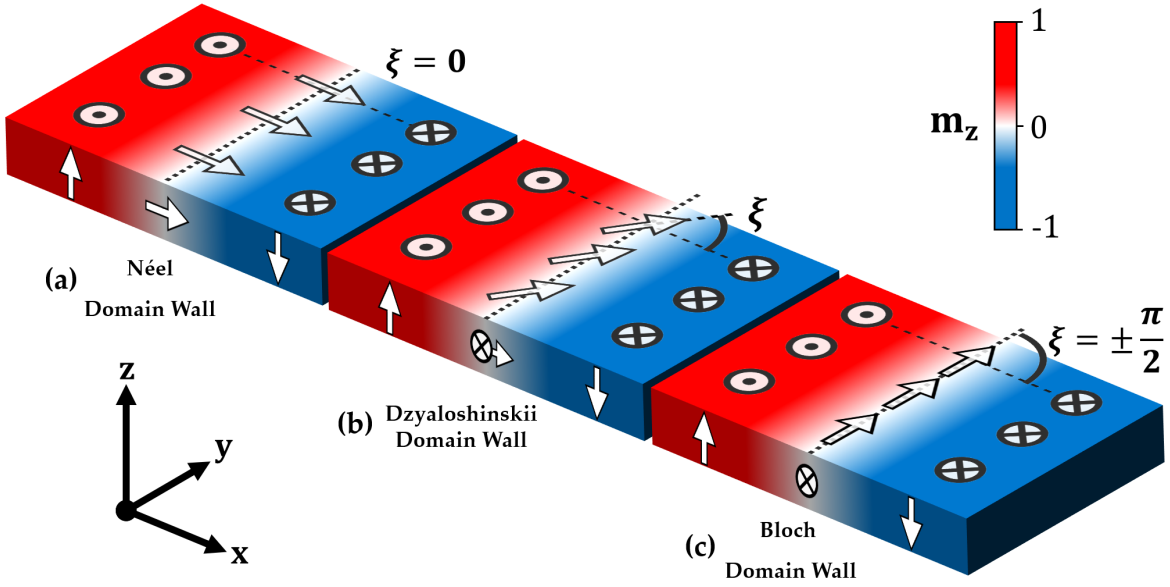

Figure 8.3: Sketch of the DW considered for the 1D model in the case of (a) a Néel DW, (b) an intermediate Dzyaloshinskii DW and (c) a Bloch DW.

Thus, the expression of the magnetization vector reads

$$\vec{m} = \begin{pmatrix} m_x(\theta(x), \xi) \\ m_y(\theta(x), \xi) \\ m_z(\theta(x), \xi) \end{pmatrix} = \begin{pmatrix} \sin\theta(x)\cos\xi \\ \sin\theta(x)\sin\xi \\ \cos\theta(x) \end{pmatrix} \tag{8.14}$$

where $\theta(x)$ is the DW profile and ξ is the helicity. In this model we assume that ξ does not depend on x. Thus, using eq. 1.3 from chapter 1, the expression of the exchange interaction can easily be obtained

$$\epsilon_{exch} = A_{ex}\left[\left(\frac{dm_x}{dx}\right)^2 + \left(\frac{dm_y}{dx}\right)^2 + \left(\frac{dm_z}{dx}\right)^2\right] \tag{8.15}$$

$$= A_{ex}\left[\left(\frac{d}{dx}(\sin\theta(x)\cos\xi)\right)^2 + \left(\frac{d}{dx}(\sin\theta(x)\sin\xi)\right)^2 + \left(\frac{d}{dx}\cos\theta(x)\right)^2\right] \tag{8.16}$$

$$= A_{ex}\left[\cos^2\xi\left(\frac{d}{dx}\sin\theta(x)\right)^2 + \sin^2\xi\left(\frac{d}{dx}\sin\theta(x)\right)^2 + \left(\frac{d}{dx}\cos\theta(x)\right)^2\right] \tag{8.17}$$

$$= A_{ex}\left[\cos^2\xi\cos^2\theta(x)\left(\frac{d\theta(x)}{dx}\right)^2 + \sin^2\xi\cos^2\theta(x)\left(\frac{d\theta(x)}{dx}\right)^2 + \sin^2\theta(x)\left(\frac{d\theta(x)}{dx}\right)^2\right] \tag{8.18}$$

$$= A_{ex}\left(\frac{d\theta(x)}{dx}\right)^2 \tag{8.19}$$

For the iDMI energy, one starts from eq. 1.14 from chapter 1 and follows the same technique as for the exchange. After some derivatives one gets :

$$\epsilon_{iDMI} = D\left[m_z\frac{dm_x}{dx} - m_x\frac{dm_z}{dx}\right] \tag{8.20}$$

$$= D\cos\xi\frac{d\theta(x)}{dx} \tag{8.21}$$

It is interesting to notice that the helicity ξ appears in the iDMI energy while it does not in the exchange energy. In fact, this is a signature that the iDMI interaction is a chiral interaction while the symmetric exchange is not.

8.2 ANNEX 2: THE SPIN-ORBIT COUPLING

8.2.1 *The orbital and spin moment*

One can find the expression of the orbital momentum of the electron with a very intuitive technique. In the Bohr model for the atom, the electron has a circular orbit around the nucleus, thus it can be seen as a current loop that will create a little magnetic field, which will be called the orbital magnetic momentum.

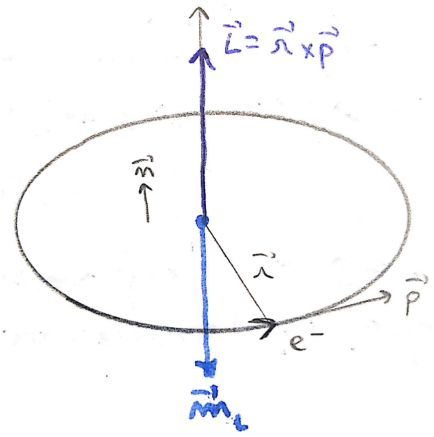

Figure 8.4: Motion of the electron (current loop) in the Bohr model for the atom

Let's consider the loop is filiform. Hence, it creates a magnetic moment $\vec{m} = IS\vec{n}$ where I is the current in the loop, S is the loop's surface and $\vec{n}$ the normal to this surface. Like $I = \frac{Q}{t}$ where Q is the charge and t the time, we can calculate the current for one period of the electron : $I = \frac{-|e|}{\frac{2\pi r}{v}} = -\frac{|e|v}{2\pi r}$. The surface is $S = \pi r^2$ so that $\vec{m} = -\frac{|e|rv}{2}\vec{n} = -\frac{|e|}{2m_e}r(m_e v)\vec{n}$. Finally we have $\vec{m} = -\frac{|e|}{2m_e}\vec{r} \times \vec{p} = -\frac{|e|}{2m_e}\vec{L}$ where $\vec{L}$ is the angular momentum of the electron, that creates a magnetic moment $\vec{m}$ because of its charge $-|e|$. We can write it in a more elegant way, noting that $\frac{|e|}{2m_e} = \frac{\mu_B}{\hbar} = \gamma_L$. Finally,

$$\vec{m_L} = \gamma_L \vec{L} = -\mu_B \frac{\vec{L}}{\hbar}$$

But the orbital magnetic moment is not the only one that exists. For example if it was the case, the hydrogen atom wouldn't be magnetic (s shell so that $l = 0$ and hence $m_L = 0$). Another contribution to the magnetic moment of an atom is the spin magnetic moment, that is :

$$\vec{m_S} = \gamma_S \vec{S} = 2\mu_B \frac{\vec{S}}{\hbar}$$

In a more general notation we have :

$$\vec{m_\alpha} = -g_\alpha \mu_B \frac{\vec{K_\alpha}}{\hbar}$$

Where g_α is the Landé factor for the corresponding magnetic moment. For $\alpha = L$ (orbital momentum) then $\vec{K_L} = \vec{L}$ and $g_L = 1$ and for $\alpha = S$ (spin momentum) then $\vec{K_S} = \vec{S}$ and $g_S = -2$.

8.2.2 *The Lorentz transformations for Electric and magnetic field*

The spin orbit coupling is the result of the motion of the electron in the electric field of the material or around the nucleus. And when two inertial[1] frame move relative to each other, the transformation of the electric and eagnetic field are the following :

$$\begin{aligned} \vec{E'_\parallel} &= \vec{E_\parallel} \\ \vec{E'_\perp} &= \gamma\left(\vec{E_\perp} + \vec{v}\times\vec{B}\right) \\ \vec{B'_\parallel} &= \vec{B_\parallel} \\ \vec{B'_\perp} &= \gamma\left(\vec{B_\perp} - \frac{\vec{v}\times\vec{E}}{c^2}\right) \end{aligned} \quad \Longleftrightarrow \quad \begin{aligned} \vec{E_\parallel} &= \vec{E'_\parallel} \\ \vec{E_\perp} &= \gamma\left(\vec{E'_\perp} - \vec{v}\times\vec{B}\right) \\ \vec{B_\parallel} &= \vec{B'_\parallel} \\ \vec{B_\perp} &= \gamma\left(\vec{B'_\perp} + \frac{\vec{v}\times\vec{E}}{c^2}\right) \end{aligned}$$

So that we can estimate the spin orbit's correction to the energy with these transformations.

8.2.3 *Spin-Orbit Correction to the Energy*

Imagine an electron moving in a solid. It will undergo the electric field of the nuclei because of the extension of its wave fonction into the electronic cloud. And, from the previous section we know that the motion of the electron in the electric field will induce a non-zero magnetic field in its rest frame :

$$\vec{B'_\perp} = -\gamma\frac{\vec{v}\times\vec{E}}{c^2}$$

And because we are interested in the non relativistic case, $\gamma \overset{v\ll c}{\simeq} 1$ so that

$$\vec{B'_\perp} = \vec{B_{SO}} = -\frac{\vec{v}\times\vec{E}}{c^2} \tag{8.22}$$

The interaction of this rest frame magnetic field with the electron's spin ($\vec{m_S} = 2\mu_B\frac{\vec{S}}{\hbar}$) can be seen as a Zeeman coupling with energy contribution :

$$\begin{aligned} E_{SO} &= -\vec{m_S}.\vec{B_{SO}} \\ &= -\frac{2\mu_B}{\hbar c^2}\vec{S}.(\vec{v}\times\vec{E}) \end{aligned}$$

If we assume a central field of the Coulomb form, **ie** $\vec{E} = -\frac{\partial V(r)}{\partial r}\frac{\vec{r}}{r}$ we have :

1 An electron moving around a nucleus is not in an inertial frame, this effect will be discussed later

$$
\begin{aligned}
E_{SO} &= -\frac{2\mu_B}{\hbar c^2}\vec{S}.(\vec{v}\times -\frac{\partial V(r)}{\partial r}\frac{\vec{r}}{r}) \\
&= \frac{2\mu_B}{\hbar c^2}\frac{1}{r}\frac{\partial V(r)}{\partial r}\vec{S}.(\vec{v}\times\vec{r}) \\
&= -\frac{2\mu_B}{\hbar m_e c^2}\frac{1}{r}\frac{\partial V(r)}{\partial r}\vec{S}.(\vec{r}\times\vec{p}) \\
E_{SO} &= -\frac{2\mu_B}{\hbar m_e c^2}\frac{1}{r}\frac{\partial V(r)}{\partial r}\vec{L}.\vec{S}
\end{aligned}
$$

So the fact that the electron is moving is the nucleus field induce a coupling of the form $\vec{L}.\vec{S}$. One of the most known consequence is the fine structure of the electron energy levels. But in the experiments, a factor $\frac{1}{2}$ takes place, and is not derived here, it is called the Thomas's precession and is due to the fact that the electron is not in an intertials frame when rotating around the nucleus. Hence, the use of the Lorentz tranformations is not adapted. One has two solutions two fix the problem, the one from Thomas and another, with hands, but very elegant.

Thomas has consider two kinds of transformations : an infinitesimal Lorentz boost (translation) followed by an infinitesimal rotation, and the factor $\frac{1}{2}$ naturally occured. One can find the calculation in the Jackson [224].

Another way is described in the following, and comes from the article of Kroemer [225]. The electron moves circularly around the nucleus so that the Lorentz tranformation cannot be used because the elctron undergo the Coulomb force $\vec{F} = q\vec{E}$. The idea is to add a magnetic field so that the Lorentz force balance the Coulomb force and so that the Lorentz transformation can be used. The additionnal magnetic field in such as

$$
\vec{F} = q\left(\vec{E} + \vec{v}\times\vec{B}\right) = \vec{0} \qquad \Longleftrightarrow \qquad \vec{E} = -\vec{v}\times\vec{B}
$$

and this additionnal field will correct the factor $\frac{1}{2}$.

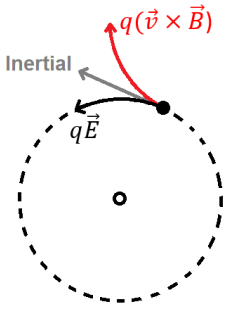

Figure 8.5: Illustration for the additionnal magnetic field to use correctly the Lorentz transformation.

In the rest frame of the electron, the magnetic field is, this time

$$\vec{B_\perp^{'}} = \gamma\left(\vec{B_\perp} - \frac{\vec{v}\times\vec{E}}{c^2}\right)$$

Let's take, without any loss of generality $\vec{B} = B_z\vec{u_z}$, $\vec{E} = E_y\vec{u_y}$ and then $\vec{v} = v_x\vec{u_x}$. We hence have $\vec{E} = v_xB_z\vec{u_y}$ and so :

$$\begin{aligned}\vec{B_\perp^{'}} &= B_z^{'}\vec{u_z}\\ &= \gamma\left(B_z - \frac{v_xE_y}{c^2}\right)\vec{u_z}\\ &= \gamma B_z\left(1-\frac{v_x^2}{c^2}\right)\vec{u_z}\\ &= B_z\sqrt{1-\frac{v_x^2}{c^2}}\end{aligned}$$

We consider the nonrelativistic case where $v \ll c$ so that we can expand the square root in power of $\left(\frac{v}{c}\right)^2$:

$$\begin{aligned}\vec{B_\perp^{'}} &= B_z\sqrt{1-\frac{v_x^2}{c^2}}\vec{u_z}\\ &= B_z\left(1-\frac{1}{2}\frac{v_x^2}{c^2} - \frac{3}{8}\left(\frac{v_x^2}{c^2}\right)^2 + ...\right)\vec{u_z}\\ &\simeq B_z\left(1-\frac{1}{2}\frac{v_x^2}{c^2}\right)\vec{u_z}\\ &= \left(B_z - \frac{1}{2}\frac{B_zv_x^2}{c^2}\right)\vec{u_z}\\ &= \left(B_z - \frac{1}{2}\frac{v_xE_y}{c^2}\right)\vec{u_z}\end{aligned}$$

Or, in vectorial form :

$$\vec{B_\perp^{'}} = \vec{B_\perp} - \frac{1}{2}\frac{\vec{v}\times\vec{E}}{c^2}$$

The only difference with equation 8.22 is the factor $\frac{1}{2}$ that is necessary to get the true expression :

$$E_{SO} = -\frac{\mu_B}{\hbar m_e c^2}\frac{1}{r}\frac{\partial V(r)}{\partial r}\vec{L}.\vec{S}$$

8.3 ANNEX 3: MAGNETIC DOMAIN WALL PROFILE

8.3.1 *Euler's equation and variationnal principle*

The micromagnetic energy can be seen as a functionnal[2] of the magnetization configuration $\vec{\mathbf{m}}(\mathbf{r})$, such as

$$E\left[\mathbf{m}(\mathbf{r})\right] = \int F\left[\mathbf{m}(\mathbf{r}), \partial_{\mathbf{r}}\mathbf{m}(\mathbf{r})\right] d\mathbf{r}$$

Where F contains all the energy terms under their micromagnetic form. In a simple 1D model with out of plane anisotropy, the magnetization configuration can be described by the angle θ between it and the normal to the plane of the magnetization.

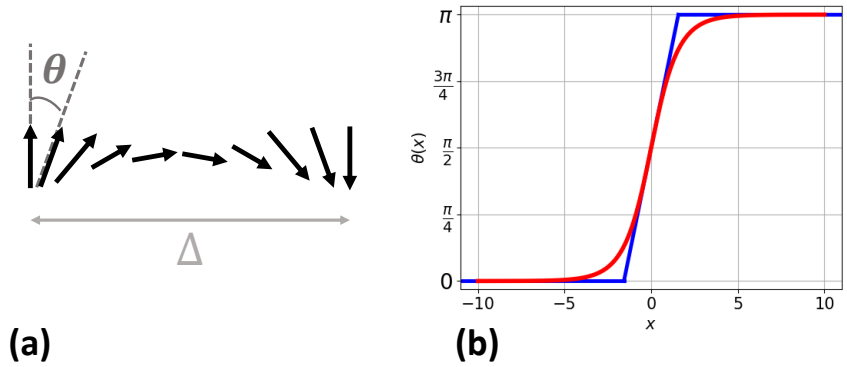

Figure 8.6: (a) Néél domain wall, of length Δ, and (b) two possible profile for the magnetization inside the domain wall.

The aim of the variationnal method is to find the magnetization profile that minimizes the energy of the domain wall. An infinity of solutions are possible but only one gives a minimal energy. On the previous figure are drawn to possible profiles, the blue one is a simple linear profile and the red one is the exact solution that gives the minimal energy, as we will see. The functional is transformed into

$$E\left[\theta(x)\right] = \int_A^B F\left[\theta(x), \partial_x\theta(x)\right] dx$$

The idea is to induce an infinitesimal change in the profile, $\varepsilon\delta\theta(x)$, keeping the boundaries fixed, $\delta\theta(A,B) = 0$. In other word the functionnal derivative with respect to θ is zero for the $\theta(x)$ that minimizes the energy. The definition of the functionnal derivative is:

$$\lim_{\varepsilon\to 0} \frac{E\left[\theta(x) + \varepsilon\delta\theta(x)\right] - E\left[\theta(x)\right]}{\varepsilon} := \int_A^B \delta\theta(x)\frac{\delta E}{\delta\theta} dx \tag{8.23}$$

And the condition for minimization is $\frac{\delta E}{\delta\theta} = 0$. The latter expression yields the Euler equation, as it is shown in the following.

2 A function of a function

Doing this we have

$$\begin{aligned} E\left[\theta+\varepsilon\delta\theta\right] &= \int_A^B F\left[\theta+\varepsilon\delta\theta, \partial_x\left(\theta+\varepsilon\delta\theta\right)\right] dx \\ &= \int_A^B F\left[\theta+\varepsilon\delta\theta, \partial_x\theta+\varepsilon\partial_x\delta\theta\right] dx \\ &= \int_A^B \left[F\left[\theta, \partial_x\theta\right] + \varepsilon\delta\theta\frac{\partial F}{\partial\theta} + \varepsilon\partial_x\delta\theta\frac{\partial F}{\partial\left(\partial_x\theta\right)} + \mathcal{O}(\varepsilon^2)\right] dx \end{aligned}$$

We neglect the order greater than 2 because the limit will automatically vanish them. The last term can be integrated by parts such as

$$\int_A^B \varepsilon\partial_x\delta\theta\frac{\partial F}{\partial\left(\partial_x\theta\right)}dx = \left[\varepsilon\delta\theta\frac{\partial F}{\partial\left(\partial_x\theta\right)}\right]_A^B - \int_A^B \varepsilon\delta\theta\partial_x\left(\frac{\partial F}{\partial\left(\partial_x\theta\right)}\right) dx$$

So that finally,

$$E\left[\theta+\delta\theta\right] = \int_A^B \left[F\left[\theta, \partial_x\theta\right] + \delta\theta\frac{\partial F}{\partial\theta} - \delta\theta\partial_x\left(\frac{\partial F}{\partial\left(\partial_x\theta\right)}\right)\right] dx + \left[\delta\theta\frac{\partial F}{\partial\left(\partial_x\theta\right)}\right]_A^B$$

Using the definition of the functionnal derivative:

$$\begin{aligned} \lim_{\varepsilon\to 0}\frac{E\left[\theta+\varepsilon\delta\theta\right]-E\left[\theta\right]}{\varepsilon} &:= \int_A^B \delta\theta(x)\frac{\delta E}{\delta\theta}dx \\ \int_A^B \delta\theta\left[\frac{\partial F}{\partial\theta} - \partial_x\left(\frac{\partial F}{\partial\left(\partial_x\theta\right)}\right)\right] dx + \left[\delta\theta\frac{\partial F}{\partial\left(\partial_x\theta\right)}\right]_A^B &:= \int_A^B \delta\theta(x)\frac{\delta E}{\delta\theta}dx \end{aligned}$$

For this to be true, we obtain two solutions:

$$\begin{cases} \frac{\delta E}{\delta\theta} = \frac{\partial F}{\partial\theta} - \partial_x\left(\frac{\partial F}{\partial(\partial_x\theta)}\right) = 0 & \text{for} \quad A < x < B \\ \left.\frac{\partial F}{\partial(\partial_x\theta)}\right|_{(A,B)} = 0 & \text{in} \quad x = A \quad \text{or} \quad x = B \end{cases} \tag{8.24}$$

The first one is the well-known Euler-Lagrange equation for the density of energy F and the second is a boundary equation. The resolution of these equations gives the energetically optimized profile $\theta(x)$. Let's now applicate these expressions to the case of a magnetic domain wall.

Another faster method is to say that if $\theta(x)$ minimizes the energy hence $E\left[\theta+\delta\theta\right] - E\left[\theta\right] = 0$, that is an other way to find the Euler's equation. We do the same thing but in a form a little bit different.

8.3.2 *Exact profile resolution*

Let's first consider the case without DMI, in order to determine the energy of a classical Bloch domain wall. In this case,

$$F\left[\theta, \partial_x\theta\right] = A\left(\partial_x\theta\right)^2 + K_{eff}\sin^2(\theta)$$

Where the first term is the micromagnetic exchange density of energy and the second contains the contributions of the anisotropies. The applications of the Euler's equation gives

$$\frac{\partial F}{\partial\theta} - \partial_x\left(\frac{\partial F}{\partial\left(\partial_x\theta\right)}\right) = 2K_{eff}\sin\theta\cos\theta - 2A\partial_x^2\theta = 0 \quad \longleftrightarrow \quad \frac{d^2\theta(x)}{dx^2} = \frac{\sin\theta\cos\theta}{\Delta^2}$$

Where $\Delta = \sqrt{\frac{A}{K_{eff}}}$ is the caracteristic width of the domain wall. One can see that the domain with is the result of the competition between the exchange and the anisotropy. If the exchange is great, the length of the domain is increasing because it wants the spins to be parallel. On the contrary, the aniso want the spins to be along a certain direction, so the greater it is, the smaller is the domain wall width. Multiplying the last equation by $\frac{d\theta(x)}{dx}$ and integrating yields

$$\begin{aligned}
\int \frac{d\theta(x)}{dx}\frac{d^2\theta(x)}{dx^2}dx &= \int \frac{d\theta(x)}{dx}\frac{\sin\theta\cos\theta}{\Delta^2}dx \\
\frac{1}{2}\int \frac{d}{dx}\left(\frac{d\theta(x)}{dx}\right)^2 dx &= \frac{1}{2}\frac{\sin^2\theta}{\Delta^2} \\
\left(\frac{d\theta(x)}{dx}\right)^2 &= \frac{\sin^2(\theta)}{\Delta^2} + C_1
\end{aligned}$$

The integration constant can be taken as $C_1 = 0$ without loss of generality. In this case we have

$$\frac{d\theta}{dx} = \pm\frac{\sin\theta}{\Delta} \quad \text{or} \quad \frac{d\theta}{\sin\theta} = \pm\frac{dx}{\Delta}$$

Let's introduce $t = \tan\frac{\theta}{2}$ so that $dt = d\theta\left(1+\tan^2\frac{\theta}{2}\right) = d\theta\left(1+t^2\right)$ and $\sin\theta = \frac{2t}{1+t^2}$, hence it simplifies the calculations and the previous eguality becomes

$$\frac{dt}{t} = \pm\frac{dx}{\Delta} \quad \longleftrightarrow \quad \pm\frac{x-x_0}{\Delta} = \ln t$$

And finally we obtain the optimal profile for the magnetization:

$$\theta(x) = 2\tan^{-1}\left(e^{\pm\frac{x-x_0}{\Delta}}\right)$$

So that it's now possible to calculate the energy of the domain wall, knowing $\sin\theta(x) = \frac{1}{\cosh\left(\pm\frac{x-x_0}{\Delta}\right)}$ and $\partial_x\theta(x) = \pm\frac{1}{\Delta\cosh\left(\pm\frac{x-x_0}{\Delta}\right)}$:

$$\begin{aligned} E\left[\theta(x)\right] = \sigma &= \int_A^B \left[A\left(\partial_x\theta(x)\right)^2 + K_{eff}\sin^2(\theta(x))\right] dx \\ &= \left(\frac{A}{\Delta^2} + K_{eff}\right)\int_A^B \frac{dx}{\cosh^2\frac{x}{\Delta}} \quad \text{let be} \quad u = \frac{x}{\Delta} \\ &= \left(\frac{A}{\Delta} + \Delta K_{eff}\right)\int_{-\infty}^{+\infty} \frac{du}{\cosh^2 u} \end{aligned}$$

Like $\left(\frac{A}{\Delta} + \Delta K_{eff}\right) = 2\sqrt{AK_{eff}}$ and $\int_{-\infty}^{+\infty}\frac{du}{\cosh^2 u} = 2$ we finally get the weel-known result

$$\sigma = 4\sqrt{AK_{eff}}$$

8.3.3 *Simple linear profile*

Let's make an Ansatz: the profile, of width l_p is linear such as

$$\begin{cases} \theta(x) = 0 & \text{for} \quad x < -\frac{l_p}{2} \\ \theta(x) = \pi\left(\frac{x}{l_p} + \frac{1}{2}\right) & \text{for} \quad -\frac{l_p}{2} < x < \frac{l_p}{2} \\ \theta(x) = \pi & \text{for} \quad x > \frac{l_p}{2} \end{cases} \tag{8.25}$$

A schematic representation of this situation is depicted by the blue profile on figure 8.6. Inserting this profile in the energy functionnal, one has:

$$\begin{aligned} \sigma &= \int_A^B \left[A\left(\partial_x\theta\right)^2 + K_{eff}\sin^2(\theta)\right] dx \\ &= \int_A^B \left[A\frac{\pi^2}{l_p^2} + K_{eff}\sin^2\left(\pi\left(\frac{x}{l_p} + \frac{1}{2}\right)\right)\right] \\ &= A\frac{\pi^2}{l_p} + \frac{K_{eff}l_p}{2} \end{aligned}$$

The domain wall width can be found by doing $\frac{dE}{dl_p} = 0 \rightarrow l_p = \pi\sqrt{2}\sqrt{\frac{a}{k_{eff}}}$. This domain wall width is over-estimated compared to the real one. The consequence is that the energy is over-estimated too, and is $\sigma = \pi\sqrt{2}\sqrt{AK_{eff}} \simeq 4.44\sqrt{AK_{eff}}$ which is a little bit greater than the real $\sigma = 4\sqrt{AK_{eff}}$. It is only because our Ansatz is a profile that does not minimizes the energy.
Now, let's take the real profile and study the impact of the DM interaction on the domain wall.

8.3.4 *The Dzyaloshinskii-Moriya contribution*

The effect of the Spin-Orbit Coupling, associated with the loss of inversion symetry lead to a term in the functional, that is:

$$F\left[\theta, \partial_x\theta\right] = A\left(\partial_x\theta\right)^2 - D\partial_x\theta + K_{eff}\sin^2(\theta)$$

Where D is the DM factor. One can clearly see the appearance of chirality: to minimize the energy, one must have D and $\partial_x\theta$ of the same sign, *ie* the sign of D imposes the sense of rotation of the magnetization.

Still using the Euler's equation, one obtain almost the same thing than before:

$$\begin{cases} \frac{\partial F}{\partial\theta} - \partial_x\left(\frac{\partial F}{\partial(\partial_x\theta)}\right) = 0 \\ \left.\frac{\partial F}{\partial(\partial_x\theta)}\right|_{(A,B)} 0 \end{cases} \longleftrightarrow \begin{cases} \partial_x^2\theta = \frac{\sin\theta\cos\theta}{\Delta^2} & A < x < B \\ \partial_x\theta = \frac{D}{2A} = \frac{1}{\Lambda} & x = A \quad \text{or} \quad x = B \end{cases}$$

The first equation gives the same solution as before, in other word the presence of DMI does not change the profile of the domain, it gives only a chiral contribution to energy. Indeed, if one calculate the domain wall energy in presence of DMI, it yields:

$$\begin{aligned} \sigma_{DW} &= \int_A^B \left[A\left(\partial_x\theta\right)^2 - D\partial_x\theta + K_{eff}\sin^2\theta\right] dx \\ &= 4\sqrt{AK_{eff}} - D\int_A^B \partial_x\theta dx \\ &= 4\sqrt{AK_{eff}} \mp D\int_A^B \frac{dx}{\Delta\cosh\left(\pm\frac{x-x_0}{\Delta}\right)} \\ &= 4\sqrt{AK_{eff}} \mp \pi D \end{aligned}$$

The "$-$" sign is the case where sign(D)=sign($\partial_x\theta$) and the "$+$" is for sign(D)=-sign($\partial_x\theta$). In conclusion, the contribution of DMI is favorable only for one sense of rotation. It's what is called the chirality.

8.4 ANNEX 4: THE SKYRMION WINDING NUMBER

8.4.1 *Definition*

When skyrmions are large enough ($R \gg a$, where R is the skyrmion's radius and a is the lattice parameter) they can be described in a continuous way, with the micromagnetic theory. The magnetization is hence described by a vector field, and possesses non trivial topological properties. This means that the magnetizarion of a skyrmion cannot be continuously deformed to the saturated state because the directions taken by this vector field is such that "knots" are generated. In order to get a better understanding, let's use a simple analogy with the unidimensional situation. Let's consider two kinds of 1D structures: non-chiral domain-walls (figire 8.7(a)) and chiral domain-walls (unidimensional skyrmion; figure 8.7(b)). We can define a number that represents the sum of all the little angles θ between neighboring spins as:

$$n_{1D} = \frac{1}{2\pi} \int_{-\infty}^{+\infty} \frac{\partial \theta}{\partial x} dx \tag{8.26}$$

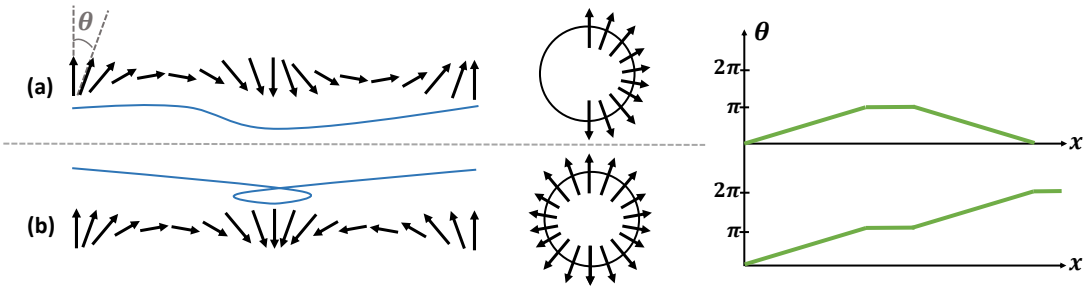

Figure 8.7: **Unidimensionnal chains for the analogy**: (a) two domain walls with opposite chirality and the associated $\theta(x)$ function and (b) the same with two domain walls with the same chirality (skyrmion-like configuration)

In 1D all the possible directions for the magnetization define a unit circle. Equation (8.26) collects all local magnetization direction and gives a number (called the "winding number" or "topological number") that tells us how many times the magnetization wraps this circle. If this number is zero, it means that we have only one direction for all the spins, *ie* it corresponds to the satured state. If this number is one, it means that the magnetization of the spin texture possesses all the possible direction, and this case generates a "knot" (see the blue curves on figure 8.7, the skyrmion's configuration generates a knots while a classical DW does not). Hence we have $n_{1D} = 0$ for the satured magnetic state and $n_{1D} = 1$ for the unidimensional skyrmion's configuration, and this difference has a very important consequence. Physically speaking, by applying an external magnetic field on 8.7(a), we can switch to the saturated state easier than in figure 8.7(b) because in the latter case the central spin will be harder to return due to the neighboring configuration. It corresponds, mathematically, to the notion of "topological protection" for the skyrmion's spin texture. Indeed, in topology, the transition between two confiugration of different topological number n_{1D} is impossible, involving a singularity. Naturally in physics there

is no singularity, but the transition from $n_{1D} = 1$ to $n_{1D} = 0$ necessitates more energy, it's why it is often said that the skyrmions have an additionnal energetic stability due to its topology.

By an analogy with this 1D situation, we can define the two-dimensionnal winding-number:

$$n = \frac{1}{4\pi} \int_{-\infty}^{+\infty} \int_{-\infty}^{+\infty} \vec{m}. \left(\frac{\partial \vec{m}}{\partial x} \times \frac{\partial \vec{m}}{\partial y} \right) dxdy = \frac{1}{4\pi} \int_{-\infty}^{+\infty} \int_{-\infty}^{+\infty} q dxdy \tag{8.27}$$

Where q is the topological charge density. The (normalized) magnetization in 2D can take values on a unit sphere. Hence, equation (8.27) defines the number of times that the magnetization wraps the unit sphere. In the case of Néél or Bloch skyrmion we will see that we obtain n=1, what can be understood looking to this picture, representing the stereographic projection of the Néél skyrmion's magnetization:

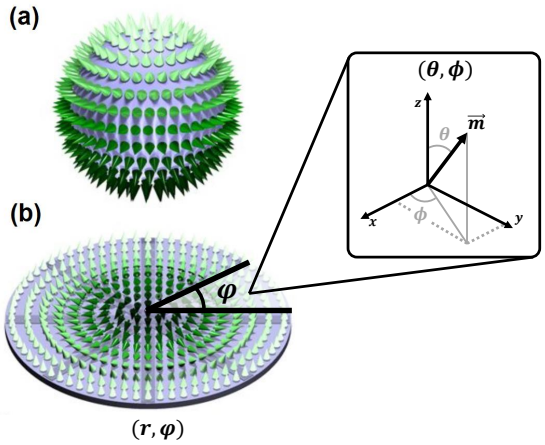

Figure 8.8: **The Néél skyrmion configuration**: (b) and its projection over a unit sphere (a). It wraps the entire sphere so that n=1. In (b) is defined the cylindrical coordinates to locate a spin and the spherical coordinates to define its orientation

This time, calculations require a little bit more effort, here we give the details. Cylindrical coordinates are used to localize a spin on the skyrmion spin texture, because of its symmetry:

$$\begin{pmatrix} x \\ y \\ z \end{pmatrix} \rightarrow \begin{pmatrix} x(r,\varphi) \\ y(r,\varphi) \\ z(r,\varphi) \end{pmatrix} = \begin{pmatrix} r\cos\varphi \\ r\sin\varphi \\ z \end{pmatrix}$$

And, for a given spin, its direction is described within the spherical coordinates:

$$\vec{m} = \begin{pmatrix} m_x(\theta,\phi) \\ m_y(\theta,\phi) \\ m_z(\theta,\phi) \end{pmatrix} = \begin{pmatrix} \sin\theta\cos\phi \\ \sin\theta\sin\phi \\ \cos\theta \end{pmatrix}$$

Where θ and ϕ are function of r and φ. The symetry of the skyrmion induce that $\theta(r,\varphi) \rightarrow \theta(r)$ (cylindrical symetry) and $\phi(r,\varphi) \rightarrow \phi(\varphi)$ (radial independance of ϕ). Therefore we must express the cartesian gradient as a function of (r,φ):

$$\begin{pmatrix} \partial_r \\ \partial_\varphi \\ \partial_z \end{pmatrix} = \begin{pmatrix} \frac{\partial x}{\partial r} & \frac{\partial y}{\partial r} & \frac{\partial z}{\partial r} \\ \frac{\partial x}{\partial \varphi} & \frac{\partial y}{\partial \varphi} & \frac{\partial z}{\partial \varphi} \\ \frac{\partial x}{\partial z} & \frac{\partial y}{\partial z} & \frac{\partial z}{\partial z} \end{pmatrix} \begin{pmatrix} \partial_x \\ \partial_y \\ \partial_z \end{pmatrix}$$
$$= \begin{pmatrix} \cos\varphi & \sin\varphi & 0 \\ -r\sin\varphi & r\cos\varphi & 0 \\ 0 & 0 & 1 \end{pmatrix} \begin{pmatrix} \partial_x \\ \partial_y \\ \partial_z \end{pmatrix}$$

Inversion of the Jacobian gives

$$\begin{pmatrix} \partial_x \\ \partial_y \\ \partial_z \end{pmatrix} = \begin{pmatrix} \cos\varphi & -\frac{\sin\varphi}{r} & 0 \\ \sin\varphi & \frac{\cos\varphi}{r} & 0 \\ 0 & 0 & 1 \end{pmatrix} \begin{pmatrix} \partial_r \\ \partial_\varphi \\ \partial_z \end{pmatrix}$$

What gives

$$\begin{aligned} \frac{\partial \vec{m}}{\partial x} \times \frac{\partial \vec{m}}{\partial y} &= \left(\cos\phi \frac{\partial \vec{m}}{\partial r} \vec{e_r} - \frac{\sin\varphi}{r} \frac{\partial \vec{m}}{\partial \varphi} \vec{e_\varphi} \right) \times \left(\sin\phi \frac{\partial \vec{m}}{\partial r} \vec{e_r} + \frac{\cos\varphi}{r} \frac{\partial \vec{m}}{\partial \varphi} \vec{e_\varphi} \right) \\ &= \frac{1}{r} \frac{\partial \vec{m}}{\partial r} \times \frac{\partial \vec{m}}{\partial \varphi} \end{aligned}$$

Therefore, in the new coordinates, the winding number becomes

$$n = \frac{1}{4\pi} \int_0^{+\infty} \int_0^{2\pi} \vec{m}. \left(\frac{\partial \vec{m}}{\partial r} \times \frac{\partial \vec{m}}{\partial \varphi} \right) dr d\varphi \tag{8.28}$$

With the new topological density $q = \frac{1}{r} \vec{m}. \left(\frac{\partial \vec{m}}{\partial r} \times \frac{\partial \vec{m}}{\partial \varphi} \right)$. Calculation of the integrand of equation 8.28 yields:

$$\begin{aligned} \vec{m}. \left(\frac{\partial \vec{m}}{\partial r} \times \frac{\partial \vec{m}}{\partial \varphi} \right) &= \begin{pmatrix} m_x(\theta(r),\phi(\varphi)) \\ m_y(\theta(r),\phi(\varphi)) \\ m_z(\theta(r),\phi(\varphi)) \end{pmatrix} \cdot \left[\begin{pmatrix} \frac{\partial m_x}{\partial r}(\theta(r),\phi(\varphi)) \\ \frac{\partial m_y}{\partial r}(\theta(r),\phi(\varphi)) \\ \frac{\partial m_z}{\partial r}(\theta(r),\phi(\varphi)) \end{pmatrix} \times \begin{pmatrix} \frac{\partial m_x}{\partial \varphi}(\theta(r),\phi(\varphi)) \\ \frac{\partial m_y}{\partial \varphi}(\theta(r),\phi(\varphi)) \\ \frac{\partial m_z}{\partial \varphi}(\theta(r),\phi(\varphi)) \end{pmatrix} \right] \\ &= \left[m_x \left[\frac{\partial m_y}{\partial r} \frac{\partial m_z}{\partial \varphi} - \frac{\partial m_y}{\partial \varphi} \frac{\partial m_z}{\partial r} \right] + m_y \left[\frac{\partial m_z}{\partial r} \frac{\partial m_x}{\partial \varphi} - \frac{\partial m_z}{\partial \varphi} \frac{\partial m_x}{\partial r} \right] + m_z \left[\frac{\partial m_x}{\partial r} \frac{\partial m_y}{\partial \varphi} - \frac{\partial m_x}{\partial \varphi} \frac{\partial m_y}{\partial r} \right] \right] \\ &= \left[\cos^3\theta \cos^2\phi \frac{\partial \theta(r)}{\partial r} \frac{\partial \phi(\varphi)}{\partial \varphi} + \sin^3\theta \sin^2\phi \frac{\partial \theta(r)}{\partial r} \frac{\partial \phi(\varphi)}{\partial \varphi} + \cos^2\theta \sin\theta \frac{\partial \theta(r)}{\partial r} \frac{\partial \phi(\varphi)}{\partial \varphi} \right] \\ &= \sin\theta(r) \frac{\partial \theta(r)}{\partial r} \frac{\partial \phi(\varphi)}{\partial \varphi} \end{aligned} \tag{8.29}$$

So that finally, the winding number is:

$$n = \frac{1}{4\pi}\int_{r=0}^{r=+\infty}\int_{\varphi=0}^{\varphi=2\pi}\sin\theta(r)\frac{d\theta(r)}{dr}\frac{d\phi(\varphi)}{d\varphi}drd\varphi = \frac{[\cos\theta(r)]_{r=0}^{r=+\infty}}{2}.\frac{[\phi(\varphi)]_{\varphi=0}^{\varphi=2\pi}}{2\pi} = p.W$$

The number p is the *polarity*, which depends on the boundary conditions of the skyrmion's radial profile $\theta(r)$. In the presence of PMA, there are two possibilies for these conditions, which are $\theta(0) = 0$ and $\theta(\infty) = \pi$, or $\theta(0) = \pi$ and $\theta(\infty) = 0$. This number has important consequence on the current-driven motion of skyrmions (see section **??**). The second number, W is called the helicity and depends on the behavior of the magnetization along the perimeter of the skyrmion. One can define $\phi(\varphi) = \kappa\varphi + \psi$ where κ is called the *vorticity* and ψ is an additional phase that defines the *chirality* of the spin texture. Hence, a spin texture is well defined by its *polarity*, *vorticity* and *chirality*, *ie* the three number (p, κ, ψ). Indeed the winding number is not sufficient to describe a spin texture, and lead to degeneracy. Examples of topological spin textures are shown on figure 8.9, for different values of (p, κ, ψ). The skyrmion spin texture possess $\mid n \mid = 1$. For each skyrmion there exist a configuration called anti-skyrmion which is defined by the transformation $\theta(\varphi) \rightarrow \theta(-\varphi)$, as it is depicted for the Néél skyrmion on fig 8.9. Therefore, for a skyrmion of winding number n, the associated anti-skyrmion has an opposite winding number $-n$.

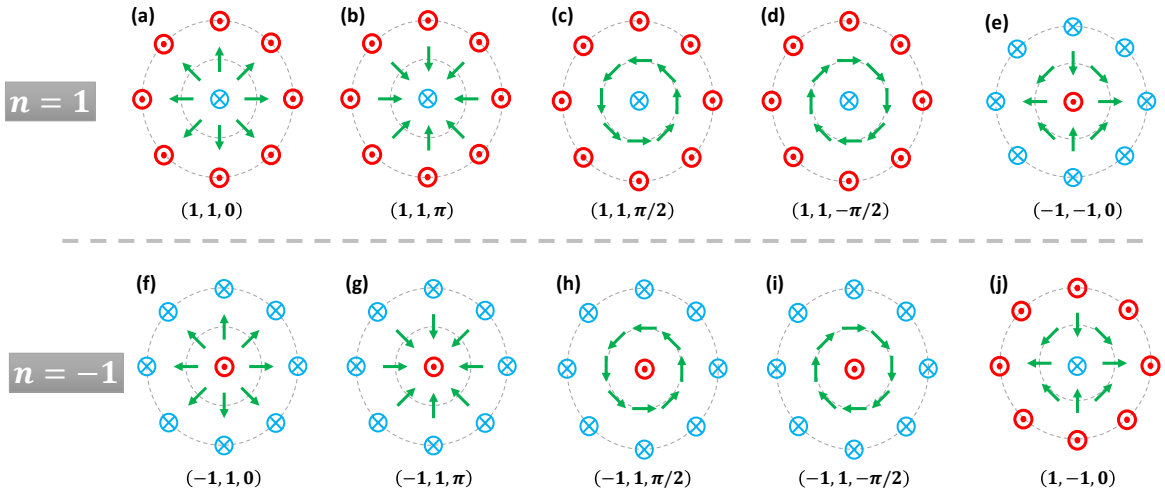

Figure 8.9: **Zoo of spin textures with different values of parameters** (p, κ, ψ). (a)-(e) Spin texture with winding number $n = 1$ and (f)-(j) with $n = -1$. The Néél skyrmion possesses 4 different configurations (a)-(b)-(f)-(g), like the Bloch skyrmion (c)-(d)-(h)-(i). (e) and (j) show the spin configuration of the Néél anti-skyrmion, for which $\theta(\varphi)$ becomes $\theta(-\varphi)$.

The winding number plays an important role in the current-driven dynamics of these spin textures, as it is described in the section **??**.

A peculiar case of spin texture is the so-called skyrmionium, that has a double radial-twist, as shown on figure **??**. The magnetization in the core is in the same direction than the one on the perimeter. Hence, the winding number is $n = 0$ because $p = 0$.

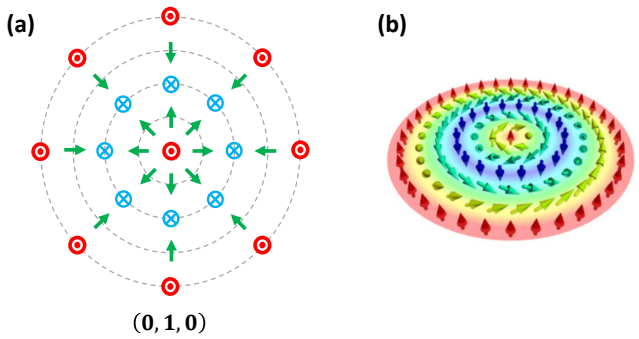

Figure 8.10: **The skyrmionium spin texture**: (a) Néél type and (b) Bloch type, (b) is adapted from

In general, whatever the number of twist along the radial direction, if the direction of the magnetization is the same in the core and on the perimeter, the winding number is zero.

8.4.2 *Conclusion*

For a magnetization's vector field like:

$$\begin{pmatrix} \sin\theta\cos\phi \\ \sin\theta\sin\phi \\ \cos\theta \end{pmatrix}$$

The winding number is given as

$$n = \frac{1}{4\pi}\int_0^{+\infty}\int_0^{2\pi} \vec{m}.\left(\frac{\partial\vec{m}}{\partial r}\times\frac{\partial\vec{m}}{\partial\varphi}\right) dr d\varphi = p.W$$

Where $p = \frac{[\cos\theta(r)]_\infty^0}{2}$ is the *polarity* that describe the radial behavior of the magnetization and $W = \frac{[\kappa\varphi+\psi]_0^{2\pi}}{2\pi}$ composed of the *vorticity* κ and the *chirality* ψ that defines the angular behavior of the magnetization.

8.5 ANNEX 5: FROM LLG TO THE THIELE EQUATION

As it is explained in section 2.3, the magnetization dynamics is described by the Landau Lifschitz Gilbert (LLG) equation. In this section, we consider the presence of interfacial spin orbit torques originating from the spin Hall effect (the damping-like term), which comes as a term in the LLG equation (see section 2.5.2.4):

$$\frac{d\vec{m}}{dt} = -\gamma\mu_0\vec{m}\times\vec{H_{eff}} + \alpha\vec{m}\times\frac{d\vec{m}}{dt} - \gamma\mu_0 H_{DL}\vec{m}\times(\vec{m}\times\vec{\sigma}) \tag{8.30}$$

where $\vec{m} = \frac{\vec{M}}{M_S}$ is the normalized magnetization, γ is the gyromagnetic ratio, α the magnetic damping and the effective field is defined as $\vec{H_{eff}} = -\frac{1}{\mu_0 M_S}\frac{\delta\mathcal{E}}{\delta\vec{m}}$ with $\mathcal{E}$ the magnetic energy density. The last term of the right hand side is the contribution of the damping-like term of SoT, where $\vec{\sigma} = \text{sgn}(\theta_{SH})\vec{j}\times\vec{n}$ is related to the spin Hall effect ($\vec{j}$ is a unit vector in the direction of the current density and $\vec{n}$ is the normal to the conducting layer, see section 2.5.2.2), and the damping like torque efficiency is defined as $H_{DL} = \frac{\hbar|\theta_{SH}|J_{HM}}{2\mu_0|e|M_S t}$.
Starting from this LLG equation, we propose in this section to introduce the Thiele formalism and to derive the Thiele equation that governs the skyrmion dynamics under some assumptions that we will described. The Thiele equation has the advantage of reducing the complexity of magnetization dynamics of LLG to the simple motion of the skyrmion as a point-like object. It is similar to the situation in solid state physics where the motion of a solid object of arbitrary shape is reduced to the motion of its center of mass. Here, the object is the skyrmion (its magnetization configuration) and the equivalent to the center of mass is the position of the center of the skyrmion.

8.5.1 *Derivation of the Thiele equation from the LLG equation*

Thus, in the following we consider a skyrmion spin texture with axial symmetry, as shown in Fig. 8.11a. The position of the skyrmion and of each spin is described within cylindrical coordinates (r, φ) and locally, the direction of each spin is described by spherical coordinates $(\theta(r), \phi(\varphi))$ (8.11b). The key assumption of the Thiele formalism is to consider the skyrmion as a rigid spin texture in translation motion. Initially (t_0), the skyrmion is located at the origin of the coordinate system (8.11a) and the spin configuration is described by $\vec{M}_0 = (\sin\theta_0(r)\cos\phi_0(\varphi), \sin\theta_0(r)\sin\phi_0(\varphi), \cos\theta_0(r))$ (Fig. 8.11b). At time $t_0 + \delta t$, the skyrmion core moved from 0 to $\vec{X}_c$ in the cylindrical coordinate system, and the magnetization is now described by $\vec{M}$. Due to the assumption of rigid translation, the magnetization at a given point $\vec{X}$ (in the cylindrical coord. system) of global magnetization configuration that includes the skyrmion reads

$$\vec{M}(\vec{X}, t) = \vec{M}_0(\vec{X} - \vec{X}_c(t)) \longleftrightarrow \begin{cases} \theta(\vec{X}, t) = \theta_0(\vec{X} - \vec{X}_c(t)) \\ \phi(\vec{X}, t) = \phi_0(\vec{X} - \vec{X}_c(t)) \end{cases} \tag{8.31}$$

Thus, the hypothesis of rigid skyrmion motion enables to describe the magnetization configuration at anytime only knowing the initial configuration and the position of the

skyrmion center. In other words, it is equivalent to keep the origin of the cylindrical coordinate system at the skyrmion center although the latter is moving.

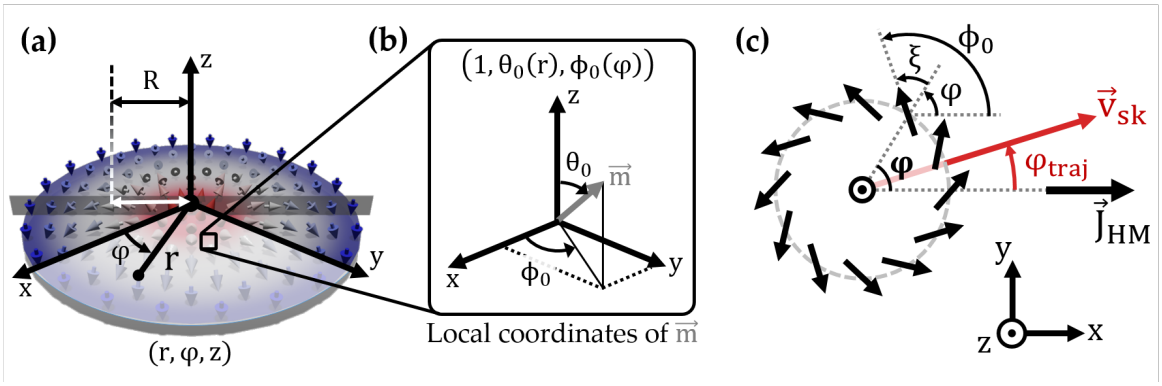

Figure 8.11: **Coordinate system for the analytical model:** Coordinate system used to describe the skyrmion spin texture and to derive the different terms of the Thiele equation. (a) Sketch of a Néel-type skyrmion, on which a given spin is located in cylindrical coordinates (r, φ, z). (b) Locally the orientation of each spin is described using spherical angles $(1, \theta(r), \phi(\varphi))$. The angle ϕ_0 is the sum of the cylindrical angle φ and the helicity ξ, as shown in (c) which is a top view of a Dzyaloshinskii skyrmion. The trajectory angle φ_{traj} is defined as the angle between the current density $\vec{J}_{HM}$ (black arrow) and the skyrmion velocity vector $\vec{v}_{sk}$ (red arrow).

Then, the idea behind the Thiele approach is a force balance obtained from the LLG equation by assuming this rigid skyrmion configuration. It is more convenient to rewrite the LLG equation in the same coordinates as the magnetization, *ie* spherical coordinates. The expression of each term of the LLG equation in the spherical coordinates are given by

$$\vec{m} = \vec{u}_r \tag{8.32}$$

$$\begin{aligned} \frac{d\vec{m}}{dt} &= \dot{\vec{u}}_r \\ &= \dot{\theta}\vec{u}_\theta + \dot{\phi}\sin\theta\vec{u}_\phi \end{aligned} \tag{8.33}$$

$$\begin{aligned} \vec{m} \times \frac{d\vec{m}}{dt} &= \vec{u}_r \times \left(\dot{\theta}\vec{u}_\theta + \dot{\phi}\sin\theta\vec{u}_\phi\right) \\ &= \dot{\theta}\vec{u}_\phi - \dot{\phi}\sin\theta\vec{u}_\theta \end{aligned} \tag{8.34}$$

$$\begin{aligned} \vec{H_{eff}} &= -\frac{1}{\mu_0 M_S}\frac{\delta\mathcal{E}}{\delta\vec{m}} \\ &= -\frac{1}{\mu_0 M_S}\left(r\frac{\delta\mathcal{E}}{\delta r}\vec{u}_r + \frac{1}{r}\frac{\delta\mathcal{E}}{\delta\theta}\vec{u}_\theta + \frac{1}{r\sin\theta}\frac{\delta\mathcal{E}}{\delta\phi}\vec{u}_\phi\right) \end{aligned} \tag{8.35}$$

$$\begin{aligned}\vec{m} \times \vec{H_{eff}} &= -\frac{1}{\mu_0 M_S}\vec{u_r} \times \left(r\frac{\delta \mathcal{E}}{\delta r}\vec{u_r} + \frac{\delta \mathcal{E}}{\delta \theta}\vec{u_\theta} + \frac{1}{\sin\theta}\frac{\delta \mathcal{E}}{\delta \phi}\vec{u_\phi} \right) \\ &= -\frac{1}{\mu_0 M_S}\frac{\delta \mathcal{E}}{\delta \theta}\vec{u_\phi} + \frac{1}{\mu_0 M_S}\frac{1}{\sin\theta}\frac{\delta \mathcal{E}}{\delta \phi}\vec{u_\theta}\end{aligned} \tag{8.36}$$

$$\begin{aligned}\vec{m} \times (\vec{m} \times \vec{\sigma}) &= \vec{u_r} \times (\vec{u_r} \times (\sigma_r \vec{u_r} + \sigma_\theta \vec{u_\theta} + \sigma_\phi \vec{u_\phi})) \\ &= -(\sigma_\theta \vec{u_\theta} + \sigma_\phi \vec{u_\phi})\end{aligned} \tag{8.37}$$

So that the LLG equation 8.30 can be rewritten in the spherical coordinates, as

$$\dot{\theta}\vec{u_\theta} + \dot{\phi}\sin\theta\vec{u_\phi} = \frac{\gamma}{M_S}\frac{\delta \mathcal{E}}{\delta \theta}\vec{u_\phi} - \frac{\gamma}{M_S}\frac{1}{\sin\theta}\frac{\delta \mathcal{E}}{\delta \phi}\vec{u_\theta} + \alpha\dot{\theta}\vec{u_\phi} - \alpha\dot{\phi}\sin\theta\vec{u_\theta} + \gamma\mu_0 H_{DL}\sigma_\theta\vec{u_\theta} + \gamma\mu_0 H_{DL}\sigma_\phi\vec{u_\phi} \tag{8.38}$$

Projecting this equation on $\vec{u_\theta}$ and $\vec{u_\phi}$ gives two scalar equations :

$$\begin{cases} \frac{\delta \mathcal{E}}{\delta \phi} = \frac{M_S}{\gamma}\sin\theta\left(-\dot{\theta} - \alpha\dot{\phi}\sin\theta + \gamma\mu_0 H_{DL}\sigma_\theta\right) \\ \frac{\delta \mathcal{E}}{\delta \theta} = \frac{M_S}{\gamma}\left(\dot{\phi}\sin\theta - \alpha\dot{\theta} - \gamma\mu_0 H_{DL}\sigma_\phi\right) \end{cases} \tag{8.39}$$

Now, let's consider the variation of total energy associated to a small displacement of the skyrmion core, $\frac{dE}{d\vec{X_c}}$. This term, being the gradient of the total energy in the cylindrical coordinates, correspond to the total force acting on the skyrmion. It can be expanded using equation 8.31 as

$$\frac{dE}{d\vec{X_c}} = -\frac{dE}{d\vec{X}} \tag{8.40}$$

$$\begin{aligned} &= -\int_V \frac{\delta \mathcal{E}}{\delta \vec{X}} d^3\vec{r} \\ &= -\int_V \left(\frac{\delta \mathcal{E}}{\delta \theta}\frac{\delta \theta}{\delta \vec{X}} + \frac{\delta \mathcal{E}}{\delta \phi}\frac{\delta \phi}{\delta \vec{X}} \right) d^3\vec{r} \\ &= -\int_V \left(\frac{\delta \mathcal{E}}{\delta \theta}\vec{\nabla}\theta + \frac{\delta \mathcal{E}}{\delta \phi}\vec{\nabla}\phi \right) d^3\vec{r} \end{aligned} \tag{8.41}$$

where the integral is performed in the cylindrical coordinates $\int_V = \iiint r dr d\phi dz$ as well as the gradient $\vec{\nabla} = (\frac{\partial}{\partial r}, \frac{1}{r}\frac{\partial}{\partial \varphi}, \partial z)$. Thus, the LLG equation, associated to the rigid skyrmion motion allowed us to get expression 8.41, which can be expanded by inserting terms of equation 8.39:

$$\begin{aligned}\frac{dE}{d\vec{X}_c} =& -\int_V \left[\frac{M_S}{\gamma}\left(\dot{\phi}\sin\theta - \alpha\dot{\theta} - \gamma\mu_0 H_{DL}\sigma_\phi\right)\vec{\nabla}\theta + \frac{M_S}{\gamma}\sin\theta\left(-\dot{\theta} - \alpha\dot{\phi}\sin\theta + \gamma\mu_0 H_{DL}\sigma_\theta\right)\vec{\nabla}\phi\right] d^3\vec{r} \\ =& \frac{M_S}{\gamma}\int_V \sin\theta\left(\dot{\theta}\vec{\nabla}\phi - \dot{\phi}\vec{\nabla}\theta\right) d^3\vec{r} + \alpha\frac{M_S}{\gamma}\int_V \left(\dot{\theta}\vec{\nabla}\theta + \dot{\phi}\sin^2\theta\vec{\nabla}\phi\right) d^3\vec{r} \\ &+ \mu_0 M_S H_{DL}\int_V \left(\sigma_\phi\vec{\nabla}\theta - \sin\theta\sigma_\theta\vec{\nabla}\phi\right) d^3\vec{r}\end{aligned} \tag{8.42}$$

Using 8.31 it is easy to see that $\dot{\theta}(\vec{X},t) = -\vec{\nabla}\theta\cdot\frac{d\vec{X}_c}{dt} = -\vec{\nabla}\theta\cdot\vec{v}_{sk}$ and $\dot{\phi}(\vec{X},t) = -\vec{\nabla}\phi\cdot\frac{d\vec{X}_c}{dt} = -\vec{\nabla}\phi\cdot\vec{v}_{sk}$, where we defined the skyrmion velocity $\vec{v}_{sk} = \frac{d\vec{X}_c}{dt}$. Thus, it gives

$$\begin{aligned}\frac{dE}{d\vec{X}_c} =& \frac{M_S}{\gamma}\int_V \sin\theta\left((\vec{\nabla}\phi\cdot\vec{v}_{sk})\vec{\nabla}\theta - (\vec{\nabla}\theta\cdot\vec{v}_{sk})\vec{\nabla}\phi\right) d^3\vec{r} \\ &+ \alpha\frac{M_S}{\gamma}\int_V \left(-(\vec{\nabla}\theta\cdot\vec{v}_{sk})\vec{\nabla}\theta - \sin^2\theta(\vec{\nabla}\phi\cdot\vec{v}_{sk})\vec{\nabla}\phi\right) d^3\vec{r} \\ &+ \mu_0 M_S H_{DL}\int_V \left(\sigma_\phi\vec{\nabla}\theta - \sin\theta\sigma_\theta\vec{\nabla}\phi\right) d^3\vec{r}\end{aligned}$$

The first term on the right hand side can be simplified by using properties of the cross product, *ie* $(\vec{u}\cdot\vec{w})\vec{v} - (\vec{v}\cdot\vec{w})\vec{u} = (\vec{u}\times\vec{v})\times\vec{w}$. Moreover, expansion of the second term lead to a tensor which is diagonal due to the axial symmetry ($\frac{\partial\theta}{\partial\varphi} = 0$ and $\frac{\partial\phi}{\partial r} = 0$). Finally, the integration along the z-axis is simplified to the ferromagnetic thickness since we consider an homogeneous magnetization along the z-axis (ultrathin film). Thus, one gets

$$\begin{aligned}\frac{dE}{d\vec{X}_c} =& \left[\frac{M_S t_{FM}}{\gamma}\int_S \sin\theta\left(\vec{\nabla}\theta\times\vec{\nabla}\phi\right) d^2\vec{r}\right]\times\vec{v}_{sk} \\ &- \alpha\left[\frac{M_S t_{FM}}{\gamma}\int_S \begin{pmatrix}\left(\frac{\partial\theta}{\partial r}\right)^2 & 0 & 0\\ 0 & \frac{\sin^2\theta}{r^2} & 0\\ 0 & 0 & 0\end{pmatrix} d^2\vec{r}\right]\cdot\vec{v}_{sk} \\ &+ \mu_0 M_S t_{FM} H_{DL}\int_S \left(\sigma_\phi\vec{\nabla}\theta - \sin\theta\sigma_\theta\vec{\nabla}\phi\right) d^2\vec{r}\end{aligned} \tag{8.43}$$

which finally leads to the Thiele equation of skyrmion dynamics:

$$\vec{F}_{DL} + \vec{G}\times\vec{v}_{sk} - \alpha\bar{\bar{\mathcal{D}}}\cdot\vec{v}_{sk} - \frac{dE}{d\vec{X}_c} = \vec{0}$$

In the case of considering steady state motion for skyrmion, one has $\frac{dE}{d\vec{X}_c} = \vec{0}$ so that the Thiele equation is

$$\vec{F}_{DL} + \vec{G}\times\vec{v}_{sk} - \alpha\bar{\bar{\mathcal{D}}}\cdot\vec{v}_{sk} = \vec{0} \tag{8.44}$$

where the different terms are defined as

$$\vec{F}_{DL} = \mu_0 M_S t_{FM} H_{DL} \int_S \left(\sigma_\phi \vec{\nabla}\theta - \sin\theta \sigma_\theta \vec{\nabla}\phi \right) d^2\vec{r} \tag{8.45}$$

$$\vec{G} = \frac{M_S t_{FM}}{\gamma} \int_S \sin\theta \left(\vec{\nabla}\theta \times \vec{\nabla}\phi \right) d^2\vec{r} \tag{8.46}$$

$$\bar{\bar{\mathcal{D}}} = \frac{M_S t_{FM}}{\gamma} \int_S \left(\left(\vec{\nabla}\theta \right)^2 + \sin^2\theta \left(\vec{\nabla}\phi \right)^2 \right) d^2\vec{r} \tag{8.47}$$

The first term, $\vec{F}_{DL}$ (eq. 8.45), is the force coming from the spin orbit torque, due to the injected current density in the HM layer (section 2.5.2). We can see that it depends on the direction of the spin accumulation $\vec{sigma}$.

The second terms, $\vec{G} \times \vec{v}_{sk}$ (eq. 8.46), is called the gyroforce force (or gyromotive force), since its direction is always perpendicular to the skyrmion trajectory. It is interesting to notice that this term has the same form as the Lorentz force, replacing the electrical charge by the topological charge. It is often compared as a topological magnus force which is responsible for the Skyrmion Hall effect.

The last term, $-\alpha \bar{\bar{\mathcal{D}}} \cdot \vec{v}_{sk}$, is a dissipative force, which is similar to viscous friction as in point mechanics. The balance between these three forces give the skyrmion trajectory direction, and their amplitude is related to the skyrmion velocity.
These forces can be written in Cartesian coordinates (Although we will only use the ones in the cylindrical coordinate system) in which they read as

$$\vec{F}_{DL} = \begin{pmatrix} F_{DL,x} \\ F_{DL,y} \\ 0 \end{pmatrix}, F_{DL,i} = \mu_0 M_S t H_{DL} \iint_S \left(m_x \frac{\partial m_z}{\partial x_i} - m_z \frac{\partial m_x}{\partial x_i} \right) dx\, dy \tag{8.48}$$

$$\vec{G} = \begin{pmatrix} 0 \\ 0 \\ G \end{pmatrix}, G = -\frac{M_S t}{\gamma} \iint_S m \cdot \left(\frac{\partial m}{\partial x} \times \frac{\partial m}{\partial y} \right) dx\, dy \tag{8.49}$$

$$\bar{\bar{\mathcal{D}}} = \begin{pmatrix} \mathcal{D}_{xx} & \mathcal{D}_{xy} \\ \mathcal{D}_{yx} & \mathcal{D}_{yy} \end{pmatrix}, \mathcal{D}_{ij} = \frac{M_S t}{\gamma} \iint_S \left(\frac{\partial m}{\partial x_i} \cdot \frac{\partial m}{\partial x_j} \right) dx\, dy \tag{8.50}$$

8.5.2 *Application to our sample geometry and derivation of the different terms*

In this section, we consider the typical geometry that we have experimentally in our HM/FM/MO_x trilayers. Thus, in the following, we consider a HM layer with negative spin Hall angle $\theta_{SH} < 0$ (such as Ta) below the FM layer ($\vec{n} = \vec{z}$), and a current density flowing in the $\vec{x}$ direction ($\vec{j} = \vec{x}$), leading to $\vec{\sigma} = \mathrm{sgn}(\theta_{SH})\vec{j} \times \vec{n} = \vec{y}$. It gives

$$\sigma_\theta = \vec{\sigma} \cdot \vec{u}_\theta = \cos\theta \sin\phi \tag{8.51}$$

$$\sigma_\phi = \vec{\sigma} \cdot \vec{u}_\phi = \cos\phi \tag{8.52}$$

Thus, if we define $\vec{f}_{DL}$ as the integrand of $\vec{F}_{DL} = \mu_0 M_S t_{FM} H_{DL} \int_S \vec{f}_{DL} d^2\vec{r}$, the expression of $\vec{f}_{DL}$ in the cylindrical coordinate system can be written as :

$$\vec{f}_{DL} = \sigma_\phi \vec{\nabla}\theta - \sin\theta \sigma_\theta \vec{\nabla}\phi \tag{8.53}$$

$$= \cos\phi \frac{\partial\theta}{\partial r}\vec{u}_r - \frac{\sin\theta\cos\theta}{r}\sin\phi \vec{u}_\varphi \tag{8.54}$$

In order to express the component of $\vec{f}_{DL}$ in the Cartesian coordinate, more relevant to compute the skyrmion trajectory in the (x,y) plane, we can use the equivalence of a vector written in the two basis $f_{DL,x}\vec{u}_x + f_{DL,y}\vec{u}_y + f_{DL,z}\vec{u}_z = f_{DL,r}\vec{u}_r + f_{DL,\varphi}\vec{u}_\varphi + f_{DL,z}\vec{u}_z$ which leads to

$$f_{DL,x} = f_{DL,r}\cos\varphi - f_{DL,\varphi}\sin\varphi \tag{8.55}$$

$$f_{DL,y} = f_{DL,r}\sin\varphi + f_{DL,\varphi}\cos\varphi \tag{8.56}$$

$$\tag{8.57}$$

Then, by reminding that $\phi = \varphi + \xi$, some trigonometry gives

$$f_{DL,x} = \cos^2\varphi\cos\xi\frac{\partial\theta}{\partial r} - \sin\varphi\cos\varphi\sin\xi\frac{\partial\theta}{\partial r} + \sin^2\varphi\cos\xi\frac{\sin\theta\cos\theta}{r} + \sin\varphi\cos\varphi\sin\xi\frac{\sin\theta\cos\theta}{r} \tag{8.58}$$

$$f_{DL,y} = \sin\varphi\cos\varphi\cos\xi\frac{\partial\theta}{\partial r} - \sin^2\varphi\sin\xi\frac{\partial\theta}{\partial r} - \sin\varphi\cos\varphi\sin\xi\frac{\sin\theta\cos\theta}{r} - \cos^2\varphi\sin\xi\frac{\sin\theta\cos\theta}{r} \tag{8.59}$$

The integration over φ simplifies a lot the problem since $\int_0^{2\pi}\cos\varphi\sin\varphi d\varphi = 0$ and $\int_0^{2\pi}\cos^2\varphi d\varphi = \int_0^{2\pi}\sin^2\varphi d\varphi = \pi$ which thus leads to

$$F_{DL,x} = \mu_0 M_S t_{FM} H_{DL}\left[\pi\int_0^\infty r\frac{\partial\theta}{\partial r} + \pi\int_0^\infty \sin\theta\cos\theta dr\right]\cos\xi \tag{8.60}$$

$$F_{DL,y} = -\mu_0 M_S t_{FM} H_{DL}\left[\pi\int_0^\infty r\frac{\partial\theta}{\partial r} + \pi\int_0^\infty \sin\theta\cos\theta dr\right]\sin\xi \tag{8.61}$$

which finally leads to the expression given in chapter 6:

$$\vec{F}_{DL} = \mu_0 M_S t_{FM} H_{DL} (\beta_1 + \beta_2) \begin{pmatrix} \cos\xi \\ -\sin\xi \\ 0 \end{pmatrix} \tag{8.62}$$

where β_1 and β_2 are dimensionless coefficient which read as

$$\beta_1 = \pi \int_{r=0}^{+\infty} r \left(\frac{\partial \theta}{\partial r} \right) dr \tag{8.63}$$

$$\beta_2 = \pi \int_{r=0}^{+\infty} \sin\theta(r) \cos\theta(r)\, dr \tag{8.64}$$

Now we discuss the gyrotropic vector, $\vec{G}$. Since $\vec{\nabla}\theta \times \vec{\nabla}\phi = \frac{1}{r}\frac{\partial \theta}{\partial r}\frac{\partial \phi}{\partial \varphi}\vec{u}_z$, one has directly

$$\int_S \sin\theta \left(\vec{\nabla}\theta \times \vec{\nabla}\phi \right) d^2\vec{r} = \int_{r=0}^{+\infty} \int_{\varphi=0}^{2\pi} \sin\theta(r) \frac{d\theta(r)}{dr} \frac{d\phi(\varphi)}{d\varphi} dr d\varphi \vec{u}_z = 4\pi n \vec{u}_z \tag{8.65}$$

where $n = p.w$ is the skyrmion winding number defined in section 2.2.1 from chapter 2. Thus, finally

$$\vec{G} = \begin{pmatrix} 0 \\ 0 \\ G \end{pmatrix}, G = -\frac{4\pi n M_S t}{\gamma} \tag{8.66}$$

Finally, we discuss about the dissipative term. In fact, the matrix given in eq. 8.43 in cylindrical coordinate needs to be written in the Cartesian coordinates. The passage matrix from Cartesian to cylindrical coordinate system is

$$P = \begin{pmatrix} \cos\varphi & -\sin\varphi & 0 \\ \sin\varphi & \cos\varphi & 0 \\ 0 & 0 & 1 \end{pmatrix} \tag{8.67}$$

and, if we note $\bar{\bar{\mathcal{D}}}_{Cart}$ (resp. $\bar{\bar{\mathcal{D}}}_{Cyl}$) the dissipative matrix in the Cartesian coordinates (resp. in cylindrical coordinate), they are linked by the expression $\bar{\bar{\mathcal{D}}}_{Cart} = P \bar{\bar{\mathcal{D}}}_{Cyl} P^{-1}$. It gives

$$\bar{\bar{\mathcal{D}}}_{Cart} = \begin{pmatrix} \cos^2\varphi \left(\frac{\partial\theta}{\partial r} \right)^2 + \sin^2\varphi \frac{\sin^2\theta}{r^2} & \sin\varphi\cos\varphi \left(\left(\frac{\partial\theta}{\partial r} \right)^2 - \frac{\sin^2\theta}{r^2} \right) & 0 \\ \sin\varphi\cos\varphi \left(\left(\frac{\partial\theta}{\partial r} \right)^2 - \frac{\sin^2\theta}{r^2} \right) & \sin^2\varphi \left(\frac{\partial\theta}{\partial r} \right)^2 + \cos^2\varphi \frac{\sin^2\theta}{r^2} & 0 \\ 0 & 0 & 0 \end{pmatrix} \tag{8.68}$$

and since $\int_0^{2\pi} \cos\varphi \sin\varphi d\varphi = 0$ and $\int_0^{2\pi} \cos^2\varphi d\varphi = \int_0^{2\pi} \sin^2\varphi d\varphi = \pi$, the integration over φ transforms $\bar{\bar{\mathcal{D}}}_{Cart}$ in a diagonal matrix. As a result, the dissipative tensor in the Cartesian coordinate reads as

$$\bar{\bar{\mathcal{D}}}_{Cart} = \begin{pmatrix} \frac{M_S t_{FM}}{\gamma} \pi \int_{r=0}^{+\infty} \left[r \left(\frac{\partial \theta}{\partial r} \right)^2 + \frac{\sin^2\theta}{r} \right] dr & 0 & 0 \\ 0 & \frac{M_S t_{FM}}{\gamma} \pi \int_{r=0}^{+\infty} \left[r \left(\frac{\partial \theta}{\partial r} \right)^2 + \frac{\sin^2\theta}{r} \right] dr & 0 \\ 0 & 0 & 0 \end{pmatrix} \tag{8.69}$$

which can be simplified to

$$\bar{\bar{\mathcal{D}}}_{Cart} = \begin{pmatrix} \frac{M_S t_{FM}}{\gamma} \beta_0 & 0 & 0 \\ 0 & \frac{M_S t_{FM}}{\gamma} \beta_0 & 0 \\ 0 & 0 & 0 \end{pmatrix} \tag{8.70}$$

where β_0 is a dimensionless coefficient given by

$$\beta_0 = \pi \int_{r=0}^{+\infty} \left[r \left(\frac{\partial \theta}{\partial r} \right)^2 + \frac{\sin^2\theta}{r} \right] dr \tag{8.71}$$

8.6 ANNEX 6: FREQUENCY SHIFT FROM BRILLOUIN LIGHT SCATTERING

In Sec. 3.2.2 we give an overview of the Brillouin Light Scattering technique, more precisely we describe the BLS setup from the LSPM in Villetaneuse, which uses a Damon-Esbach geometry to probe the frequency shift of counter propagating spin waves. Here, we demonstrate that in this geometry, the frequency shift Δf is linked to the iDMI coefficient.
In the Damon-Esbach configuration shown in Fig. 3.14, the magnetization can be written as

$$\vec{M} = \vec{m}(t) + \vec{M}_0 = \begin{pmatrix} M_0 \\ m_{0y} e^{i(w_m t - ky)} \\ m_{0z} e^{i(w_m t - ky)} \end{pmatrix} \tag{8.72}$$

In this geometry the micromagnetic iDMI energy density reads as

$$E_{DM} = \vec{D}.\left[\vec{M} \times \left(\frac{\partial \vec{M}}{\partial y}\right)\right] \tag{8.73}$$

Thus, since $\vec{M} = \vec{M}_0 + \vec{m}(t)$, and $\vec{D} = D(\vec{z} \times \vec{y}) = -D\vec{x}$ one obtain directly

$$E_{DM} = -\frac{D}{M_S^2}\left(m_y \frac{\partial m_z}{\partial y} - m_z \frac{\partial m_y}{\partial y}\right)$$

It allows to calculate the effective field from the iDMI energy $\mu_0 \vec{H}_{eff}^{DMI} = -\frac{\delta E_{DM}}{\delta \vec{M}}$, where the functional derivative is defined as $\frac{\delta F}{\delta g} = \frac{\partial F}{\partial g} - \frac{d}{dy}\left(\frac{\partial F}{\partial\left(\frac{\partial g}{\partial y}\right)}\right)$.

$$\begin{aligned}
&\frac{\delta E_{DM}}{\delta M_0} = 0 \\
&\frac{\delta E_{DM}}{\delta m_y} = \frac{\partial E_{DM}}{\partial m_y} - \frac{d}{dy}\left(\frac{\partial E_{DM}}{\partial\left(\frac{\partial m_y}{\partial y}\right)}\right) = -\frac{2D}{M_S^2}\frac{\partial m_z}{\partial y} \\
&\frac{\delta E_{DM}}{\delta m_z} = \frac{\partial E_{DM}}{\partial m_z} - \frac{d}{dy}\left(\frac{\partial E_{DM}}{\partial\left(\frac{\partial m_z}{\partial y}\right)}\right) = \frac{2D}{M_S^2}\frac{\partial m_y}{\partial y}
\end{aligned}$$

Using the definition of $\vec{m}$ it leads to

$$\mu_0 \vec{H}_{eff}^{DMI} = -\frac{2D}{M_S^2}\left(\vec{x} \times \frac{\partial \vec{m}}{\partial y}\right) = -\frac{2D}{M_S^2}\left(\vec{x} \times ik\vec{m}\right)$$

Thus, we see from the last expression that the direction of $\mu_0 \vec{H}_{eff}^{DMI}$ depends on the sign of the magnon's wave vector. Thus we can see that for one sign of k the frequency of the spin wave is increased while it is decreased for the opposite sign of k. In conclusion, we have shown that the presence of iDMI induces a non reciprocity in the frequency of counter-propagating spin waves.

We can go further and quantify the frequency shift due to iDMI by inserting $\mu_0 \vec{H}_{eff}^{DMI}$ in the LL equation

$$\frac{d\vec{M}}{dt} = -\gamma \vec{M} \times \mu_0 \vec{H}_{eff}^{DMI}$$
$$iw_m \vec{m} = i\frac{2\gamma}{M_S^2} Dk \left(\vec{M} \times (\vec{x} \times \vec{m}) \right)$$
$$w_m \vec{m} = i\frac{2\gamma}{M_S^2} Dk \begin{pmatrix} m_y^2 + m_z^2 \\ M_0 m_y \\ M_0 m_z \end{pmatrix}$$

Then, as $M_0 = M_S$ (magnetization saturated along x) and neglegting second order term $|\vec{m}| = m_y^2 + m_z^2$, one gets

$$\left(w_m - \frac{2\gamma}{M_S} Dk \right) \vec{m} = \vec{0}$$

And then it allows to see that for two spin waves propagating in opposite directions we have a frequency shift :

$$\Delta f = \frac{w_m(k) - w_m(-k)}{2\pi} = \frac{2\gamma}{\pi M_S} Dk$$

This simple calculation demonstrate the direct relation between the frequency shift Δf observed on BLS spectra and the iMDI constant D. We can see that BLS is a direct way to obtain the iDMI constant both in ampltitude and sign.
Brillouin Light Scattering also allows to measure the damping (proportional to the width of the peaks) and the anisotropy (proportional to the average position of the peaks). Thus, BLS is a technique that allows to get a lot of information on the magnetic parameters from only one spectra. However, the acquisition of one spectra is a long experiment (around 10h to accumaulate enough data (40000 photons) to be able to fit with the Lorentzians).

8.7 ANNEX 7: ESTIMATION OF THE CURRENT DENSITY IN FULL-SHEET SAMPLE

In order to estimate the current density everywhere in the bottom Ta layer (thickness t, resistivity ρ), we elaborated a simple model where a charge current is flowing between two point-contact electrodes (resistivity $\rho_0 \ll \rho$, see Fig. 8.12a). One electrode feeds charges in the Ta layer (the source, red circle on Fig. 8.12b) while the other evacuates them (the sink, black circle on Fig. 8.12b). The charges coming from the source are distributed over a partial-sphere (surface $2\pi Rt$) limited by the thickness of the Ta layer (represented by the dotted line in Fig. 8.12a). For the model we consider only the steady-state (charge distribution at equilibrium) so that $\vec{\nabla}.\vec{J} = 0$. By simply using the Gauss theorem one gets the electric field $E = \pm\frac{\rho I}{2\pi Rt}$ where the sign stands for respectively a source and a sink. An applied current is obtained when charges circulate from the source to the sink. Then, by putting a source at $x = -\frac{L}{2}$ and a sink at $x = +\frac{L}{2}$, one can obtain the current density $\vec{J}(x,y)$ through $\vec{J} = \frac{1}{\rho}\vec{E}$, and one gets :

$$\vec{J} = \frac{I}{2\pi t}\left[\left(\frac{(x-\frac{L}{2})}{(x-\frac{L}{2})^2+y^2} - \frac{(x+\frac{L}{2})}{(x+\frac{L}{2})^2+y^2}\right)\vec{u_x} + \left(\frac{y}{(x-\frac{L}{2})^2+y^2} - \frac{y}{(x+\frac{L}{2})^2+y^2}\right)\vec{u_y}\right]$$

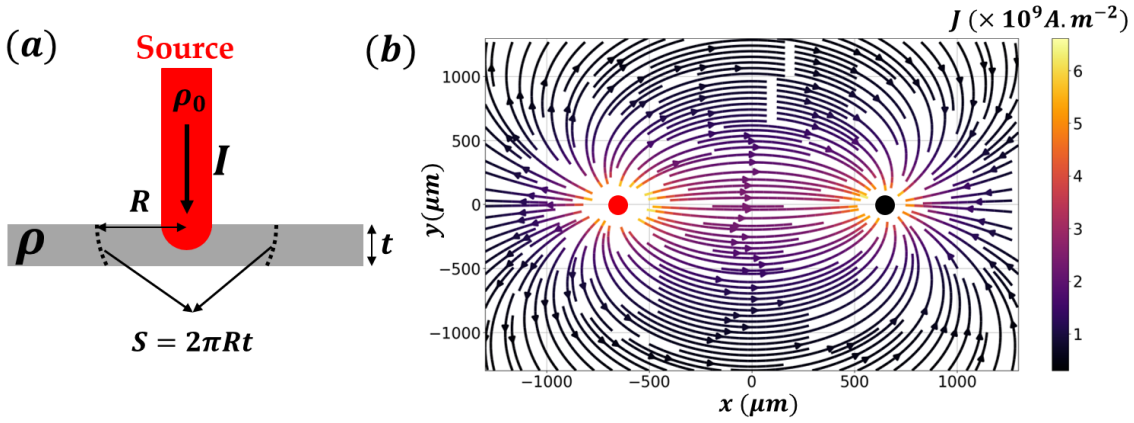

Figure 8.12: **Current distribution in full-sheet samples:** (a) Schematic representation of the cross-section geometry used for the model. The source is feeding charges that are distributed over the partial sphere defined by the dashed lines. Then, by adding a sink to the source, the current density and direction is obtained (for $I = 15\ mA$, $L = 1300\ \mu m$ and $t = 3\ nm$, typical experimental parameters), as shown in (b) where the source is depicted by the red circle and the sink by the black circle.

Then, using the experimental distance between the source and sink (L), injected current (I) and bottom Ta thickness (t), the current density is determined using this simple model and the average location of the skyrmion bubbles or labyrinthine DWs compared to the current density distribution. For example, in Fig. 5.3 from chapter 5, the experimental parameters are $L = 1.3\ mm$, $I = 15\ mA$ and $t_{Ta} = 3\ nm$, and give the resulting current density shown in Fig. 8.12b. Using this, we can extract the typical current density in the experiment region

$J \simeq 5 \times 10^9\ A.m^{-2}$. Applying this method to estimate the current density in the other experimental figures from chapter 5 leads to the same order of magnitude.

BIBLIOGRAPHY

[1] E. E. Fullerton and J. R. Childress, 'Spintronics and the emergence of the digital world', *SciTech Europa*, vol. Quarterly 30, p. 22, (cit. on p. xxv).

[2] M. N. Baibich, J. M. Broto, A. Fert, F. N. Van Dau, F. Petroff, P. Etienne, G. Creuzet, A. Friederich and J. Chazelas, 'Giant magnetoresistance of (001)fe/(001)cr magnetic superlattices', *Phys. Rev. Lett.*, vol. 61, pp. 2472–2475, 21 1988. DOI: 10.1103/PhysRevLett.61.2472 (cit. on p. xxv).

[3] *Spintronics market - growth, trends, covid-19 impact, and forecasts (2022 - 2027)*, *Mordor Intelligence*, 2021 (cit. on p. xxv).

[4] R. Ferreira, E. Paz, P. P. Freitas, J. Wang and S. Xue, 'Large Area and Low Aspect Ratio Linear Magnetic Tunnel Junctions With a Soft-Pinned Sensing Layer', *IEEE Transactions on Magnetics*, vol. 48, no. 11, pp. 3719–3722, 2012. DOI: 10.1109/TMAG.2012.2200468 (cit. on p. xxv).

[5] P. P. Freitas, R. Ferreira and S. Cardoso, 'Spintronic Sensors', *Proceedings of the IEEE*, vol. 104, no. 10, pp. 1894–1918, 2016. DOI: 10.1109/JPROC.2016.2578303 (cit. on p. xxv).

[6] D. Apalkov, B. Dieny and J. M. Slaughter, 'Magnetoresistive Random Access Memory', *Proceedings of the IEEE*, vol. 104, no. 10, pp. 1796–1830, 2016. DOI: 10.1109/JPROC.2016.2590142 (cit. on p. xxv).

[7] J. Grollier, D. Querlioz, K. Y. Camsari, K. Everschor-Sitte, S. Fukami and M. D. Stiles, 'Neuromorphic spintronics', *Nature Electronics*, vol. 3, no. 7, pp. 360–370, 2020. DOI: 10.1038/s41928-019-0360-9 (cit. on p. xxv).

[8] O. Boulle, V. Cros, J. Grollier, L. G. Pereira, C. Deranlot, F. Petroff, G. Faini, J. Barnaś and A. Fert, 'Shaped angular dependence of the spin-transfer torque and microwave generation without magnetic field', *Nature Physics*, vol. 3, no. 7, pp. 492–497, 2007. DOI: 10.1038/nphys618 (cit. on p. xxv).

[9] A. Fert, N. Reyren and V. Cros, 'Advances in the physics of magnetic skyrmions and perspective for technology', *Nature Review Materials*, vol. 46, no. 17031, 2017. DOI: https://www.nature.com/articles/natrevmats201731 (cit. on pp. xxv, 13, 31, 35, 39).

[10] A. Fert, V. Cros and J. Sampaio, 'Skyrmions on the track', *Nature Nanotechnology*, vol. 8, no. 3, pp. 152–156, 2013. DOI: 10.1038/nnano.2013.29 (cit. on pp. xxv, 13, 31).

[11] R. Tomasello, E. Martinez, R. Zivieri, L. Torres, M. Carpentieri and G. Finocchio, 'A strategy for the design of skyrmion racetrack memories', *Scientific Reports*, vol. 4, no. 1, p. 6784, 2014. DOI: 10.1038/srep06784 (cit. on p. xxv).

[12] H. Du, D. Liang, C. Jin *et al.*, 'Electrical probing of field-driven cascading quantized transitions of skyrmion cluster states in MnSi nanowires', *Nature Communications*, vol. 6, no. 1, p. 7637, 2015. DOI: 10.1038/ncomms8637 (cit. on p. xxv).

[13] S. Woo, K. Litzius, B. Krueger *et al.*, 'Observation of room-temperature magnetic skyrmions and their current-driven dynamics in ultrathin metallic ferromagnets', *Nature Materials*, vol. 15, no. 5, pp. 501–506, 2016. DOI: 10.1038/nmat4593 (cit. on pp. xxvi, 35).

[14] 'Private communication', *Writing, Unpublished*, (cit. on p. xxvi).

[15] X. Zhang, M. Ezawa and Y. Zhou, 'Magnetic skyrmion logic gates: Conversion, duplication and merging of skyrmions', *Scientific Reports*, vol. 5, no. 1, p. 9400, 2015. DOI: 10.1038/srep09400 (cit. on p. xxvi).

[16] S. Luo, M. Song, X. Li, Y. Zhang, J. Hong, X. Yang, X. Zou, N. Xu and L. You, 'Reconfigurable Skyrmion Logic Gates', *Nano Letters*, vol. 18, no. 2, pp. 1180–1184, 2018. DOI: 10.1021/acs.nanolett.7b04722 (cit. on p. xxvi).

[17] M. Chauwin, X. Hu, F. Garcia-Sanchez, N. Betrabet, A. Paler, C. Moutafis and J. S. Friedman, 'Skyrmion logic system for large-scale reversible computation', *Phys. Rev. Applied*, vol. 12, p. 064 053, 6 2019. DOI: 10.1103/PhysRevApplied.12.064053 (cit. on p. xxvi).

[18] C. Tang, L. Alahmed, J. Xu, M. Shen, N. A. Jones, M. Sadi, U. Guin, W. Zhao and P. Li, 'Effects of Temperature and Structural Geometries on a Skyrmion Logic Gate', *IEEE Transactions on Electron Devices*, vol. 69, no. 4, pp. 1706–1712, 2022. DOI: 10.1109/TED.2021.3130217 (cit. on p. xxvi).

[19] D. Yu, H. Yang, M. Chshiev and A. Fert, 'Skyrmions-based logic gates in one single nanotrack completely reconstructed via chirality barrier', *National Science Review*, nwac021, 2022. DOI: 10.1093/nsr/nwac021 (cit. on pp. xxvi, 119, 161, 162).

[20] X. Zhang, Y. Zhou, M. Ezawa, G. P. Zhao and W. Zhao, 'Magnetic skyrmion transistor: Skyrmion motion in a voltage-gated nanotrack', *Scientific Reports*, vol. 5, no. 1, p. 11 369, 2015. DOI: 10.1038/srep11369 (cit. on pp. xxvi, 119).

[21] I.-S. Hong and K.-J. Lee, 'Magnetic skyrmion field-effect transistors', *Applied Physics Letters*, vol. 115, no. 7, p. 072 406, 2019. DOI: 10.1063/1.5110752 (cit. on pp. xxvi, 58, 119).

[22] *Web of science, URL - Low power spintronics* (cit. on p. xxvi).

[23] *Web of science, URL - Magnetic skyrmions* (cit. on p. xxvi).

[24] T. Moriya, 'New mechanism of anisotropic superexchange interaction', *Phys. Rev. Lett.*, vol. 4, pp. 228–230, 5 1960. DOI: 10.1103/PhysRevLett.4.228 (cit. on pp. xxvi, 12).

[25] ——, 'Anisotropic superexchange interaction and weak ferromagnetism', *Phys. Rev.*, vol. 120, pp. 91–98, 1 1960. DOI: 10.1103/PhysRev.120.91 (cit. on pp. xxvi, 12).

[26] I. Dzyaloshinsky, 'A thermodynamic theory of "weak" ferromagnetism of antiferromagnetics', *Journal of Physics and Chemistry of Solids*, vol. 4, no. 4, pp. 241–255, 1958. DOI: https://doi.org/10.1016/0022-3697(58)90076-3 (cit. on pp. xxvi, 12).

[27] R. A. Duine, K.-J. Lee, S. S. P. Parkin and M. D. Stiles, 'Synthetic antiferromagnetic spintronics', *Nature Physics*, vol. 14, no. 3, pp. 217–219, 2018. DOI: 10.1038/s41567-018-0050-y (cit. on p. 4).

[28] R. Juge, N. Sisodia, J. U. Larrañaga *et al.*, 'Skyrmions in synthetic antiferromagnets and their nucleation via electrical current and ultra-fast laser illumination', *Nature Communications*, vol. 13, no. 1, p. 4807, 2022. DOI: 10.1038/s41467-022-32525-4 (cit. on pp. 4, 144).

[29] L. Shen, X. Li, Y. Zhao, J. Xia, G. Zhao and Y. Zhou, 'Current-Induced Dynamics of the Antiferromagnetic Skyrmion and Skyrmionium', *Physical Review Applied*, vol. 12, no. 6, p. 064 033, 2019. DOI: 10.1103/PhysRevApplied.12.064033 (cit. on p. 4).

[30] C. Jin, C. Song, J. Wang and Q. Liu, 'Dynamics of antiferromagnetic skyrmion driven by the spin Hall effect', *Applied Physics Letters*, vol. 109, no. 18, p. 182 404, 2016. DOI: 10.1063/1.4967006 (cit. on pp. 4, 144).

[31] J. Barker and O. A. Tretiakov, 'Static and Dynamical Properties of Antiferromagnetic Skyrmions in the Presence of Applied Current and Temperature', *Physical Review Letters*, vol. 116, no. 14, p. 147 203, 2016. DOI: 10.1103/PhysRevLett.116.147203 (cit. on p. 4).

[32] R. O'Handley, *Modern Magnetic Materials: Principles and Applications*. Wiley, 1999 (cit. on p. 5).

[33] Curie, P., 'Sur la symétrie dans les phénomènes physiques, symétrie d'un champ électrique et d'un champ magnétique', *J. Phys. Theor. Appl.*, vol. 3, no. 1, pp. 393–415, 1894. DOI: 10.1051/jphystap:018940030039300 (cit. on p. 7).

[34] Néel, Louis, 'Anisotropie magnétique superficielle et surstructures d'orientation', *J. Phys. Radium*, vol. 15, no. 4, pp. 225–239, 1954. DOI: 10.1051/jphysrad:01954001504022500 (cit. on p. 8).

[35] S. Monso, B. Rodmacq, S. Auffret, G. Casali, F. Fettar, B. Gilles, B. Dieny and P. Boyer, 'Crossover from in-plane to perpendicular anisotropy in Pt/CoFe/AlOx sandwiches as a function of Al oxidation: A very accurate control of the oxidation of tunnel barriers', *Applied Physics Letters*, vol. 80, no. 22, pp. 4157–4159, 2002. DOI: 10.1063/1.1483122 (cit. on p. 8).

[36] P. F. Carcia, A. D. Meinhaldt and A. Suna, 'Perpendicular magnetic anisotropy in Pd/Co thin film layered structures', *Applied Physics Letters*, vol. 47, no. 2, pp. 178–180, 1985. DOI: 10.1063/1.96254 (cit. on p. 8).

[37] A. Manchon, C. Ducruet, L. Lombard *et al.*, 'Analysis of oxygen induced anisotropy crossover in Pt/Co/MOx trilayers', *Journal of Applied Physics*, vol. 104, no. 4, p. 043 914, 2008. DOI: 10.1063/1.2969711 (cit. on pp. 8, 18, 19).

[38] A. Manchon, S. Pizzini, J. Vogel *et al.*, 'X-ray analysis of oxygen-induced perpendicular magnetic anisotropy in trilayers', *Journal of Magnetism and Magnetic Materials*, vol. 320, no. 13, pp. 1889–1892, 2008. DOI: 10.1016/j.jmmm.2008.02.131 (cit. on pp. 8, 18).

[39] A. Manchon, S. Pizzini, J. Vogel *et al.*, 'X-ray analysis of the magnetic influence of oxygen in PtCoAlOx trilayers', *Journal of Applied Physics*, vol. 103, no. 7, 07A912, 2008. DOI: 10.1063/1.2829896 (cit. on pp. 8, 18).

[40] A. V. Khvalkovskiy, D Apalkov, S Watts *et al.*, 'Basic principles of STT-MRAM cell operation in memory arrays', *Journal of Physics D: Applied Physics*, vol. 46, no. 7, p. 074 001, 2013. DOI: 10.1088/0022-3727/46/7/074001 (cit. on pp. 8, 9).

[41] M. T. Johnson, P. J. H. Bloemen, F. J. A. d. Broeder and J. J. d. Vries, 'Magnetic anisotropy in metallic multilayers', *Reports on Progress in Physics*, vol. 59, no. 11, pp. 1409–1458, 1996. DOI: 10.1088/0034-4885/59/11/002 (cit. on pp. 9, 17).

[42] F. den Broeder, W. Hoving and P. Bloemen, 'Magnetic anisotropy of multilayers', *Journal of Magnetism and Magnetic Materials*, vol. 93, pp. 562–570, 1991. DOI: 10.1016/0304-8853(91)90404-X (cit. on pp. 9, 17).

[43] W. B. Zeper, F. J. A. M. Greidanus, P. F. Carcia and C. R. Fincher, 'Perpendicular magnetic anisotropy and magneto-optical Kerr effect of vapor-deposited Co/Pt-layered structures', *Journal of Applied Physics*, vol. 65, no. 12, pp. 4971–4975, 1989. DOI: 10.1063/1.343189 (cit. on pp. 9, 17, 18).

[44] H. Draaisma, W. de Jonge and F. den Broeder, 'Magnetic interface anisotropy in Pd/Co and Pd/Fe multilayers', *Journal of Magnetism and Magnetic Materials*, vol. 66, no. 3, pp. 351–355, 1987. DOI: 10.1016/0304-8853(87)90169-7 (cit. on pp. 9, 17).

[45] U. Gradmann, 'MAGNETIC SURFACE ANISOTROPIES', *Journal of Magnetism and Magnetic Materials*, no. 54-57, p. 733, 1986. DOI: https://doi.org/10.1016/0304-8853(86)90230-1 (cit. on pp. 9, 17).

[46] ——, 'Chapter 1 magnetism in ultrathin transition metal films', Handbook of Magnetic Materials, vol. 7, pp. 1–96, 1993. DOI: https://doi.org/10.1016/S1567-2719(05)80042-3 (cit. on p. 10).

[47] E. P. Wohlfarth and K. H. J. Buschow, Eds., *Ferromagnetic materials: a handbook on the properties of magnetically ordered substances*. Amsterdam ; New York : New York: North-Holland Pub. Co. ; Sole distributors for the U.S.A. and Canada, Elsevier North-Holland, 1980 (cit. on p. 10).

[48] J. Kohlhepp, H. J. Elmers, S. Cordes and U. Gradmann, 'Power laws of magnetization in ferromagnetic monolayers and the two-dimensional Ising model', *Physical Review B*, vol. 45, no. 21, pp. 12 287–12 291, 1992. DOI: 10.1103/PhysRevB.45.12287 (cit. on p. 10).

[49] Y. Li and K. Baberschke, 'Dimensional crossover in ultrathin Ni(111) films on W(110)', *Physical Review Letters*, vol. 68, no. 8, pp. 1208–1211, 1992. DOI: 10.1103/PhysRevLett.68.1208 (cit. on p. 10).

[50] H. Callen and E. Callen, 'The present status of the temperature dependence of magnetocrystalline anisotropy, and the l(l+1)2 power law', *Journal of Physics and Chemistry of Solids*, vol. 27, no. 8, pp. 1271–1285, 1966. DOI: https://doi.org/10.1016/0022-3697(66)90012-6 (cit. on p. 10).

[51] P. Asselin, R. F. L. Evans, J. Barker, R. W. Chantrell, R. Yanes, O. Chubykalo-Fesenko, D. Hinzke and U. Nowak, 'Constrained monte carlo method and calculation of the temperature dependence of magnetic anisotropy', *Phys. Rev. B*, vol. 82, p. 054 415, 5 2010. DOI: 10.1103/PhysRevB.82.054415 (cit. on p. 10).

[52] R. Skomski, O. N. Mryasov, J. Zhou and D. J. Sellmyer, 'Finite-temperature anisotropy of magnetic alloys', *Journal of Applied Physics*, vol. 99, no. 8, 08E916, 2006. DOI: 10.1063/1.2176892. eprint: https://doi.org/10.1063/1.2176892 (cit. on p. 10).

[53] J.-U. Thiele, K. R. Coffey, M. F. Toney, J. A. Hedstrom and A. J. Kellock, 'Temperature dependent magnetic properties of highly chemically ordered fe55xnixpt45l10 films', *Journal of Applied Physics*, vol. 91, no. 10, pp. 6595–6600, 2002. DOI: 10.1063/1.1470254 (cit. on p. 10).

[54] S. Okamoto, N. Kikuchi, O. Kitakami, T. Miyazaki, Y. Shimada and K. Fukamichi, 'Chemical-order-dependent magnetic anisotropy and exchange stiffness constant of fept (001) epitaxial films', *Phys. Rev. B*, vol. 66, p. 024 413, 2 2002. DOI: 10.1103/PhysRevB.66.024413 (cit. on p. 10).

[55] L. Ranno, *Private Communication*, (cit. on p. 10).

[56] M. Fang, W. Zhang, X. Wu, W. Guo, H. Xia, Y. Wang, W. Wang and J. Shen, 'Recent advances in tunable spin–orbit coupling using ferroelectricity', *APL Materials*, vol. 9, no. 6, p. 060 704, 2021. DOI: 10.1063/5.0052553 (cit. on pp. 11, 12).

[57] K. V. Shanavas, Z. S. Popović and S. Satpathy, 'Theoretical model for Rashba spin-orbit interaction in d electrons', *Physical Review B*, vol. 90, no. 16, p. 165 108, 2014. DOI: 10.1103/PhysRevB.90.165108 (cit. on p. 11).

[58] F. Herman, C. D. Kuglin, K. F. Cuff and R. L. Kortum, 'Relativistic Corrections to the Band Structure of Tetrahedrally Bonded Semiconductors', *Physical Review Letters*, vol. 11, no. 12, pp. 541–545, 1963. DOI: 10.1103/PhysRevLett.11.541 (cit. on p. 11).

[59] A. Fert and P. Levy, 'Role of anisotropic exchange interactions in determining the properties of spin-glasses', *Phys. Rev. Lett.*, vol. 44, p. 1538, 1980 (cit. on pp. 15, 97).

[60] J. Cho, N.-H. Kim, S. Lee *et al.*, 'Thickness dependence of the interfacial Dzyaloshinskii-Moriya interaction in inversion symmetry broken systems', *Nature Communications*, vol. 6, no. 1, p. 7635, 2015. DOI: 10.1038/ncomms8635 (cit. on p. 18).

[61] R. Lo Conte, G. V. Karnad, E. Martinez *et al.*, 'Ferromagnetic layer thickness dependence of the Dzyaloshinskii-Moriya interaction and spin-orbit torques in Pt\Co\AlO $_x$ ', *AIP Advances*, vol. 7, no. 6, p. 065 317, 2017. DOI: 10.1063/1.4990694 (cit. on p. 18).

[62] D. d. S. Chaves, F. Ajejas, V. Krizakova, J. Vogel and S. Pizzini, 'Dependence of Dzyaloshinskii-Moriya interaction on the oxygen coverage in Pt/Co/MOx trilayers', *Physical Review B*, vol. 99, no. 14, p. 144 404, 2019, arXiv: 1708.08516. DOI: 10.1103/PhysRevB.99.144404 (cit. on pp. 19, 20, 118).

[63] A. Belabbes, G. Bihlmayer, S. Blügel and A. Manchon, 'Oxygen-enabled control of Dzyaloshinskii-Moriya Interaction in ultra-thin magnetic films', *Scientific Reports*, vol. 6, no. 1, p. 24 634, 2016. DOI: 10.1038/srep24634 (cit. on pp. 19, 20).

[64] M. Arora, J. M. Shaw and H. T. Nembach, 'Variation of sign and magnitude of the Dzyaloshinskii-Moriya interaction of a ferromagnet with an oxide interface', *Physical Review B*, vol. 101, no. 5, p. 054 421, 2020. DOI: 10.1103/PhysRevB.101.054421 (cit. on pp. 20, 98).

[65] G. Chen, A. Mascaraque, H. Jia *et al.*, 'Large dzyaloshinskii-moriya interaction induced by chemisorbed oxygen on a ferromagnet surface', *Science Advances*, vol. 6, no. 33, eaba4924, 2020. DOI: 10.1126/sciadv.aba4924. eprint: https://www.science.org/doi/pdf/10.1126/sciadv.aba4924 (cit. on p. 20).

[66] G. Chen, M. Robertson, M. Hoffmann *et al.*, 'Observation of Hydrogen-Induced Dzyaloshinskii-Moriya Interaction and Reversible Switching of Magnetic Chirality', *Physical Review X*, vol. 11, no. 2, p. 021 015, 2021. DOI: 10.1103/PhysRevX.11.021015 (cit. on pp. 20, 105).

[67] J. Torrejon, J. Kim, J. Sinha, S. Mitani, M. Hayashi, M. Yamanouchi and H. Ohno, 'Interface control of the magnetic chirality in CoFeB/MgO heterostructures with heavy-metal underlayers', *Nature Communications*, vol. 5, no. 1, p. 4655, 2014. DOI: 10.1038/ncomms5655 (cit. on pp. 21, 92, 93, 103).

[68] X. Ma, G. Yu, C. Tang, X. Li, C. He, J. Shi, K. L. Wang and X. Li, 'Interfacial Dzyaloshinskii-Moriya Interaction: Effect of 5 d Band Filling and Correlation with Spin Mixing Conductance', *Physical Review Letters*, vol. 120, no. 15, p. 157 204, 2018. DOI: 10.1103/PhysRevLett.120.157204 (cit. on pp. 21, 97).

[69] P. Jadaun, L. F. Register and S. K. Banerjee, 'The microscopic origin of DMI in magnetic bilayers and prediction of giant DMI in new bilayers', *npj Computational Materials*, vol. 6, no. 1, p. 88, 2020. DOI: 10.1038/s41524-020-00351-1 (cit. on p. 21).

[70] S. Tacchi, R. E. Troncoso, M. Ahlberg, G. Gubbiotti, M. Madami, J. Åkerman and P. Landeros, 'Interfacial dzyaloshinskii-moriya interaction in Pt/CoFeB films: Effect of the heavy-metal thickness', *Phys. Rev. Lett.*, vol. 118, p. 147 201, 14 2017. DOI: 10.1103/PhysRevLett.118.147201 (cit. on p. 21).

[71] X. Ma, G. Yu, X. Li *et al.*, 'Interfacial control of dzyaloshinskii-moriya interaction in heavy metal/ferromagnetic metal thin film heterostructures', *Phys. Rev. B*, vol. 94, p. 180 408, 18 2016. DOI: 10.1103/PhysRevB.94.180408 (cit. on p. 21).

[72] W. Zhang, R. Chen, B. Jiang, X. Zhao, W. Zhao, S. S. Yan, G. Han, S. Yu, G. Liu and S. Kang, 'Tunable interfacial dzyaloshinskii–moriya interaction in symmetrical au/[fe/au]n multilayers', *Nanoscale*, vol. 13, pp. 2665–2672, 4 2021. DOI: 10.1039/D0NR06488B (cit. on p. 22).

[73] M. Weisheit, S. Fahler, A. Marty, Y. Souche, C. Poinsignon and D. Givord, 'Electric field-induced modification of magnetism in thin-film ferromagnets', *Science Reports*, vol. 315, pp. 349–351, 2007 (cit. on pp. 22, 105).

[74] W. G. Wang and C. L. Chien, 'Voltage-induced switching in magnetic tunnel junctions with perpendicular magnetic anisotropy', *Journal of Physics D: Applied Physics*, vol. 46, no. 074004, p. 074 004, 2013. DOI: 10.1088/0022-3727/46/7/074004 (cit. on pp. 22, 105).

[75] W. Zhang, H. Zhong, R. Zang, Y. Zhang, S. Yu, G. Han, G. L. Liu, S. S. Yan, S. Kang and L. M. Mei, 'Electrical field enhanced interfacial Dzyaloshinskii-Moriya interaction in MgO/Fe/Pt system', *Applied Physics Letters*, vol. 113, no. 12, p. 122 406, 2018. DOI: 10.1063/1.5050447 (cit. on p. 22).

[76] T. Srivastava, M. Schott, R. Juge *et al.*, 'Large-Voltage Tuning of Dzyaloshinskii-Moriya Interactions: A Route toward Dynamic Control of Skyrmion Chirality', *Nano Letters*, vol. 18, no. 8, pp. 4871–4877, 2018. DOI: 10.1021/acs.nanolett.8b01502 (cit. on pp. 22, 26, 27, 79, 87, 92, 93, 98, 113, 118, 119, 122).

[77] M. Schott, L. Ranno, H. Béa, C. Baraduc, S. Auffret and A. Bernand-Mantel, 'Electric field control of interfacial Dzyaloshinskii-Moriya interaction in Pt/Co/AlOx thin films', *Journal of Magnetism and Magnetic Materials*, vol. 520, p. 167 122, 2021. DOI: 10.1016/j.jmmm.2020.167122 (cit. on pp. 22, 27, 105).

[78] W.-G. Wang, M. Li, S. Hageman and C. L. Chien, 'Electric-field-assisted switching in magnetic tunnel junctions', *Nature Materials*, vol. 11, no. 1, pp. 64–68, 2012. DOI: 10.1038/nmat3171 (cit. on p. 22).

[79] Y. Shiota, T. Nozaki, F. Bonell, S. Murakami, T. Shinjo and Y. Suzuki, 'Induction of coherent magnetization switching in a few atomic layers of FeCo using voltage pulses', *Nature Materials*, vol. 11, no. 1, pp. 39–43, 2012. DOI: 10.1038/nmat3172 (cit. on p. 22).

[80] T. Maruyama, Y. Shiota, T. Nozaki *et al.*, 'Large voltage-induced magnetic anisotropy change in a few atomic layers of iron', *Nature Nanotechnology*, vol. 4, no. 3, pp. 158–161, 2009. DOI: 10.1038/nnano.2008.406 (cit. on p. 22).

[81] C.-G. Duan, J. P. Velev, R. F. Sabirianov, Z. Zhu, J. Chu, S. S. Jaswal and E. Y. Tsymbal, 'Surface magnetoelectric effect in ferromagnetic metal films', *Phys. Rev. Lett.*, vol. 101, p. 137 201, 13 2008. DOI: 10.1103/PhysRevLett.101.137201 (cit. on p. 22).

[82] L. Reichel, S. Oswald, S. Fähler, L. Schultz and K. Leistner, 'Electrochemically driven variation of magnetic properties in ultrathin copt films', *Journal of Applied Physics*, vol. 113, no. 14, p. 143 904, 2013. DOI: 10.1063/1.4799413 (cit. on p. 22).

[83] F. Bonell, Y. T. Takahashi, D. D. Lam, S. Yoshida, Y. Shiota, S. Miwa, T. Nakamura and Y. Suzuki, 'Reversible change in the oxidation state and magnetic circular dichroism of fe driven by an electric field at the feco/mgo interface', *Applied Physics Letters*, vol. 102, no. 15, p. 152 401, 2013. DOI: 10.1063/1.4802030 (cit. on p. 22).

[84] N. Tournerie, A. P. Engelhardt, F. Maroun and P. Allongue, 'Influence of the surface chemistry on the electric-field control of the magnetization of ultrathin films', *Phys. Rev. B*, vol. 86, p. 104 434, 10 2012. DOI: 10.1103/PhysRevB.86.104434 (cit. on p. 22).

[85] B. Dieny and M. Chshiev, 'Perpendicular magnetic anisotropy at transition metal/oxide interfaces and applications', *Reviews of Modern Physics*, vol. 89, no. 2, p. 025 008, 2017. DOI: 10.1103/RevModPhys.89.025008 (cit. on pp. 22, 23, 118).

[86] A. Fassatoui, L. Ranno, J. P. Garcia, C. Balan, J. Vogel, H. Bea, and S. Pizzin, 'Kinetics of ion migration in the electric field-driven manipulation of magnetic anisotropy of pt/co/oxide multilayers', *Small*, vol. 17, no. 38, p. 2 102 427, 2021. DOI: https://doi.org/10.1002/smll.202102427 (cit. on pp. 22, 24, 25, 86, 111).

[87] A. Fassatoui, J. P. Garcia, L. Ranno, J. Vogel, A. Bernand-Mantel, H. Béa, S. Pizzini and S. Pizzini, 'Reversible and irreversible voltage manipulation of interfacial magnetic anisotropy in Pt/Co/Oxide multilayers', *Phys. Rev. Applied*, vol. 14, p. 064 041, 2020. DOI: https://doi.org/10.1063/1.4939446 (cit. on pp. 22, 113).

[88] U. Bauer, L. Yao, A. J. Tan, P. Agrawal, S. Emori, H. L. Tuller, S. van Dijken and G. S. D. Beach, 'Magneto-ionic control of interfacial magnetism', *Nature Materials*, vol. 14, no. 2, pp. 174–181, 2015. DOI: 10.1038/nmat4134 (cit. on pp. 22–24).

[89] C. Bi, Y. Liu, T. Newhouse-Illige, M. Xu, M. Rosales, J. Freeland, O. Mryasov, S. Zhang, S. te Velthuis and W. Wang, 'Reversible Control of Co Magnetism by Voltage-Induced Oxidation', *Physical Review Letters*, vol. 113, no. 26, p. 267 202, 2014. DOI: 10.1103/PhysRevLett.113.267202 (cit. on p. 22).

[90] Y. Nakatani, M. Hayashi, S. Kanai, S. Fukami and H. Ohno, 'Electric field control of Skyrmions in magnetic nanodisks', *Applied Physics Letters*, vol. 108, no. 15, p. 152 403, 2016. DOI: 10.1063/1.4945738 (cit. on pp. 25, 26).

[91] M. Schott, A. Bernand-Mantel, L. Ranno, S. Pizzini, J. Vogel, H. Béa, C. Baraduc, S. Auffret, G. Gaudin and D. Givord, 'The Skyrmion Switch: Turning Magnetic Skyrmion Bubbles on and off with an Electric Field', *Nano Letters*, vol. 17, no. 5, pp. 3006–3012, 2017. DOI: 10.1021/acs.nanolett.7b00328 (cit. on pp. 25, 26, 90, 92, 113, 119, 124).

[92] Y. Zhou, R. Mansell and S. van Dijken, 'Voltage control of skyrmions: Creation, annihilation, and zero-magnetic field stabilization', *Applied Physics Letters*, vol. 118, no. 17, p. 172 409, 2021. DOI: 10.1063/5.0047892 (cit. on p. 25).

[93] C. Ma, X. Zhang, J. Xia, M. Ezawa, W. Jiang, T. Ono, S. N. Piramanayagam, A. Morisako, Y. Zhou and X. Liu, 'Electric Field-Induced Creation and Directional Motion of Domain Walls and Skyrmion Bubbles', *Nano Letters*, vol. 19, no. 1, pp. 353–361, 2019. DOI: 10.1021/acs.nanolett.8b03983 (cit. on p. 25).

[94] K. Nawaoka, S. Miwa, Y. Shiota, N. Mizuochi and Y. Suzuki, 'Voltage induction of interfacial Dzyaloshinskii-Moriya interaction in Au/Fe/MgO artificial multilayer', *Applied Physics Express*, vol. 8, no. 6, p. 063 004, 2015. DOI: 10.7567/APEX.8.063004 (cit. on p. 26).

[95] H. Yang, O. Boulle, V. Cros, A. Fert and M. Chshiev, 'Controlling Dzyaloshinskii-Moriya Interaction via Chirality Dependent Atomic-Layer Stacking, Insulator Capping and Electric Field', *Scientific Reports*, vol. 8, no. 1, p. 12 356, 2018. DOI: 10.1038/s41598-018-30063-y (cit. on pp. 26, 99, 118).

[96] L. Herrera Diez, Y. Liu, D. Gilbert *et al.*, 'Nonvolatile Ionic Modification of the Dzyaloshinskii-Moriya Interaction', *Physical Review Applied*, vol. 12, no. 3, p. 034 005, 2019. DOI: 10.1103/PhysRevApplied.12.034005 (cit. on pp. 27, 113).

[97] A. Thiaville, S. Rohart, E. Jué, V. Cros and A. Fert, 'Dynamics of Dzyaloshinskii domain walls in ultrathin magnetic films', *EPL (Europhysics Letters)*, vol. 100, no. 5, p. 57 002, 2012. DOI: 10.1209/0295-5075/100/57002 (cit. on pp. 31–33, 94, 128).

[98] K. J. A. Franke, C. Ophus, A. K. Schmid and C. H. Marrows, 'Switching between magnetic bloch and néel domain walls with anisotropy modulations', *Phys. Rev. Lett.*, vol. 127, p. 127 203, 12 2021. DOI: 10.1103/PhysRevLett.127.127203 (cit. on p. 32).

[99] A. N. Bogdanov and D. A. Yablonskii, 'Thermodynamically stable "vortices" in magnetically ordered crystals.The mixed state of magnets', *Zh. Eksp. Teor. Fiz*, vol. 95, pp. 187–182, 1989 (cit. on pp. 35, 38).

[100] W. Jiang, P. Upadhyaya, W. Zhang *et al.*, 'Blowing magnetic skyrmion bubbles', *Science*, vol. 349, no. 6245, pp. 283–286, 2015. DOI: 10.1126/science.aaa1442 (cit. on pp. 35, 79, 92, 93, 103).

[101] O. Boulle, J. Vogel, H. Yang *et al.*, 'Room-temperature chiral magnetic skyrmions in ultrathin magnetic nanostructures', *Nature Nanotechnology*, vol. 11, no. 5, pp. 449–454, 2016. DOI: 10.1038/nnano.2015.315 (cit. on pp. 35, 39).

[102] X. Zhang, Y. Zhou, K. Mee Song, T.-E. Park, J. Xia, M. Ezawa, X. Liu, W. Zhao, G. Zhao and S. Woo, 'Skyrmion-electronics: Writing, deleting, reading and processing magnetic skyrmions toward spintronic applications', *Journal of Physics: Condensed Matter*, vol. 32, no. 14, p. 143 001, 2020. DOI: 10.1088/1361-648X/ab5488 (cit. on pp. 35, 40).

[103] T. Skyrme, 'A unified field theory of mesons and baryons', *Nuclear Physics*, vol. 31, pp. 556–569, 1962. DOI: 10.1016/0029-5582(62)90775-7 (cit. on p. 35).

[104] G. E. Brown and M. Rho, Eds., *The multifaceted skyrmion*. Singapore ; Hackensack, NJ: World Scientific, 2010, OCLC: ocn428025889 (cit. on p. 38).

[105] A. N. Bogdanov and U. K. Rößler, 'Chiral Symmetry Breaking in Magnetic Thin Films and Multilayers', *Physical Review Letters*, vol. 87, no. 3, p. 037 203, 2001. DOI: 10.1103/PhysRevLett.87.037203 (cit. on p. 38).

[106] U. K. Rößler, A. N. Bogdanov and C. Pfleiderer, 'Spontaneous skyrmion ground states in magnetic metals', *Nature*, vol. 442, no. 7104, pp. 797–801, 2006. DOI: 10.1038/nature05056 (cit. on p. 38).

[107] S. Mühlbauer, B. Binz, F. Jonietz, C. Pfleiderer, A. Rosch, A. Neubauer, R. Georgii and P. Böni, 'Skyrmion Lattice in a Chiral Magnet', *Science*, vol. 323, no. 5916, pp. 915–919, 2009. DOI: 10.1126/science.1166767 (cit. on p. 38).

[108] X. Z. Yu, Y. Onose, N. Kanazawa, J. H. Park, J. H. Han, Y. Matsui, N. Nagaosa and Y. Tokura, 'Real-space observation of a two-dimensional skyrmion crystal', *Nature*, vol. 465, no. 7300, pp. 901–904, 2010. DOI: 10.1038/nature09124 (cit. on p. 38).

[109] X. Z. Yu, N. Kanazawa, Y. Onose, K. Kimoto, W. Z. Zhang, S. Ishiwata, Y. Matsui and Y. Tokura, 'Near room-temperature formation of a skyrmion crystal in thin-films of the helimagnet FeGe', *Nature Materials*, vol. 10, no. 2, pp. 106–109, 2011. DOI: 10.1038/nmat2916 (cit. on p. 38).

[110] S. Heinze, K. von Bergmann, M. Menzel, J. Brede, A. Kubetzka, R. Wiesendanger, G. Bihlmayer and S. Blügel, 'Spontaneous atomic-scale magnetic skyrmion lattice in two dimensions', *Nature Physics*, vol. 7, no. 9, pp. 713–718, 2011. DOI: 10.1038/nphys2045 (cit. on p. 39).

[111] W. Koshibae and N. Nagaosa, 'Theory of antiskyrmions in magnets', *Nature Communications*, vol. 7, no. 1, p. 10 542, 2016. DOI: 10.1038/ncomms10542 (cit. on p. 39).

[112] X. Z. Yu, Y. Tokunaga, Y. Kaneko, W. Z. Zhang, K. Kimoto, Y. Matsui, Y. Taguchi and Y. Tokura, 'Biskyrmion states and their current-driven motion in a layered manganite', *Nature Communications*, vol. 5, no. 1, p. 3198, 2014. DOI: 10.1038/ncomms4198 (cit. on p. 39).

[113] S. Zhang, F. Kronast, G. van der Laan and T. Hesjedal, 'Real-Space Observation of Skyrmionium in a Ferromagnet-Magnetic Topological Insulator Heterostructure', *Nano Letters*, vol. 18, no. 2, pp. 1057–1063, 2018. DOI: 10.1021/acs.nanolett.7b04537 (cit. on p. 39).

[114] A. G. Kolesnikov, M. E. Stebliy, A. S. Samardak and A. V. Ognev, 'Skyrmionium – high velocity without the skyrmion Hall effect', *Scientific Reports*, vol. 8, no. 1, p. 16 966, 2018. DOI: 10.1038/s41598-018-34934-2 (cit. on pp. 39, 40).

[115] J.-S. B. Tai and I. I. Smalyukh, 'Static Hopf Solitons and Knotted Emergent Fields in Solid-State Noncentrosymmetric Magnetic Nanostructures', *Physical Review Letters*, vol. 121, no. 18, p. 187 201, 2018. DOI: 10.1103/PhysRevLett.121.187201 (cit. on p. 40).

[116] T. Kawakami, T. Mizushima, M. Nitta and K. Machida, 'Stable Skyrmions in S U (2) Gauged Bose-Einstein Condensates', *Physical Review Letters*, vol. 109, no. 1, p. 015 301, 2012. DOI: 10.1103/PhysRevLett.109.015301 (cit. on p. 40).

[117] M. Augustin, S. Jenkins, R. F. L. Evans, K. S. Novoselov and E. J. G. Santos, 'Properties and dynamics of meron topological spin textures in the two-dimensional magnet CrCl3', *Nature Communications*, vol. 12, no. 1, p. 185, 2021. DOI: 10.1038/s41467-020-20497-2 (cit. on p. 40).

[118] X. Z. Yu, W. Koshibae, Y. Tokunaga, K. Shibata, Y. Taguchi, N. Nagaosa and Y. Tokura, 'Transformation between meron and skyrmion topological spin textures in a chiral magnet', *Nature*, vol. 564, no. 7734, pp. 95–98, 2018. DOI: 10.1038/s41586-018-0745-3 (cit. on p. 40).

[119] K. L. Metlov and K. Y. Guslienko, 'Stability of magnetic vortex in soft magnetic nano-sized circular cylinder', *Journal of Magnetism and Magnetic Materials*, vol. 242-245, pp. 1015–1017, 2002. DOI: 10.1016/S0304-8853(01)01360-9 (cit. on p. 40).

[120] L. Shen, J. Xia, X. Zhang, M. Ezawa, O. A. Tretiakov, X. Liu, G. Zhao and Y. Zhou, 'Current-Induced Dynamics and Chaos of Antiferromagnetic Bimerons', *Physical Review Letters*, vol. 124, no. 3, p. 037 202, 2020. DOI: 10.1103/PhysRevLett.124.037202 (cit. on p. 40).

[121] B. Göbel, A. Mook, J. Henk, I. Mertig and O. A. Tretiakov, 'Magnetic bimerons as skyrmion analogues in in-plane magnets', *Physical Review B*, vol. 99, no. 6, p. 060 407, 2019. DOI: 10.1103/PhysRevB.99.060407 (cit. on p. 40).

[122] N. Kent, N. Reynolds, D. Raftrey *et al.*, 'Creation and observation of Hopfions in magnetic multilayer systems', *Nature Communications*, vol. 12, no. 1, p. 1562, 2021. DOI: 10.1038/s41467-021-21846-5 (cit. on p. 40).

[123] X. S. Wang, A. Qaiumzadeh and A. Brataas, 'Current-Driven Dynamics of Magnetic Hopfions', *Physical Review Letters*, vol. 123, no. 14, p. 147 203, 2019. DOI: 10.1103/PhysRevLett.123.147203 (cit. on p. 40).

[124] A. Bernand-Mantel, L. Camosi, A. Wartelle, N. Rougemaille, M. Darques and L. Ranno, 'The skyrmion-bubble transition in a ferromagnetic thin film', *SciPost Physics*, vol. 4, no. 5, p. 027, 2018. DOI: 10.21468/SciPostPhys.4.5.027 (cit. on pp. 41, 90, 92, 108, 133, 134, 136, 148).

[125] K. Everschor-Sitte, J. Masell, R. M. Reeve and M. Kläui, 'Perspective: Magnetic skyrmions—Overview of recent progress in an active research field', *Journal of Applied Physics*, vol. 124, no. 24, p. 240 901, 2018. DOI: 10.1063/1.5048972 (cit. on p. 41).

[126] W. Jiang, G. Chen, K. Liu, J. Zang, S. G. te Velthuis and A. Hoffmann, 'Skyrmions in magnetic multilayers', *Physics Reports*, vol. 704, pp. 1–49, 2017. DOI: 10.1016/j.physrep.2017.08.001 (cit. on p. 41).

[127] A Mougin, M Cormier, J. P Adam, P. J Metaxas and J Ferré, 'Domain wall mobility, stability and walker breakdown in magnetic nanowires', *Europhysics Letters (EPL)*, vol. 78, no. 5, p. 57 007, 2007. DOI: 10.1209/0295-5075/78/57007 (cit. on p. 44).

[128] R. Tomasello, E. Martinez, R. Zivieri, L. Torres, M. Carpentieri and G. Finocchio, 'A strategy for the design of skyrmion racetrack memories', *Scientific Reports*, vol. 4, no. 1, p. 6784, 2015. DOI: 10.1038/srep06784 (cit. on p. 45).

[129] J. Sampaio, V. Cros, S. Rohart, A. Thiaville and A. Fert, 'Nucleation, stability and current-induced motion of isolated magnetic skyrmions in nanostructures', *Nature Nanotechnology*, vol. 8, no. 11, pp. 839–844, 2013. DOI: 10.1038/nnano.2013.210 (cit. on p. 45).

[130] L. Berger, 'Emission of spin waves by a magnetic multilayer traversed by a current', *Physical Review B*, vol. 54, no. 13, pp. 9353–9358, 1996. DOI: 10.1103/PhysRevB.54.9353 (cit. on p. 45).

[131] J. Slonczewski, 'Current-driven excitation of magnetic multilayers', *Journal of Magnetism and Magnetic Materials*, vol. 159, no. 1-2, pp. L1–L7, 1996. DOI: 10.1016/0304-8853(96)00062-5 (cit. on p. 45).

[132] C. Abert, H. Sepehri-Amin, F. Bruckner, C. Vogler, M. Hayashi and D. Suess, 'Fieldlike and Damping-like Spin-Transfer Torque in Magnetic Multilayers', *Physical Review Applied*, vol. 7, no. 5, p. 054 007, 2017. DOI: 10.1103/PhysRevApplied.7.054007 (cit. on p. 45).

[133] Z. Diao, Z. Li, S. Wang, Y. Ding, A. Panchula, E. Chen, L.-C. Wang and Y. Huai, 'Spin-transfer torque switching in magnetic tunnel junctions and spin-transfer torque random access memory', *Journal of Physics: Condensed Matter*, vol. 19, no. 16, p. 165 209, 2007. DOI: 10.1088/0953-8984/19/16/165209 (cit. on p. 46).

[134] S. Urazhdin, N. O. Birge, W. P. Pratt and J. Bass, 'Current-driven magnetic excitations in permalloy-based multilayer nanopillars', *Phys. Rev. Lett.*, vol. 91, p. 146 803, 14 2003. DOI: 10.1103/PhysRevLett.91.146803 (cit. on p. 46).

[135] S. I. Kiselev, J. C. Sankey, I. N. Krivorotov, N. C. Emley, R. J. Schoelkopf, R. A. Buhrman and D. C. Ralph, 'Microwave oscillations of a nanomagnet driven by a spin-polarized current', *Nature*, vol. 425, no. 6956, pp. 380–383, 2003. DOI: 10.1038/nature01967 (cit. on p. 46).

[136] E. Jué, 'Dynamique du déplacement de parois magnétiques dans les couches ultra-minces à forte interaction spin-orbite', Ph.D. dissertation, 2013 (cit. on p. 47).

[137] A. Manchon, J. Železný, I. Miron, T. Jungwirth, J. Sinova, A. Thiaville, K. Garello and P. Gambardella, 'Current-induced spin-orbit torques in ferromagnetic and antiferromagnetic systems', *Reviews of Modern Physics*, vol. 91, no. 3, p. 035 004, 2019. DOI: 10.1103/RevModPhys.91.035004 (cit. on pp. 51, 56).

[138] I. Mihai Miron, G. Gaudin, S. Auffret, B. Rodmacq, A. Schuhl, S. Pizzini, J. Vogel and P. Gambardella, 'Current-driven spin torque induced by the Rashba effect in a ferromagnetic metal layer', *Nature Materials*, vol. 9, no. 3, pp. 230–234, 2010. DOI: 10.1038/nmat2613 (cit. on p. 51).

[139] M. I. Dyakonov and V. I. Perel, 'Current-induced spin orientation of electrons in semiconductors', *Physics Letters A*, vol. 35, no. 6, pp. 459–460, 1971. DOI: 10.1016/0375-9601(71)90196-4 (cit. on p. 51).

[140] ——, 'Current-induced spin orientation of electrons in semiconductors', *Physics Letters A*, vol. 35, no. 6, pp. 459–460, 1971. DOI: https://doi.org/10.1016/0375-9601(71)90196-4 (cit. on p. 51).

[141] J. Masell and K. Everschor-Sitte, 'Current-induced dynamics of chiral magnetic structures: Creation, motion, and applications', in *Chirality, Magnetism and Magnetoelectricity: Separate Phenomena and Joint Effects in Metamaterial Structures*, E. Kamenetskii, Ed. Cham: Springer International Publishing, 2021, pp. 147–181. DOI: 10.1007/978-3-030-62844-4_7 (cit. on p. 51).

[142] P. M. Haney, H.-W. Lee, K.-J. Lee, A. Manchon and M. D. Stiles, 'Current induced torques and interfacial spin-orbit coupling: Semiclassical modeling', *Phys. Rev. B*, vol. 87, p. 174 411, 17 2013. DOI: 10.1103/PhysRevB.87.174411 (cit. on p. 51).

[143] F. Büttner, I. Lemesh and G. S. D. Beach, 'Theory of isolated magnetic skyrmions: From fundamentals to room temperature applications', *Scientific Reports*, vol. 8, no. 1, p. 4464, 2018. DOI: 10.1038/s41598-018-22242-8 (cit. on p. 51).

[144] H. L. Wang, C. H. Du, Y. Pu, R. Adur, P. C. Hammel and F. Y. Yang, 'Scaling of Spin Hall Angle in 3d, 4d, and 5d Metals from Y 3 Fe 5 O 12 /Metal Spin Pumping', *Physical Review Letters*, vol. 112, no. 19, p. 197 201, 2014. DOI: 10.1103/PhysRevLett.112.197201 (cit. on pp. 51, 53).

[145] Y. K. Kato, R. C. Myers, A. C. Gossard and D. D. Awschalom, 'Observation of the Spin Hall Effect in Semiconductors', *Science*, vol. 306, no. 5703, pp. 1910–1913, 2004. DOI: 10.1126/science.1105514 (cit. on p. 53).

[146] G. Pietro and M. I. Mihai, 'Current-induced spin–orbit torques', *Philosophical Transactions of the Royal Society A: Mathematical, Physical and Engineering Sciences*, vol. 369, no. 1948, pp. 3175–3197, 2011. DOI: 10.1098/rsta.2010.0336 (cit. on p. 55).

[147] A. Manchon and S. Zhang, 'Theory of nonequilibrium intrinsic spin torque in a single nanomagnet', *Physical Review B*, vol. 78, no. 21, p. 212 405, 2008. DOI: 10.1103/PhysRevB.78.212405 (cit. on p. 56).

[148] A. V. Khvalkovskiy, K. A. Zvezdin, Y. V. Gorbunov, V. Cros, J. Grollier, A. Fert and A. K. Zvezdin, 'High Domain Wall Velocities due to Spin Currents Perpendicular to the Plane', *Physical Review Letters*, vol. 102, no. 6, p. 067 206, 2009. DOI: 10.1103/PhysRevLett.102.067206 (cit. on p. 56).

[149] K. Obata and G. Tatara, 'Current-induced domain wall motion in Rashba spin-orbit system', *Physical Review B*, vol. 77, no. 21, p. 214 429, 2008. DOI: 10.1103/PhysRevB.77.214429 (cit. on p. 56).

[150] A. V. Khvalkovskiy, V. Cros, D. Apalkov, V. Nikitin, M. Krounbi, K. A. Zvezdin, A. Anane, J. Grollier and A. Fert, 'Matching domain-wall configuration and spin-orbit torques for efficient domain-wall motion', *Physical Review B*, vol. 87, no. 2, p. 020 402, 2013. DOI: 10.1103/PhysRevB.87.020402 (cit. on pp. 56, 57).

[151] A. A. Thiele, 'Steady-state motion of magnetic domains', *Phys. Rev. Lett.*, vol. 30, pp. 230–233, 6 1973. DOI: 10.1103/PhysRevLett.30.230 (cit. on p. 57).

[152] S. Woo, K. Litzius, B. Krueger *et al.*, 'Observation of room-temperature magnetic skyrmions and their current-driven dynamics in ultrathin metallic ferromagnets', *Nature materials*, vol. 15, pp. 501–506, 2016. DOI: https://www.nature.com/articles/nmat4593 (cit. on pp. 58, 94).

[153] R. Juge, S.-G. Je, D. d. S. Chaves *et al.*, 'Current-Driven Skyrmion Dynamics and Drive-Dependent Skyrmion Hall Effect in an Ultrathin Film', *Physical Review Applied*, vol. 12, no. 4, p. 044 007, 2019. DOI: 10.1103/PhysRevApplied.12.044007 (cit. on pp. 58, 108, 129, 130, 147, 149, 153–155).

[154] W. Jiang, X. Zhang, G. Yu *et al.*, 'Direct observation of the skyrmion Hall effect', *Nature Physics*, vol. 13, no. 2, pp. 162–169, 2017. DOI: 10.1038/nphys3883 (cit. on pp. 58, 108, 143).

[155] K. Litzius, I. Lemesh, B. Krüger *et al.*, 'Skyrmion Hall effect revealed by direct time-resolved X-ray microscopy', *Nature Physics*, vol. 13, no. 2, pp. 170–175, 2017. DOI: 10.1038/nphys4000 (cit. on pp. 58, 143).

[156] C Reichhardt and C. J. Olson Reichhardt, 'Noise fluctuations and drive dependence of the skyrmion Hall effect in disordered systems', *New Journal of Physics*, vol. 18, no. 9, p. 095 005, 2016. DOI: 10.1088/1367-2630/18/9/095005 (cit. on pp. 58, 108).

[157] J. Iwasaki, M. Mochizuki and N. Nagaosa, 'Current-induced skyrmion dynamics in constricted geometries', *Nature Nanotechnology*, vol. 8, pp. 742–747, 2013 (cit. on pp. 58, 94).

[158] P. Kelly and R. Arnell, 'Magnetron sputtering: A review of recent developments and applications', *Vacuum*, vol. 56, no. 3, pp. 159–172, 2000. DOI: 10.1016/S0042-207X(99)00189-X (cit. on p. 62).

[159] T. Srivastava, 'Engineering and dynamical control of interfacial properties in ultra-thin films to tune magnetic spin textures', Ph.D. dissertation, 2019, p. 73 (cit. on pp. 64, 87).

[160] M. Schott, 'Propriétés magnétiques du système Pt/Co/AlOx et ses variations sous champ électrique', p. 227, 2017 (cit. on p. 64).

[161] S. M. George, 'Atomic Layer Deposition: An Overview', *Chemical Reviews*, vol. 110, no. 1, pp. 111–131, 2010. DOI: 10.1021/cr900056b (cit. on p. 64).

[162] J. K. LL.D., 'Xxiv. on reflection of polarized light from the equatorial surface of a magnet', *The London, Edinburgh, and Dublin Philosophical Magazine and Journal of Science*, vol. 5, no. 30, pp. 161–177, 1878. DOI: 10.1080/14786447808639407 (cit. on p. 68).

[163] Z. Q. Qiu and S. D. Bader, 'Surface magneto-optic kerr effect', *Review of Scientific Instruments*, vol. 71, no. 3, pp. 1243–1255, 2000. DOI: 10.1063/1.1150496 (cit. on p. 68).

[164] M. Faraday, 'Diary', vol. 71, 1845 (cit. on p. 68).

[165] L. Brillouin, 'Diffusion de la lumière et des rayons X par un corps transparent homogène', *Annales de Physique*, vol. 9, no. 17, pp. 88–122, 1922. DOI: 10.1051/anphys/192209170088 (cit. on p. 74).

[166] T. Srivastava, 'Mapping different skyrmion phases in double wedges of Ta/FeCoB/TaOx trilayers', *Physical Review B*, p. 5, 2019 (cit. on pp. 80, 83, 87, 93).

[167] M. Chsiev and F. Ibrahim, *Private communication*, (cit. on p. 87).

[168] F. Ibrahim, A. Hallal, A. Kalitsov, D. Stewart, B. Dieny and M. Chshiev, 'Unveiling temperature-dependence mechanisms of perpendicular magnetic anisotropy at Fe/MgO interfaces', *Phys. Rev. Applied*, vol. 17, p. 054 041, 5 2022. DOI: 10.1103/PhysRevApplied.17.054041 (cit. on p. 87).

[169] A. Singh, S. Gupta, M. Kuteifan, M. Lubarda, V. Lomakin and O. Mryasov, 'Effect of interlayer exchange coupling parameter on switching time and critical current density in composite free layer', *Journal of Applied Physics*, vol. 115, no. 17, p. 17D111, 2014. DOI: 10.1063/1.4861215 (cit. on p. 87).

[170] Y. Liu, L. Hao and J. Cao, 'Effect of annealing conditions on the perpendicular magnetic anisotropy of ta/cofeb/mgo multilayers', *AIP Advances*, vol. 6, no. 4, p. 045 008, 2016. DOI: 10.1063/1.4947132 (cit. on p. 88).

[171] J. W. Koo, S. Mitani, T. T. Sasaki, H. Sukegawa, Z. C. Wen, T. Ohkubo, T. Niizeki, K. Inomata and K. Hono, 'Large perpendicular magnetic anisotropy at fe/mgo interface', *Applied Physics Letters*, vol. 103, no. 19, p. 192 401, 2013. DOI: 10.1063/1.4828658 (cit. on p. 88).

[172] C. B. Lee, B. S. Kang, A. Benayad, M. J. Lee, S.-E. Ahn, K. H. Kim, G. Stefanovich, Y. Park and I. K. Yoo, 'Effects of metal electrodes on the resistive memory switching property of NiO thin films', *Applied Physics Letters*, vol. 93, no. 4, p. 042 115, 2008. DOI: 10.1063/1.2967194 (cit. on p. 88).

[173] J. Wang, L. Yang, S. Yang, Y. Jia, M. Chen, Y. Qiao, P. Guo, S. Zhu and F. Wang, 'Effect of Phase Elements on Oxidation Behavior of Nanocrystalline Coatings at 1050 °C', *Materials*, vol. 14, no. 1, p. 202, 2021. DOI: 10.3390/ma14010202 (cit. on p. 88).

[174] H.-G. Lee, *Chemical thermodynamics for metals and materials*. London : River Edge, NJ: Imperial College Press ; World Scientific Pub, 1999, p. 130 (cit. on p. 88).

[175] R. Kumar, C.-E. Fillion, B. Lovery *et al.*, *Control of skyrmion chirality in ta/fecob/taox trilayers by taox oxidation and fecob thickness*, 2020. DOI: 10.48550/ARXIV.2009.13136 (cit. on pp. 92–94).

[176] R. A. Khan, P. M. Shepley, A. Hrabec, A. W. J. Wells, B. Ocker, C. H. Marrows and T. A. Moore, 'Effect of annealing on the interfacial dzyaloshinskii-moriya interaction in ta/cofeb/mgo trilayers', *Applied Physics Letters*, vol. 109, no. 13, p. 132 404, 2016. DOI: 10.1063/1.4963731 (cit. on pp. 92, 93).

[177] R. Lo Conte, E. Martinez, A. Hrabec *et al.*, 'Role of b diffusion in the interfacial dzyaloshinskii-moriya interaction in Ta/co20Fe60b20/MgO nanowires', *Phys. Rev. B*, vol. 91, p. 014 433, 1 2015. DOI: 10.1103/PhysRevB.91.014433 (cit. on pp. 92, 93).

[178] I Benguettat-El Mokhtari, D Ourdani, Y Roussigné, R. B. Mos, M Nasui, S. M. Chérif, A Stachkevich, M. S. Gabor and M Belmeguenai, 'Investigation of the correlation between perpendicular magnetic anisotropy, spin mixing conductance and interfacial Dzyaloshinskii–Moriya interaction in CoFeB-based systems', *Journal of Physics D: Applied Physics*, vol. 53, no. 50, p. 505 003, 2020. DOI: 10.1088/1361-6463/abb488 (cit. on pp. 92, 93).

[179] G. Yu, P. Upadhyaya, Q. Shao *et al.*, 'Room-temperature skyrmion shift device for memory application', *Nano Letters*, vol. 17, no. 1, pp. 261–268, 2017. DOI: 10.1021/acs.nanolett.6b04010 (cit. on pp. 92, 93, 125).

[180] A. K. Chaurasiya, S. Choudhury, J. Sinha and A. Barman, 'Dependence of interfacial dzyaloshinskii-moriya interaction on layer thicknesses in Ta/Co−Fe−B/tao$x$ heterostructures from brillouin light scattering', *Phys. Rev. Applied*, vol. 9, p. 014 008, 1 2018. DOI: 10.1103/PhysRevApplied.9.014008 (cit. on pp. 92, 93).

[181] Y. Jibiki, M. Goto, E. Tamura *et al.*, 'Skyrmion brownian circuit implemented in continuous ferromagnetic thin film', *Applied Physics Letters*, vol. 117, no. 8, p. 082 402, 2020. DOI: 10.1063/5.0011105 (cit. on pp. 92, 93).

[182] C.-E. Fillion, J. Fischer, R. Kumar *et al.*, 'Gate-controlled skyrmion and domain wall chirality', *Nature Communications*, vol. 13, no. 1, p. 5257, 2022. DOI: 10.1038/s41467-022-32959-w (cit. on pp. 93, 105).

[183] H. T. Nembach, J. M. Shaw, M. Weiler, E. Jué and T. J. Silva, 'Linear relation between Heisenberg exchange and interfacial Dzyaloshinskii–Moriya interaction in metal films', *Nature Physics*, vol. 11, no. 10, pp. 825–829, 2015. DOI: 10.1038/nphys3418 (cit. on p. 94).

[184] G. Yu, P. Upadhyaya, X. Li, W. Li, S. K. Kim, Y. Fan, K. L. Wong, Y. Tserkovnyak, P. K. Amiri and K. L. Wang, 'Room-temperature creation and spin-orbit torque manipulation of skyrmions in thin films with engineered asymmetry', *Nano Letters*, vol. 16, pp. 1981–1988, 2016. DOI: 10.1021/acs.nanolett.5b05257 (cit. on pp. 94, 112).

[185] A. Hoffmann, 'Spin Hall Effects in Metals', *IEEE Transactions on Magnetics*, vol. 49, no. 10, pp. 5172–5193, 2013. DOI: 10.1109/TMAG.2013.2262947 (cit. on p. 94).

[186] L. Liu, C.-F. Pai, Y. Li, H. W. Tseng, D. C. Ralph and R. A. Buhrman, 'Spin-torque Switching with the Giant Spin Hall Effect of Tantalum', *Science*, vol. 336, no. 6081, pp. 555–558, 2012. DOI: 10.1126/science.1218197 (cit. on pp. 94, 108, 142).

[187] S. Emori, U. Bauer, S.-M. Ahn, E. Martinez and G. S. D. Beach, 'Current-driven dynamics of chiral ferromagnetic domain walls', *Nature Materials*, vol. 12, no. 7, pp. 611–616, 2013. DOI: 10.1038/nmat3675 (cit. on pp. 94, 108).

[188] L. H. Diez, M. Voto, A. Casiraghi *et al.*, 'Enhancement of the Dzyaloshinskii-Moriya interaction and domain wall velocity through interface intermixing in Ta/CoFeB/MgO', *Physical Review B*, vol. 99, no. 5, p. 054 431, 2019. DOI: 10.1103/PhysRevB.99.054431 (cit. on p. 97).

[189] S.-G. Je, D.-H. Kim, S.-C. Yoo, B.-C. Min, K.-J. Lee and S.-B. Choe, 'Asymmetric magnetic domain-wall motion by the Dzyaloshinskii-Moriya interaction', *Physical Review B*, vol. 88, no. 21, p. 214 401, 2013. DOI: 10.1103/PhysRevB.88.214401 (cit. on p. 98).

[190] H. Yang, A. Thiaville, S. Rohart, A. Fert and M. Chshiev, 'Anatomy of Dzyaloshinskii-Moriya Interaction at Co / Pt Interfaces', *Physical Review Letters*, vol. 115, no. 26, p. 267 210, 2015. DOI: 10.1103/PhysRevLett.115.267210 (cit. on pp. 98, 99).

[191] S. Zhang and Z. Li, 'Roles of nonequilibrium conduction electrons on the magnetization dynamics of ferromagnets', *Phys. Rev. Lett.*, vol. 93, p. 127 204, 12 2004. DOI: 10.1103/PhysRevLett.93.127204 (cit. on p. 103).

[192] E Tamura, C Liu, S Miki, J Cho, M Goto, H Nomura, R Nakatani and Y Suzuki, 'Skyrmion confinement and dynamics in tracks patterned with magnetic anisotropy: Theory and simulations', *arXiv:2005.04860*, no. 2005.04860, 2020 (cit. on p. 110).

[193] F. Ibrahim, A. Hallal, B. Dieny and M. Chshiev, 'Establishing characteristic behavior of voltage control of magnetic anisotropy by ionic migration', *Physical Review B*, vol. 98, p. 214 441, 2018. DOI: https://doi.org/10.1103/PhysRevB.98.214441 (cit. on p. 113).

[194] A. J. Tan, M. Huang, C. O. Avci, F. Buettner, M. Mann, W. Hu, C. Mazzoli, S. Wilkins, H. L. Tuller and G. S. D. Beach, 'Magneto-ionic control of magnetism using a solid-state proton pump', *Nat. Mater.*, vol. 18, p. 35, 2019. DOI: 10.1038/s41563-018-0211-5 (cit. on pp. 113, 119).

[195] K.-Y. Lee, S. Jo, A. J. Tan *et al.*, 'Fast magneto-ionic switching of interface anisotropy using yttria-stabilized zirconia gate oxide', *Nano Lett.*, vol. 20, no. 5, p. 3435, 2020. DOI: 10.1021/acs.nanolett.0c00340 (cit. on p. 113).

[196] B. Mohammad, M. A. Jaoude, V. Kumar, D. M. Al Homouz, H. A. Nahla, M. Al-Qutayri and N. Christoforou, 'State of the art of metal oxide memristor devices', *Nanotechnology Reviews*, vol. 5, no. 3, 2016. DOI: 10.1515/ntrev-2015-0029 (cit. on p. 113).

[197] C. Grezes, F. Ebrahimi, J. G. Alzate1, X. Cai1, J. A. Katine, J. Langer, B. Ocker, P. K. Amiri, and K. L. Wang, 'Ultra-low switching energy and scaling in electric-field-controlled nanoscale magnetic tunnel junctions with high resistance-area product', *Appl. Phys. Lett.*, vol. 108, p. 012 403, 2016. DOI: https://doi.org/10.1063/1.4939446 (cit. on p. 119).

[198] V. H., M. N. SAKIB, S. GANGULY, M. STAN, M. W. DANIELS, A. MADHAVAN, M. D. STILES and A. W. GHOSH, 'Temporal memory with magnetic racetracks', *IEEE Journal on Exploratory Solid-State Computational Devices and Circuits*, vol. 6, p. 107, 2020. DOI: 10.1109/JXCDC.2020.3022381 (cit. on p. 119).

[199] A. Madhavan, T. Sherwood and D. Strukov, 'Race logic: A hardware acceleration for dynamic programming algorithms', *ACM SIGARCH Computer Architecture News*, vol. 42, no. 3, pp. 517–528, 2014. DOI: 10.1145/2678373.2665747 (cit. on p. 119).

[200] Q. Xia and J. J. Yang, 'Memristive crossbar arrays for brain-inspired computing', *Nature Materials*, vol. 18, no. 4, pp. 4871–4877, 2019. DOI: 10.1021/acs.nanolett.8b01502 (cit. on p. 119).

[201] A. Bernand-Mantel, C. B. Muratov and T. M. Simon, 'Unraveling the role of dipolar versus dzyaloshinskii-moriya interactions in stabilizing compact magnetic skyrmions', *Phys. Rev. B*, vol. 101, p. 045 416, 2020. DOI: 10.1103/PhysRevB.101.045416 (cit. on pp. 119, 133).

[202] S. L. Zhang, G. van der Laan, W. W. Wang, A. A. Haghighirad and T. Hesjedal, 'Direct observation of twisted surface skyrmions in bulk crystals', *Phys. Rev. Lett.*, vol. 120, p. 227 202, 22 2018. DOI: 10.1103/PhysRevLett.120.227202 (cit. on pp. 128, 129).

[203] C. Jin, C. Zhang, C. Song, J. Wang, H. Xia, Y. Ma, J. Wang, Y. Wei, J. Wang and Q. Liu, 'Current-induced motion of twisted skyrmions', *Applied Physics Letters*, vol. 114, no. 19, p. 192 401, 2019. DOI: 10.1063/1.5095686 (cit. on p. 128).

[204] S. Castillo-Sepúlveda, R. Corona, A. Núñez and D. Altbir, 'Twisted skyrmions through dipolar interactions', *Journal of Magnetism and Magnetic Materials*, vol. 484, pp. 451–455, 2019. DOI: https://doi.org/10.1016/j.jmmm.2019.03.014 (cit. on p. 128).

[205] W. Legrand, J.-Y. Chauleau, D. Maccariello, N. Reyren, S. Collin, K. Bouzehouane, N. Jaouen, V. Cros and A. Fert, 'Hybrid chiral domain walls and skyrmions in magnetic multilayers', *Science Advances*, vol. 4, no. 7, eaat0415, 2018. DOI: 10.1126/sciadv.aat0415 (cit. on p. 129).

[206] F. Nasr, 'Properties of 1-kink skyrmions', *Master 2 internship*, 2020 (cit. on p. 129).

[207] P. Géhanne, A. Thiaville, S. Rohart and V. Jeudy, 'Chiral magnetic domain walls under transverse fields: A semi-analytical model', *Journal of Magnetism and Magnetic Materials*, vol. 530, p. 167 916, 2021. DOI: 10.1016/j.jmmm.2021.167916 (cit. on p. 134).

[208] S. Tarasenko, A. Stankiewicz, V. Tarasenko and J. Ferré, 'Bloch wall dynamics in ultrathin ferromagnetic films', *Journal of Magnetism and Magnetic Materials*, vol. 189, no. 1, pp. 19–24, 1998. DOI: 10.1016/S0304-8853(98)00230-3 (cit. on p. 134).

[209] L. Ranno, *Private Communication*, (cit. on p. 136).

[210] W. Legrand, N. Ronceray, N. Reyren, D. Maccariello, V. Cros and A. Fert, 'Modeling the shape of axisymmetric skyrmions in magnetic multilayers', *Phys. Rev. Applied*, vol. 10, p. 064 042, 6 2018. DOI: 10.1103/PhysRevApplied.10.064042 (cit. on pp. 136, 141, 145).

[211] M. Bode, M. Heide, K. von Bergmann, P. Ferriani, S. Heinze, G. Bihlmayer, A. Kubetzka, O. Pietzsch, S. Blügel and R. Wiesendanger, 'Chiral magnetic order at surfaces driven by inversion asymmetry', *Nature*, vol. 447, no. 7141, pp. 190–193, 2007. DOI: 10.1038/nature05802 (cit. on p. 137).

[212] P. Ferriani, K. von Bergmann, E. Y. Vedmedenko, S. Heinze, M. Bode, M. Heide, G. Bihlmayer, S. Blügel and R. Wiesendanger, 'Atomic-scale spin spiral with a unique rotational sense: Mn monolayer on w(001)', *Phys. Rev. Lett.*, vol. 101, p. 027 201, 2 2008. DOI: 10.1103/PhysRevLett.101.027201 (cit. on p. 137).

[213] D. Serrate, P. Ferriani, Y. Yoshida, S.-W. Hla, M. Menzel, K. von Bergmann, S. Heinze, A. Kubetzka and R. Wiesendanger, 'Imaging and manipulating the spin direction of individual atoms', *Nature Nanotechnology*, vol. 5, no. 5, pp. 350–353, 2010. DOI: 10.1038/nnano.2010.64 (cit. on p. 137).

[214] M. Dai and J.-M. Hu, 'Field-free spin–orbit torque perpendicular magnetization switching in ultrathin nanostructures', *npj Computational Materials*, vol. 6, no. 1, p. 78, 2020. DOI: 10.1038/s41524-020-0347-0 (cit. on p. 142).

[215] M.-W. Yoo, V. Cros and J.-V. Kim, 'Current-driven skyrmion expulsion from magnetic nanostrips', *Phys. Rev. B*, vol. 95, p. 184 423, 18 2017. DOI: 10.1103/PhysRevB.95.184423 (cit. on pp. 143, 144).

[216] T. Dohi, S. DuttaGupta, S. Fukami and H. Ohno, 'Formation and current-induced motion of synthetic antiferromagnetic skyrmion bubbles', *Nature Communications*, vol. 10, no. 1, p. 5153, 2019. DOI: 10.1038/s41467-019-13182-6 (cit. on p. 144).

[217] X. Zhang, Y. Zhou and M. Ezawa, 'Magnetic bilayer-skyrmions without skyrmion Hall effect', *Nature Communications*, vol. 7, no. 1, p. 10 293, 2016. DOI: 10.1038/ncomms10293 (cit. on p. 144).

[218] S. Woo, K. M. Song, X. Zhang *et al.*, 'Current-driven dynamics and inhibition of the skyrmion Hall effect of ferrimagnetic skyrmions in GdFeCo films', *Nature Communications*, vol. 9, no. 1, p. 959, 2018. DOI: 10.1038/s41467-018-03378-7 (cit. on p. 144).

[219] H. Belrhazi and M. El Hafidi, 'Nucleation and manipulation of single skyrmions using spin-polarized currents in antiferromagnetic skyrmion-based racetrack memories', *Scientific Reports*, vol. 12, no. 1, p. 15 225, 2022. DOI: 10.1038/s41598-022-19587-6 (cit. on p. 144).

[220] K.-W. Kim, K.-W. Moon, N. Kerber, J. Nothhelfer and K. Everschor-Sitte, 'Asymmetric skyrmion Hall effect in systems with a hybrid Dzyaloshinskii-Moriya interaction', *Physical Review B*, vol. 97, no. 22, p. 224 427, 2018. DOI: 10.1103/PhysRevB.97.224427 (cit. on p. 145).

[221] H. Vakili, Y. Xie and A. W. Ghosh, 'Self-focusing hybrid skyrmions in spatially varying canted ferromagnetic systems', *Phys. Rev. B*, vol. 102, p. 174 420, 17 2020. DOI: 10.1103/PhysRevB.102.174420 (cit. on p. 145).

[222] A. Hrabec, J. Sampaio, M. Belmeguenai, I. Gross, R. Weil, S. M. Chérif, A. Stashkevich, V. Jacques, A. Thiaville and S. Rohart, 'Current-induced skyrmion generation and dynamics in symmetric bilayers', *Nature Communications*, vol. 8, no. 1, p. 15 765, 2017. DOI: 10.1038/ncomms15765 (cit. on pp. 153, 154).

[223] R. Juge, 'Exploring different facets of magnetic skyrmion nucleation and dynamics in ultra-thin films', p. 35, 2020. DOI: https://tel.archives-ouvertes.fr/tel-02947020 (cit. on p. 154).

[224] J. D. Jackson, *Classical electrodynamics*, 3rd ed. New York, NY: Wiley, 1999 (cit. on p. 173).

[225] H. Kroemer, 'The Thomas precession factor in spin–orbit interaction', *American Journal of Physics*, vol. 72, no. 1, pp. 51–52, 2004. DOI: 10.1119/1.1615526 (cit. on p. 173).